January 2014

Solution Synthesized Nanostructured Thermoelectric Materials

Scott William Finefrock
Purdue University

Recommended Citation

Finefrock, Scott William, "Solution Synthesized Nanostructured Thermoelectric Materials" (2014). *Open Access Dissertations*. 1074.
https://docs.lib.purdue.edu/open_access_dissertations/1074

Graduate School Form 30
(Updated 11/20/2014)

PURDUE UNIVERSITY
GRADUATE SCHOOL
Thesis/Dissertation Acceptance

This is to certify that the thesis/dissertation prepared

By Scott William Finefrock

Entitled
Solution Synthesized Nanostructured Thermoelectric Materials

For the degree of Doctor of Philosophy

Is approved by the final examining committee:

Yue Wu	John Morgan
Timothy S. Fisher	
R. Byron Pipes	
James Caruthers	

To the best of my knowledge and as understood by the student in the Thesis/Dissertation Agreement, Publication Delay, and Certification/Disclaimer (Graduate School Form 32), this thesis/dissertation adheres to the provisions of Purdue University's "Policy on Integrity in Research" and the use of copyrighted material.

Approved by Major Professor(s): Yue Wu

Approved by: John Morgan 11/13/2014

Head of the Department Graduate Program Date

SOLUTION SYNTHESIZED NANOSTRUCTURED THERMOELECTRIC MATERIALS

A Dissertation
Submitted to the Faculty
of
Purdue University
by
Scott William Finefrock

In Partial Fulfillment of the
Requirements for the Degree
of
Doctor of Philosophy

December 2014
Purdue University
West Lafayette, Indiana

ACKNOWLEDGEMENTS

During my years at Purdue, teamwork, guidance, and support from the people around me have been irreplaceable. As a first year graduate student, I received training from several members of Professor Wu’s group including Haoran Yang, Genqiang Zhang, and Daxin Liang. Later on, I enjoyed helpful discussions about my projects and even participated in collaborative projects with Haiyu Fang, Yanming Sun, Jonatan Albarracin Caballero, and Haoran Yang. I also worked together with Gautam Yadav and Jaewon Lee on lab safety and other upkeep. In conversations with my group members, I was consistently impressed with their creativity and effective problem solving. I thank them all.

I also certainly want to thank the undergraduate and high school students who played a part in my research, particularly Jackie Huynh, Jonathan Pfluger, James Ward, Anita Bhat, Kimberly Rios, and Xiaoqin Zhu. Whether they performed experiments alongside me for one month or one year, I benefited from their insight and hard work.

At various times during my Ph.D., I found a need to reach out to collaborators in many areas. I so appreciate having had the opportunity to work with and learn from electrical

engineers including Professor Ali Shakouri, Dr. Je-Hyeong Bahk, and Amr Mohammed; mechanical engineers including Professor Xiulin Ruan and Yan Wang; physicists including Dr. John Ferguson and Dr. Jiuning Hu; and chemists including Dr. Douglas Dudis and Charles Cooke. They filled gaps in my knowledge and skills and we accomplished more together than I ever could have without them.

My advisor, Yue Wu, has had more influence on my progress as a research scientist than any other individual. I joined his group with minimal experience in nanomaterials research and no experience in thermoelectrics. With his detailed guidance especially during the first two years of my graduate studies, I learned how to perform and report research on nanomaterials. And I so appreciate the freedom he gave me during my third and fourth years to exercise my own creativity and judgment in planning, performing, and evaluating results from experiments. Throughout my entire graduate student experience, Professor Wu was consistently supportive, believing in my abilities and potential.

Finally, I am so grateful to my parents, other family members, and especially my wife for their emotional support. There were a few seasons during my Ph.D. when the outlook seemed bleak and their encouragement made such a difference. I thank them for sharing a broader perspective and believing I would succeed.

TABLE OF CONTENTS

Page

Page

LIST OF TABLES

LIST OF FIGURES

Figure Page

Figure Page

Figure Page

Figure Page

Figure Page

ABSTRACT

Finefrock, Scott W. Ph.D., Purdue University, December 2014. Solution Synthesized Nanostructured Thermoelectric Materials. Major Professor: Yue Wu.

Thermoelectric heat engines are currently used in several niche applications for electricity generation or cooling. Many additional applications would be practical if thermoelectric materials with improved performance could be made. Over the past twenty years, many nanostructured materials have been shown to possess improved performance compared to their bulk counterparts mostly due to the reduction in thermal conductivity associated with nanostructured materials. Several classes of solution synthesized nanostructured materials have achieved high performance, yet significant room for improvement exists for solution synthesized nanostructured PbTe.

This dissertation describes the solution synthesis of ultra-thin PbTe nanowires at a scale of over ten grams per batch. These materials are washed, dried, and compressed at high temperature to form millimeter-scale nanocomposite discs that, in principle, could be diced into pillars for the traditional thermoelectric device architecture. The properties of unintentionally Te-doped PbTe nanowire-based discs are understood in terms of the phase diagram of the Pb-Te system. The properties are similar to those of bulk PbTe, except for the differences in the mobility and lattice component of thermal conductivity. Unintentionally Te-doped PbTe discs have carrier concentrations that are too low to achieve high performance at high temperature where PbTe is best suited, so two doping strategies using Bi and Na are described, which are shown to effectively raise the carrier concentration to the desired range. Finally, the synthesis of PbTe nanowires is enhanced by replacing the highly toxic reducing reagent, hydrazine, with the relatively benign, ascorbic acid. Nanowires of essentially the same diameter are synthesized using ascorbic acid, albeit at a much slower rate as shown by studies of aliquots taken at different times.

In addition to achieving high performance, it is also desirable to create flexible thermoelectric materials as these could be used in a variety of energy harvesting and cooling applications. The recently invented PbTe nanocrystal coated glass fiber composite is one example of such a flexible thermoelectric material. Here, the 3ω method is used to determine the thermal conductivity of PbTe nanocrystal coated glass fiber composites in the axial direction. Careful consideration of the effect of radiation helps to ensure more accurate measurement results. Additionally, two of the major issues with PbTe nanocrystal coatings are relieved by replacing PbTe with Ag_2Te nanocrystals. Prototype flexible thermoelectric devices made from Ag_2Te nanocrystal coated nylon mesh are shown to produce significantly more power than similar devices made using PbTe nanocrystal coated glass fibers.

CHAPTER 1. INTRODUCTION

1.1 Modern Energy and Refrigeration Issues

In recent years, the world has seen rapid increases in population and energy demand.[1] It has been predicted that renewable energy sources will ultimately become more prominent in order to satisfy the energy demands in the long-term.[2,3] In the short-term, regulations within the U.S. will require vehicles to be more fuel efficient.[4] Regulations have also been enacted that target greenhouse gas emissions in general.[5] Future regulations are likely given the growing concerns about carbon dioxide and the potential effects of its large-scale release into the atmosphere as part of traditional fossil fuel-based energy generation.[6] In response to the long- and short-term energy issues, several technologies are being investigated, which could play a variety of niche and large-scale roles.

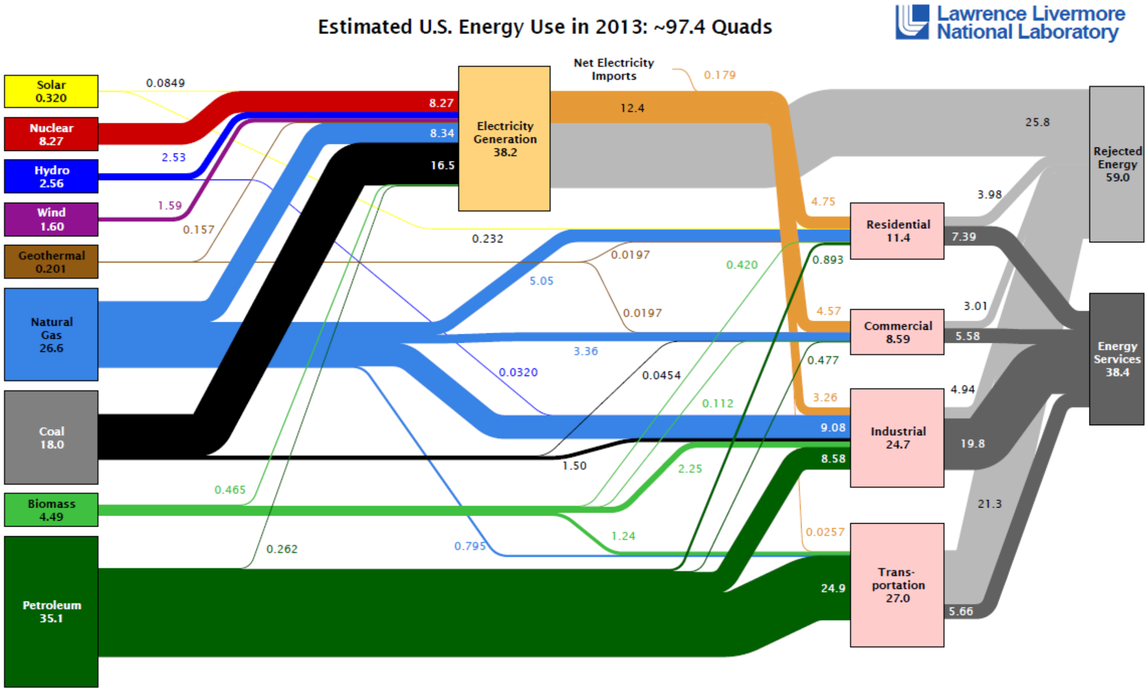

Estimated U.S. Energy Use in 2013: ~97.4 Quads

Source: LLNL 2014. Data is based on DOE/EIA-0035(2014-03), March, 2014. If this information or a reproduction of it is used, credit must be given to the Lawrence Livermore National Laboratory and the Department of Energy, under whose auspices the work was performed. Distributed electricity represents only retail electricity sales and does not include self-generation. EIA reports consumption of renewable resources (i.e., hydro, wind, geothermal and solar) for electricity in BTU-equivalent values by assuming a typical fossil fuel plant "heat rate." The efficiency of electricity production is calculated as the total retail electricity delivered divided by the primary energy input into electricity generation. End use efficiency is estimated as 65% for the residential and commercial sectors 80% for the industrial sector, and 21% for the transportation sector. Totals may not equal sum of components due to independent rounding. LLNL-MI-410527

Figure 1.1 Energy use within the United States, illustrating the significant amount of waste heat associated with energy conversion.[7] Chart made by Lawrence Livermore National Laboratory working under the auspices of the Department of Energy.

Thermoelectric devices are one such technology, which could address the problem that most common forms of energy generation are accompanied by large amounts of waste heat dissipation, as shown in Figure 1.1.[7] Although the second law of thermodynamics requires a certain amount of such heat dissipation, considerable heat is wasted in excess of that required by the Carnot efficiency.[8] Vehicles powered by fossil fuels could particularly benefit from improved efficiency and such improvements are expected to play a major role in achieving recent carbon dioxide emissions regulations.[9,10]

Another pressing engineering challenge is the global elimination of ozone depleting substances, particularly from household refrigerators.[11] Within the United States, the Clean Air Act specifies the elimination of both chlorofluorocarbons and hydro chlorofluorocarbons within set time frames.[12] Alternatives to traditional compressor-based refrigeration such as thermoelectrics could help fulfill the requirements.[13]

1.2 Thermoelectric Devices and Applications

Thermoelectric devices are heat engines. They are comprised of thermoelectric materials which can generate power when placed in a temperature gradient. Conversely, when electric power is supplied to the device, heat is removed from one side of the device. The typical device architecture is shown in Figure 1.2.[14] Some advantages of thermoelectric devices are that they are silent, scalable, and have no moving parts.

While considerable effort has been made in thermoelectrics in the past two decades, they have actually been used for power generation and cooling since the 1950's.[15] Devices from that era included kerosene lamps with thermoelectric elements to co-generate electricity, domestic refrigerators, and portable refrigerators for biological samples. Radioisotope thermoelectric generators, which generally use heat from the decay of radioactive polonium, have been used in space missions and have been of interest to the United States Navy.[16,17]

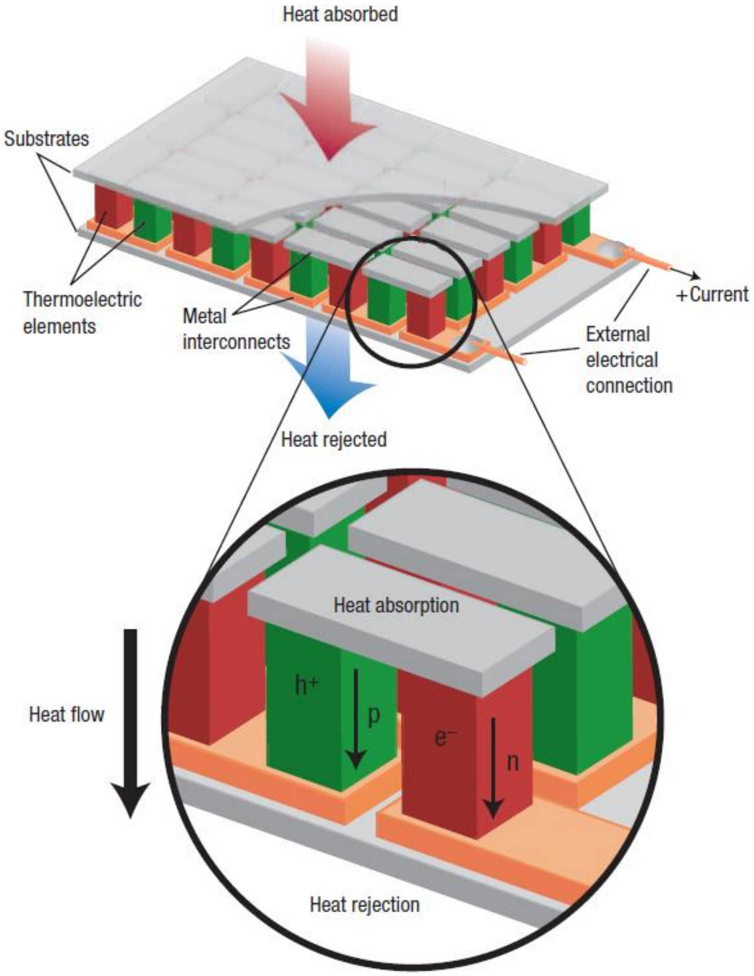

Figure 1.2 Typical thermoelectric device architecture. Reprinted by permission from Macmillan Publishers Ltd: Nature materials (Snyder, G. J. & Toberer, E. S. Complex thermoelectric materials. Nat. Mater. 7, 105–114), copyright 2008.

Currently, thermoelectrics have a variety of practical applications. Thermoelectric coolers are manufactured by RMT Ltd. and Marlow Industries for temperature control in laser diodes and optical monitors in part due to the precise temperature control obtainable using thermoelectrics.[18,19] As thermoelectric devices can even be made on the micro-scale, they have been used when microelectronic elements are to be cooled.[20]

Thermoelectrics have also been used in some cases for microprocessor cooling.[21] To a larger extent, thermoelectrics have been used for miniature food refrigerators that are available at consumer distribution stores.[21] The company, Gentherm, has developed seats for automobiles, which are cooled using thermoelectrics.[22,23] While traditional vehicle air conditioning systems are more efficient for cooling the entire passenger space of the vehicle, thermoelectrics have the distinct advantage of applying more direct cooling to the passengers, thus they are ultimately more energy efficient. Lastly, thermoelectric powered wrist watches, which operate using the wearer's body heat, have been sold by Seiko and Citizen.[24]

If thermoelectric devices could be made more efficient, many additional applications could be realized. There could be broader application of thermoelectric refrigeration.[13] Small internal combustion engines, such as those in lawn mowers, could be replaced by thermoelectric generators.[21] Cogeneration of electricity could be achieved by thermoelectrics using heat from wood stoves.[25] As mentioned previously, thermoelectrics could be used for waste heat recovery in vehicles. Prototypes of such generators were made as early as 1988 and are currently being further developed by General Motors and the United States Department of Energy.[9,25–27] The military is interested in thermoelectric generators, which could harvest electricity from various battlefield heat sources to reduce the number of batteries soldiers must carry.[28] There is also the potential to harvest body heat for wearable computing, particularly if flexible thermoelectrics could be developed.[29–32]

Thermoelectrics could even make an impact in large-scale stationary power generation and the manufacturing industry. For example, thermoelectric generators could be used in power plants to harvest electricity using the temperature gradient between the flue gas and the steam in the boiler as well as between the downstream flue gas and the ambient temperature.[33] Thermoelectric generators could also harvest energy from heat from incinerators such as those used on a large scale in Japan.[25] There is a potential for high grade waste heat recovery in manufacturing processes for which heat exchange with fluids is not employed.[34] Thermoelectrics are also of interest for solar electricity generation. While historical efficiencies were quite low, thermal concentration has recently led to significant improvements.[6,17,35] Clearly, thermoelectrics have the potential to play several important roles in improving energy efficiency.

1.3 Thermoelectric Device Efficiency and the Figure of Merit

Thermoelectric devices operate based on the Seebeck and Peltier effects. The Seebeck effect describes the voltage generated in materials that are exposed to a temperature gradient. Electrical carriers, electrons and/or holes, diffuse from hot to cold and accumulate at the cold end, resulting in a voltage according to

$$S = -\frac{\Delta V}{\Delta T} \tag{1.1}$$

where S is the Seebeck coefficient, ΔT is the temperature difference, and ΔV is the corresponding voltage difference. The Peltier effect describes the heat absorbed or dissipated when electrons flow from one material into another according to

$$Q_P = I \cdot \Pi_{a-b} \tag{1.2}$$

where Q_P is the heat dissipated, I is the current, and $\Pi_{a-b}$is the Peltier coefficient associated with a junction between materials a and b. Furthermore, the Thompson relation specifies that the Peltier and Seebeck coefficients are related by

$$\Pi_{a-b} = T \cdot (S_a - S_b) \tag{1.3}$$

where T is absolute temperature. In general, materials in which electron transport dominates (n-type) have negative Seebeck coefficients while materials in which hole transport dominates (p-type) have positive Seebeck coefficients. Thus devices can be built according to Figure 1.3, which represents the cross section of the basic element of the larger thermoelectric device shown in Figure 1.2.

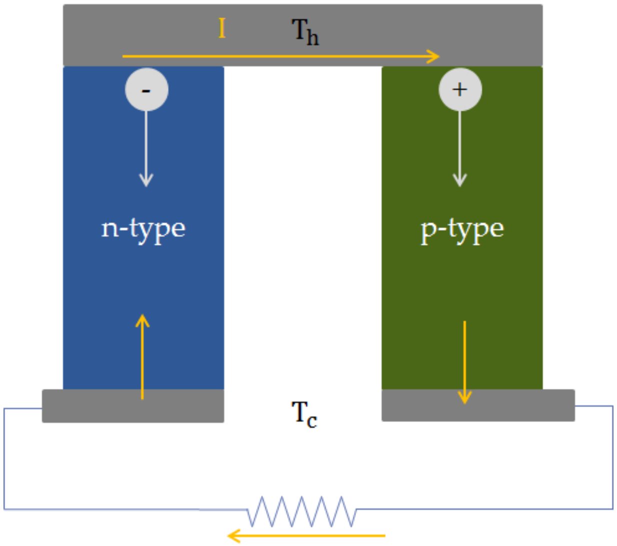

Figure 1.3 Cross section of a thermoelectric device

For the case of a reversible thermoelectric device, the heat transfer occurring in the device can be described as follows. At the hot end, heat flows into the device according the Peltier effect:

$$Q_{P,h} = IT_h(S_p - S_n) \tag{1.4}$$

where the subscript, h refers to the hot side, and the subscripts p and n refer to the p-type and n-type materials. At the cold end, heat flows out of the device according to the Peltier effect:

$$Q_{P,c} = IT_c(S_p - S_n) \tag{1.5}$$

where the subscript, c refers to the cold side. Work is generated according to:

$$W = IV \tag{1.6}$$

$$W = I[(S_p - S_n) \cdot (T_h - T_c)] \tag{1.7}$$

Therefore, the efficiency of the thermoelectric heat engine is given by

$$\eta = \frac{IT_h(S_p - S_n) - IT_c(S_p - S_n)}{IT_h(S_p - S_n)} \tag{1.8}$$

which simplifies to

$$\eta = \frac{T_h - T_c}{T_h} \tag{1.9}$$

Thus, the ideal thermoelectric device possesses the Carnot efficiency regardless of the current flowing or the Seebeck coefficients of the p-type and n-type materials comprised therein. In this ideal picture, charge carriers circulate unimpeded through the device and heat conducted by lattice vibrations is negligible.

As real thermoelectric heat engines are comprised of semiconductors with non-zero electrical resistance and thermal conductance, the efficiency of real devices is limited by Joule heating and heat conduction. The energy balance for real devices is treated rigorously in several texts.[36–38] When optimized for maximum efficiency, the expression for device efficiency is

$$\eta = \frac{T_h - T_c}{T_h} \frac{\sqrt{1 + (ZT)_D} - 1}{\sqrt{1 + (ZT)_D} + T_c/T_h} \tag{1.10}$$

where $(ZT)_D$ is a function of materials properties according to

$$(ZT)_D = \frac{\left(S_p - S_n\right)^2}{\left(\sqrt{\kappa_p \rho_p} + \sqrt{\kappa_n \rho_n}\right)^2} T_{ave} \tag{1.11}$$

where κ is thermal conductivity, ρ is electrical resistivity, and T_{ave} is the average of T_h and T_c. Therefore, the device efficiency is strongly affected by the properties of the thermoelectric materials that are used to generate the Seebeck voltage. In a vast majority of the technical literature, the properties of individual materials are studied. In order to assess the potential of a single material for thermoelectric applications, the value of $(ZT)_D$is evaluated assuming that a material with equal κ and ρ as well as an equal, but opposite value for S exists. In these cases, the value of $(ZT)_D$ would be

$$(ZT)_D = \frac{S^2}{\kappa \rho} T_{ave} \tag{1.12}$$

Thus, the value ZT is defined for a single material according to

$$ZT = \frac{S^2}{\kappa \rho} T \tag{1.13}$$

or equivalently,

$$ZT = \frac{S^2\sigma}{\kappa}T \tag{1.14}$$

where T is the temperature at which the three materials properties are evaluated and σ is electrical conductivity. This value, ZT, is commonly referred to as a material's thermoelectric figure of merit. The relationship between η, T_h, and ZT is described in Figure 1.4, which also shows the efficiencies of several of other heat engines.[8]

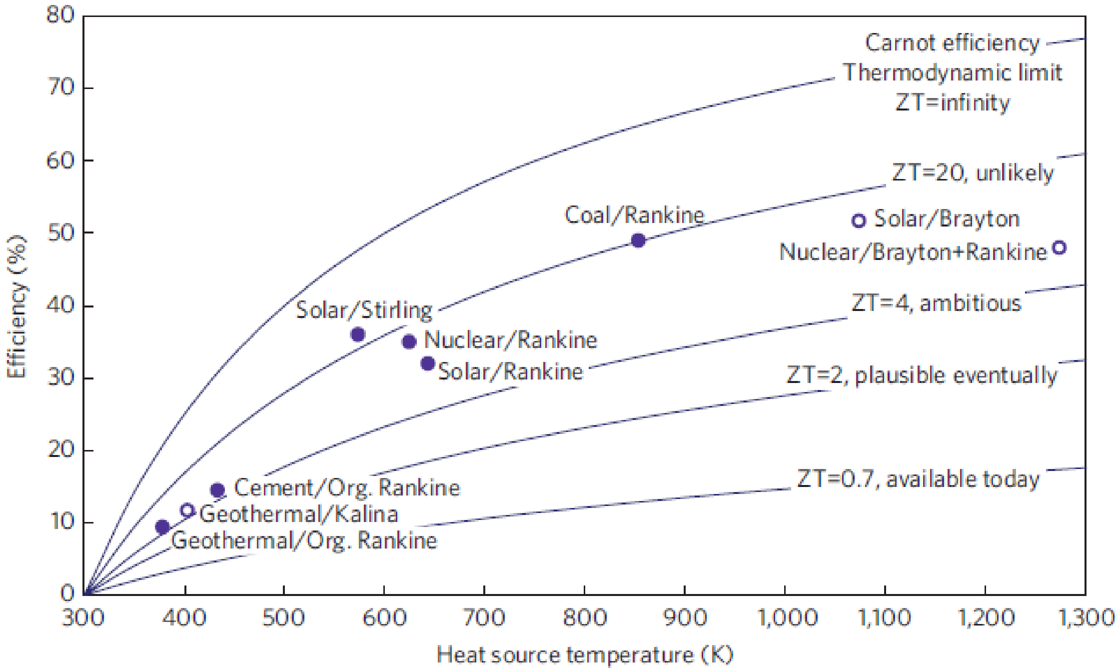

Figure 1.4 Theoretical maximum efficiency of a thermoelectric generator as a function of ZT and T_h as compared with other heat engines. T_c is 300 K. Reprinted by permission from Macmillan Publishers Ltd: Nature materials (Vining, C. B. An inconvenient truth about thermoelectrics. Nat. Mater. 8, 83–85), copyright 2009.

This graph illustrates important trends. Thermoelectric device efficiency increases with increasing material ZT. Also, thermoelectric devices made from materials with figures of merit of 4 or lower have lower efficiencies than the other heat engines shown, and this difference is quite large at temperatures above 600 K where Rankine cycles operate efficiently.

For the design of thermoelectric devices, two additional considerations should be taken into account, which result in a lower efficiency than that show in Figure 1.4. First, in many cases, thermoelectric generators are operated using waste heat which is essentially free. Thus operation at maximum power is more cost effective than operating at conditions of maximum efficiency. Under such maximum power conditions, the device efficiency is given by[39]

$$\eta = \frac{T_h - T_c}{2T_h - \frac{T_h - T_c}{2} + \frac{4T}{(ZT)_D}} \qquad (1.15)$$

Thus, ZT remains an important parameter in such operating conditions. Second, the length of the thermoelectric materials should be optimized to achieve the maximum power output. Real thermoelectric devices consist of a layered structure, as shown in Figure 1.2, including electrical interconnects, ceramic plates, and heat exchangers on both the hot and cold sides. Thus, a significant portion of the overall available temperature difference takes place across materials other than the thermoelectric materials. This results in a reduced Seebeck voltage. The maximum power output is achieved when approximately half of the available temperature difference takes place across the thermoelectric materials.[40,41] These two considerations highlight the fact that the thermoelectric materials are only part of a larger device, in which many engineering and materials challenges exist. Nevertheless, as the inadequacy of thermoelectric materials properties has been a major barrier for thermoelectric device applications, investigations into high ZT materials remains at the forefront of thermoelectrics research.[14]

1.4 Challenges in Finding High ZT Materials

The fundamental challenge in creating materials with high ZT is that improving one of the three relevant properties tends to degrades another. For example, the carrier concentration and hence, electrical conductivity of a material can be easily increased by doping, yet this results in a reduced Seebeck coefficient as shown in Figure 1.5.[14,42] The power factor, which is given by

$$PF = S^2\sigma \tag{1.16}$$

is useful for finding the approximate optimum in carrier concentration and for comparing materials for which the thermal conductivity is unknown. Based on Figure 1.5, semiconductors possess the optimal carrier concentration and are the best thermoelectric materials.

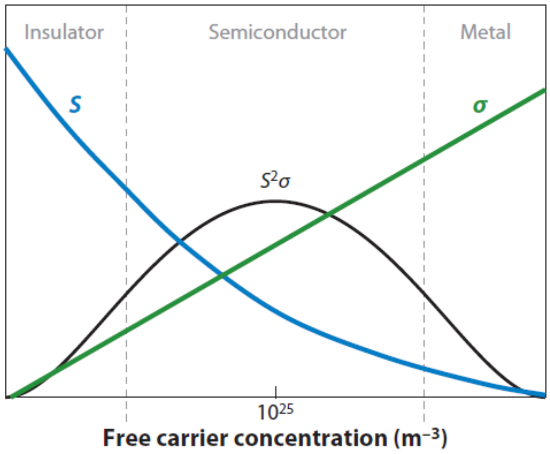

Figure 1.5 Variation of electronic properties with carrier concentration.[42]

The decrease in Seebeck coefficient with increasing carrier concentration shown in Figure 1.5 can be explained using the simplified definition of the Seebeck coefficient as the average energy of carriers with respect to the Fermi level. Using an n-type material as an example, when the Fermi level is just above the middle of the band gap, there is a large difference in energy between the bottom of the conduction band, where the carriers are, and the Fermi level. If the carrier concentration increases, the Fermi level moves upward; this reduces the difference in energy and the magnitude of the Seebeck coefficient.

The relationship between the Seebeck coefficient and carrier concentration for materials with single parabolic bands (SPB) is given more precisely by

$$S = \frac{k_b}{e}\left[\frac{\left(r+\frac{5}{2}\right)}{\left(r+\frac{3}{2}\right)}\cdot\frac{F_{r+\frac{3}{2}}(\zeta^*)}{F_{r+\frac{1}{2}}(\zeta^*)} - \zeta^*\right] \tag{1.17}$$

where k_b is the Boltzmann constant, e is the charge on a proton, r is the scattering coefficient, F is the Fermi integral, and ζ^* is the reduced Fermi level, which is given by

$$\zeta^* = \frac{\zeta}{k_b T} \tag{1.18}$$

where ζ is the Fermi level with respect to the top of the valence band (for p-type semiconductors) or the bottom of the conduction band (for n-type semiconductors).[43] The Fermi integral is given by

$$F_i(\zeta^*) = \int_0^\infty \frac{E^i}{1 + e^{(E-\zeta^*)}} dE \tag{1.19}$$

where i is known as the order of the integral. The scattering coefficient depends on the scattering mechanism. It is equal to -0.5, 0.5, and 1.5 for acoustic phonon scattering, polar optical scattering and ionized impurity scattering, respectively. In practice, the reduced Fermi level can be found using the carrier concentration, n or p, according to

$$n = 2^{\frac{1}{2}}(m_d^* k_b T)^{\frac{3}{2}} F_{\frac{1}{2}}(\zeta^*) \frac{1}{\pi^2 \hbar^3} \tag{1.20}$$

Where $\hbar$ is the reduced Plank's constant and m_d^* is the density of states effective mass that is given by

$$m_d^* = N^{\frac{2}{3}}\left[(m_\perp^*)^2 m_{/\!/}^*\right] \tag{1.21}$$

where N is the valley degeneracy for the band that is relevant for transport, $m_\perp^*$ is the effective mass in the transverse direction, and $m_{/\!/}^*$ is the effective mass in the longitudinal direction. For PbTe and other traditional semiconductors used in thermoelectrics, the values of m_d^* and r are well established in literature.[44,45] Thus, the above equations can be used to predict the Seebeck coefficient accurately in the regime where the SPB approximation is valid.

For metals and degenerate semiconductors, a simpler relationship between Seebeck coefficient and carrier concentration is satisfactory:

$$S = \left[\frac{2\pi^{\frac{2}{3}} k_b^2 T m_d^*}{3^{\frac{5}{3}} e \hbar^2 n^{\frac{2}{3}}}\right] \cdot \left(r + \frac{3}{2}\right) \tag{1.22}$$

Here, the inverse relationship between Seebeck coefficient and carrier concentration can be seen more readily.[43] For the non-degenerate (low carrier concentration) limit, the Pisarenko relation is satisfactory:

$$S = \frac{k_b}{e}\left\{\left(r + \frac{5}{2}\right) + \ln\left[\frac{2(2\pi m_d^* k_b T)^{\frac{3}{2}}}{nh^3}\right]\right\} \tag{1.23}$$

where h is Plank's constant.[43] The three relationships between Seebeck coefficient and carrier concentration are shown graphically in Figure 1.6.

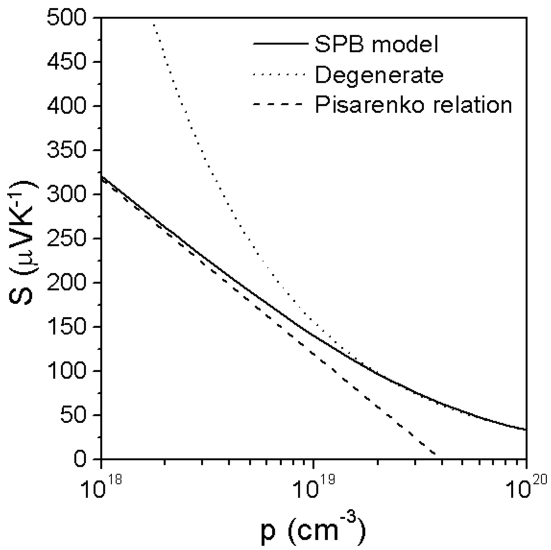

Figure 1.6 Seebeck coefficient versus carrier concentration at 300 K for p-type PbTe.

Of the three models, the full SPB model provides the most accurate relationship across a broad range of carrier concentrations. The relationship for degenerate semiconductors is shown to be a good approximation at high carrier concentration, while the Pisarenko relation matches well at very low carrier concentrations. For materials with non-parabolic bands, there exists a more complicated relationship between the Seebeck coefficient the carrier concentration, yet it remains an inverse relationship, which limits the power factor. In general, the power factor is maximized at high carrier concentrations when the Fermi level is within the conduction or valence band.[46]

A second example of how the improvement in one property tends to degrade another is the relationship between the electrical conductivity and the thermal conductivity. The relationship is given by

$$\kappa_e = L\sigma T \tag{1.24}$$

where κ_e is the electronic component of thermal conductivity, and L is the Lorenz number.[14] This is known as the Wiedemman-Franz law and it is particularly important for metals and highly degenerate semiconductors with σ > 1,000 S/cm. For common thermoelectric materials, lattice vibrations and occasionally electron-hole pairs also contribute to the total thermal conductivity so that

$$\kappa = \kappa_l + \kappa_e + \kappa_{bi} \tag{1.25}$$

where κ_l is the contribution to thermal conductivity by lattice vibrations and κ_{bi} is the contribution from the bipolar effect.[43] The relationship between the thermal conductivity and the carrier concentration for temperatures at which the bipolar contribution is negligible is shown in Figure 1.7.[42] So while an increase in carrier concentration increases the electrical conductivity, it also increases the thermal conductivity, which limits the potential increase in the figure of merit.

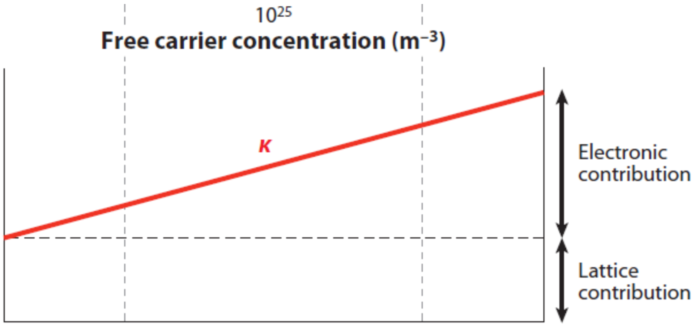

Figure 1.7 Relationship between thermal conductivity and carrier concentration[42]

Figure 1.7 also shows that the lattice contribution is roughly independent of carrier concentration. It is desirable to obtain materials with low values for the lattice contribution to thermal conductivity. Fortunately, there exist guiding principles for such a search. In the simple illustration of a crystal as a system of masses and springs, the group velocity of heat carrying lattice vibrations, also known as phonons, is smaller for crystals with heavy elements and weak bonds.[47] This smaller group velocity leads to a lower thermal conductivity.[48,49] Thus, materials comprised of heavy elements that are held together by weak bonds tend to have lower values of κ_l. The trend of thermal conductivity versus atomic weight is shown graphically in Figure 1.8.[50]

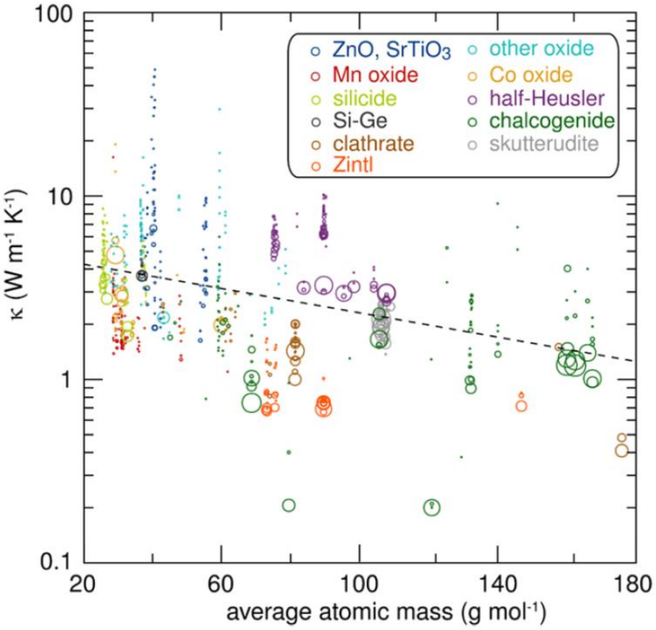

Figure 1.8 Variation of thermal conductivity with atomic weight for several classes of thermoelectric materials. Reprinted with permission from Gaultois, M. W. et al. Data-Driven Review of Thermoelectric Materials: Performance and Resource Considerations. Chem. Mater. 25, 2911–2920. Copyright (2013) American Chemical Society.

Good thermoelectric materials should also have high charge carrier mobilities. In general, increasing mobility allows for an increase in electrical conductivity without a significant decrease in the Seebeck coefficient at low temperature. In general, smaller band gaps are associated with higher mobilities. Still, small band gaps limit the Seebeck coefficient at high temperature.[51] More precisely, for equivalent valence and conduction bands, the maximum Seebeck coefficient is achieved when the Fermi level is at the middle of the band gap

$$S_{max} \approx \frac{E_g}{2eT} \qquad (1.26)$$

where E_g is the band gap.[51,52] Small band gaps have the additional problem of an increased bipolar contribution to thermal conductivity. In this process, thermal excitation causes the band gap energy, E_g, to be absorbed as excitons are formed at the hot end and the same band gap energy, E_g, to be released as excitons recombine at the cold end. As a result of these effects, there exists an approximate relationship between the optimal band gap and operating temperature.[53]

$$E_g \approx 4k_bT \qquad (1.27)$$

In the 1950's and 1960's, the consideration of all of the above optimizations led to the selection of heavily doped Bi_2Te_3, PbTe, and Si/Ge as the best thermoelectric materials with optimal performance at around room temperature, 700K, and 1000 K, respectively. As pure ingots of these materials do not have sufficiently high figures of merit to allow for large-scale applications of thermoelectrics, several approaches have been developed to modify these materials to increase their ZT values.

1.5 Common Approaches to Increase ZT

Perhaps the oldest and most general approach to increase ZT is to control the structure and composition of the material to reduce thermal conductivity while only slightly reducing charge carrier mobility. For several decades, alloying has been employed to reduce the lattice thermal conductivity.[54] The strategy put forward by Airepteyants is to alloy on the cation site for p-type materials and on the anion site for n-type materials in order to prevent a significant decrease in mobility. Conceptually, holes reside preferentially on the anion site, thus alloying on the cation site has a small effect on hole transport. The reverse is true of electrons.[55] As alloy scattering is known to mostly affect short wavelength phonons, nanostructures have recently been employed to scatter longer wavelength phonons to achieve a greater reduction in thermal conductivity.[56] When the additional interfaces are engineered correctly, phonons can be scattered more than charge carriers.[6,57] Such preferential scattering of phonons is summarized in the concept of the phonon glass-electron crystal.[58]

While the above strategies are aimed at a reduction in lattice thermal conductivity, there also exist strategies to improve the power factor. Early on in thermoelectrics research, there were attempts to increase the Seebeck coefficient by changing the scattering parameter from -0.5 to 1.5 by introducing additional ionized impurities.

However, this was generally not successful because of the significant reduction in charge carrier mobility without the anticipated increase in Seebeck coefficient.[59] In 1993, Hicks and Dresselhaus performed calculations on Bi_2Te_3 quantum wires and quantum wells and suggested that significant increases in ZT are possible with ultra-thin wires and sheets.[60,61] In general, the theory behind the enhancement is that electronic density of states is quite different for quantum confined structures as compared with bulk materials.[62] The densities of states of quantum wires and quantum dots resemble a delta function, which was shown to be optimal for thermoelectric materials.[63]

Another approach that has gained some popularity in recent years is energy filtering.[46,62] The principal of energy filtering can be explained as follows. As the Seebeck coefficient is associated with the average energy of carriers with respect to the Fermi level, the contribution of carriers above the Fermi level is partially offset by the contribution of carriers below the Fermi level.[46] Therefore, it has been hypothesized that a sharp energy dependence of the carrier scattering time could reduce the negative contribution of carriers below the Fermi level. In summary, several approaches to increase ZT have been theorized. The current challenge is to demonstrate the effectiveness of these approaches in real materials.

1.6 Materials and Synthetic Approaches to Achieve High ZT

The efforts to design and synthesize improved thermoelectric materials can roughly be divided into three categories: 1) non-traditional thermoelectric materials with complex crystal structures or even non-crystalline materials, 2) nano-sized traditional thermoelectric materials, and 3) millimeter-scale nanocomposites of traditional thermoelectric materials.

1.6.1 Non-Traditional Thermoelectric Materials

Several classes of non-traditional thermoelectric materials with novel compositions and structures such as skutterudites, clathrates, and half-Heuslers have been synthesized and characterized in attempts to demonstrate the phonon-glass electron-crystal concept. These materials are appropriate for thermoelectric applications because they have high charge carrier mobilities and low lattice thermal conductivities. In the case of skutterudites and clathrates, this is in part due to their large unit cells with cages that can be partially filled in order to achieve increased phonon scattering.[64–67] Meanwhile, half-Heuslers benefit from many potential alloy combinations to reduce the thermal conductivity.[68,69] Conducting polymers have also received some attention due their intrinsically low thermal conductivities. New strategies to increase mobility and obtain optimal carrier concentration have led to ZT values well above 0.1 at room temperature.[70–73]

1.6.2 Nano-Sized Traditional Thermoelectric Materials

In the second approach, nanowires or superlattice thin films of several traditional thermoelectric materials have been synthesized in attempts to improve performance using quantum confinement and/or phonon scattering.[74,75] In some cases, enhanced ZT

is in fact observed experimentally for single nanowires and superlattices.[76–78] In response to the results for single nanowires, some research has focused on the synthesis of nanowire arrays in which large numbers of nanowires could operate in parallel to generate useful amounts of power.[79] Some research groups have even begun to address the challenges associated with making devices that capitalize on the advantages of nanowire structures.[80] As thermoelectric power generation scales with the cross section area for heat transport, nanoscale devices have certain disadvantages. In devices made from nanowire arrays, for example, the benefits of quantum confined nanowires are partially offset by the reduced fill factor (volume of nanowires per device volume) required to achieve true quantum confinement within individual nanowires.[81] Meanwhile, thin film superlattices are generally grown by MBE, and are therefore very costly to produce.[82]

1.6.3 Nanocomposites of Traditional Thermoelectric Materials

As there are significant issues associated with single nanowire and superlattice thermoelectric materials, many research groups have focused instead on a third approach to achieve high ZT, the synthesis of bulk materials with nanoscale features, which are commonly known as nanocomposites. Such materials do not benefit from electronic quantum confinement effects, but have been shown to benefit from increased phonon scattering. Most research on nanocomposite thermoelectric materials has focused on materials with compositions that are nearly identical to traditional thermoelectric materials, yet which contain nanoscale features. Three general approaches to synthesize nanocomposite thermoelectric materials are 1) ball milling, 2) solid state synthesis, and 3) solution synthesis.

In the ball milling approach, a large-grained ingot or appropriate elements are ball milled for hours or days. The resulting nanoscale powder is then compressed at high temperature to form a millimeter-scale disc.[83] Several classes of materials have observed an increase in ZT due to the ball-milling strategy. These include: $(Bi,Sb)_2(Te,Se)_3$,[84] Si/Ge,[85,86] and even new materials such as skutterudites.[87] However, for some materials such as PbTe, rapid grain growth occurs during the hot pressing step and no enhancement in ZT as compared with bulk has been observed.[83]

The growth of semiconductors by solid state synthesis generally involves long times and high temperatures, thus large grains are typically created. However, the solid state synthesis of several thermoelectric materials has recently been modified to include small amounts of impurity elements that lead to the formation of nanoprecipitates upon cooling to room temperature.[88] Initial research focused on lead antimony silver telluride.[89] Many impurities have been investigated, particularly in the PbTe system, with varying success.[90–93] Recently, the science of solid state synthesized nanocomposites has advanced to include concepts such as band alignment to prevent mobility reduction,[94,95] mesoscale grain formation by grinding and spark plasma sintering (SPS),[96] and band engineering by selective alloying.[97]

In the solution synthesis approach, nanostructures of traditional thermoelectric materials are grown from the bottom up in solution. These can then be washed, dried and compressed into millimeter-scale discs. The details of this process and the resulting material properties are discussed in chapter 2.

1.7 Dissertation Outline

The remainder of this dissertation focuses on solution synthesized nanostructured thermoelectric materials. In chapter 2, the synthesis and thermoelectric properties of materials described in literature are reviewed. It will be seen that significant room for improvement exists in the PbTe system. The following chapters describe experiments and results for nanostructured PbTe materials. Chapters 3 and 4 describe the large-scale synthesis of PbTe nanowires and their thermoelectric properties. Chapter 5 describes the synthesis and properties of doped PbTe nanowires designed to achieve carrier concentrations closer to the optimal range. As the nanowire synthesis in chapters 3-5 relies on the highly toxic reducing agent, hydrazine, a novel environmentally benign synthesis is developed, which is described in chapter 6. Then chapter 7 begins the theme of flexible thermoelectric materials and describes thermal conductivity measurements of flexible PbTe nanocrystal coated glass fibers. Continuing in the same theme, chapter 8 describes the synthesis and characterization of prototype flexible thermoelectric devices made by coating Ag_2Te nanocrystals onto nylon mesh.

CHAPTER 2. REVIEW OF THE THERMOELECTRIC PROPERTIES OF SOLUTION SYNTHESIZED MATERIALS

2.1 Introduction

Among the efforts to synthesize nanocomposite thermoelectric materials, solution synthesis offers several potential advantages over other methods such as ball milling and the formation of secondary phases using solid state synthesis. Benefits of solution synthesis methods include low synthesis temperatures, short synthesis times, and compatibility with large-scale chemical synthesis practices in industry.[98] These and perhaps other attractive attributes of solution synthesis methods have led to significant interest from academic laboratories and even from the thermoelectrics industry.[99] The first part of this chapter contains a review of the methods involved in making solution synthesized nanocomposites. The second part then reviews the thermoelectric properties of several classes of solution synthesized materials and compares these properties with those of corresponding bulk materials. The methods involved in creating the highest performance solution synthesized materials are discussed in order to highlight the practices that should be employed or considered in future research. The review mainly focuses on chalcogenide materials.

2.2 Solution Synthesis of Nanocomposite Thermoelectrics

The creation of solution synthesized nanocomposite thermoelectric materials generally requires three steps, which are: solution synthesis, washing, and consolidation. These are discussed in detail in the following sections.

2.2.1 Solution Synthesis

There is much diversity in the methods available to synthesize thermoelectric materials in solution. The methods reviewed here include: 1) hydro/solvothermal synthesis, 2) atmospheric pressure synthesis at or below boiling temperature in a solvent of water and/or ethylene glycol 3) ligated chalcogen injection into cation precursor solution in long-chain hydrocarbon solvent, and 4) microwave synthesis. In each case, a wide variety of nanostructure morphologies can be achieved by adjusting the synthesis conditions.

2.2.1.1 Hydro/solvothermal

In the hydro/solvothermal synthesis method the solvent, reactants, and (optionally) a surfactant are loaded into an autoclave, which is then sealed and placed in an oven above the atmospheric pressure boiling point of the solvent. As a result, the pressure increases in the closed vessel during the reaction, in some syntheses even beyond the critical point.[100] Typical conditions used are 100-250 °C and 1-150 bar with reaction times of 4-24 hours.[101] The properties of water and other solvents vary significantly with temperature and pressure such that the solubility of many inorganic substances increases during hydrothermal reactions. Due in part to the closed nature of hydrothermal syntheses, the chemistry of many syntheses is poorly understood. Nevertheless, hydro/solvothermal reactions have been used extensively to make nanostructured binary and ternary oxides as well as chalcogenides.[101–103]

2.2.1.2 Atmospheric Pressure Synthesis at or Below Boiling Temperature in a Solvent of Water and/or Ethylene Glycol

Many chalcogenide syntheses can also take place at atmospheric pressure in glass reaction vessels, often in an inert environment achieved using a Schlenk line. Reagents are mixed in a solvent and allowed to react at elevated temperature.[102,104,105] Temperatures employed range from room temperature to reflux conditions and reaction times range from hours to days.[106–111] Often, products are formed by the reduction of cation precursors with the help of an external reducing agent. Surfactants can be used to control product morphology as well as to lend solubility to the as-grown nanostructures.

2.2.1.3 Ligated Chalcogen Injection into Cation Precursor Solution in Long-Chain Hydrocarbon Solvent

Nanostructured chalcogenides can be synthesized by separately dissolving a cation precursor using a ligand in a long-chain hydrocarbon solvent and a chalcogen precursor using trioctylphosphine (TOP) or a similar solvent. The cation solution is brought to high temperature and the chalcogen source is rapidly injected, causing the formation of colloidal chalcogenide nanostructures.[102,112–116] The syntheses generally take place at atmospheric pressure and temperatures of 100-300 °C. Reactions are generally very rapid; the synthesis solutions are quenched in a water bath only a few minutes after chalcogen injection. The presence of strongly binding ligands serves to both protect the nanocrystals from overgrowth and to make the nanocrystals soluble in organic solvents such as hexane, toluene, and chloroform.

2.2.1.4 Microwave Synthesis

Microwave synthesis has been employed to make a variety of nanostructured materials, often with much shorter reaction times than other methods. Generally, microwave synthesis simply involves the application of microwave heating instead of traditional heating methods such as ovens or heating mantles. Hydro/solvothermal,[117–120] atmospheric pressure synthesis at or below boiling temperature in a solvent of water and/or ethylene glycol,[121–123] and ligated chalcogen synthesis[124] have all been accomplished using microwave heating. A wide variety of nanostructured thermoelectric materials have been made using these methods.

2.2.2 Washing the As-Synthesized Material

Regardless of the synthesis method, as-synthesized nanostructures are dispersed within a mixture of solvent, unreacted precursor, other reagents, and usually a surfactant or ligand. In order to separate pure, dry nanostructured powder, the as-synthesized material is generally combined with an anti-solvent and centrifuged. It is then re-dispersed in a solvent. This process is generally repeated several times, which removes most of the impurities within the product. An optional second purification step involves a hydrazine soak, the goal of which is to remove the surfactant or ligand.[125] If not removed, such organic material would likely hinder inter-grain contact and charge transport in nanocomposite discs. In fact, some researchers have developed synthesis methods that use small molecule structure directing agents instead of long chain hydrocarbons or polymers to further avoid the issues associated with large surfactants.[126–129]

2.2.3 Consolidation of the Material

After washing and optional ligand stripping, the material is vacuum dried to form pure nanostructured powder. Once dry, it is preferable to reduce contact with air as many thermoelectric materials including PbTe are known to slowly oxidize in air.[130] To make millimeter-scale, high relative density discs, the powder is consolidated at high temperature under uniaxial pressure in a process known as hot pressing. High temperatures are necessary to achieve good grain to grain contact and therefore high mobility, yet this can also lead to grain growth, which could nullify the benefits of synthesizing nanostructured material. Therefore, many researchers favor the use of rapid consolidation methods such as SPS, which can achieve high relative density with limited grain growth.[131–133] In some cases, solution processable materials are not fully dried into powder, but rather are cast into films that would be more suitable for thin film thermoelectrics.[134]

2.3 Thermoelectric Properties of Solution Synthesized Materials

2.3.1 p-type and n-type $(Bi,Sb)_2(Te,Se)_3$

Bismuth telluride has been widely studied since the 1950’s and has excellent thermoelectric properties in the temperature range of 200 – 450 K.[135,136] Bismuth telluride has a low thermal conductivity of 1.4 W/mK at 300 K and a sufficiently high mobility such that bulk ingots obtained by traditional solid state routes possess ZT values in the range of 0.9-1.1.[14,135] Binary Bi_2Te_3 can be p-type due to Bi vacancies or Bi_{Te} anti-site defects. Alternatively, it can be n-type due to Te vacancies or Te_{Bi} anti-site defects.[137,138] Alloying with Sb is an effective way to ensure p-type behavior while alloying with Se tends to lead to n-type behavior.[139] The carrier concentration can be adjusted using the fraction of Sb and Se.[140,141] The solution synthesis of $(Bi,Sb)_2(Te,Se)_3$ nanostructures began at least as early as 2003.[142] Research on the thermoelectric properties of bulk nanocomposites made by solution synthesized nanoscale powder has progressed quickly since then.

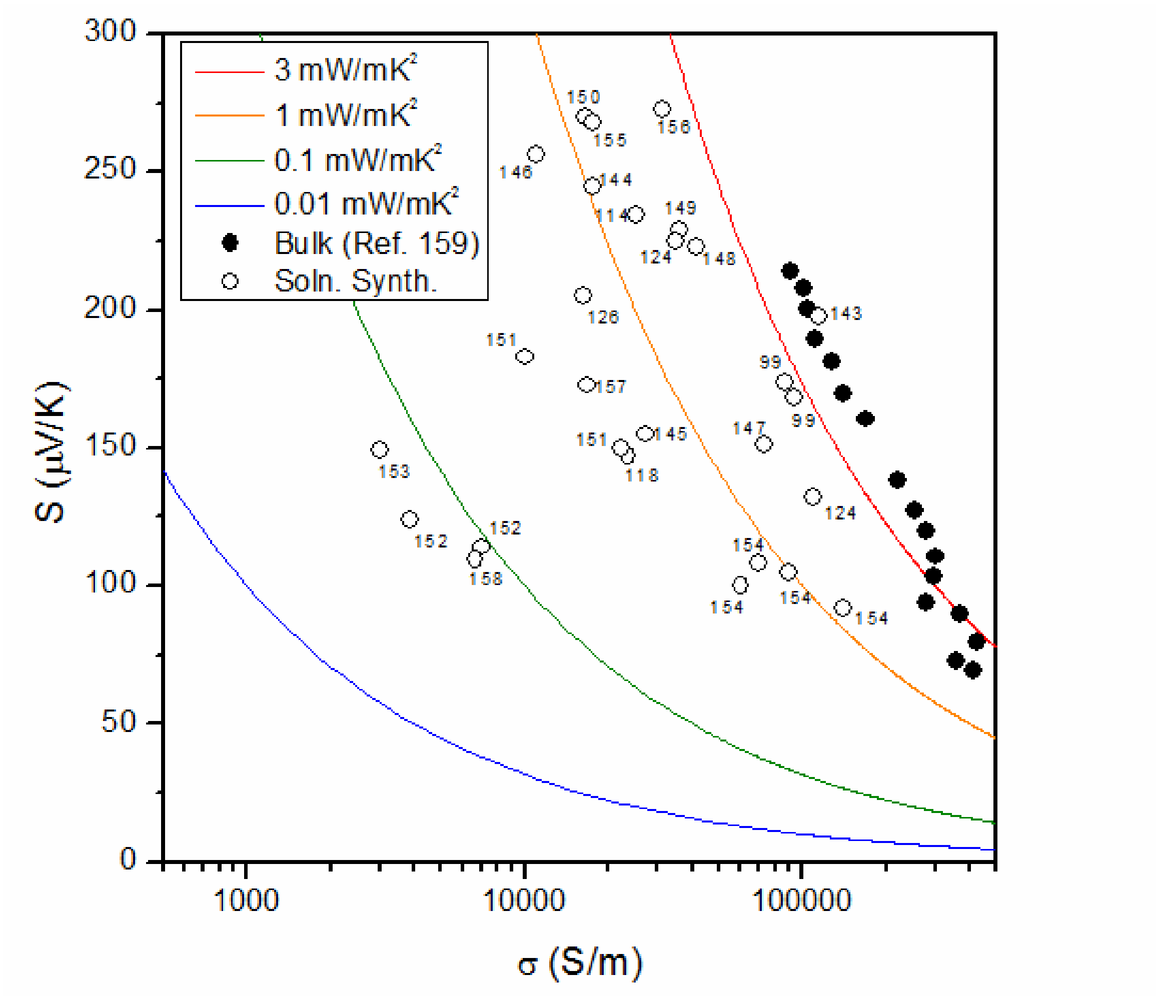

Figure 2.1 Seebeck coefficient versus electrical conductivity near room temperature for p-type $(Bi,Sb)_2(Te,Se)_3$. Data from references 152, 153, 166, 114, 146, 148, and 151 adapted with permission from the American Chemical Society. Copyright 2010 and 2012. See literature cited section for full reference details.

In Figure 2.1, the near room temperature Seebeck coefficient versus the near room temperature electrical conductivity of p-type solution synthesized $(Bi,Sb)_2(Te,Se)_3$ and bulk single crystalline $(Bi,Sb)_2(Te,Se)_3$ is shown along lines of equal power factor.[99,114,118,124,126,143–159] Immediately apparent is the wide range of Seebeck coefficients observed in the various materials, which is indicative of a wide range of carrier concentrations.[141] For $(Bi,Sb)_2(Te,Se)_3$ to exhibit high ZT, the Seebeck coefficient at 300 K should be in the range of 120-290 μV/K, corresponding to carrier concentrations of $4 \times 10^{18} - 7 \times 10^{19}$ /cm^3.[135,140] Therefore, more than half of the samples represented in Figure 2.1 appear to have carrier concentrations that are within the optimal range. The figure also shows that only one of the solution synthesized samples has a power factor equal to that of the single crystals. This is likely related to the reduced mobility associated with small grains and porosity in the solution synthesized samples. Still, several solution synthesized materials possess power factors of nearly 3 mW/mK^2, which combined with low thermal conductivity due to nanoscale grains, lead to high ZT values.

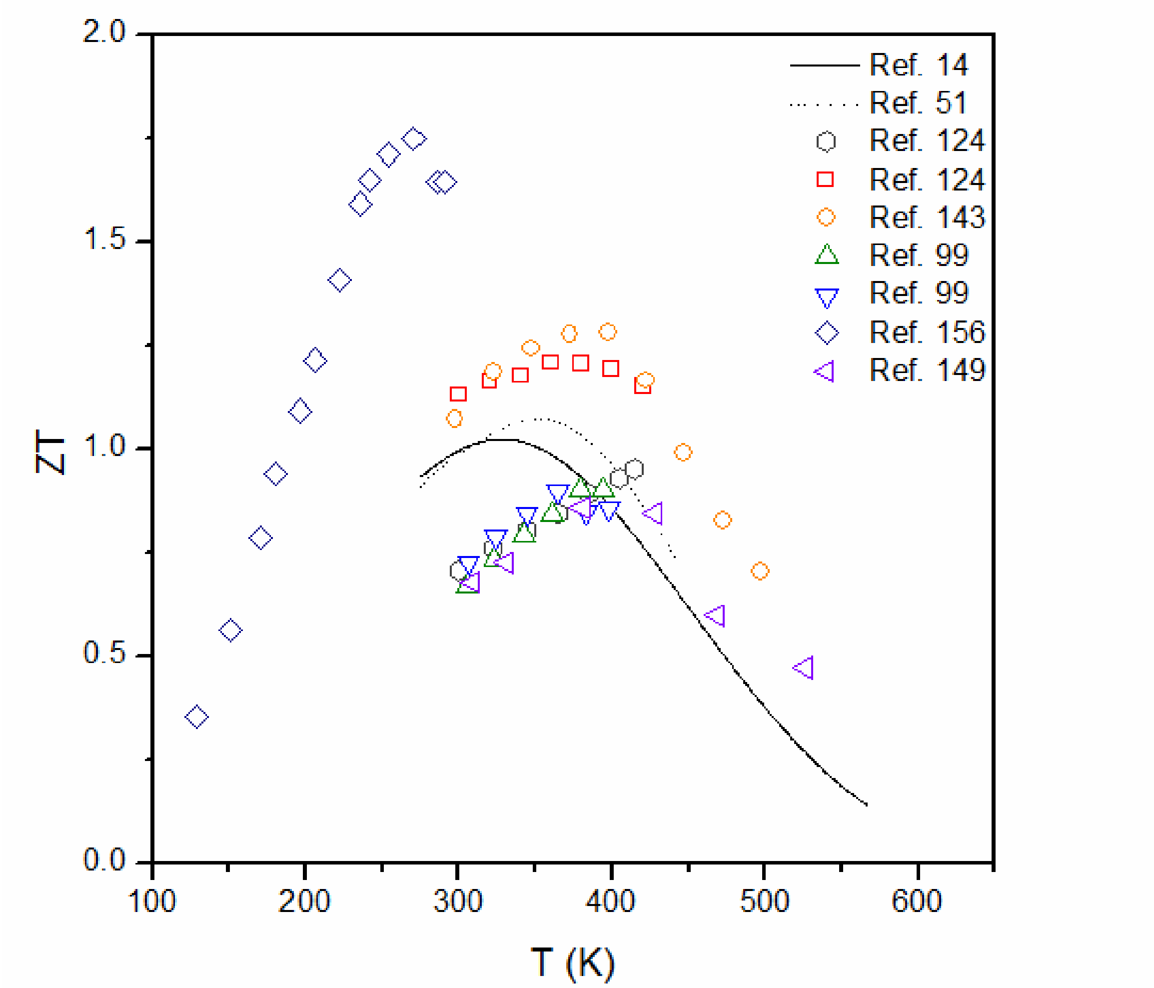

Figure 2.2 ZT versus temperature for solution synthesized (symbols) and bulk (lines) p-type $(Bi,Sb)_2(Te,Se)_3$.

In Figure 2.2, the ZT versus temperature for seven of the best solution synthesized p-type $(Bi,Sb)_2(Te,Se)_3$ materials is plotted along with those of two solid state synthesized p-type $(Bi,Sb)_2(Te,Se)_3$ samples without intentional nanostructuring.[14,51,99,124,143,149,156] Clearly, solution synthesized $(Bi,Sb)_2(Te,Se)_3$ can exhibit excellent performance, even exceeding that of bulk $(Bi,Sb)_2(Te,Se)_3$. The seven high ZT solution synthesized materials share a few common themes. First, all incorporate Sb. Second, all address the issue of insulating large molecule surfactants by either a surfactant removal process involving hydrazine or the use of small molecule structure directing agents instead of large molecules. Third, nearly all involve a post synthesis heat treatment at 300 °C or higher. Fourth, nearly all final materials have relative densities above 90%. The seven solution synthesized materials differ greatly with regard to the synthesis and compression methods. Of the seven materials, four are made by hydrothermal synthesis,[143,149,156] two are made by microwave synthesis,[124] and one is made by moderate temperature synthesis involving long chain hydrocarbon-based solvents and ligands.[99] Regarding compression methods, four are cold pressed and annealed,[124,156] two are hot pressed,[99,143] and one is SPS'd.[149]

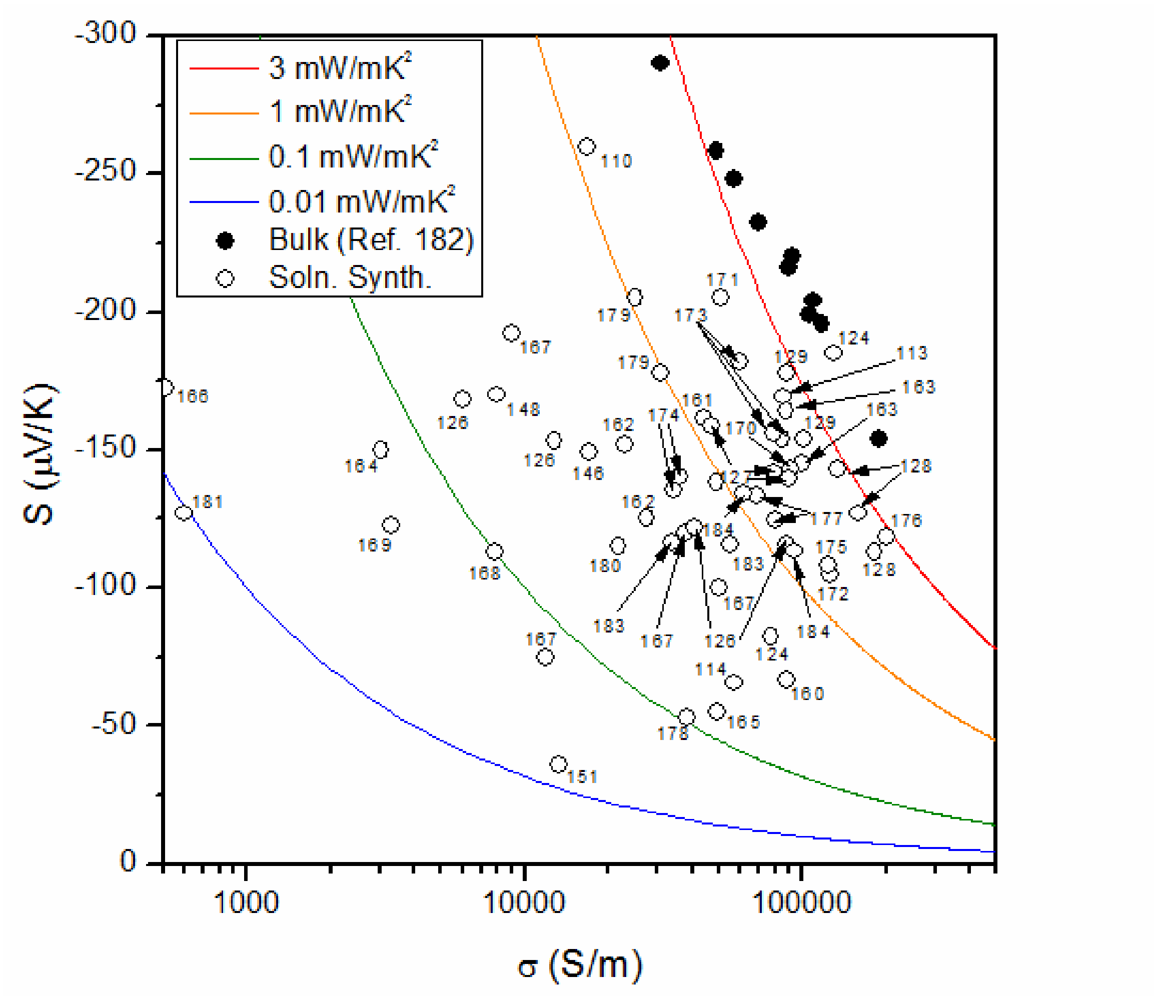

Figure 2.3 Seebeck coefficient versus electrical conductivity near room temperature for n-type $(Bi,Sb)_2(Te,Se)_3$. Data from references 110, 113, 114, 128, 146, 148, 151, 161, 167, 171, and 184 adapted with permission from the American Chemical Society. Copyright 2010, 2012, and 2013. See literature cited section for full reference details.

Figure 2.3 shows the near room temperature electronic properties of n-type solution synthesized $(Bi,Sb)_2(Te,Se)_3$ and large grained $(Bi,Sb)_2(Te,Se)_3$ grown by a traditional solid state method.[110,113,114,124,126–129,146,148,151,160–184] For n-type $(Bi,Sb)_2(Te,Se)_3$ the highest ZT values are achieved by materials with carrier concentrations in the range of 3 x 10^{18} – 9 x 10^{19} /cm^3, which are associated with Seebeck coefficients in the range of 100

– 290 μV/K at 300 K.[135,141] Most of the 53 samples represented in Figure 2.3 have Seebeck coefficients in the appropriate range. As with p-type $(Bi,Sb)_2(Te,Se)_3$, only one solution synthesized n-type sample has a power factor equal to that of bulk $(Bi,Sb)_2(Te,Se)_3$. All others have power factors less than 3 mW/mK^2, likely a result of reduced mobility. However, some power factors are very nearly equal to 3 mW/mK^2 leading to good ZT values.

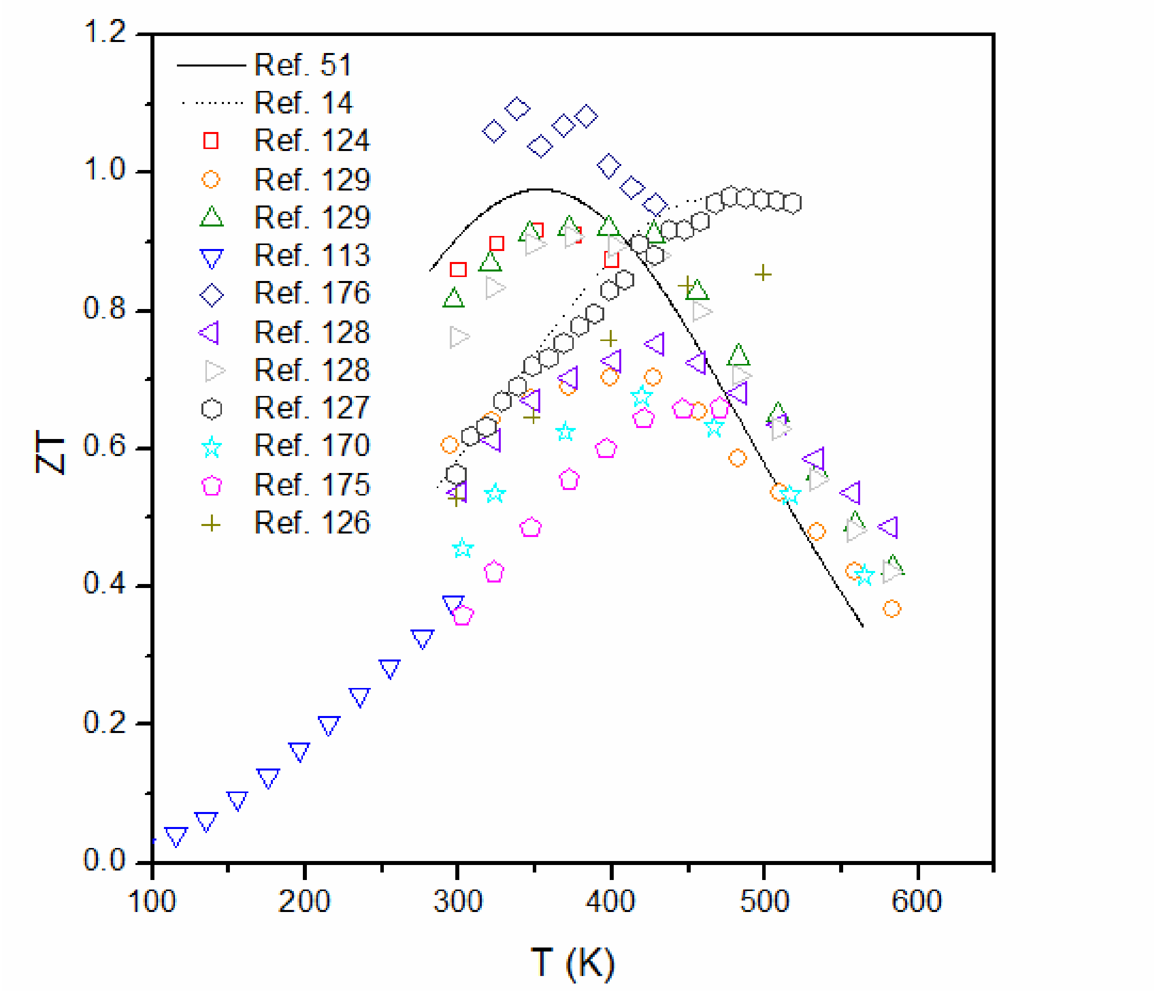

Figure 2.4 ZT versus temperature for solution synthesized (symbols) and bulk (lines) n-type $(Bi,Sb)_2(Te,Se)_3$. Data from references 113 and 128 adapted with permission from the American Chemical Society. Copyright 2012 and 2013. See literature cited section for full reference details.

Figure 2.4 shows the temperature dependence of ZT for 11 of the best solution synthesized n-type $(Bi,Sb)_2(Te,Se)_3$ samples and two bulk reference samples.[14,51,113,124,126–129,170,175,176] As with p-type $(Bi,Sb)_2(Te,Se)_3$, the performance of n-type solution synthesized $(Bi,Sb)_2(Te,Se)_3$ can be as good as and even better than that of bulk $(Bi,Sb)_2(Te,Se)_3$ synthesized by solid state methods. The 11 high ZT solution synthesized materials shown here share two common themes. First, all are either treated with a hydrazine-based surfactant removal step or are synthesized using small molecule structure directing agents instead of large molecule surfactants. Second, all 11 samples are treated at 250 °C or higher at some point after the solution synthesis step. In other ways, the materials are quite different. Some but not all of the materials incorporate Se. With regard to the solution synthesis, seven samples are synthesized in water or ethylene glycol at atmospheric pressure,[126–129,170,175] two are synthesized by co-precipitation of Bi and Te oxides in water at room temperature followed by calcination and high temperature reduction,[176] one is synthesized at moderate temperature with a long chain hydrocarbon solvent and ligands,[113] and one is made by microwave synthesis.[124] Regarding compression methods, seven are SPS'd,[113,127–129,170,176] three are hot pressed,[126,175] and one is cold pressed and annealed.[124]

2.3.2 p-type and n-type PbTe

PbTe is one of the best thermoelectric materials with peak performance at 600-950 K.[185] It was investigated thoroughly in the 1950's and 1960's, yet its maximum ZT was understated for many years due to inaccurate estimation of thermal conductivity at high temperature.[43] Recently, the ZT was reevaluated and found to be 1.4 at 750 K for both p-type and n-type bulk polycrystalline PbTe.[186,187] Being comprised of heavy elements, PbTe benefits from a low lattice thermal conductivity of 1.5-2.3 W/mK at 300 K.[186,187] Highly doped p-type PbTe benefits from the presence of two valence bands which converge at high temperature to result in a high Seebeck coefficient even for materials with carrier concentrations of 1 x 10^{20} /cm^3.[186,188–190] Meanwhile, n-type PbTe benefits from high electron mobility.[187] PbTe is stable in a very small range of compositions.[191,192] Therefore, while excess Te leads to p-type behavior, dopants such as Na, K, or Tl are required to achieve optimized carrier concentrations of 1 x 10^{20} /cm^3.[186,193,194] Similarly, while excess Pb leads to n-type behavior, dopants such as I, La, or Bi are required to achieve optimized carrier concentrations of 2-5 x 10^{19} /cm^3.[43,195,196] Solution synthesis of PbTe nanostructures dates back to at least 2000.[197] Over the next several years, many methods for the solution synthesis of PbTe nanostructures were published. The first thorough investigation of the thermoelectric properties of solution synthesized PbTe was completed by Nolas and published in 2007.[198] Several reports of the thermoelectric properties of solution synthesized PbTe have followed, which are summarized here.

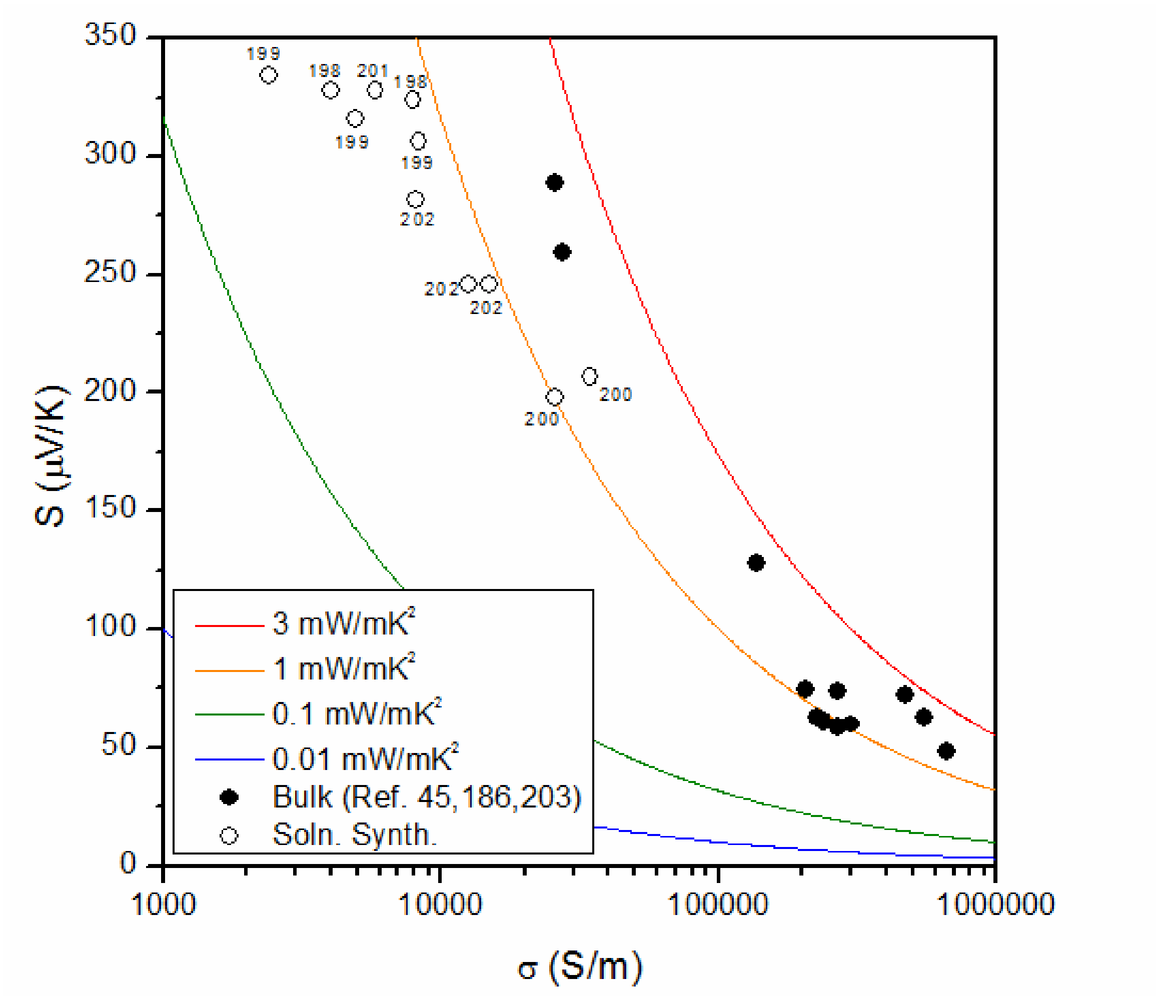

Figure 2.5 Seebeck coefficient versus electrical conductivity near room temperature for p-type PbTe.

Figure 2.5 presents the electronic properties of p-type solution synthesized PbTe at or near 300 K.[198–202] Also shown are the properties of several Na-doped single crystalline and large grained polycrystalline bulk PbTe samples and lines of equal power factor.[45,186,203] This graph reveals several important trends. First, the majority of materials made by solution synthesis have electrical conductivities less than 10,000 S/m while highly doped bulk samples possess electrical conductivities in excess of 200,000

S/m. Second, nearly all materials made by solution synthesis have Seebeck coefficients greater than 200 μV/K while doping during solid state synthesis allows the Seebeck coefficient to be tuned from 250 down to 50 μV/K. Third, all solution synthesized materials have power factors that are lower than those of Na-doped large-grained PbTe. The optimal range of carrier concentration for bulk p-type PbTe is associated with room temperature Seebeck coefficients in the range of 50 – 65 μV/K.[185,186] Therefore, the Seebeck coefficient data for solution synthesized p-type PbTe suggests that their carrier concentrations are far below the optimal range. Clearly, improved doping strategies are necessary.

Nearly all of the currently available solution synthesized PbTe materials contain only Pb and Te, which results in low carrier concentrations. Meanwhile Ag has been incorporated as a dopant, apparently by the addition of Ag_2Te to dry PbTe powder prior to compression[200] as well as by the addition of Ag precursor during a solution synthesis.[201] While Ag_2Te addition led to an increase in the carrier concentration by a factor of five compared to similar material without Ag_2Te,[200] no significant increase in carrier concentration was observed when Ag precursor was added during the solution synthesis.[199,201] Furthermore, Ag has been shown to be unable to achieve the desired range of carrier concentrations because Ag acts as an electron acceptor when substituted for Pb or as an electron donor at interstitial sites when present in high concentrations.[204] While p-type doping by Na and K has been successfully employed in bulk PbTe synthesized by solid state routes, solution-phase doping by Na or K appears unlikely. Their cations are commonly present in the solution synthesis of PbTe, yet they are not incorporated in the material perhaps due to high solubility in aqueous solutions and difficulty in being reduced. Thallium has also been shown to be an effective p-type dopant, yet it is highly toxic.[194,196,205–207] Clearly, p-type doping of solution synthesized PbTe is formidable obstacle, which needs addressed.

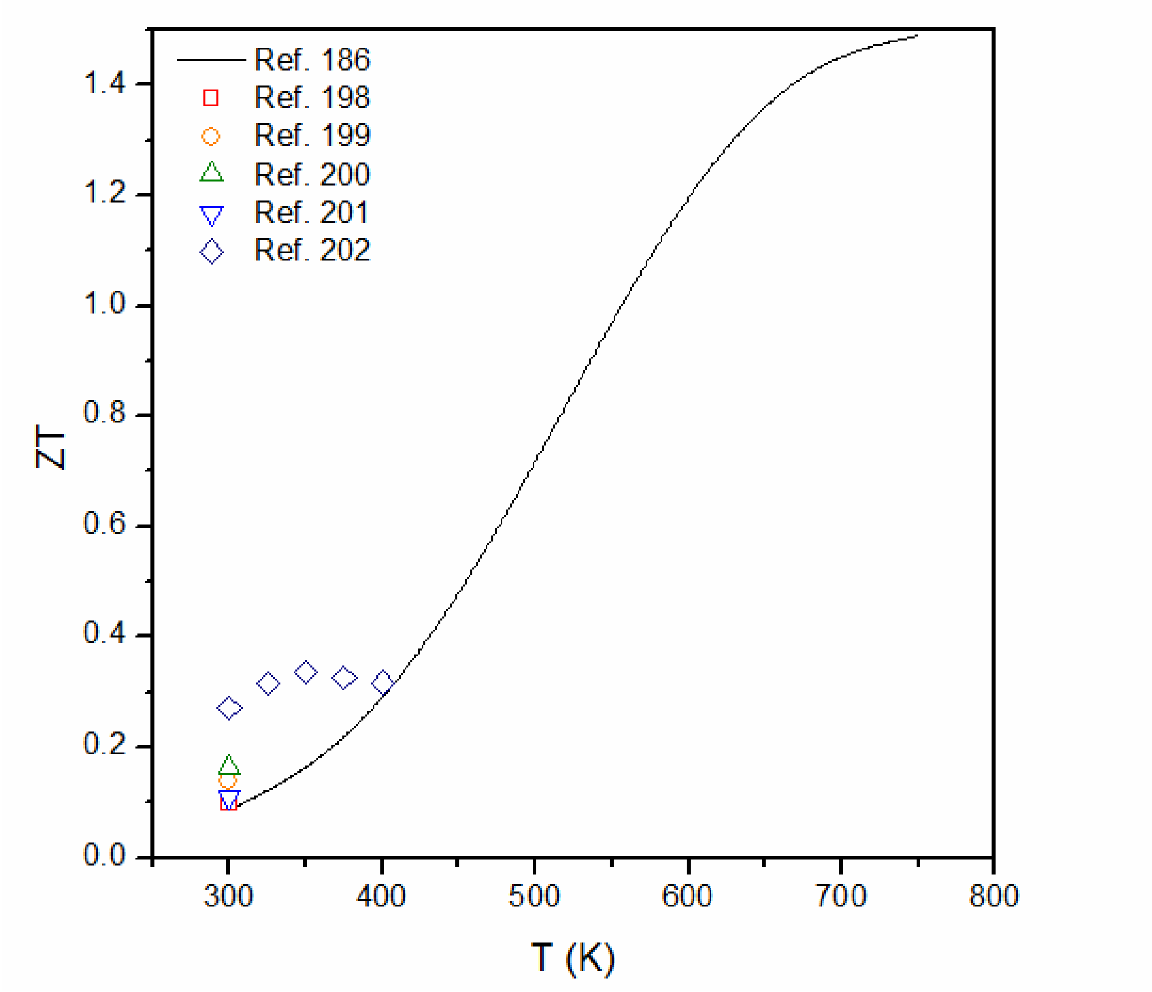

Figure 2.6 ZT versus temperature for solution synthesized (symbols) and bulk (lines) p-type PbTe.

Figure 2.6 shows the thermoelectric figure of merit vs. temperature for the highest performance solution synthesized p-type PbTe along with Na-doped bulk polycrystalline PbTe optimized for maximum ZT at temperatures above 600 K.[186,198–202] At 300 K, several solution synthesized materials possess a higher ZT than bulk PbTe at the same temperature. The improvement is due in part to a reduced thermal conductivity; however, much of this reduction is associated with the electronic component. Still, in a few cases, there is also a reduction in the lattice thermal conductivity by 20-50% compared to bulk values due to fine grain structures and porosity.[202] Unfortunately the figures of merit of most of the solution synthesized materials have not been measured at high temperature. Measurements up to 400 K on SPS'd PbTe nanowires described in detail in chapter 4 reveal a maximum ZT of 0.33 at 350 K. While this is higher than the ZT of highly doped PbTe at the same temperature, the doping level in the nanowire-based material achieved by excess Te is insufficient to suppress minority carrier contributions and achieve high ZT above 600 K. This further highlights the need to develop effective p-type doping methods for solution synthesized PbTe. Initial studies on doping with Na_2Te powder prior to high temperature compression are discussed in chapter 5.

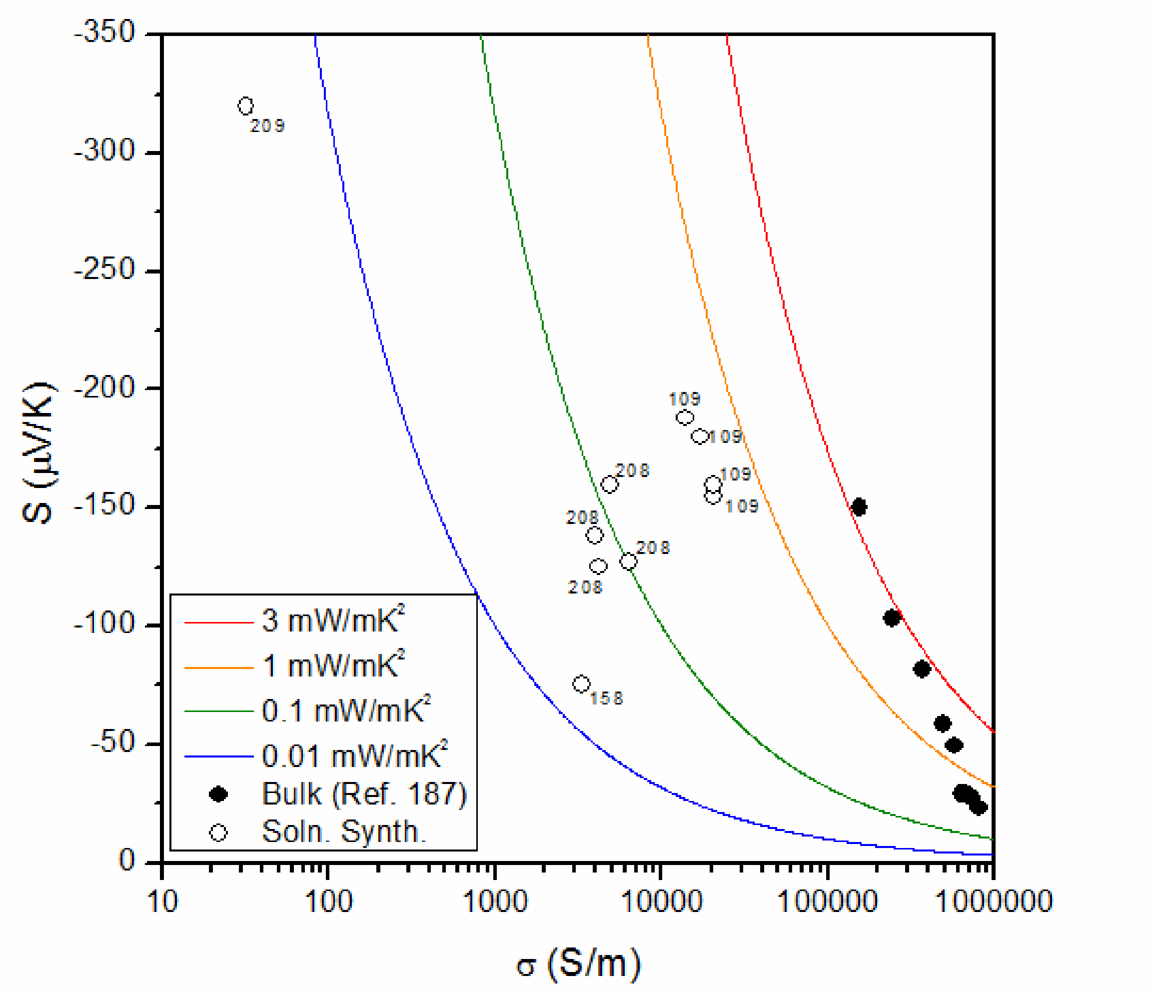

Figure 2.7 Seebeck coefficient versus electrical conductivity near room temperature for n-type PbTe. Data from reference 209 adapted with permission from the American Chemical Society. Copyright 2014. See literature cited section for full reference details.

Figure 2.7 shows the electronic properties of n-type solution synthesized PbTe at or near 300 K.[109,158,208,209] Properties of bulk n-type PbTe synthesized by solid state methods are shown along with lines of equal power factor for comparison.[187] The trends illustrated are similar to those of p-type PbTe. Solution synthesized n-type tends to have significantly lower electrical conductivity, higher Seebeck coefficient, and lower power factor compared with solid state synthesized PbTe. The optimal carrier concentration is associated with Seebeck coefficient magnitudes in the range of 40-75 μV/K at 300 K.[187,210] Thus, n-type solution synthesized PbTe appears to exhibit insufficient doping even though several of the materials represented in Figure 2.7 are doped with Bi.

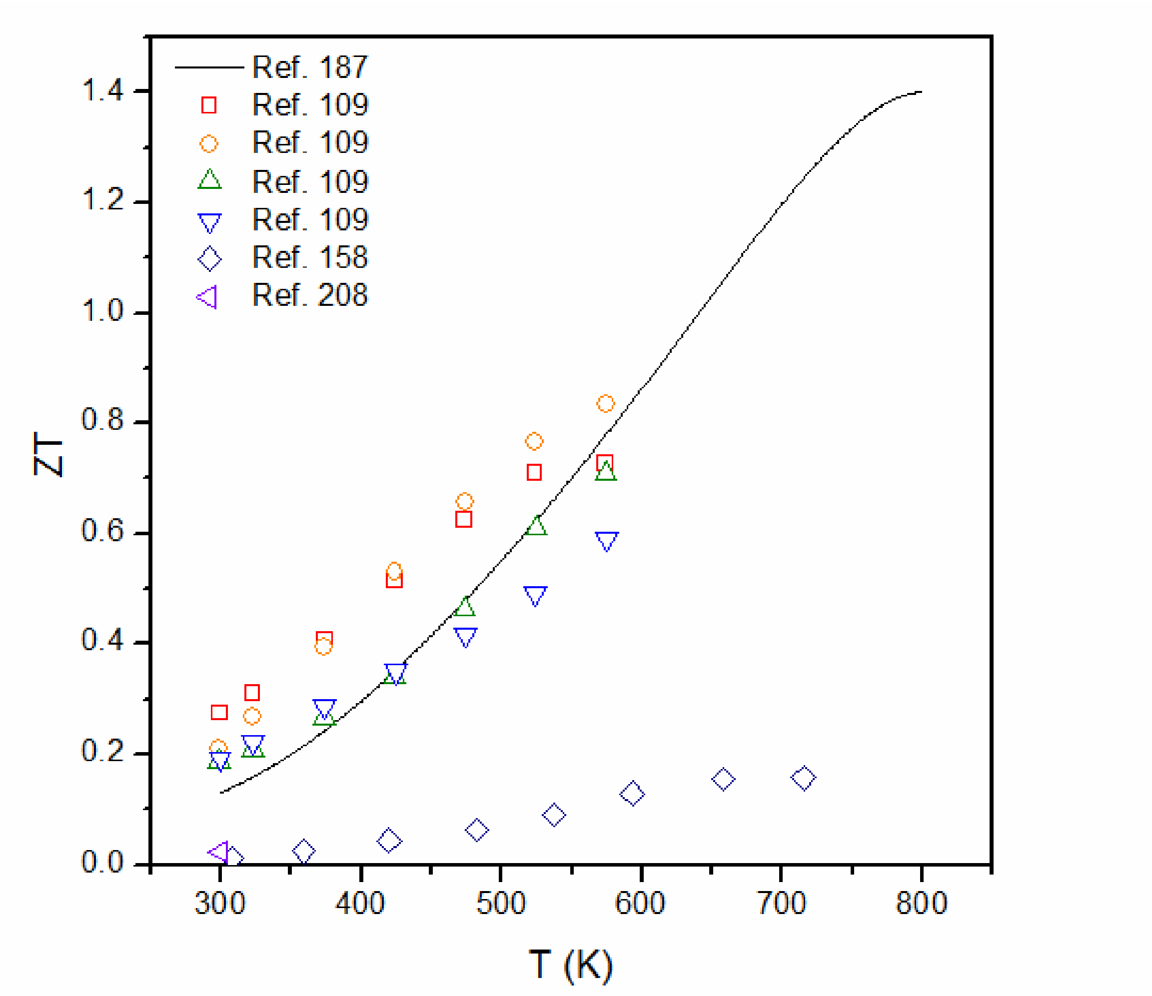

Figure 2.8 ZT versus temperature for solution synthesized (symbols) and bulk (lines) n-type PbTe.

Figure 2.8 shows the thermoelectric figure of merit vs. temperature for the solution synthesized n-type PbTe with the highest performance along with I-doped polycrystalline PbTe optimized for maximum ZT at temperatures above 600 K.[109,158,187,208] The performance of Cao's solution synthesized un-doped PbTe nearly parallels that of bulk PbTe up to 575 K.[109] While these results are impressive, a close inspection of the thermoelectric properties of the material reveals some peculiar phenomena. For example, the electrical conductivity of the best material increases slightly with temperature from 300 – 575 K, which is quite unlike the drastic decrease observed in bulk PbTe.[187] Also, the Seebeck coefficients at 300 K suggest carrier concentrations of 2 x 10^{18} – 5 x 10^{18} /cm^3, yet at the temperatures employed in the synthesis and consolidation steps, the PbTe phase diagram predicts carrier concentrations of less than 2 x 10^{17} /cm^3.[191] Such deviations from expectation require significant additional experimentation to both verify and better explain the results. To summarize, some progress has been made in the area of solution synthesized p- and n-type PbTe thermoelectrics, yet the lack of effective doping strategies has prevented the realization of high ZT at temperatures above 600 K where PbTe is best suited.

2.3.3 p-type Ternary and Quaternary Copper Chalcogenides

During the last few years, ternary and quaternary copper chalcogenides have received attention as promising thermoelectric materials that are comprised of earth-abundant elements. Materials of interest such as Cu_2SnSe_3 (CTS), $Cu_2ZnSnSe_4$, $Cu_2ZnGeSe_4$ (CZGSe), $Cu_2CdSnSe_4$ (CCTSe), and $Cu_2HgSnSe_4$ have much larger band gaps than typical thermoelectric materials, yet their complex crystal structures lead to low lattice thermal conductivities and moderate ZT values in the temperature range of 600-850 K.[211,212] Stoichiometric compounds tend to have unsuitably low electrical conductivities, but doping with In, Ga, or excess Cu leads to an increase in electrical conductivity by as much as two orders of magnitude and often a simultaneous decrease in total thermal conductivity due to increased disorder within the crystal lattice.[211,212] Therefore, highly doped materials tend to have the largest ZT values. In some cases, loading too much excess Cu leads to phase segregation of CuSe and $Cu_{2-x}Se$.[213]

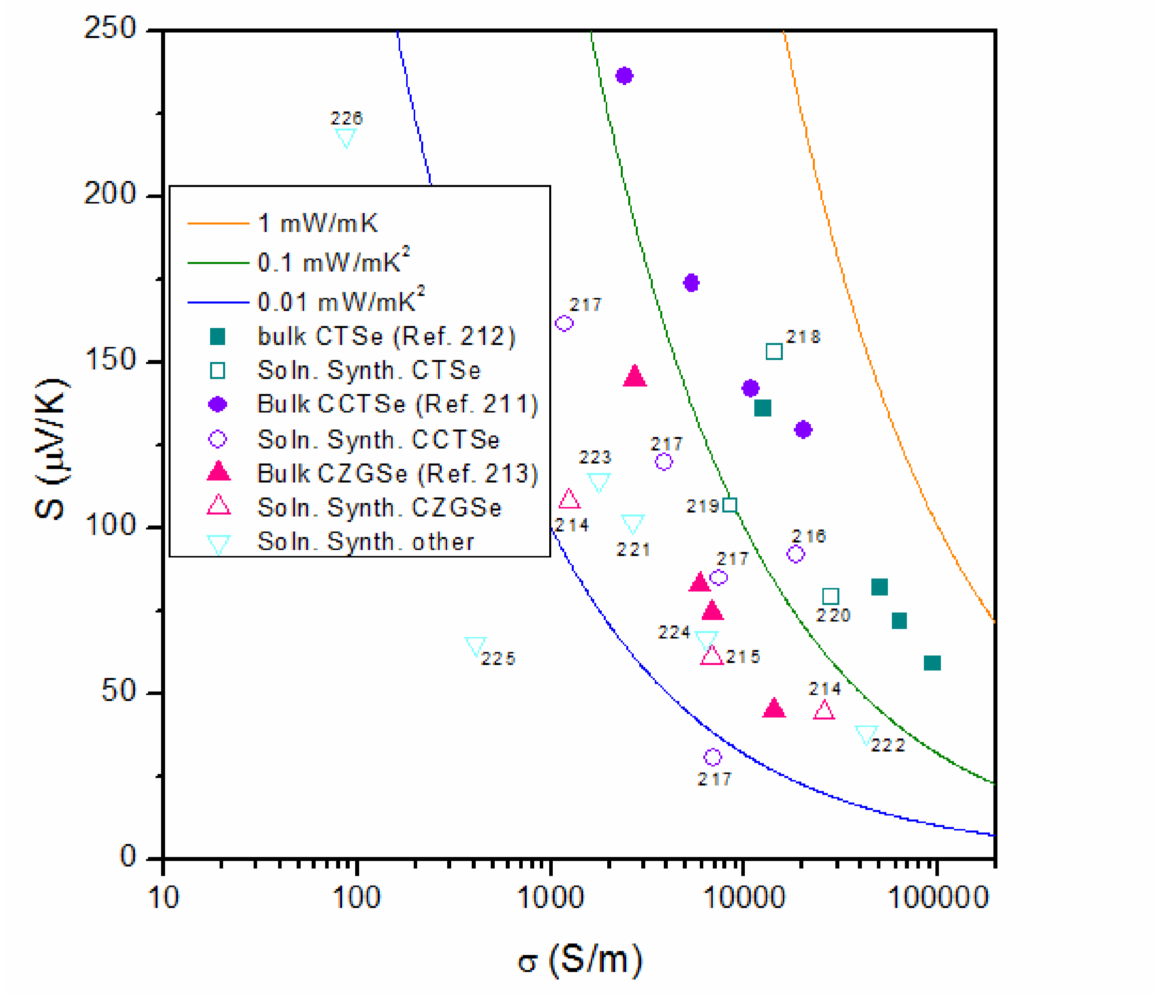

Figure 2.9 Seebeck coefficient versus electrical conductivity near room temperature for ternary and quaternary copper chalcogenides. Data from references 212, 213, 214, 216, 221, 224, and 225 adapted with permission from the American Chemical Society. Copyright 2010, 2011, and 2012. See literature cited section for full reference details.

Figure 2.9 shows the near room temperature electronic properties of several ternary and quaternary solution synthesized copper chalcogenides and three of the best related bulk materials.[211–226] All materials have positive Seebeck coefficients due to copper excess and/or chalcogen deficiency. The near room temperature electrical conductivities and power factors of the materials presented are significantly lower than those of low band gap materials such as $(Bi,Sb)_2(Te,Se)_3$ and doped PbTe, a phenomenon that is mostly due to low mobility. This agrees with the general trend of mobility having an inverse relationship with band gap.[51]

Within the group of Cu_2SnSe_3 materials, the In doping used in the bulk material clearly leads to higher electrical conductivities and lower Seebeck coefficients than are possible in the solution synthesized materials. However, in one case, the near room temperature power factor observed in solution synthesized Cu_2SnSe_3 is actually larger than that of bulk Cu_2SnSe_3.[218]

Regarding $Cu_2CdSnSe_4$ and $Cu_2ZnGeSe_4$, carrier concentration adjustment by excess Cu can be easily achieved in bulk materials by a simple adjustment of the ratio of elemental starting materials as shown by the broad range of electrical conductivities and Seebeck coefficients. Interestingly, carrier concentration adjustment using excess Cu can also be achieved in solution synthesized nanomaterials. The Cabot group determined that during the synthesis, Cu-Se type nanocrystals form first, followed by the addition of Cd, Zn, Sn, or Ge. Therefore the amount of excess Cu can be conveniently controlled by adjusting the reaction time and temperature.[214,217] The success of this method is evidenced by the wide range of electrical conductivities and Seebeck coefficients observed in these solution synthesized materials. In the case of $Cu_2CdSnSe_4$, the solution synthesized materials possesses power factors far below those of bulk $Cu_2CdSnSe_4$.

Conversely, solution synthesized $Cu_2ZnGeSe_4$ samples have similar and even larger power factors than bulk $Cu_2ZnGeSe_4$ near room temperature.

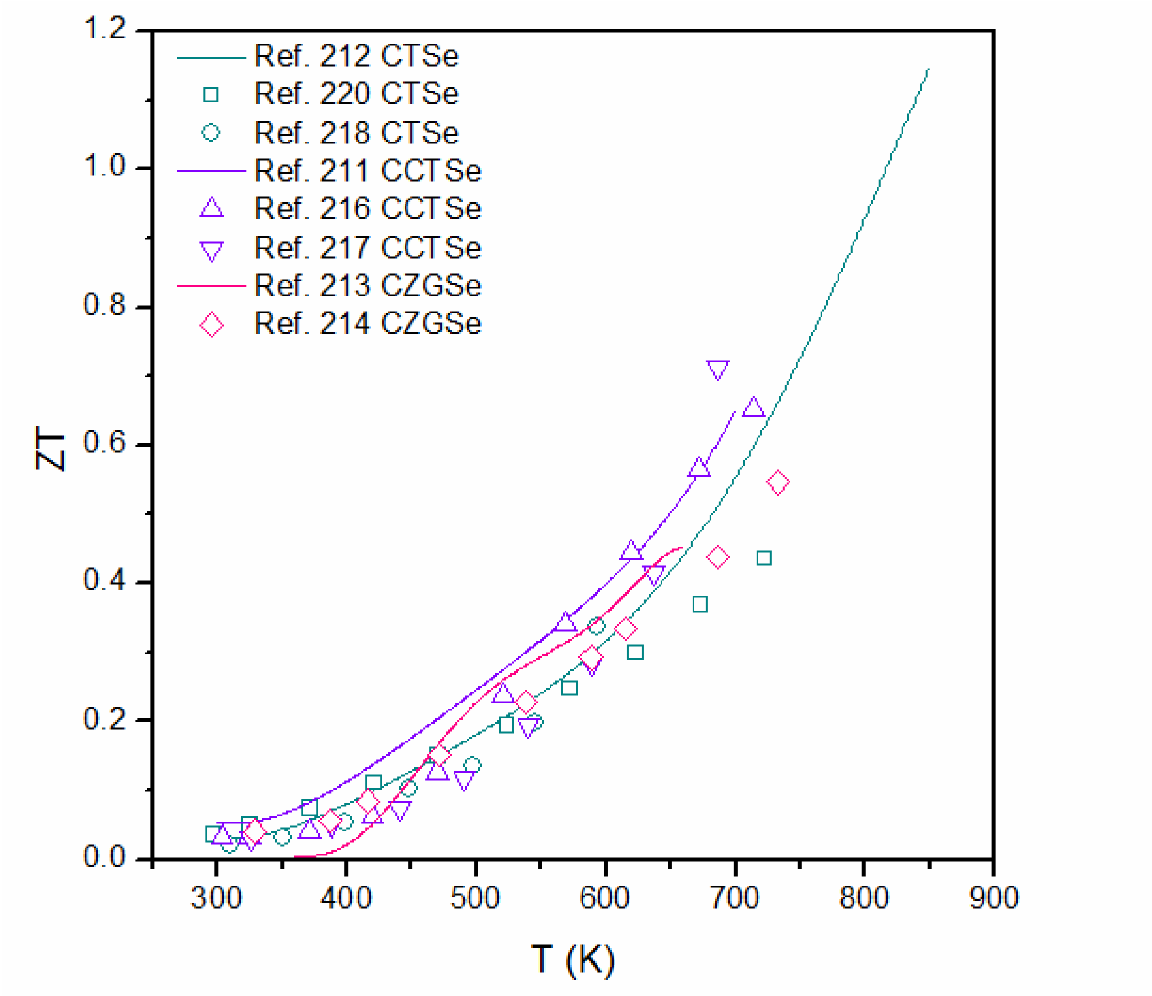

Figure 2.10 ZT versus temperature for solution synthesized (symbols) and bulk (lines) ternary and quaternary copper chalcogenides. Data from references 212, 213, 214, and 216 adapted with permission from the American Chemical Society. Copyright 2010, 2011, and 2012. See literature cited section for full reference details.

Figure 2.10 shows the ZT vs. temperature for several of the best solution synthesized materials along with bulk materials with similar compositions.[211–214,216–218,220]

Interestingly all bulk materials possess similar ZT values from room temperature to 700 K with $Cu_2CdSnSe_4$ possessing the best properties in that range. ZT values as high as 1.14 at 850 K have been observed in Cu_2SnSe_3, yet stable measurements at these temperatures require that samples are coated with glass to prevent Se sublimation.[212] Such a coating would act as a thermal shunt in real devices.

Despite the reduced power factor observed in some cases in Figure 2.9, solution synthesized materials possess ZT values nearly equal to or greater than bulk counterparts due to thermal conductivity reduction. A close inspection of the five articles on the solution synthesized materials reveals several similarities and differences. All five materials are synthesized by reactions of dissolved Se with solutions of the appropriate cation precursors in the temperature range of 180-300 °C in oleylamine, 1-octadecene, or a combination of the two. All five synthesis methods produce nanocrystals with sizes in the range of 5-25 nm, which experience some extent of grain growth during the subsequent hot pressing or annealing steps at 350-550 °C. With regard to the issue of insulating ligands, three of the materials experience a thorough hydrazine washing in which nanocrystals that are initially dissolved in hexane are transferred to an 85% hydrazine phase with repeated hexane rinses. Meanwhile, two of the five materials are treated with repeated dissolution in chloroform and precipitation using isopropanol until the nanocrystals are no longer soluble in organic solvent; they are then annealed in Ar at 500 °C. It is interesting that both the hydrazine-based and non-hydrazine-based methods yield high ZT values.

A comparison of the two solution synthesized $Cu_2CdSnSe_4$ materials with similar Seebeck coefficients reveals that the hydrazine wash followed by hot pressing leads to a room temperature electrical conductivity that is 2.4 times greater than that of material that is not hydrazine washed, but rather is annealed and cold pressed.[216,217] Yet, as the room temperature thermal conductivity of the hydrazine washed material is 3.2 times larger, the ZT values are quite similar. The necessity of using highly toxic hydrazine is therefore debatable for these materials; this topic deserves more investigation. In summary, the area of solution synthesized ternary and quaternary copper chalcogenides has experienced rapid progress in the past few years and ZT values similar to bulk values have already been achieved.

2.4 Conclusions and Recommendations for Future Work

Remarkable milestones have been achieved in the solution synthesis of thermoelectric materials in the past 15 years. In particular, solution synthesized p-type and n-type $(Bi,Sb)_2(Te,Se)_3$ and ternary and quaternary copper chalcogenides have reached and in some cases even surpassed the ZT values of the corresponding large-grained bulk materials. For these materials that have achieved high performance, future research should begin to consider other important variables such as mechanical properties, thermal cycling stability, and overall synthesis cost to more thoroughly prove that thermoelectric devices made using these materials are commercially viable. In the case of PbTe, significant progress has been made, yet there is much room for improvement. The following four chapters of this dissertation address several important areas including the development of a scalable high yield synthesis method, improved understanding of the high temperature compression process, effective doping methods, and the development of a hydrazine-free method for the solution synthesis of nanostructured PbTe.

CHAPTER 3. LARGE-SCALE SYNTHESIS OF LEAD TELLURIDE NANOWIRES

3.1 Introduction

The synthesis of many kinds of semiconductor nanowires has received much attention due to the unique capabilities and properties associated with 1D structures. For example, they can possess good chemical and biological sensing characteristics,[227] enhanced light absorption for optoelectronic devices,[228,229] and high mobility along their axes due to ballistic carrier transport.[230] For the purposes of this dissertation, the most interesting benefits of the nanowire morphology are enhanced thermoelectric properties due to quantum confinement and boundary scattering of phonons.[75] Several methods have been developed to synthesize PbTe nanowires such as lithographically patterned electrodeposition[231,232] and chemical vapor deposition.[233,234] These methods offer some size control, yet they generally suffer from complicated multi-step fabrication procedures, high temperatures, and especially, low yield.

At the same time, solution synthesis of Te nanowires has been explored extensively. Due in part to the anisotropic crystal structure of Te, a variety of reaction conditions can lead to growth of Te nanowires along the [001] direction. Many surfactants such as polyvinyl alchohol,[235] starch,[236] sodium dodecylbenzenesulfonate,[237] cetyltrimethylammonium bromide,[238,239] and polyvinylpyrrolidone (PVP),[240–242] can assist in 1D growth. A few research groups have followed the synthesis of Te nanowires with a conversion to various metal telluride nanowires[103,243] such as Bi_2Te_3,[171,244–246] CdTe,[247] Ag_2Te,[105,248] and PbTe[247,249–251] while retaining nanowire morphology. However, one critical aspect of this research area that is missing is the synthesis of telluride nanowires at large-scale. Recently, several types of sulfide based nanocrystals have been synthesized at the multi-gram scale, such as Cu_2S,[252] CdS,[252] Cu_2SnSe_3,[220] Cu_2ZnSnS_4,[224] and others mainly for their applications in photovoltaic solar cells. However, the fundamental challenge for large-scale growth of metal telluride nanowires for thermoelectrics and other technologies has not yet been addressed.

The following is a description of the first multi-gram solution-phase production of PbTe nanowires with high yield (>80%) using a robust, one-pot approach at low temperature and atmospheric pressure in a solvent of ethylene glycol. As shown in Figure 3.1, Te nanowires are synthesized first and then converted into PbTe by adding a Pb precursor.

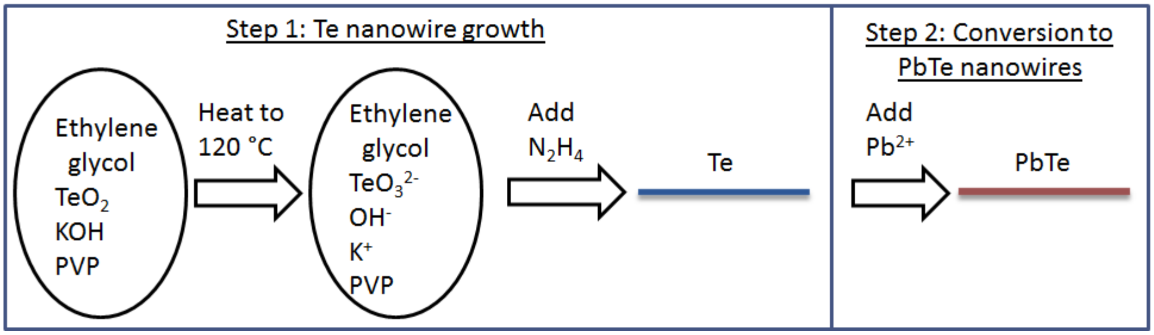

Figure 3.1 Scheme for the two-step synthesis of PbTe nanowires.

3.2 Synthesis Method

The required chemicals including TeO_2 (≥99%), PVP (Molecular Weight 40,000), KOH (90%), N_2H_4 (98%), and $Pb(CH_3CO_2)_2 \cdot 3H_2O$ (≥99.99%), are purchased from Sigma Aldrich while ethylene glycol (≥99%) is purchased from VWR. The large-scale (>800 ml) synthesis takes place in a one liter Chemglass CHEMRxnHUB reactor in which the jacket fluid is heated and cooled using a Huber high precision thermoregulator.

For the synthesis of PbTe nanowires, 21.50 g PVP, 6.86 g TeO_2 (43.0 mmol), 19.50 g KOH, and 650 ml ethylene glycol are added to the reactor. The jacket temperature setpoint is increased to above 120 °C and mechanical stirring is initiated. As the reaction mixture is heated, the color changes from white/opaque, to clear (signifying the dissolution of TeO_2), to transparent yellow as shown in Figure 3.2a-c. When the reaction temperature reaches 120 °C, 26.0 ml N_2H_4 is rapidly injected, resulting in an immediate color change from transparent yellow to opaque black (Figure 3.2c-d), and nitrogen gas protection is applied to the reactor via a Schlenk line. Minimal overshoot in temperature is observed in this step as show in Figure 3.2e. As the Te nanowires form, a Pb precursor solution is made by dissolving 4.3 g PVP and 16.93 g $Pb(CH_3CO_2)_2 \cdot 3H_2O$ (43.0 mmol) into 125 ml ethylene glycol by stirring on a 120 °C hot plate. One hour after N_2H_4 injection, this Pb precursor solution is injected into the reaction mixture. One hour after the Pb precursor injection, the jacket temperature setpoint is decreased to 20 °C. When the reaction mixture is cooled to near room temperature, the products are collected in a Pyrex container.

Then, the as-synthesized PbTe nanowires are washed three times with deionized (DI) water. During the first washing step, the reaction solution is mixed with DI water at a volume ratio of 1:1 and centrifuged for approximately one hour. The nearly clear supernatant is discarded, fresh DI water is added, and the solution is mixed to re-disperse the nanowires. For the second washing step, the mixture is centrifuged for a shorter time (10 minutes) to obtain a clear supernatant. The supernatant is discarded, fresh DI water is added, and the solution is mixed. For the third washing step, the mixture is centrifuged briefly (1 minute) to obtain a clear supernatant which is discarded. This water washing is followed by a one hour soak in 2.3 M hydrazine in ethanol to completely remove the organic surfactant.[171,253] The mixture is then centrifuged briefly (5 minutes) and the supernatant is discarded. Finally, the material is washed three times with ethanol; only brief centrifuge times (3 minutes) are required to obtain a clear supernatant. The material is then dried overnight in vacuum at room temperature and brought directly into a nitrogen filled glove box for grinding with a mortar and pestle and for weighing. The use of the glove box is presumed to be beneficial for the prevention of an oxide layer known to form quickly at room temperature.[130]

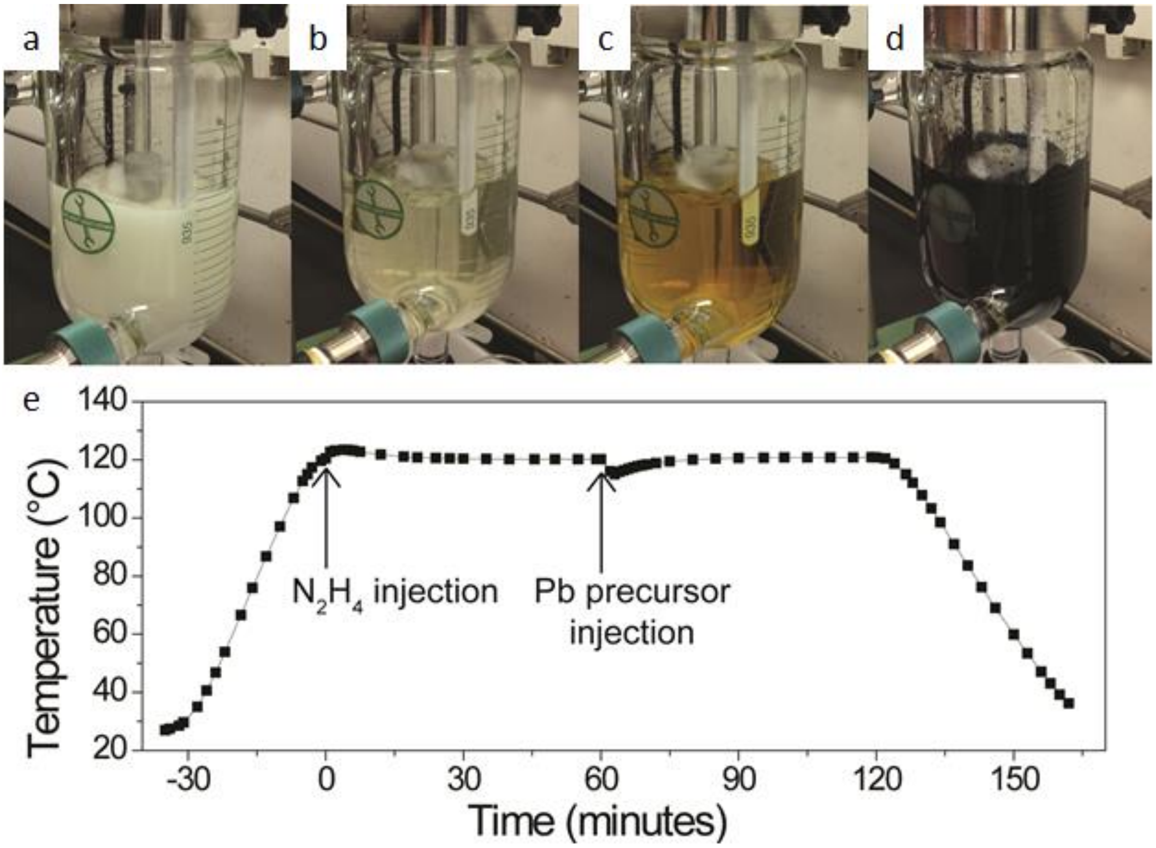

Figure 3.2 (a-d) Reaction solution color over time. (a) -26 minutes. (b) -18.5 minutes. (c) -1 minute. (d) +1 minute. (e) Reaction solution temperature over time with time = 0 minutes corresponding to the time of N_2H_4 injection.

3.3 Results

The success of this synthesis strategy is first confirmed by X-ray diffraction (XRD). As shown in Figure 3.3, products from the first synthesis step can be indexed as pure phase Te (JCPDS # 35-1452) although the (101) peak and others are markedly reduced in size likely due to nanowires lying with c-axes perpendicular to the substrate as observed using transmission electron microscopy (TEM).[254] Products from the synthesis of PbTe can be indexed as pure phase PbTe (JCPDS # 01-077-0246).

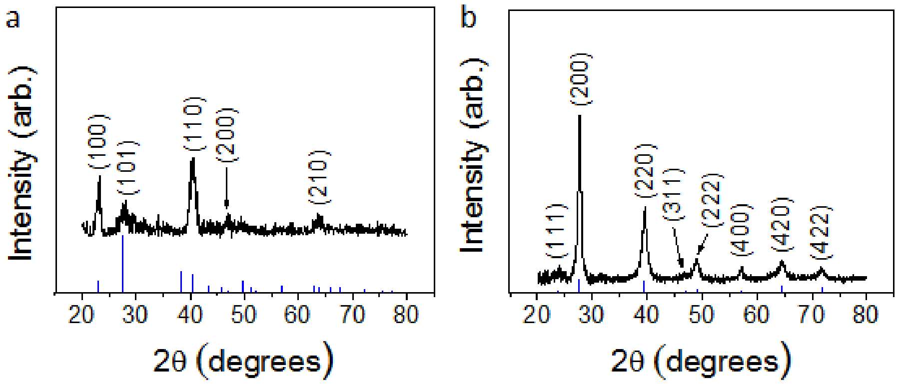

Figure 3.3 XRD patterns of synthesis products. (a) Te nanowires. Blue lines are standard peaks for Te (JCPDS # 35-1452). (b) PbTe nanowires. Blue lines are standard peaks for PbTe (JCPDS # 01-077-0246).

Energy dispersive X-ray spectroscopy (EDS) analysis of washed and dried PbTe nanowire powder shows the composition to be Te-rich (44.80 ± 0.44 atomic % Pb, 55.20 ± 0.44 atomic % Te). The lack of Te peaks in the XRD pattern is likely due to the large surface to volume ratio of the nanowires, which allows for significant deviations from stoichiometry while retaining a single crystalline phase.

TEM studies on aliquots taken during the Te nanowire growth step show that Te rapidly grows one dimensionally even during the first five minutes after N_2H_4 injection, (Figure 3.4), likely following the reaction mechanism suggested by Liang et al.[243] As the reaction proceeds, nanowire morphology is retained as shown in Figure 3.4. Note that the recipe used during the aliquot study was a slight variation from that described above. For the aliquot study, the Te growth step from the procedure for synthesizing Bi_2Te_3 nanowires described in the publication on this work was used.[160]

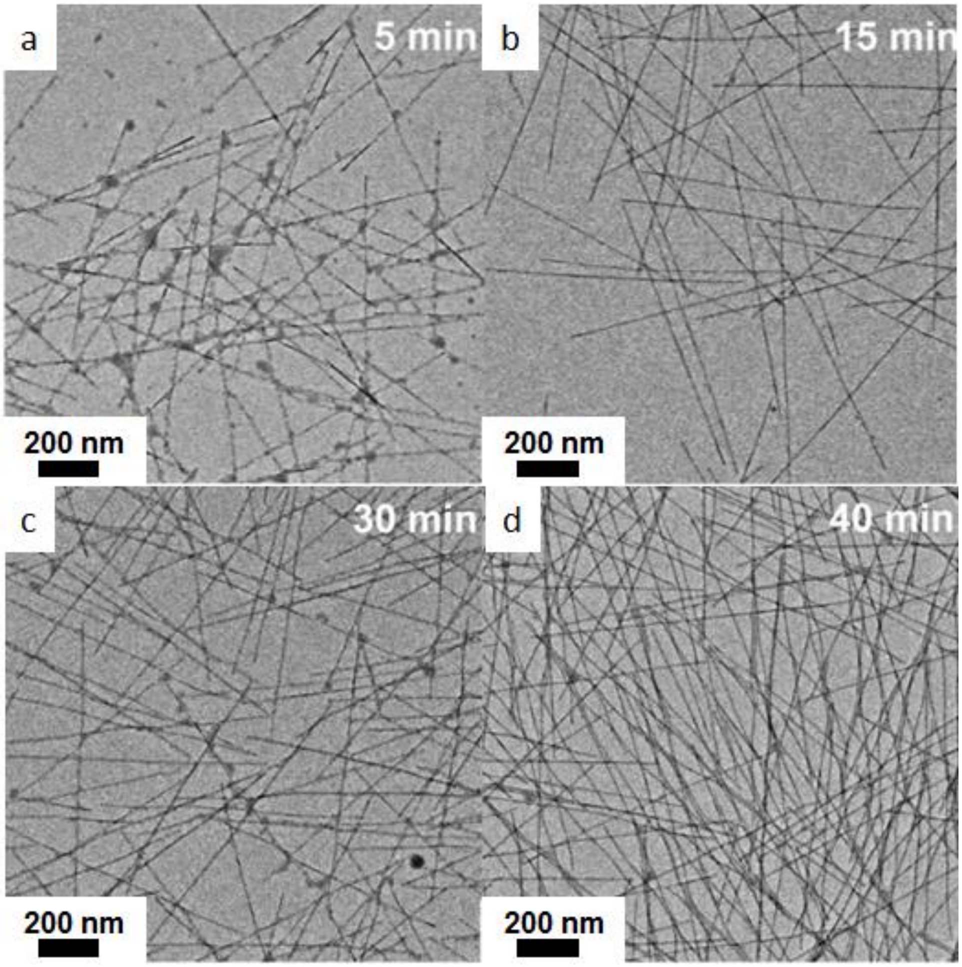

Figure 3.4 TEM of material in aliquots taken at various times after N_2H_4 addition during the Te nanowire growth step. (a) 5 minutes. (b) 15 minutes. (c) 30 minutes. (d) 40 minutes.

Length measurements of the Te nanowire aliquot images (Figure 3.5) reveal that most of the growth in length occurs during the initial 15 minutes, with only small increases in length afterwards. Similarly, the diameter ceases to increase after the initial 15 minutes.

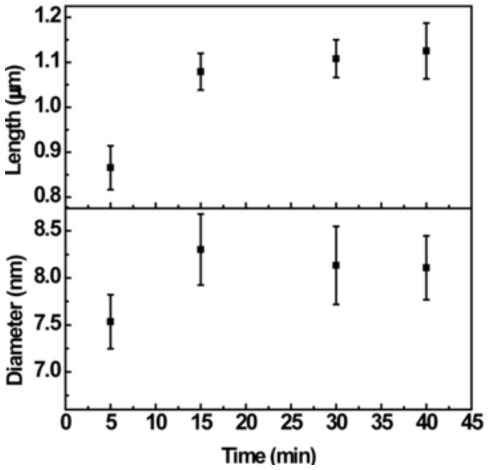

Figure 3.5 Average length and diameter of Te nanowires versus time after N_2H_4 addition.

A high-resolution transmission electron microscope (HRTEM) image of a typical Te nanowire and the corresponding fast Fourier transform (FFT) in Figure 3.6 show that the axial direction of the nanowires is aligned with the [001] direction. Overall the formation of ultra-thin nanowires is attributed to the anisotropic crystal structure of Te,[239] radial growth passivation by PVP,[240,241] and the use of at least eight times excess hydrazine, which encourages rapid formation of many small nuclei, which then grow one dimensionally.[255]

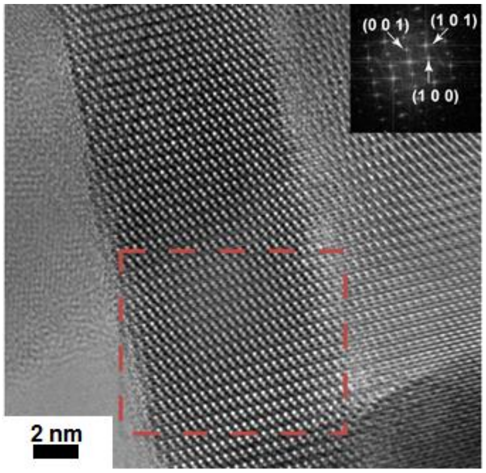

Figure 3.6 HRTEM of Te nanowire from an aliquot taken after the completion of the first synthesis step. The inset is the FFT of the boxed area.

The TEM image of the final product of the PbTe synthesis (Figure 3.7) shows that the original Te nanowire morphology is partially preserved. The PbTe nanowire length varies greatly and is shorter than that of the Te nanowire templates; this suggests that there is some extent of nanowire breaking during the Pb insertion step. The diameter of the PbTe nanostructures tends to vary slightly from batch to batch, yet it is consistently slightly larger than that of the preliminary Te nanowires. An example of this diameter distribution comparison is shown in Figure 3.8.

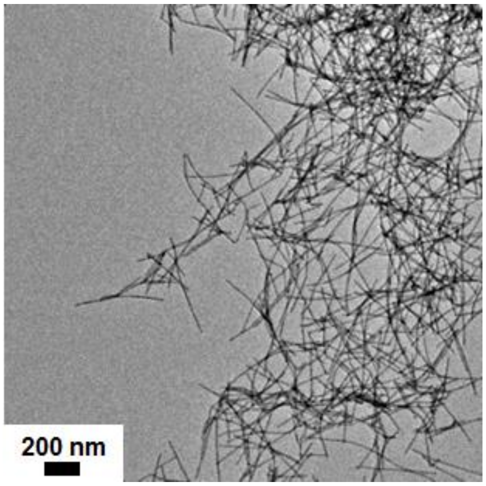

Figure 3.7 TEM of PbTe nanowires obtained after the second synthesis step.

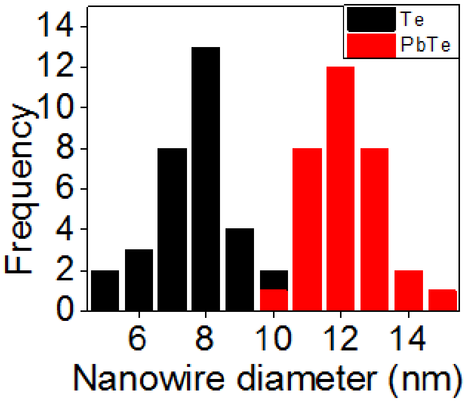

Figure 3.8 Diameter distributions of Te and PbTe nanowires.

The HRTEM image (Figure 3.9a) and corresponding FFT (inset) of the PbTe nanowire products shows that the nanowire axis is aligned with the [220] direction. However, some nanowires such as the one shown in Figure 3.9b have axes aligned with the [222] direction, which is similar to other results for PbTe-Bi_2Te_3 nanowire-based heterostructures.[256]

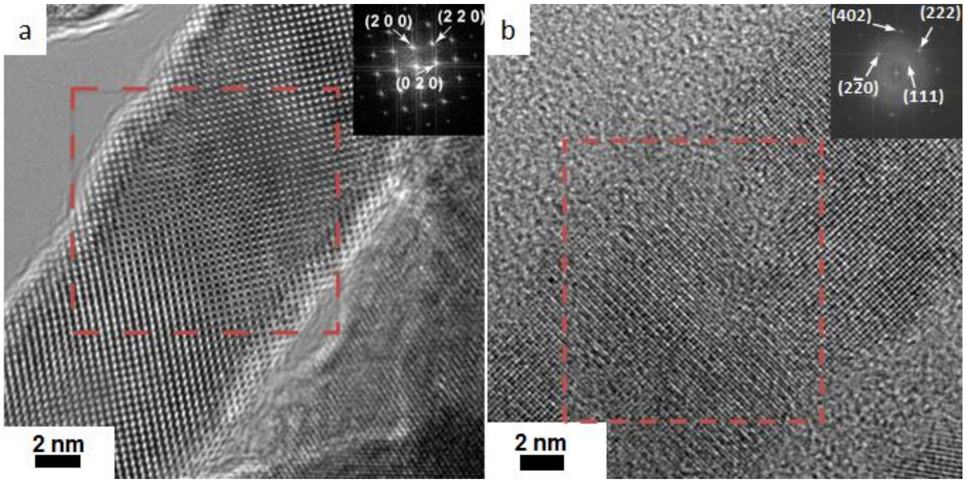

Figure 3.9 HRTEM of PbTe nanowires. Insets contain FFT of the boxed area. (a) A nanowire with axis aligned with the [220] direction. (b) A nanowire with axis aligned with the [222] direction.

Of the numerous parameters in the synthesis of Te and PbTe nanowires, the amount of N_2H_4 and the speed of N_2H_4 injection during the first step are particularly crucial in order to obtain small diameter nanowires. TEM images of products taken at the end of the Te growth step (Figure 3.10) show how the Te nanowire diameter decreases from 15.8 nm to 12.6 as the amount of N_2H_4 increases by a factor of 1.7. The Te nanowire diameter can be further reduced to 8.1 nm by increasing the N_2H_4 injection rate through the use of multiple injection syringes simultaneously. From the three syntheses represented in Figure 3.10, the reduction in diameter with increasing amount of N_2H_4 added is not monotonic, yet this is likely associated with an unintentional difference in N_2H_4 addition speed.

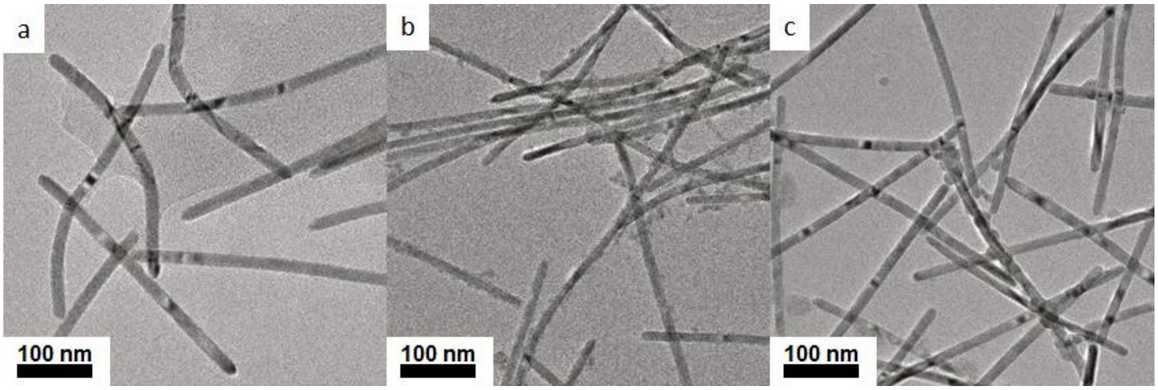

Figure 3.10 TEM image of Te nanowires synthesized using N_2H_4:Te molar ratios of (a) 12.7:1, (b) 19.1:1, (c) 21.2:1.

TEM images of the PbTe obtained after the second step in these reactions (Figure 3.11) show how the metal telluride nanowire diameter varies directly with the Te nanowire diameter obtained during the first reaction step.

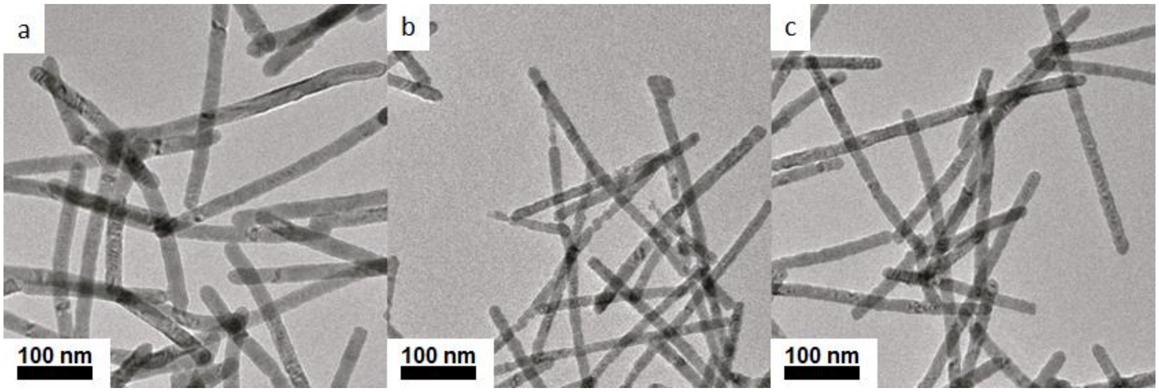

Figure 3.11 TEM image of PbTe nanowires obtained after the second step of syntheses in which the N_2H_4:Te molar ratios for the first step were a) 12.7:1, b) 19.1:1, c) 21.2:1.

As shown in Figure 3.5, time is the critical parameter in order to control the Te nanowire length. It is expected that PbTe nanowires with shorter lengths could, in principal, be synthesized by quenching the first reaction step after less than five minutes, washing and re-dispersing the products, and then introducing the appropriate precursor at high temperature. However, this is not possible in practice due to the insufficient cooling rate of the one liter reactor.

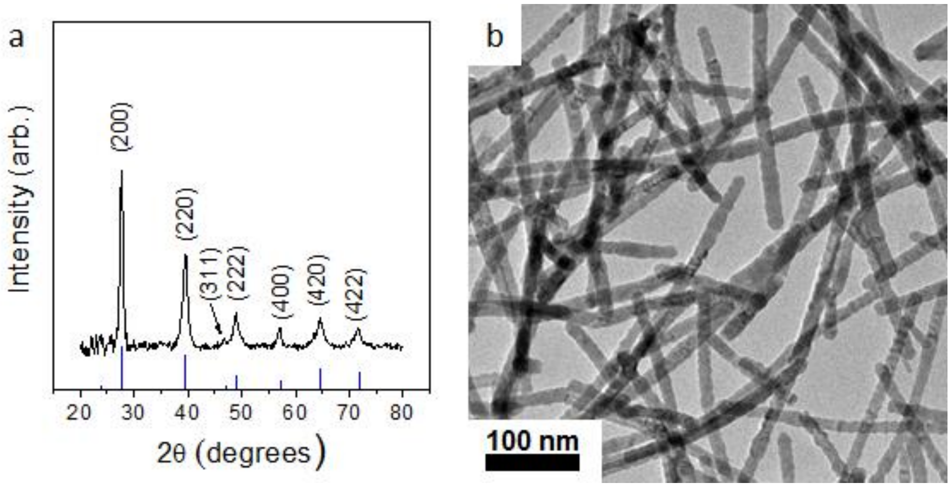

Figure 3.12 Characterization of PbTe nanowires eight months after their synthesis. (a) XRD pattern. Blue lines are standard peaks for PbTe (JCPDS # 01-077-0246). (b) TEM.

When stored at room temperature in the original reaction solution, PbTe nanowires are found to be stable for at least eight months with regard to their crystal structure and morphology. This claim is supported by XRD and TEM results in Figure 3.12, which show no significant difference compared with PbTe nanowires characterized within two weeks of their synthesis (Figure 3.3 and Figure 3.7).

As-synthesized PbTe nanowires can be washed, stripped of the PVP surfactant, and vacuum dried using a previously published procedure.[171] The resulting material can then be ground into a fine powder and weighed to determine the overall reaction yield (Figure 3.13). Approximately 11.7 grams of PbTe nanowire powder is produced per batch. Given theoretical yields determined by the weights of the starting precursors, the yield of the reaction is approximately 81.5%.

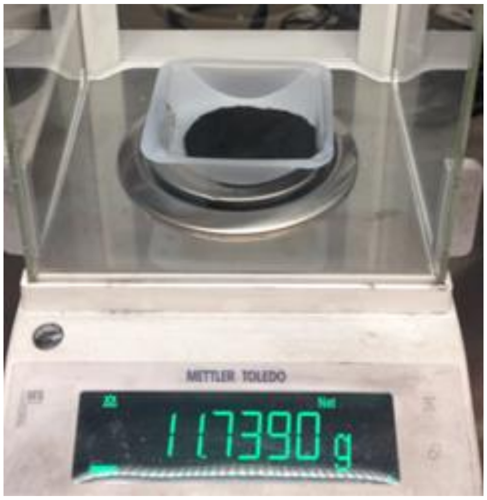

Figure 3.13 Purified, dry PbTe nanowire powder from one synthesis batch.

3.4 Conclusions

In summary, this chapter describes the high yield one-pot solution-phase production of PbTe nanowires using Te nanowire templates at low temperature and atmospheric pressure. TEM analysis reveals nanowire morphology of all products, while XRD indicates phase purity. After purification and drying of the nanowire products, greater than 80% yield is achieved. As compared with common 0.25-3 mmol batches of PbTe nanowires,[171,247,249–251,255] the large scale and yield of this synthesis considerably reduces the overall time needed to make the 7-10 grams of material required to make nanocomposite discs by SPS. This therefore opens new possibilities to study numerous nanocomposite disc samples as described in chapter 4.

CHAPTER 4. STRUCTURE, COMPOSITION, AND THERMOELECTRIC PROPERTIES OF UNINTENTIONALLY DOPED SPARK PLASMA SINTERED LEAD TELLURIDE NANOWIRES

4.1 Introduction

As described in chapter 2, great strides have been made in the solution synthesis and consolidation of high ZT materials such as $(Bi,Sb)_2(Te,Se)$ and ternary and quaternary copper selenides, yet the same level of success has not been achieved for solution synthesized PbTe. Beginning with the synthesis method described in chapter 3, this chapter continues to address this issue through a study on solution synthesized PbTe nanowires compressed into nanocomposite disks by SPS. This initial study investigates PbTe without any intentional dopant addition to focus on the effect of SPS temperature on the structure, composition, and thermoelectric properties of the nanocomposite discs produced.

Like other thermoelectric materials, nanostructures of PbTe have been made using a variety of methods such as hydrothermal synthesis,[199,201,249,257–259] reaction of a cation-oleate precursor with triocytlphosphine-Te in organic solvent,[148,260–262] and others such as atmospheric pressure synthesis at or below boiling temperature in a solvent of water and/or ethylene glycol.[109,200,208,253,263] While these synthesis methods each have certain advantages, the PbTe nanowire synthesis described in chapter 3 is chosen for further research on PbTe nanocomposites due to its inexpensive reagents, ease, short reaction times, and small nanostructure size.

Washed, dried, and ground PbTe nanowires are consolidated into disc-shaped samples by SPS at 405 °C, 450 °C, and 500 °C. All sintering conditions result in discs that possess grains with sizes of 5-30 µm as well as sub-100 nm grains. Their compositions can be understood in terms of published phase diagrams and other data. Regarding the thermoelectric properties, both the mobility and lattice contribution to thermal conductivity are reduced as compared with bulk PbTe. The Seebeck coefficients of the SPS'd samples do not deviate significantly from those predicted by the SPB model. The maximum ZT observed is 0.33 at 350 K for PbTe nanowires SPS'd at 450 °C.

4.2 Experimental Methods

The nanowire synthesis and washing method used for these studies is identical to that described in chapter 3. Seven to eight grams of PbTe nanowire powder are loaded into a 20 mm diameter cylindrical graphite die with graphite sheet lining the circumference as well as the faces of the rams. The material is SPS'd under a uniaxial pressure of 48 MPa at high temperature for five minutes. Sintering temperatures of 405 °C, 450 °C, and 500 °C are used to make samples henceforth denoted as SPS 405, SPS 450, and SPS 500, respectively. The minimum temperature of 405 °C is chosen based on instrument limitations; meanwhile at 500 °C extensive undesirable grain growth occurs (discussed later), so the effect of SPS temperatures above 500 °C is not explored. After sintering, the compressed material is extracted from the graphite die. The graphite sheet is removed from the actual PbTe portion of the disc by sanding. The disc is further polished by sanding until there is no evidence of graphite detected by XRD or EDS.

Samples of the discs are prepared for scanning electron microscopy (SEM) by inducing a fracture in the disc to expose an unpolished fracture surface. Fracture surfaces are also used for EDS. Samples are prepared for HRTEM by taking a small portion of the disc and grinding it with a mortar and pestle to form a fine powder. This powder is dispersed in ethanol and drop cast onto a TEM grid. For post-consolidation XRD analysis, a small portion of the disc is removed and ground into a fine powder in a nitrogen environment. The powder is then placed on double-sided tape on an amorphous glass substrate.

The polished discs are formed into appropriate sizes for electrical measurements. For Seebeck coefficient measurements, 9 mm diameter disc samples are prepare by sanding part of the original 20 mm discs. These are placed on a home-built Seebeck measurement system consisting of a vacuum chamber containing two copper blocks with embedded heaters and thermocouples to measure the hot and cold side temperatures and voltages simultaneously. The temperature and voltage gradients are in the in-plane direction. For electrical conductivity and Hall measurements, 5 mm x 5 mm x 0.8 mm samples are made by sanding part of the original 20 mm diameter discs. Then 100 nm of gold are thermally evaporated onto the four corners. Care is taken to ensure the electrodes are small compared to the width and length of the sample. An

MMR Hall measurement system is employed to measure the electrical conductivity and Hall coefficient in the in-plane direction using a magnetic field of ±0.5 Tesla.

The thermal diffusivity and specific heat of the SPS'd discs are measured at Thermophysical Properties Research Laboratory, Inc. Thermal diffusivity measurements are performed using the laser flash method on circular disc samples with diameters of 10 or 12.5 mm, while specific heat is measured using differential scanning calorimetry on smaller irregularly shaped samples. Density is determined by measuring sample dimensions and mass and the total thermal conductivity is obtained according to

$$\kappa = \alpha C_p \rho_m \tag{4.1}$$

where α is thermal diffusivity, C_p is the mass specific heat, and ρ_m is density. As the laser flash method determines the thermal diffusivity in the cross-plane direction, the thermal conductivity calculated is that of the cross plane direction.

For sample SPS 405 and for sample SPS 500, a single disc is used for all three measurements. Due to the brittle nature of PbTe that leads to undesired fractures, one disc is used for electrical measurements and a second disc is used for thermal measurements in the case of SPS 450. Based on room temperature electric conductivity measurements of the two SPS 450 discs, the use of two different discs is expected to cause a slight (~15%) underestimation of ZT for SPS 450. For all samples, care is taken to only test portions of the disc that did not experience any exposure to temperatures above 400 K after the completion of the SPS process. This low temperature limitation prevents further diffusion within the material, particularly of Te from the Te-rich PbTe phase to the regions of pure Te. This concept is discussed in further detail later in chapter 4.

4.3 Results

4.3.1 Structure and Composition

Digital photographs of discs compressed at the three temperatures are shown in Figure 4.1. All discs possess a metallic luster, typical of PbTe that is not severely oxidized.[196] The relative density of typical discs tends to increase with increasing sintering temperature from 0.69-0.72 for SPS 405 to 0.82-0.88 for SPS 450 and up to 0.86-0.88 for SPS 500. This rise in relative density can be understood in part by observing the SEM images of fracture surfaces of the three samples in Figure 4.1. The SPS temperature causes the grain size measured using SEM images and the method described previously[264] to vary from approximately 5 µm for SPS 405 and SPS 450 to approximately 30 µm for SPS 500. Thus, significant grain growth occurs during SPS. Such grain growth also occurred during hot pressing in a study on ball milled Tl-doped PbTe.[83]

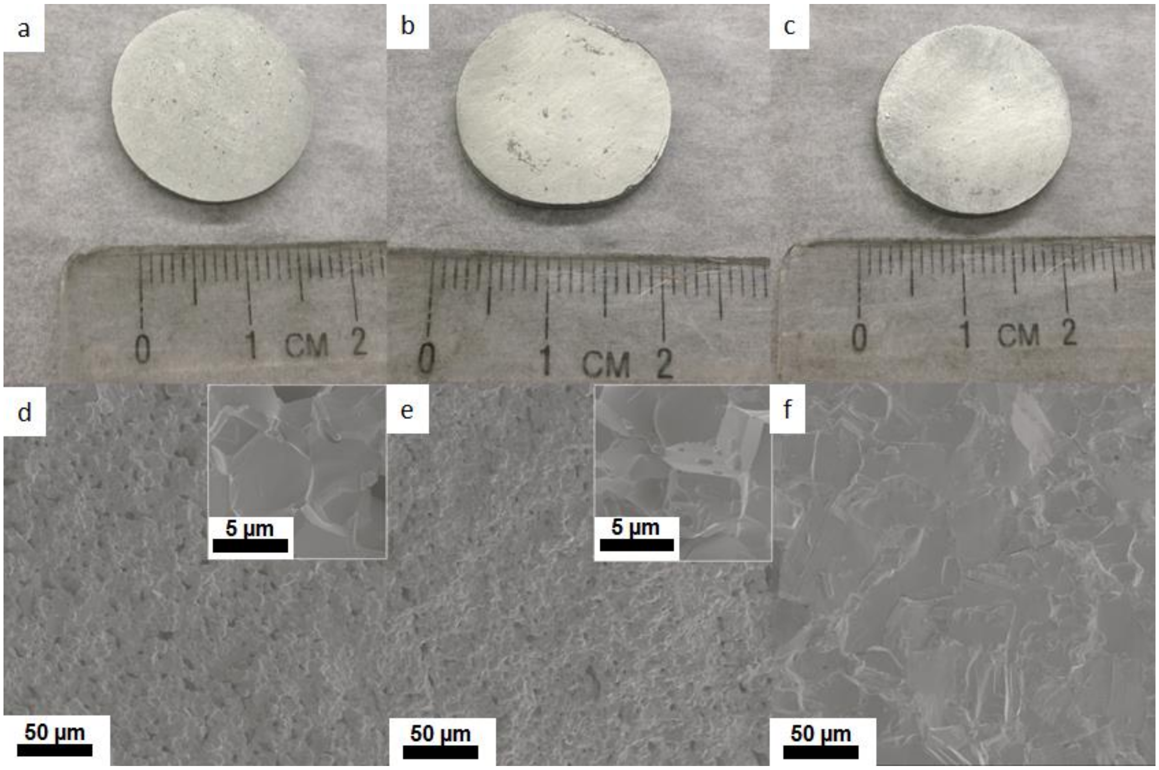

Figure 4.1 Digital photographs of (a) SPS 405, (b) SPS 450, and (c) SPS 500. SEM images of (d) SPS 405, (e) SPS 450, and (f) SPS 500. Insets in (d) and (e) are high magnification SEM images of SPS 405 and SPS 450, respectively.

As mentioned in chapter 3, the original PbTe nanowire powder is Te-rich (44.80 ± 0.44 atomic % Pb, 55.20 ± 0.44 atomic % Te). EDS analysis of the fracture surfaces reveals that all SPS'd samples are less Te-rich than the washed and dried nanowire powder and that the amount of excess Te decreases with increasing SPS temperature. The SPS 405, SPS 450, and SPS 500 discs have Pb:Te atomic ratios of 47.74:52.26, 48.16:51.84, and 49.45:50.55, respectively. This trend can be explained by the phase diagram of the Pb-Te system as well as the temperature dependence of the vapor pressure of Te. PbTe is stable in a very narrow range of compositions (<0.02 atomic % excess Pb or Te). As shown in Figure 4.2, Te-rich PbTe exhibits a eutectic at 405 °C,[191] which leads to the presence of a small amount of Te-rich liquid during SPS at 405 °C and above.

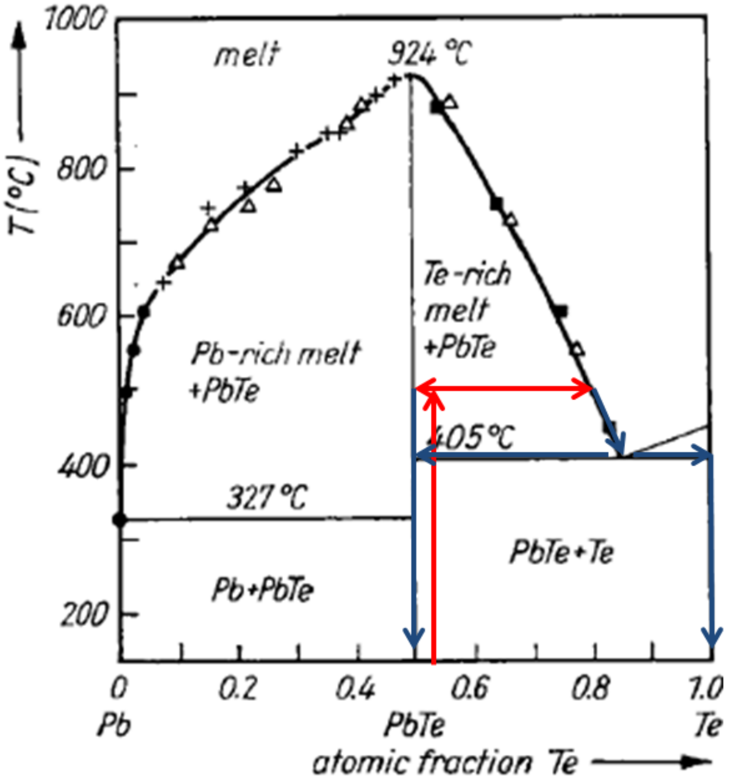

Figure 4.2 Pb-Te phase diagram with the approximate variation of composition during the SPS process for SPS 500 shown as an example. Adapted by permission from John Wiley & Sons: Physica Status Solidi (a) (Mühlberg M, Hesse D. TEM precipitation studies in Te-rich as-grown PbTe single crystals. Phys. status solidi. 76:513–24), copyright 1984.

As shown in Figure 4.3, the vapor pressure of Te increases monotonically with temperature for both pure Te and the Te rich melt at equilibrium with PbTe,[192,265] therefore as the SPS process takes place in a low pressure Ar atmosphere of about 2 mbar, significant Te sublimation and/or evaporation occurs, especially at higher SPS temperature. This explains the greatly reduced Te content in the SPS’d discs as compared with the washed and dried nanowire powder as well as the trend in disc composition vs. SPS temperature.

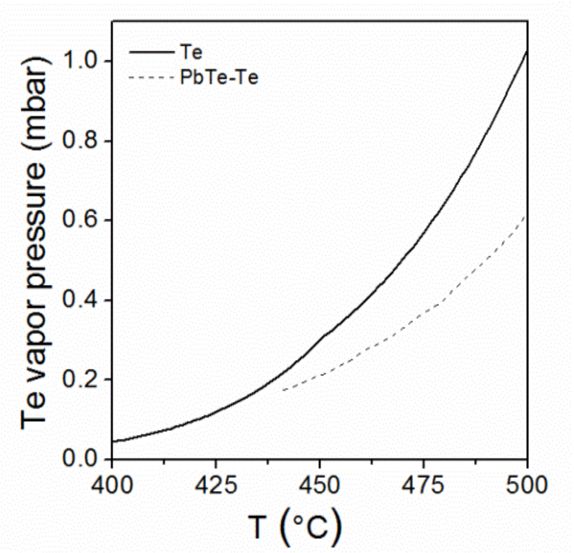

Figure 4.3 Vapor pressure of Te versus temperature.[192,265]

EDS elemental mapping shown in Figure 4.4 through Figure 4.6 provides insight into the micro scale spatial variation of the composition of the fracture surfaces of the SPS’d discs.

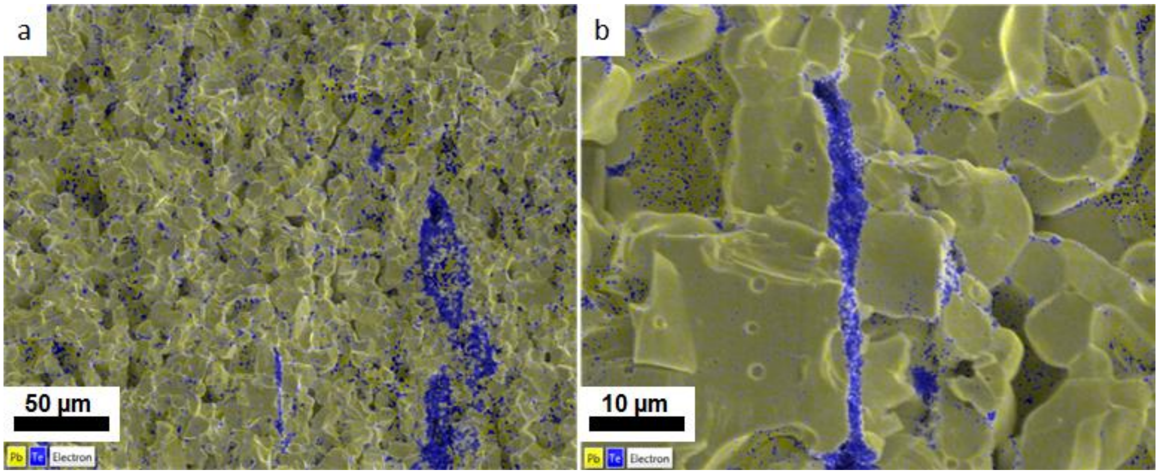

Figure 4.4 EDS elemental maps of the fracture surface of SPS 405. (a) Low magnification image, focusing on the Pb-Te distribution. (b) High magnification image, focused on a Te-rich region.

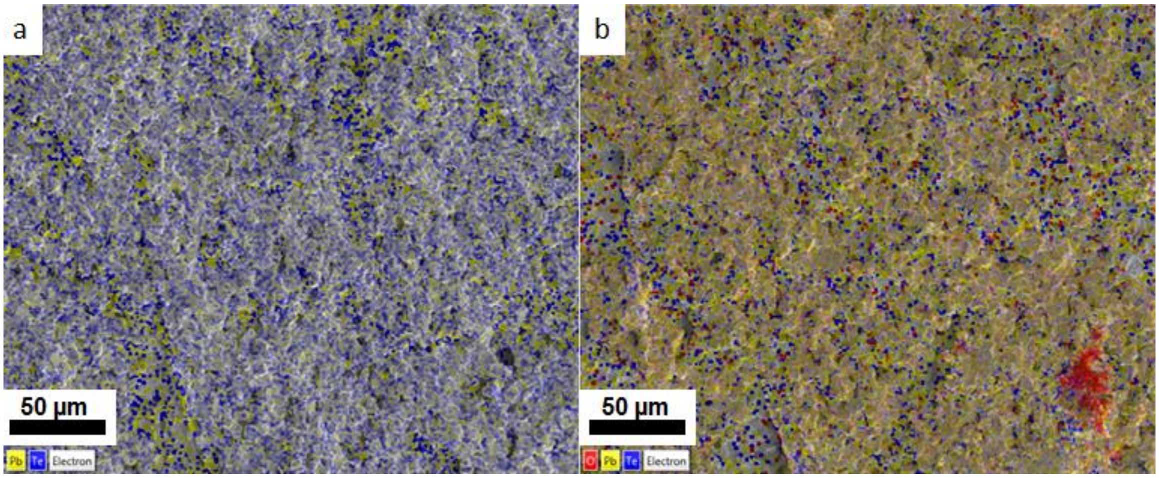

Figure 4.5 EDS elemental maps of the fracture surface of SPS 450. (a) Low magnification image, focusing on the Pb-Te distribution. (b) Low magnification image, in which the mapping software identifies an oxygen-rich region.

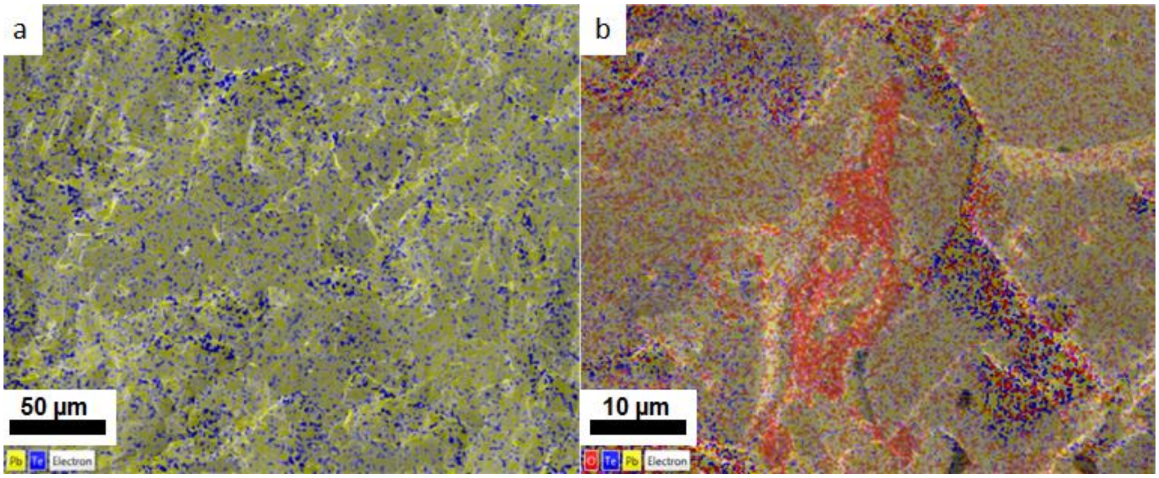

Figure 4.6 EDS elemental maps of the fracture surface of SPS 500. (a) Low magnification image, focusing on the Pb-Te distribution. (b) High magnification image, in which the mapping software identifies an oxygen-rich region.

In Figure 4.4a, the low magnification map shows several micro scale regions that are clearly Te-rich, as indicated by the blue color. These regions are likely due to the incomplete evaporation of excess Te during the high temperature step of the SPS process; the phase diagram in Figure 4.2 specifies that upon cooling, excess Te should phase separate from PbTe. The high magnification image in Figure 4.4b shows that sub-micron Te-rich regions also exist at the boundaries between some of the PbTe grains.

Unlike the elemental maps of SPS 405, the map of SPS 450 shown in Figure 4.5a does not unequivocally show Te-rich regions. This is likely due in part to the additional Te evaporation that occurs at this SPS temperature. Figure 4.5b shows an elemental map of SPS 450, which is acquired under settings which allowed for the identification of oxygen.

Interestingly, the lower right portion of the map shows a red region, which is likely associated with an oxide of Pb and/or Te.

The elemental maps of SPS 500 are similar to those of SPS 450 in that there is not clear evidence of Te-rich regions. This is certainly expected as SPS 500 is nearly stoichiometric in composition due to the high amount of Te evaporation during the SPS process. As with SPS 450, when the EDS mapping program is allowed to identify oxygen, regions such as the one shown in Figure 4.6b are shown to be oxygen rich.

Powder XRD on material taken from the discs helps to corroborate the SEM and EDS results regarding the grain growth and the nature of the impurities within the materials, respectively. As shown in Figure 4.7a, the main peaks from the discs can be indexed as PbTe (JCPDS # 01-077-0246). The peaks are noticeably sharper than those of the PbTe nanowire powder (Figure 3.3). According the general principal of the Scherrer equation, the significant reduction in XRD peak width points to a corresponding increase in grain size.[266] Regarding impurities, the Te regions observed in the elemental map of SPS 405 agree with the small peak at 38.25° seen in Figure 4.7b, which is associated with the (102) planes of Te. This peak is essentially absent from the XRD patterns on SPS 450 and SPS 500. In those samples, small peaks exist that appear to be associated with oxides. In SPS 450, a small peak at 28.7° exists, which could be associated with a major standard peak from PbO_2. In SPS 500, the same peak at 28.7° exists along with a small peak at 28.5°, which could be associated with a major standard peak from $PbTeO_3$. The small size of these peaks suggests that the extent of oxidation is minimal, which agrees with the small fraction of oxygen rich areas observed in the elemental maps.

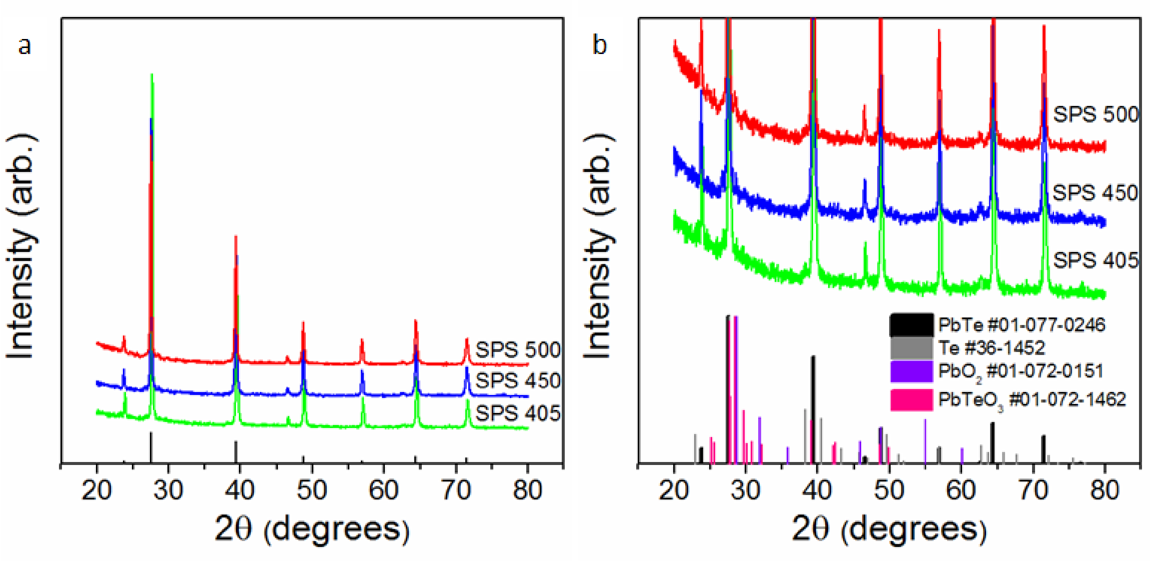

Figure 4.7 XRD patterns of SPS'd PbTe nanowires. (a) Overall view with standard peaks for PbTe (JCPDS # 01-077-0246) shown as black lines. (b) Zoomed in view, which reveals small peaks associated with impurities.

While SEM images and XRD (Figure 4.1 and Figure 4.7) give evidence that grain growth occurs during the SPS process, HRTEM images in Figure 4.8 show the presence of nanoscale grains. In fact, all three samples possess regions, such as the ones shown, with grain sizes of the same order of magnitude as the diameter of the pre-sintered PbTe nanowires, which could be associated with the original ultra-thin nanowires. Such nano-sized grains, combined with the fine microstructural features observed by SEM are expected to reduce the lattice contribution to thermal conductivity.

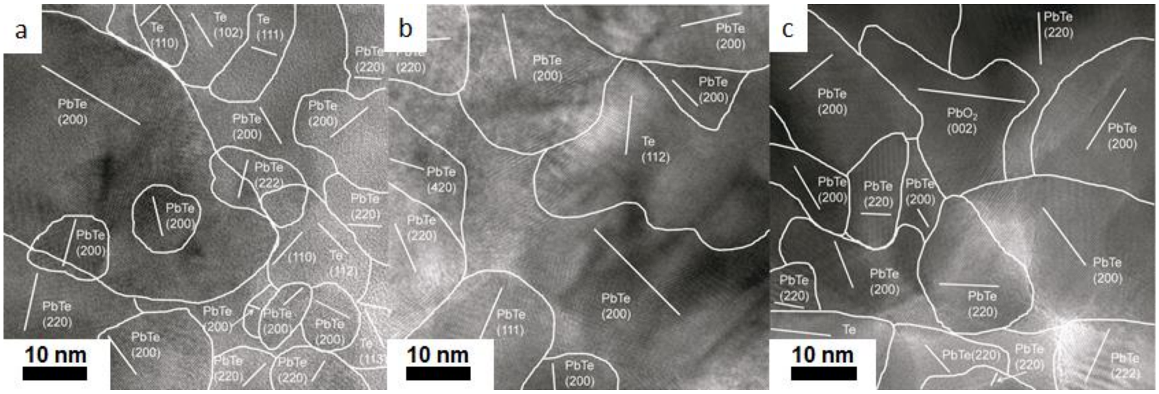

Figure 4.8 HRTEM of small grained regions of SPS'd PbTe nanowires with grain boundaries and lattice fringes shown as white lines. (a) SPS 405. (b) SPS 450. (c) SPS 500.

The HRTEM images also show the presence of both PbTe and Te grains for samples sintered at all three temperatures. The presence of Te grains agrees with the EDS results and the phase diagram of PbTe.[191] The image of SPS 500 indicates a region of PbO_2, which agrees with both the EDS and XRD analysis. It is likely due to a small, unintentional amount of oxidation of the pre-sintered PbTe nanowires.

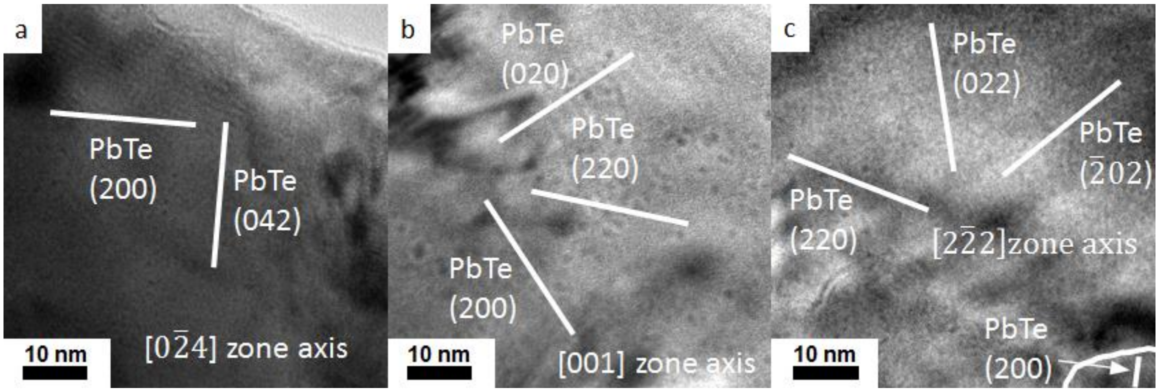

Figure 4.9 HRTEM of large grained regions of SPS'd PbTe nanowires with grain boundaries and lattice fringes shown as white lines. (a) SPS 405. (b) SPS 450. (c) SPS 500.

Additional HRTEM images of the SPS'd discs shown in Figure 4.9 reveal large (approximately 60nm by 60 nm) single crystalline regions. The observation of these regions agrees with the SEM and XRD results which show the presence of large grains as a result of all three SPS temperatures.

4.3.2 Thermoelectric Properties

Results from electrical measurements on the SPS'd samples are shown in Figure 4.10. For all three samples, the electrical conductivity (Figure 4.10a) decreases with increasing temperature as is typical for extrinsic PbTe. Meanwhile, the Seebeck coefficient (Figure 4.10b) increases monotonically with temperature, further signifying that the onset of thermal excitation of carriers does not take place in the temperature range investigated here. While the Seebeck coefficients of the three samples are two to four times larger than those of heavily doped bulk PbTe in this temperature range, the low electrical conductivity results in a reduced power factor, (Figure 4.10c) for the SPS'd nanowire discs.

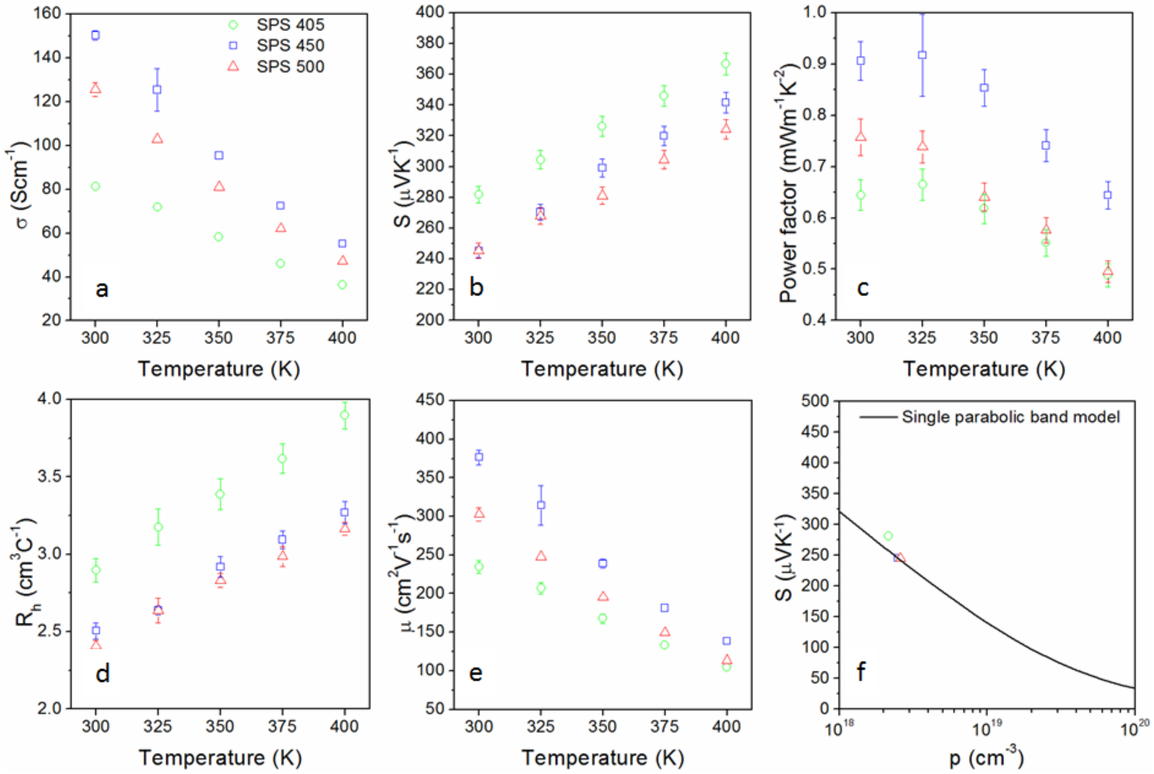

Figure 4.10 (a) Electrical conductivity, (b) Seebeck coefficient, (c) Power factor, (d) Hall coefficient, (e) Mobility, and (f) Pisarenko plot of the three SPS'd PbTe nanowire discs. The SPB model-based calculation is also shown in (f) for comparison.

Variable temperature Hall measurements (Figure 4.10d) show that the Hall coefficient slowly increases with temperature for all samples, which is typical of p-type PbTe and is usually explained by the relative movement of the L and Σ valence bands with temperature at a fixed hole concentration.[97,189,267] The carrier concentration is calculated as

$$p = \frac{1}{eR_h} \tag{4.2}$$

where p is the carrier concentration and R_h is the Hall Coefficient at 300 K. This equation assumes that the Hall factor is equal to one; this assumption is generally satisfied in p-type PbTe.[46,268] The hole concentration is found to increase from 2.2 x 10^{18} cm^{-3} for SPS 405 to 2.6 x 10^{18} cm^{-3} for SPS 500.

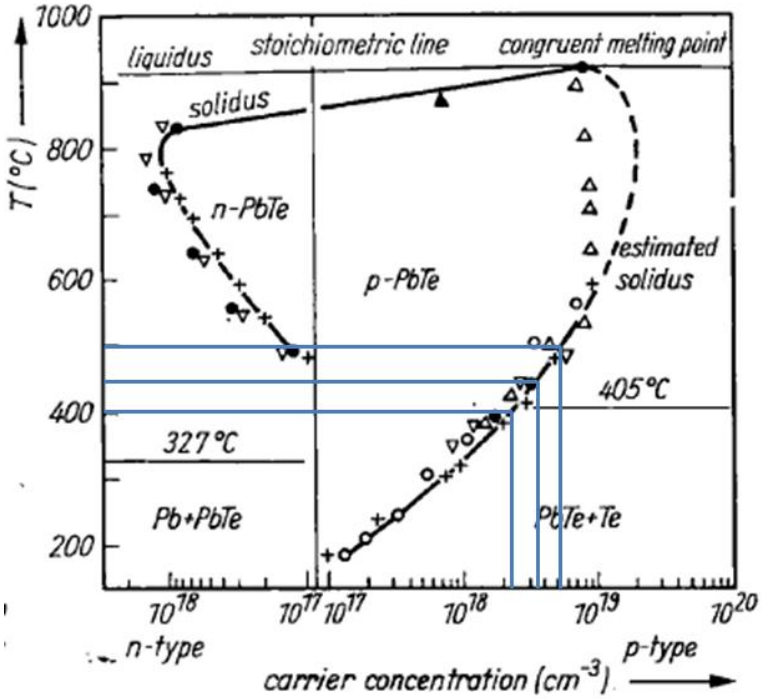

Figure 4.11 Phase diagram of the Pb-Te system near the 50 atomic % Pb line. Adapted by permission from John Wiley & Sons: Physica Status Solidi (a) (Mühlberg M, Hesse D. TEM precipitation studies in Te-rich as-grown PbTe single crystals. Phys. status solidi. 76:513–24), copyright 1984.

The variation in carrier concentration with SPS temperature can be explained using the near stoichiometric PbTe portion of the Pb-Te phase diagram shown in Figure 4.11.[191] For binary PbTe, the carrier concentration is dependent on the amount of excess Pb or Te in the PbTe phase, thus slightly more than 50 atomic % Te corresponds to a carrier concentration of 1 x 10^{17} and additional Te in the PbTe phase results in higher carrier concentrations. Therefore, the horizontal axis of the phase diagram shown in Figure

4.11 is the carrier concentration instead of the atomic % Te. [268] The solubility limit of excess Te in PbTe increases with temperature from less than 0.001 atomic % at 200 °C up to 0.015 atomic % at 600 °C, which results in carrier concentrations of as high as 8x 10^{18} cm^{-3}.[191]

During the SPS process, the high temperatures presumably facilitate the dissolution of the available excess Te into the PbTe phase. Barring significant diffusion limitations, the amount of Te dissolved in the PbTe phase should be in accordance with the amount predicted by the phase diagram. As the cooling to room temperature after the SPS process is fairly rapid (<45 minutes), some of the excess Te should be frozen into the PbTe phase. The extent to which the excess Te is indeed frozen in is shown in Table 4-1. Clearly, the experimentally determined carrier concentration increases with SPS temperature as predicted. However, it appears that during cooling from the higher SPS temperatures, the excess Te is sufficiently mobile to leave the PbTe phase as suggested by the deviation between the predicted and experimental carrier concentrations.

Table 4-1 Variation of carrier concentration with SPS temperature.

Sample	Carrier concentration predicted by phase diagram (cm^{-3})	Carrier concentration calculated using Hall measurement (cm^{-3})
SPS 405	2.2×10^{18}	$2.15 \pm 0.06 \times 10^{18}$
SPS 450	3.4×10^{18}	$2.49 \pm 0.05 \times 10^{18}$
SPS 500	5.1×10^{18}	$2.59 \pm 0.04 \times 10^{18}$

After the SPS process, the hole concentration decreases if the discs are exposed to temperatures above 400 K for long periods of time in accordance with the low carrier concentration predicted by the phase diagram.[191] Therefore, all transport property measurements are performed at 400 K and below to obtain agreement between data obtained during heating and cooling.

Charge carrier mobility is calculated according to

$$\mu = \sigma(T) R_h(300\ K) \tag{4.3}$$

The use of the Hall coefficient at 300 K is motivated by the fact that the increase in the Hall coefficient with increasing temperature stems from the changing relative contributions of the heavy and light valence bands and not from an actual change in carrier concentration.[269,270] The mobility steadily decreases with increasing temperature for all samples as shown in Figure 4.10e, which is typical for extrinsic PbTe as the acoustic phonon scattering becomes stronger at higher temperatures. However, the mobility is suppressed compared to the bulk values due to porosity and presumably due to the microstructure and nanostructure as well. Interestingly, the mobility does not increase monotonically with SPS temperature as might be expected based on the trends in grain size and relative density. Instead SPS 450 shows the highest mobility of the three samples and this contributes to SPS 450 possessing the highest power factor.

In Figure 4.10f, the Seebeck coefficient is plotted as a function of carrier concentration for the three SPS'd samples at 300 K. For comparison, the Seebeck coefficient calculated based on the SPB model assuming acoustic phonon scattering and an effective mass of 0.36 times the free electron mass is also shown in Figure 4.10f.[43,44] The experimental Seebeck coefficients for SPS 450 and SPS 500 are in good agreement with the values predicted by the SPB model (<2 % different), while the Seebeck coefficient of SPS 405 is about 10 % larger than the SPB value at 300 K. Several previous studies on nanostructured PbTe have attributed similar discrepancies to a change in the energy dependence of charge carrier scattering.[199,200,208,271] Meanwhile, a more recent study suggests that apparent deviations from theoretical relations and historical data for PbTe could be due to electronically inhomogeneous PbTe samples leading to discrepancies between the carrier concentration determined by Hall measurements and the true carrier concentration.[272] In the case of the data for SPS 405, the modest 10% deviation from the SPB value could be explained by the presence of additional scattering mechanisms or perhaps even by electronic inhomogeneity resulting from the phase segregation during the SPS process.

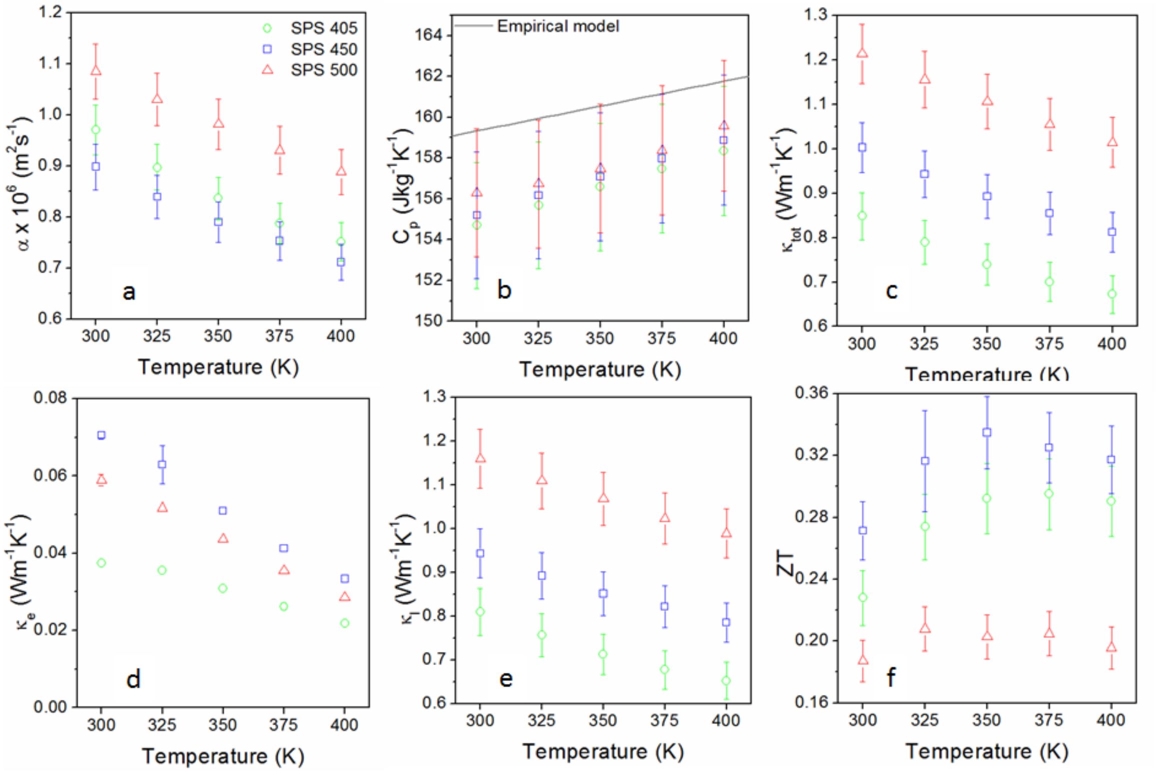

Figure 4.12 Thermal properties of SPS'd PbTe. (a) Thermal diffusivity. (b) Specific heat capacity. (c) Total thermal conductivity. (d) Electronic component of thermal conductivity. (e) Lattice component of thermal conductivity. (f) ZT.

The result for the thermal properties measurements and ZT are shown in Figure 4.12. The thermal diffusivities (Figure 4.12a) of the three samples decrease with temperature and are approximately two to four times lower than p-type PbTe grown by melting elemental precursors.[97] The specific heat (Figure 4.12b) of the three samples increases slightly from 300 K to 400 K and throughout the entire temperature range is within 3 % of the commonly used empirical model,[186]

$$C_p\ (k_b \text{ per atom}) = 3.07 + 4.7 \cdot 10^{-4} \cdot (T - 300) \qquad (4.4)$$

The total thermal conductivity is shown in Figure 4.12c. As expected for this temperature range, thermal conductivity monotonically decreases with temperature. Furthermore, the thermal conductivity increases monotonically with increasing SPS temperature, which is likely due to the trends in grain size and relative density.

The electronic component of thermal conductivity is calculated by the Wiedemann-Franz Law. While the traditional value for the Lorenz number,[47]

$$L = \frac{\pi^2}{3} \cdot \left(\frac{k_b}{e}\right)^2 = 2.45 \cdot 10^{-8} \mathrm{W\Omega/K^2} \tag{4.5}$$

gives a good approximation, a more accurate value can be calculated using the SPB model assuming acoustic phonon scattering. First, the reduced Fermi level can be calculated at each temperature of interest using experimental values for the Seebeck coefficient using equation 1.17 in which the scattering coefficient is -0.5.

$$S = \frac{k_b}{e}\left(\frac{F_1(\zeta^*)}{F_0(\zeta^*)} - \zeta^*\right) \tag{4.6}$$

The Lorenz number can then be calculated using the equation[273]

$$L = \left(\frac{k_b}{e}\right)^2 \cdot \frac{3F_0(\zeta^*) \cdot F_2(\zeta^*) - 4[F_1(\zeta^*)]^2}{[F_0(\zeta^*)]^2} \tag{4.7}$$

In practice, it is convenient to create a correlation between the Seebeck coefficient and the Lorenz number, which is shown graphically in Figure 4.13.

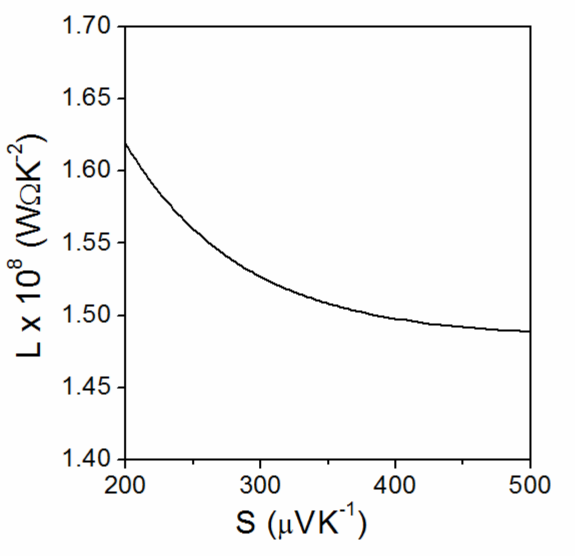

Figure 4.13 Lorenz number as a function of Seebeck coefficient under the approximation of the SPB model and acoustic phonon scattering.

As the carrier concentrations and electrical conductivities of the discs are lower than highly doped PbTe, the electronic components of thermal conductivity are below 0.1 W/mK for all samples. The lattice components of thermal conductivity are calculated assuming that the bipolar component is negligible. As shown in Figure 4.12e, the lattice components of thermal conductivity are in the range of 0.6 – 1.2 W/mK; thus the lattice contribution dominates the heat transport. The lattice components of thermal conductivity are approximately 1.8-2.5 times smaller in the SPS'd materials than in bulk PbTe.[43,186]

The ZT calculated for the SPS'd PbTe nanowire discs is presented in Figure 4.12f. As the electrical measurements are performed in the in-plane direction and the thermal conductivity is that of the cross-plane direction, the ZT values are only accurate if the samples are isotropic. The SEM and TEM images of the discs suggest that the discs are nearly isotropic, although it is difficult to quantify the extent of isotropy. Overall, the measurement of in-plane electrical properties and cross-plane thermal properties for the purposes of ZT calculations is a natural result of using thin disc samples made by high temperature compression. Uniaxially compressed samples with heights of at least ten mm are sometimes used for evaluation of the thermal conductivity perpendicular to the pressing direction and/or the electric properties parallel to the pressing direction.[187,216] However, such samples are not commonly made within the solution synthesis community for whom the preparation of enough material to make ten mm tall compressed discs/cylinders would be quite time consuming.

The three samples exhibit maximum ZT values in the range of 325 – 375 K, which is typical of PbTe with low carrier concentration.[196,274] The combination of a high mobility and low lattice thermal conductivity in SPS 450 results in a maximum ZT of 0.33 at 350 K, the highest observed in this study. As shown in Figure 2.6, this and other values for ZT observed in the present study are significantly larger than those of other solution synthesized PbTe samples from literature. Figure 2.5 shows that the room temperature Seebeck coefficients and electrical conductivities of the SPS'd material from the present study are not markedly different from those of other solution synthesized samples. Thus, the carrier concentration and even the mobility do not appear to be responsible for the high ZT values observed in the present study. Instead, the ratio of charge carrier mobility to lattice thermal conductivity is the key difference between the SPS's material in this study and other solution synthesized PbTe, as described in detail below.

Figure 4.14 shows how the hole mobility of the SPS'd material is in a similar range as that of many other solution synthesized PbTe samples, despite the porosity of the SPS'd samples.[198–201] In principal, the high charge carrier mobilities of the SPS's samples could be associated with the formation of the Te-rich liquid during the SPS process that could help lead to good inter-grain contact in the final solid disc.

Also shown in Figure 4.14 is how the lattice component of thermal conductivity for the SPS'd materials in this study are around two times lower than other solution synthesized materials. Interestingly, several solution synthesized materials have lattice thermal conductivities that are similar to or even larger than that of large grained PbTe.[43] The lattice component of thermal conductivity is generally thought to be associated with three main structural features including porosity, microstructure, and nanostructure.[96,109,262] The porosity of the SPS's samples is generally larger than that of the other solution synthesized materials, the microstructure of the SPS'd samples is similar to that of the other solution synthesized materials, and the extent of nano-sized features in the various materials is either unexplored or difficult to quantify. Future research should aim to explore the relative importance of these three types of structural features in achieving such a low lattice thermal conductivity in the SPS'd material.

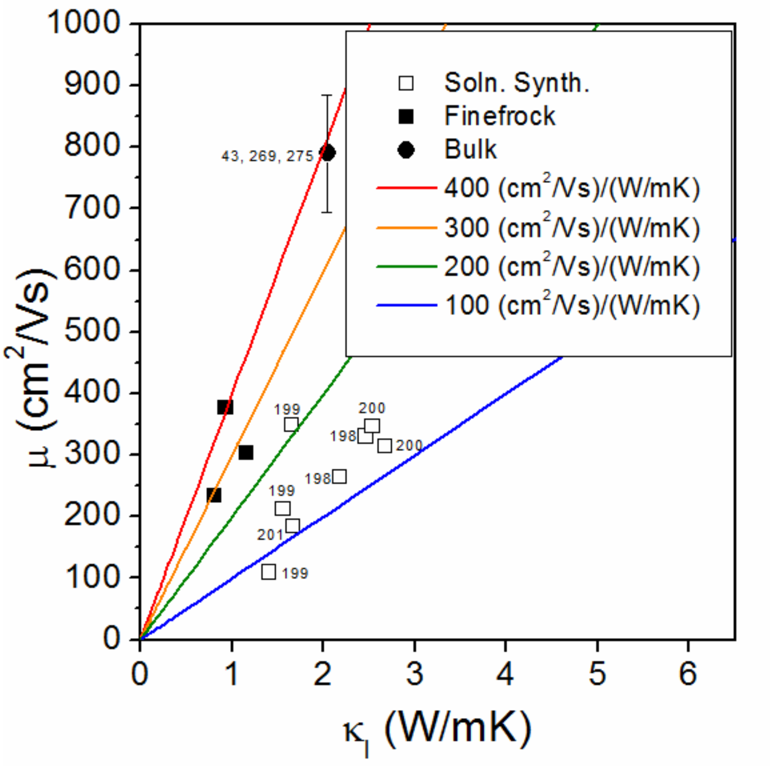

Figure 4.14 Hall mobility versus lattice thermal conductivity for solution synthesized and bulk PbTe at or near room temperature.

The colored lines in Figure 4.14 represent constant values of the ratio of mobility to lattice thermal conductivity. The SPS'd samples in this study possess room temperature ratios of 262 to 404 (cm^2/Vs)/(W/mK) while most of the other solution synthesized materials possess ratios of less than 200 (cm^2/Vs)/(W/mK). This is the key reason why the SPS'd material in the present study has an increased ZT compared with the solution synthesized material in literature.

The relatively large ratios of mobility to lattice thermal conductivity and associated ZT increase in the SPS's samples could be associated with the care that was taken to eliminate oxygen exposure prior to SPS. In principle, oxide phases in the material could present a significant barrier to charge carriers but have a relatively small impact on lattice vibrations such that oxidation could ultimately reduce the ratio of mobility to lattice thermal conductivity. Much prior work on solution synthesized p-type PbTe discusses oxide phases observed using XRD.[198–200] In fact, oxide phases are also observed in the present study. Unfortunately, without actual XRD patterns presented in literature, it is not possible to quantitatively compare the extent of oxidation in the various materials.

The comparison between the ZT values of the present unintentionally Te-doped solution synthesized PbTe and large-grained highly Na-doped in Figure 2.6 is mostly useful for simply emphasizing the need to increase the carrier concentration in the solution synthesized material in order to reach the optimum range. This need is addressed in chapter 5. A full assessment of whether the porosity, microstructure, and nanostructure of the SPS'd samples leads to an increase in ZT compared to large-grained material would require knowledge of the ZT of a large-grained PbTe sample with a similar carrier concentration as the SPS'd samples across the same range of temperatures considered in the present study. A search through the literature revealed no such knowledge available. Fortunately, knowledge of the lattice thermal conductivity and charge carrier mobility of large grained PbTe with carrier concentrations in the range of 2-3 x 10^{18} /cm^3 is available in literature.[43,269,275] Thus, the concept of the ratio or the charge carrier mobility to the lattice thermal conductivity can be used to evaluate the effect of the porosity, microstructure, and nanostructure in the present SPS'd samples.

Figure 4.14 shows that the high mobility of 790 ± 96 cm^2/Vs and high lattice thermal conductivity of 2.04 W/mK for the large-grained material lead to a ratio of 388 $(cm^2/Vs)/(W/mK)$ at room temperature. Note that the values of the mobility reported for large-grained p-type PbTe are obtained using equation (4.3, generally at temperatures of nearly 300 K, thus they are appropriate for comparison with the results from the present study on SPS'd PbTe. The ratio for the SPS 450 sample, 404 $(cm^2/Vs)/(W/mK)$, is quite similar to the large-grained value while those of SPS 405 and SPS 500 are significantly lower. Therefore, the ZT versus temperature curve for SPS 450 could be expected to be similar to or slightly enhanced compared with similarly doped large-grained p-type PbTe. The ZT versus temperature curves for SPS 405 and SPS 500 could be expected to be noticeably lower than that of similarly doped large-grained p-type PbTe. Thus, the conclusions regarding the best SPS'd PbTe sample are similar to those of the best solution synthesized p- and n-type $(Bi,Sb)_2(Te,Se)_3$ discussed in chapter 2; the figure of merit is quite similar to that of the corresponding large-grained material and cost comparison of the synthesis methods is one logical next step.

4.4 Conclusions

In summary, PbTe nanowires with diameters of around 12 nm are synthesized in solution at 120 °C using intermediate Te nanowire templates. These are compressed into millimeter-scale discs using SPS. Samples formed by SPS at 405 °C, 450 °C, and 500 °C possess micrometer-sized grains as well as nanometer-sized grains, which results in a reduced thermal conductivity compared to bulk PbTe. All samples are p-type with low carrier concentrations in the range of 2.2 – 2.6 x 10^{18} cm^{-3} in accordance with the low solubility of excess Te in PbTe. This results in a maximum figure of merit of 0.33 at 350 K. This is significantly larger than the ZT values of other solution synthesized p-type PbTe in literature. Based on the ratio of charge carrier mobility to lattice thermal conductivity, this ZT value is expected to be quite similar to that of similarly doped large-grained PbTe.

CHAPTER 5. THERMOELECTRIC PROPERTIES OF BISMUTH AND SODIUM DOPED LEAD TELLURIDE NANOWIRES

5.1 Introduction

One of the clear lessons from the results described in chapter 4 is that excess Te or Pb cannot lead to the range of carrier concentrations required to obtain high ZT at high temperature where PbTe is best suited. A doping strategy must be developed. As described in chapter 2, several challenges exist in the area of doped solution synthesized PbTe. The research described in this chapter begins to address these challenges through two doping strategies.

In the first strategy, Bi precursor is added during the solution synthesis of PbTe nanowires to form Bi-doped PbTe nanowires that are hot pressed or SPS'd to form n-type discs. The carrier concentration is controlled using the amount of Bi precursor added. The use of Bi as a dopant is motivated by two factors. First, Bi cations normally exist in the +3 valence state. With Pb existing in the +2 valence state in PbTe, Bi_{Pb} defects should, in principal, contribute one free electron for charge transport. Much prior literature shows that Bi does indeed act as an n-type dopant in PbTe.[43,196,276–279] Second, prior experiments on the synthesis of Bi_2Te_3 nanowires using Te nanowire templates show that Bi readily diffuses into Te nanowires.[160,171] Therefore it is expected.

that, unlike K, Bi precursor in solution should react with the Te nanowires during PbTe synthesis to dope PbTe.

In the second strategy, PbTe nanowires are synthesized using the procedure described in chapter 3, a small amount of Na_2Te powder is added to the dry PbTe nanowire power, the two are mixed, and they are then hot pressed to form p-type discs with high carrier concentrations. The use of Na is motivated by its well-known ability to dope PbTe to carrier concentrations in excess of 10^{20} /cm^3.[186,280] Hot pressing is chosen instead of SPS because long sintering times are, in fact, desirable in order to allow for Na to diffuse from the Na_2Te powder to the PbTe to form Na_{Pb} defects required to achieve high hole concentrations.[281]

A thorough evaluation of the thermoelectric properties of the Bi- and Na-doped discs is yet to be completed. However, initial studies provide evidence of the efficacy of the doping methods and suggest paths to achieve improved ZT for doped PbTe nanowire discs.

5.2 Experimental Methods

5.2.1 Bi-Doped PbTe Nanowire Synthesis and Disc Preparation

Bi-doped PbTe nanowires are synthesized using a slightly modified version of the synthesis procedure described in section 3.2. First, 43 mmol of Te nanowires are grown in an identical manner to that described in section 3.2. Then, a mixed precursor solution of Pb and Bi is prepared by combining 16.93 g $Pb(CH_3CO_2)_2•3H_2O$ (43.0 mmol), a specified amount of $Bi(NO_3)_3•5H_2O$ (Aldrich, 98%), 4.3 g PVP and 125 ml ethylene glycol in a beaker. Table 5-1 shows the sample names and corresponding amounts of Bi precursor for different doping levels.

Table 5-1 Bi-doped PbTe nanowire sample names and synthesis recipe details.

Sample name	Bi:Pb molar precursor ratio	$Bi(NO_3)_3•5H_2O$ added (g)
0.5 % Bi	0.005	0.104
1.0 % Bi	0.01	0.209
2.0 % Bi	0.02	0.417
3.0 % Bi	0.03	0.626

The solution is stirred on a 120 °C hot plate for about ten minutes, which causes the $Pb(CH_3CO_2)_2•3H_2O$ and PVP to dissolve. The hot plate is then turned off to help the $Bi(NO_3)_3•5H_2O$ remain dissolved. The hot plate is set to 120 °C for five to ten minutes prior to addition to the Te nanowire solution. One hour after the initiation of Te nanowire growth using N_2H_4, the Pb/Bi precursor solution is added into the reaction mixture. One hour after the Pb/Bi precursor addition, the jacket temperature setpoint is decreased to 20 °C. When cooled, the products are collected in a Pyrex container.

The material is washed using the same procedure as that described in section 3.2. After the final (seventh) centrifuge step, the nanowire powder that is still wet with ethanol is loaded onto a long graphite sheet and into a horizontal tube furnace. The material is annealed with 100 sccm forming gas (4% H_2 in N_2) flow at a pressure of approximately four torr with a tube furnace set point temperature schedule shown in Figure 5.1. The slow increase to 100 °C in the first two hours is intended to fully remove the ethanol. The brief step at 350 °C is intended to cause Te to sublime in order to bring the Pb:Te ratio close to one. Ultimately, the goal is to prevent the material from melting during the eventual SPS procedure, as requested by the SPS instrument staff.

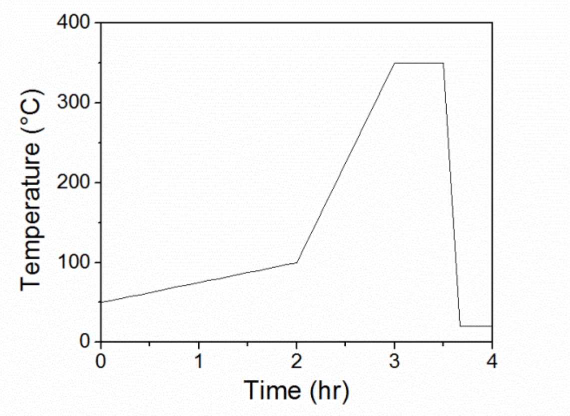

Figure 5.1 Tube furnace set point temperature during the Bi-doped PbTe annealing.

After annealing, the fully dry chunk material is transferred to a nitrogen filled glove box where it is ground into a fine power. The material is SPS'd into a high relative density disc using a procedure identical to that described in chapter 4. A SPS temperature of 450 °C is chosen because of the fine grain structure and high mobility of the SPS 450 material from chapter 4.

The approximate values of the Seebeck coefficients of several samples are determined using an MMR SB100 Seebeck measurement system. In this system, the sample is connected to two gold electrodes using Ag paint. Then, one end of the sample and of a piece of constantan reference material are heated a few °C and the voltages across the sample and reference are measured. The ratio of the sample and reference voltages and the known Seebeck coefficient of the reference material are used to estimate the Seebeck coefficient of the sample.

5.2.2 Na-Doped PbTe Nanowire Disc Preparation

For most discs, PbTe nanowire powder is prepared using a method identical to that described in chapter 3. For a small number of discs, the procedure is slightly modified; the hydrazine washing step is accomplished without stirring. The material that receives thorough mixing during the hydrazine washing step is henceforth referred to as fully hydrazine washed PbTe while the material that is washed with hydrazine without stirring is henceforth referred to as partially hydrazine washed PbTe. These names reflect the fact that, without stirring, some of the PbTe remains packed at the bottom of the container and may not come in contact with the hydrazine in the solution above. The nanowire powder is prepared for hot pressing by grinding PbTe nanowires together with Na_2Te powder (Materion Advanced Chemicals, 60 mesh, 99.9%) using a mortar and pestle at a proportion of 0.01 g Na_2Te for every 1.99 g PbTe nanowires. Typically, high accuracy in composition is achieved by preparing a stock solution of 0.1 g Na_2Te and 0.9 g PbTe nanowires, which is fully mixed. For individual discs, an appropriate amount of stock solution is added to PbTe nanowires to achieve the desired overall Na_2Te percentage.

The combined powder is loaded into a 12.7 mm stainless steel die with graphite sheet lining the circumference as well as the top and bottom rams. The die is hand pressed and loaded onto a four post Carver press with temperature controlled plates. Approximately 68 MPa are applied to the die by raising the bottom plate and the plates are heated to 500 °C. The typical hot press plate temperature and applied pressure over time are shown in Figure 5.2. During the heating step, the bottom plate is periodically raised further in order to maintain a pressure of 68 MPa while the material is compressed. After both plates are at 500 °C for 30 minutes, the pressure and temperature are allowed to drop naturally. Cooling fully to room temperature requires at least six hours. As with SPS'd discs, the hot pressed discs are extracted from the die and then sanded to fully remove the graphite sheet. Certain hot pressed discs are annealed in a horizontal tube furnace under specified conditions.

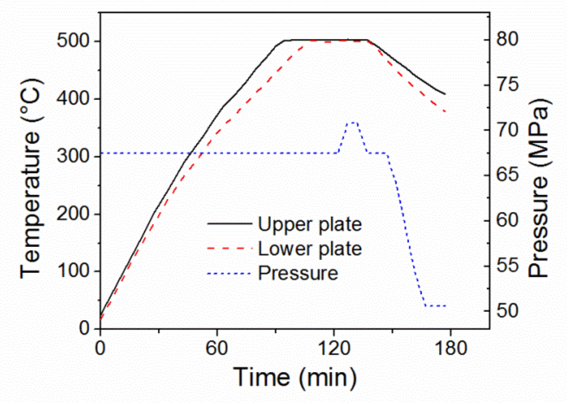

Figure 5.2 Typical hot press temperatures and pressure over time for disc fabrication.

5.3 Results

5.3.1 Structure and Composition

5.3.1.1 Bi-Doped PbTe Nanowires

The addition of Bi precursor during the solution synthesis of PbTe nanowires does not have a great impact on the morphology or phase of the resulting washed material as shown below. TEM images of the four samples with different amounts of Bi are shown in Figure 5.3. The nanowires shown have essentially the same diameter as unintentionally-doped PbTe nanowires described in chapter 3. Some larger nanostructures are also observed under TEM (not shown). However, it is difficult to quantify the relative amounts of these nanostructures or determine if they are associated with the Bi precursor addition.

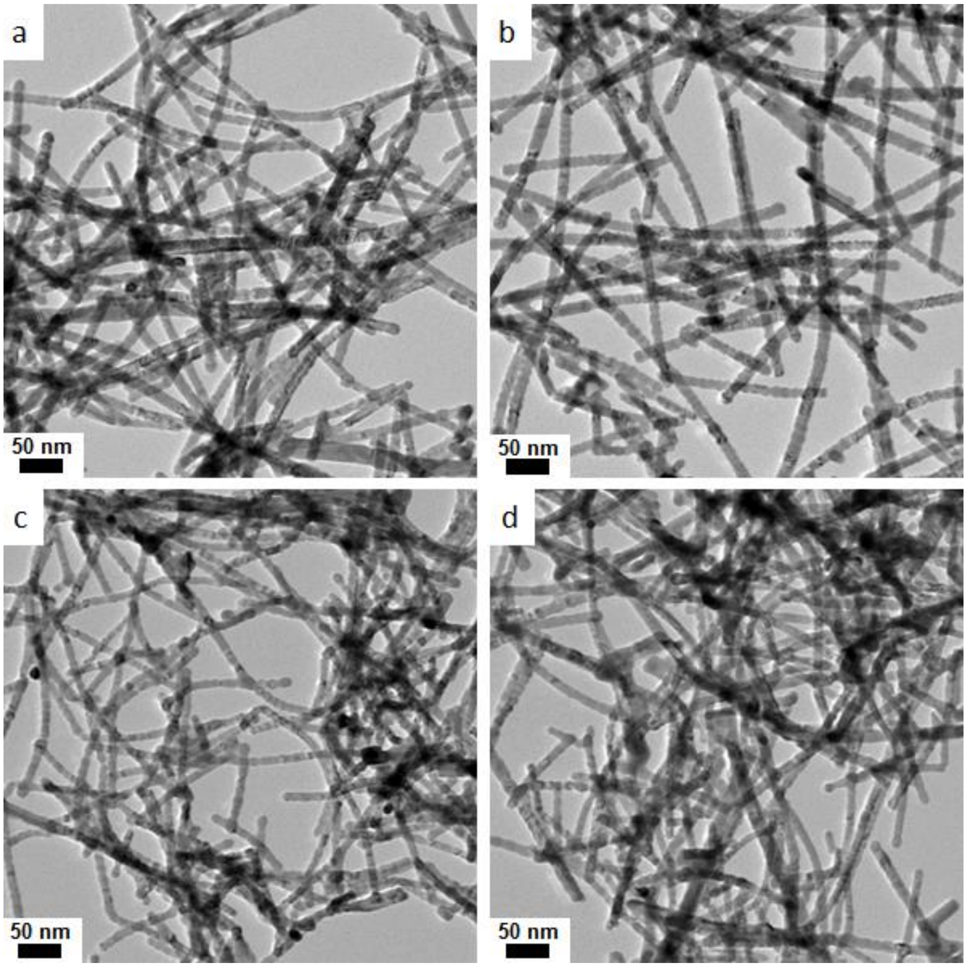

Figure 5.3 TEM images of Bi-doped PbTe nanowires. (a) 0.5 % Bi. (b) 1.0 % Bi. (c) 2.0 % Bi. (d) 3.0 % Bi.

The XRD patterns of the four samples shown in Figure 5.4 are all indicative of pure PbTe. The usual large peak width associated with small grain size is observed for all four samples. Interestingly, no peaks associated with Bi_2Te_3 are observed. This suggests that the relatively large nanoparticles observed in some TEM images are not Bi_2Te_3. Instead, the results suggest that the Bi is present as very small Bi_2Te_3 particles, which contribute undiscernible broad peaks, as Bi_{Pb} defects in the PbTe nanowires as desired, or as Bi bonded to the surface of the PbTe nanowires. In all of these hypotheses, the Bi atoms are expected to be well distributed in the washed nanowire material. The benefit of such a distribution is that the short sintering times involved in SPS are more likely to be sufficient to allow for Bi diffusion and incorporation as a dopant in the final disc.

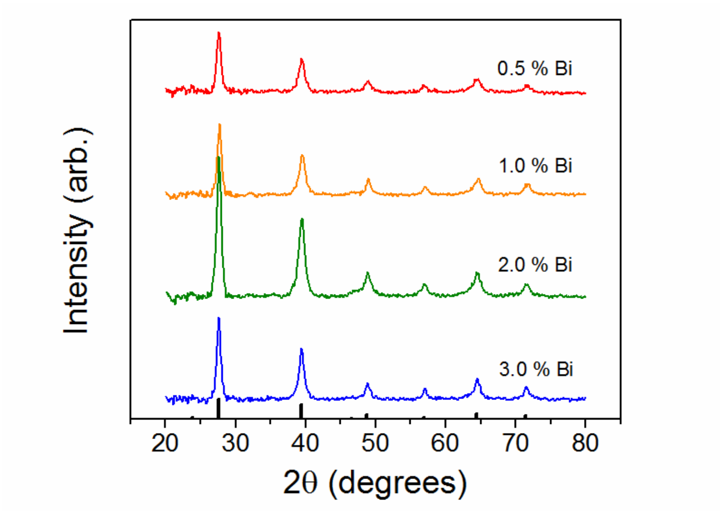

Figure 5.4 XRD patterns of water washed Bi-doped PbTe nanowires. Black lines are standard peaks for PbTe (JCPDS # 01-077-0246).

Based on results from literature, the diffusion coefficient of Bi atoms in PbTe at 450 °C is 1.6 nm^2/s.[282] In the five minutes that the material is at 450 °C during SPS process, the diffusion length is estimated as 21.9 nm according to the formula,

$$L_D = \sqrt{t \cdot D_{Bi,PbTe}} \tag{5.1}$$

where L_D is the diffusion length, t is time, and $D_{Bi,PbTe}$ is the diffusion coefficient of Bi in PbTe. With the additional consideration of the heating and cooling steps as well as the 350 °C annealing prior to SPS, the true diffusion length is even longer. As even only

21.9 nm is larger than the typical PbTe nanowire diameter, the Bi should reach an equilibrium distribution within the PbTe, particularly if the Bi atoms are initially located within the PbTe nanowires or on their surfaces.

5.3.1.2 Compressed Discs of Bi-Doped PbTe Nanowires

The discs of Bi-doped PbTe nanowires made by SPS are analyzed using XRD. The results in Figure 5.5 show that the majority of the material in the discs is PbTe. The sharp peaks indicate that significant grain growth occurs during the SPS process, which is also observed in the discs of PbTe described in chapter 4. The XRD patterns of all four Bi-doped discs possess small peaks at around 38.0 °, which could be associated with a variety of materials including Te, $PbBi_2Te_4$, $PbBi_4Te_7$, $PbBi_6Te_{10}$, or Bi_2Te_3.

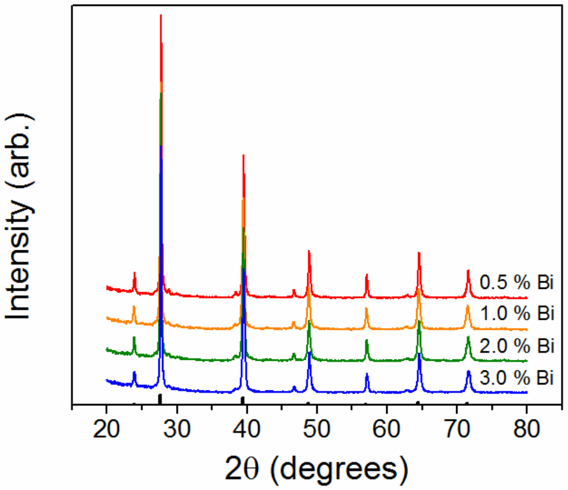

Figure 5.5 XRD patterns of SPS'd discs of Bi-doped PbTe nanowires. Black lines are standard peaks for PbTe (JCPDS # 01-077-0246).

It is unlikely that the peak represents Te as the annealed Bi-doped PbTe nanowires are shown by EDS to have Pb:Te ratios of one or slightly larger. It is interesting, then, that a secondary phase is formed at all because the pseudo-binary phase diagram for the PbTe-Bi_2Te_3 system shows that Bi is miscible at up to 7 % in PbTe at 450 °C and over 4 % at 400 °C.[283] While the solubility decreases with decreasing temperature, it is interesting that the dissolved Bi is not all frozen into the structure more effectively, but that some phase segregates at low temperature.

Also present, although not easily discernable, in the XRD pattern in Figure 5.5 are peaks at about 28.7 °, 29.9 °, an 42.6 °, which could be associated with $PbTeO_3$. The presence of oxide in the final material could be due to the brief exposure of the annealed material to oxygen during the transfer to an inert environment.

5.3.1.3 Na-Doped Compressed Discs of PbTe Nanowires

The structure and composition of the Na-doped PbTe are evaluated using XRD, SEM, and EDS elemental mapping. The effect of not mixing the PbTe nanowires during the hydrazine washing step is emphasized in the SEM and EDS mapping results. The XRD pattern for a Na-doped hot pressed disc made using fully hydrazine washed PbTe is shown in Figure 5.6. The sharp peaks imply that significant grain growth occurs during the hot pressing process, which is expected, especially considering the long sintering time and slow cooling process. The lack of noticeable impurity peaks suggests that the material is pure PbTe without any other crystalline phase.

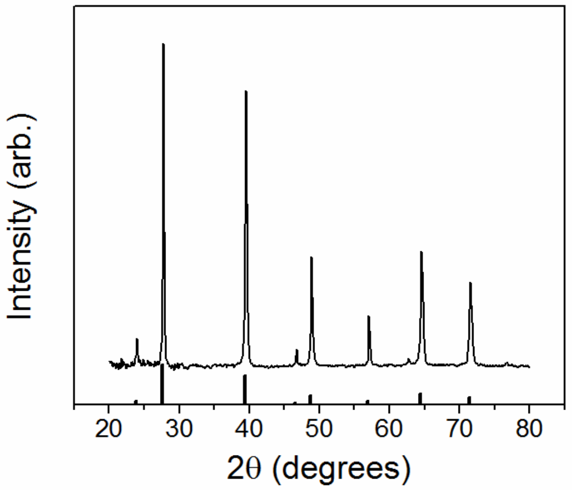

Figure 5.6 XRD pattern of Na-doped hot pressed fully hydrazine washed PbTe nanowires. Black lines are standard peaks for PbTe (JCPDS # 01-077-0246).

The SEM images of the discs made from fully and partially hydrazine washed PbTe are shown in Figure 5.7. The low magnification images reveal that the fully washed sample is significantly more porous than the partially washed sample. This is reflected in the relative densities of the two discs: 72 % and 90 % for the fully and partially washed samples. The high magnification images reveal two important facts. First, the average grain sizes of the fully washed and the partially washed materials are 3.2 and 5.6 µm, respectively. Second, the partially washed material has fine topological features that are generally near grain boundaries, while the fully washed material does not possess such features to the same extent.

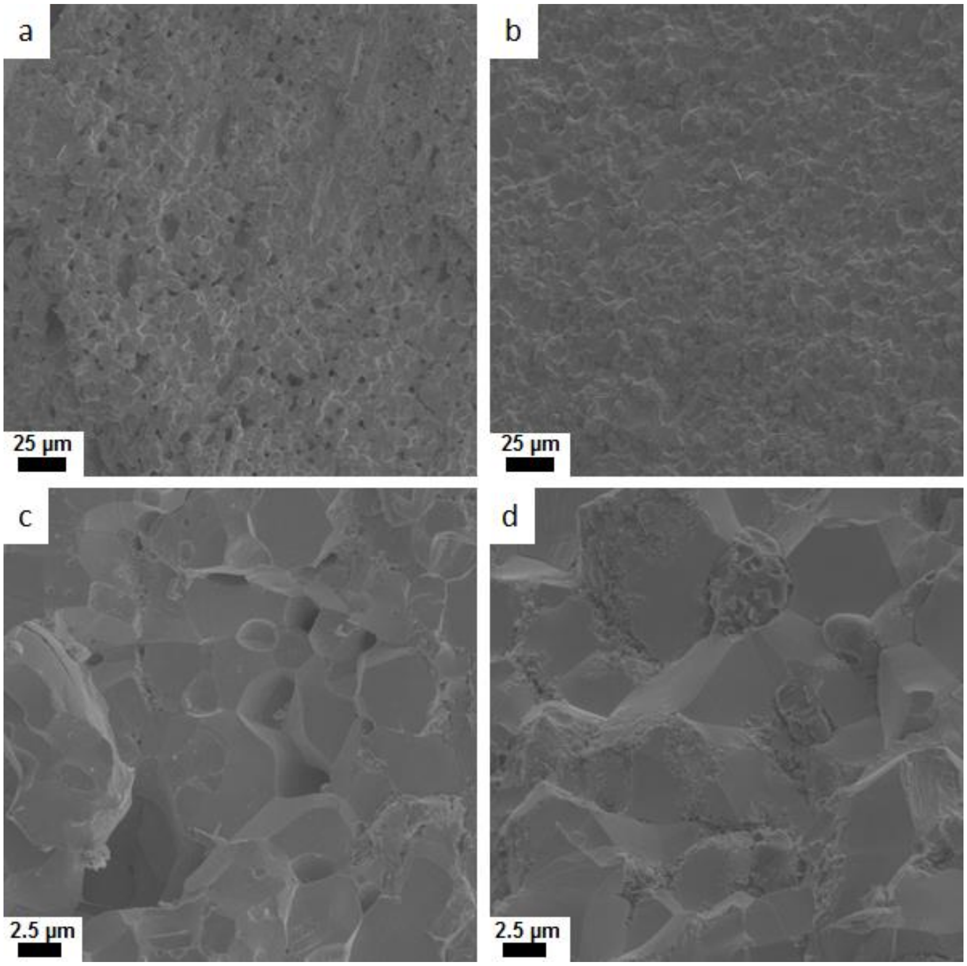

Figure 5.7 SEM images of fracture surfaces of Na-doped hot pressed PbTe nanowires. (a, c) Fully hydrazine washed PbTe. (b, d) Partially washed PbTe.

Elemental maps of the Na, Pb, Te, C, and O detected by EDS in two discs are shown in Figure 5.8 and Figure 5.9. The maps of the fully washed material show that Na is largely localized in micro scale regions within the disc. Furthermore, the O is preferentially located with the Na. This could perhaps be associated with oxidation of the Na during the hot pressing process or even after the sample is fractured when the fracture surface is exposed to oxygen. The maps also reveal a slender region in which Te is present in large amounts and where Pb is relatively absent. Thus, it appears that the excess Te present in the PbTe nanowire powder phase segregates to some extent. Finally, the maps show that C is not concentrated in specific areas, but is distributed throughout the sample. Thus, the apparent presence of carbon may be an artifact of the EDS data collection process.

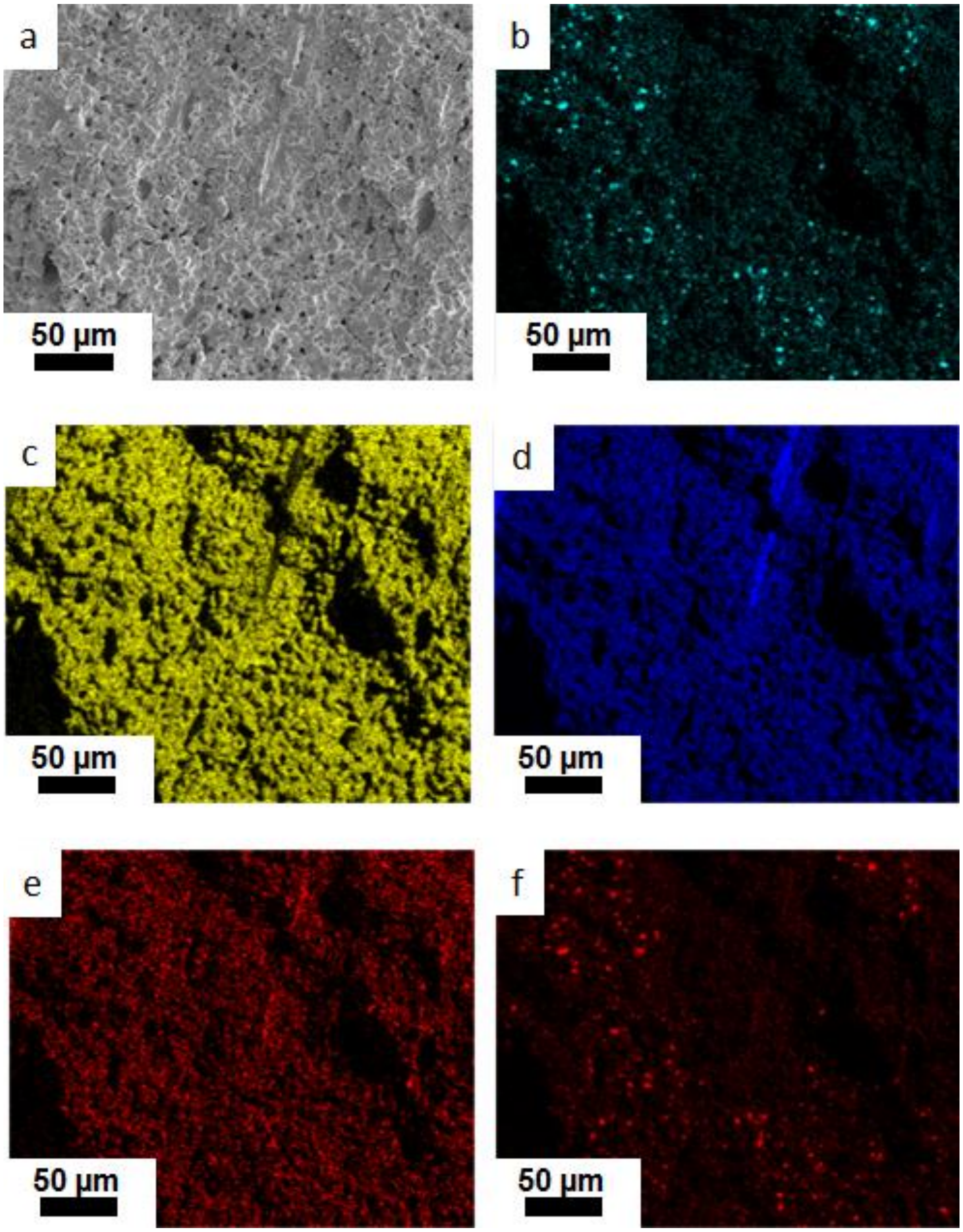

Figure 5.8 Elemental maps of Na-doped hot pressed fully hydrazine washed PbTe nanowires. (a) Secondary electron image. (b) Na. (c) Pb. (d) Te. (e) C. (f) O.

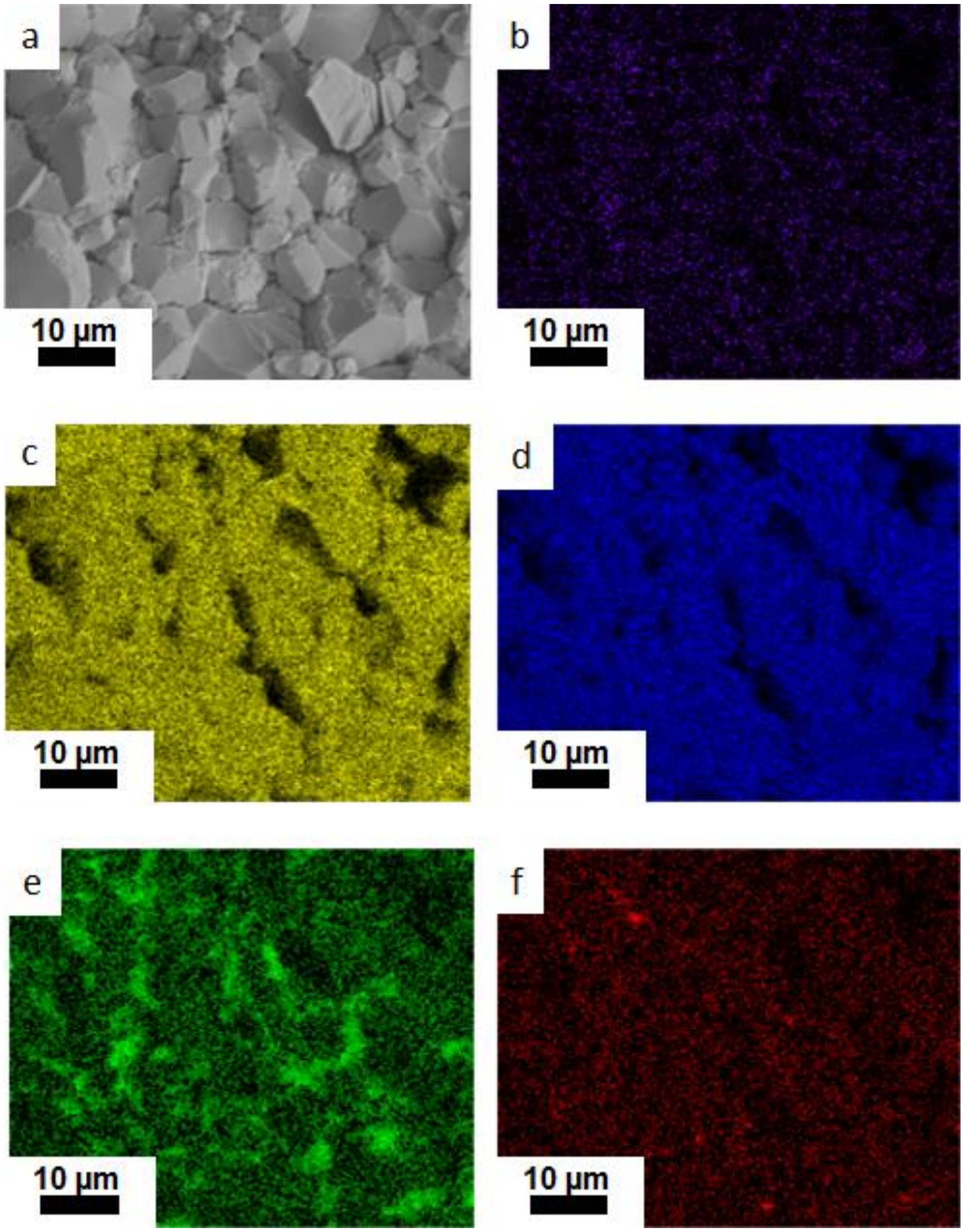

Figure 5.9 Elemental maps of Na-doped hot pressed partially hydrazine washed PbTe nanowires. (a) Secondary electron image. (b) Na. (c) Pb. (d) Te. (e) C. (f) O.

The elemental maps of the partially washed material in Figure 5.9 show very different features compared to those of fully washed material. The Na appears uniformly distributed throughout the surface. There is no apparent Te phase segregation. There are regions in which O is concentrated, yet these do not correspond to regions of concentrated Na. Thus, in many ways, the material appears to be uniform Na-doped PbTe with a small amount of oxidation. However, the C map reveals an interesting phenomenon. There are regions in which the C signal is quite strong, which correspond to the regions of the secondary electron image where there are fine topological features. It appears, then, that the fine structural features at the grain boundaries of the partially mixed material are associated with C. This is likely due to the incomplete removal of PVP during the hydrazine washing step. Further experimentation is required to more fully prove this hypothesis.

As discussed later, the effectiveness of Na-doping in fully washed PbTe is significantly improved by annealing. Interestingly, the annealing conditions applied do not result in grain growth by orders of magnitude. For discs annealed in an environment of forming gas at 600 torr at 550 °C for two hours, or an environment of flowing forming gas at about four torr at 700 °C for ten hours, the average grain sizes remain below 10 µm as shown in Figure 5.10. The porosity in the original hot pressed materials is still present after annealing.

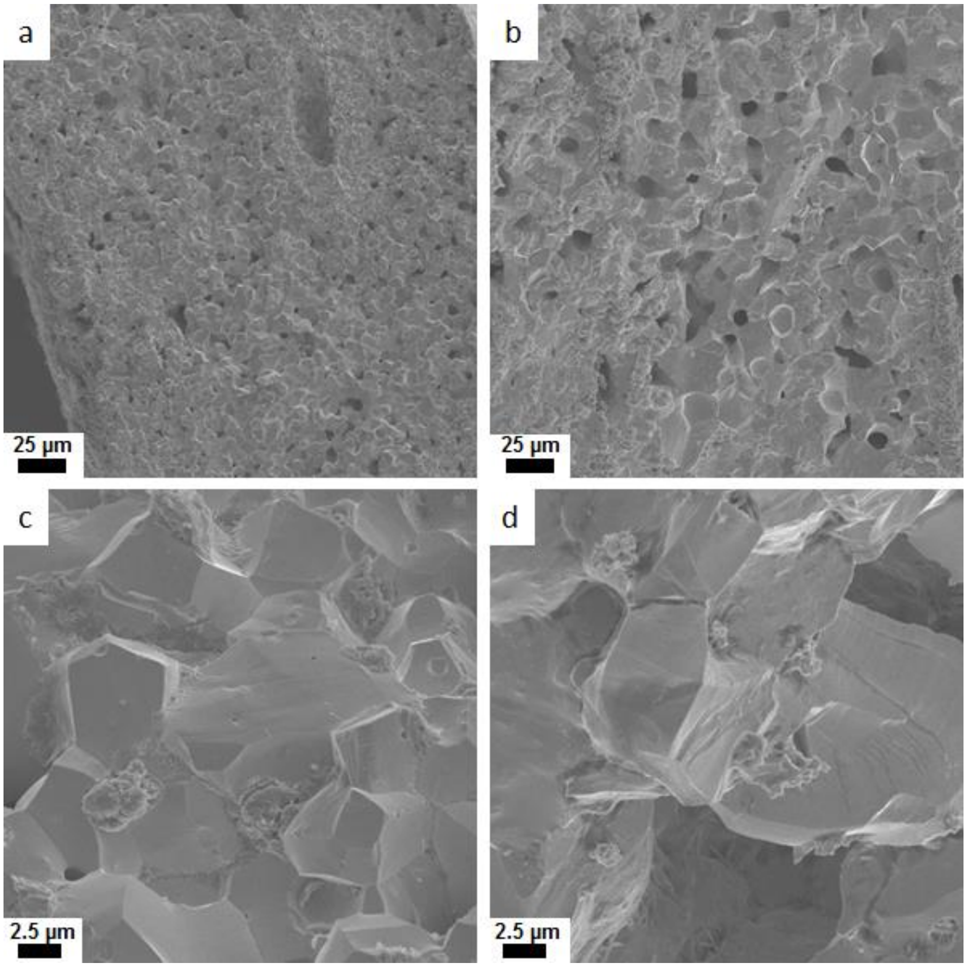

Figure 5.10 SEM images of fracture surfaces of annealed Na-doped hot pressed fully washed PbTe nanowires. (a, c) Annealed at 550 °C for 2 hours. (b, d) Annealed at 700 °C for 10 hours.

5.3.2 Thermoelectric Properties

5.3.2.1 Compressed Discs of Bi-Doped PbTe Nanowires

The effectiveness of the Bi doping method is shown by the Seebeck coefficients estimated using an MMR SB100 Seebeck measurement system. As shown in Figure 5.11, all four discs possess negative Seebeck coefficients across the entire range of temperatures investigated. Additionally, the absolute value of the room temperature Seebeck coefficient monotonically decreases with increasing doping level, which strongly suggests a monotonic increase in carrier concentration.[187] The Bi-doping strategy therefore provides an ability to control the carrier concentration of PbTe, so the optimal carrier concentration should be attainable.

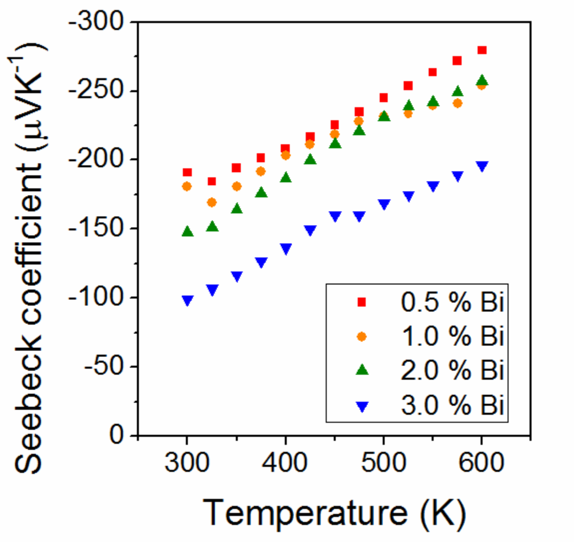

Figure 5.11 Seebeck coefficient of SPS'd Bi-doped PbTe nanowire discs estimated using an MMR system.

The effectiveness of the doping strategy is further suggested by a monotonic increase in the electrical conductivity with the amount of Bi added. The room temperature electrical conductivities are 3.8, 141, and 232 S/cm for the 0.5 %, 1.0 %, and 2.0 % samples. The electrical conductivity of the 3.0 % Bi sample is uncertain at this point and should be evaluated as part of a fuller study on the thermoelectric properties of Bi-doped PbTe.

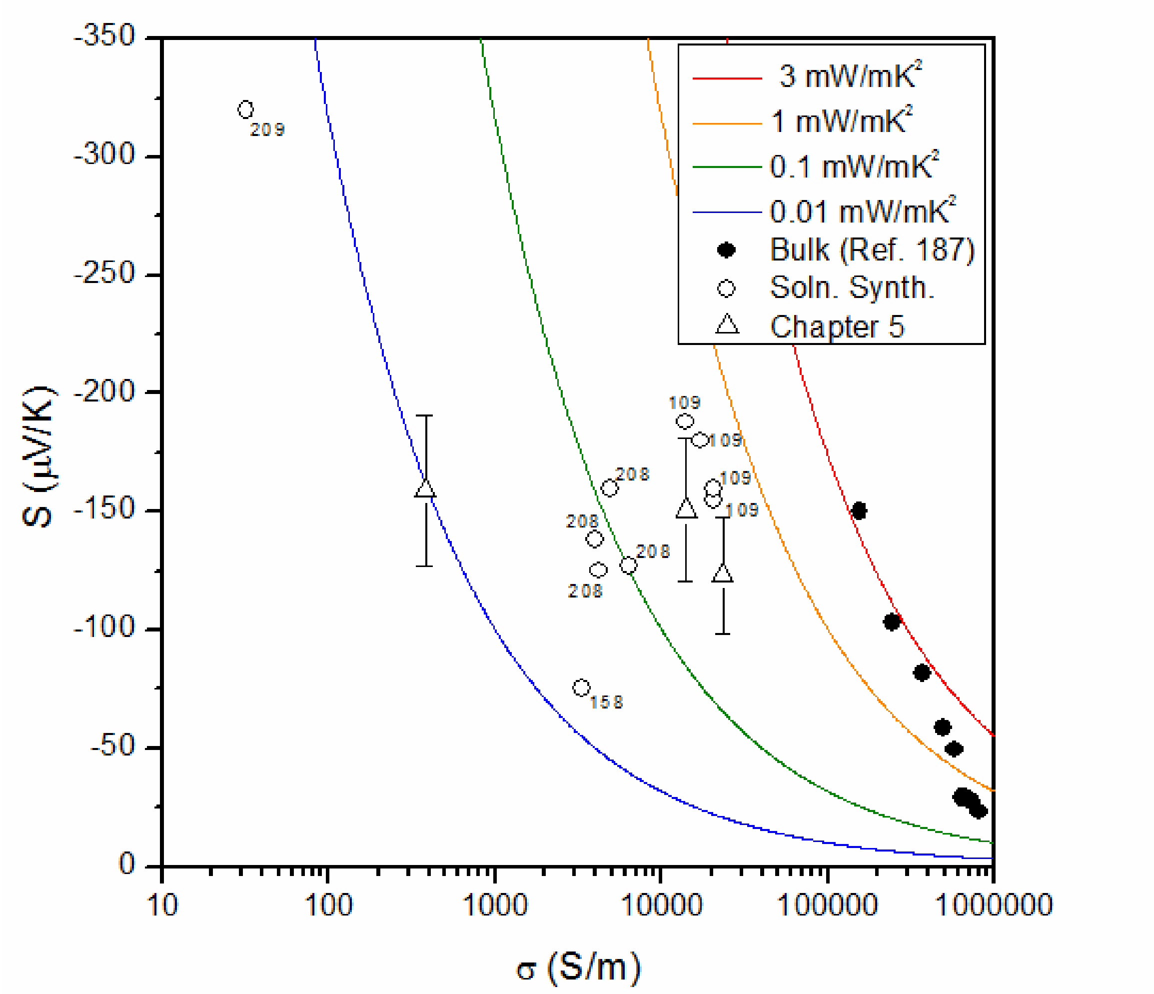

Figure 5.12 Seebeck coefficient versus electrical conductivity near room temperature for n-type PbTe. Data from reference 209 adapted with permission from the American Chemical Society. Copyright 2014. See literature cited section for full reference details.

Given that the room temperature electrical properties of the Bi-doped samples are known or have at least been estimated, Figure 5.12 shows a comparison with other n-type PbTe from literature. The Seebeck coefficient is estimated as two thirds of the value obtained using the MMR system, which is based on general observations and comparisons for materials tested on both the MMR system and a more accurate system.

While the sample doped with 0.5 % Bi has a very low power factor, the samples doped with 1 and 2 % Bi fair quite well compared with other solution synthesized materials. Based on the results from chapter 4, the thermal conductivity can vary greatly among solution synthesized PbTe, thus the Bi-doped PbTe samples may indeed have larger ZT values than other solution synthesized n-type PbTe samples. A more complete set of measurements is required to make this determination. This is left as the subject of future work.

5.3.2.2 Na-Doped Compressed Discs of PbTe Nanowires

Electrical measurements on Na-doped compressed discs of PbTe nanowires reveal that the Na-doping strategy can be effective in certain cases. The disc made from fully washed PbTe nanowires apparently has a low carrier concentration as suggested by the low room temperature electrical conductivity (32 S/cm) and high estimated room temperature Seebeck coefficient (319 μV/K).[186] However, high temperature annealing is shown to raise the carrier concentration significantly. After annealing in an environment of forming gas at 600 torr at 550 °C for two hours, the electrical conductivity increases to around 1,100 S/cm and the estimated room temperature Seebeck coefficient drops to 55 μV/K. After annealing in an environment of forming gas at four torr at 700 °C for ten hours, the room temperature electrical conductivity of a Na-doped hot pressed PbTe sample increases to 1,340 S/cm and the estimated room temperature Seebeck coefficient drops to 45 μV/K. It is interesting that annealed materials have such high electrical conductivities despite the significant amounts of porosity shown in Figure 5.10. Future work on Na-doped fully washed PbTe nanowires should aim to reduce the porosity to further increase the mobility, while preserving the small grain size.

Meanwhile, the disc made from partially washed PbTe nanowires appears to have a relatively high carrier concentration as suggested by the high room temperature electrical conductivity (>500 S/cm) and low estimated room temperature Seebeck coefficient (176 μV/K). A room temperature Hall measurement of the disc confirms that the carrier concentration is $3.2 \pm 0.5 \times 10^{19}$ /cm^3, which is over ten times larger than that of PbTe nanowires doped with excess Te.

Due to the promising results for Na-doped partially washed PbTe nanowires, the electrical conductivity and Seebeck coefficient are measured using the accurate measurement systems described in chapter 4. The results are shown in Figure 5.13. The electrical conductivity unexpectedly increases from 300 to 350 K. It then decreases with temperature as expected for highly doped PbTe.[43] It is important to note that the electrical conductivity does reach a local minimum at high temperature as this would be indicative of bipolar transport associated with low doping levels. The Seebeck coefficient monotonically increases with temperature and is nearly equal to that of bulk Na-doped PbTe with a carrier concentration of 3.6×10^{19} /cm^3 from literature.[186]

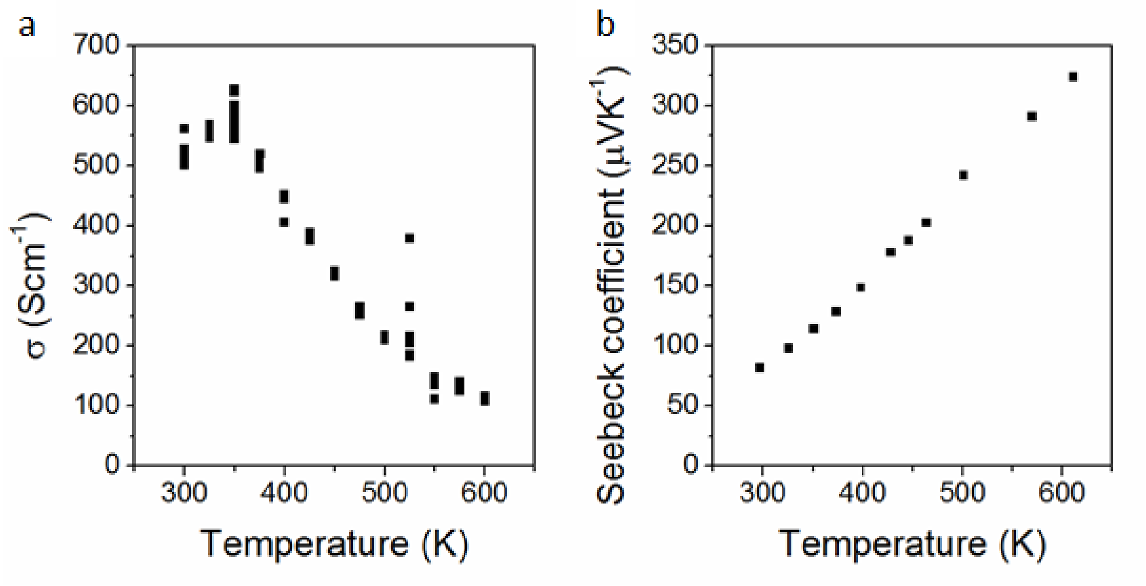

Figure 5.13 Electrical properties of Na-doped hot pressed partially hydrazine washed PbTe nanowires. (a) Electrical conductivity. (b) Seebeck coefficient.

The power factor calculated based on the data in Figure 5.13 is shown in Figure 5.14. The results reveal two very important facts. First, the maximum power factor observed is in the temperature range of 500 to 550 K, which is much higher than that of the SPS'd PbTe nanowire discs discussed in chapter 4. Second, the maximum power factor is around 40 % larger for the Na-doped material than the Te-doped material.

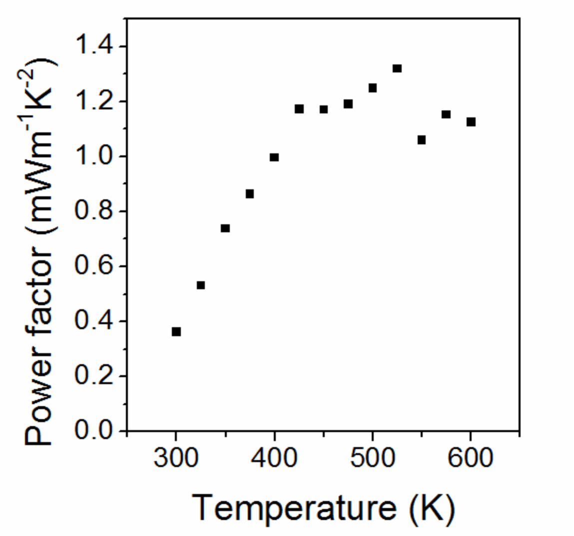

Figure 5.14 Power factor of Na-doped hot pressed partially hydrazine washed PbTe nanowires.

One issue with Na-doped hot pressed partially washed PbTe nanowires is that the room temperature electrical conductivity changes after high temperature procedures. Immediately after hot pressing, the electrical conductivity is 521 S/cm, but this changes to 679 S/cm after annealing at 427 °C, and then changes to 519 S/cm after the Seebeck measurement up to 338 °C. Finally, after electrical conductivity measurements up to 327 °C the room temperature electrical conductivity drops to 349 S/cm. This change in electrical conductivity could be associated with the two phase PbTe/C nature of the material observed by elemental mapping. In principal, thermal expansion coefficient mismatch could cause the bonding between the materials to weaken after repeated temperature cycling. Therefore, future work should focus on annealed Na-doped hot pressed fully washed PbTe nanowires, which are more likely to be stable at high temperature.

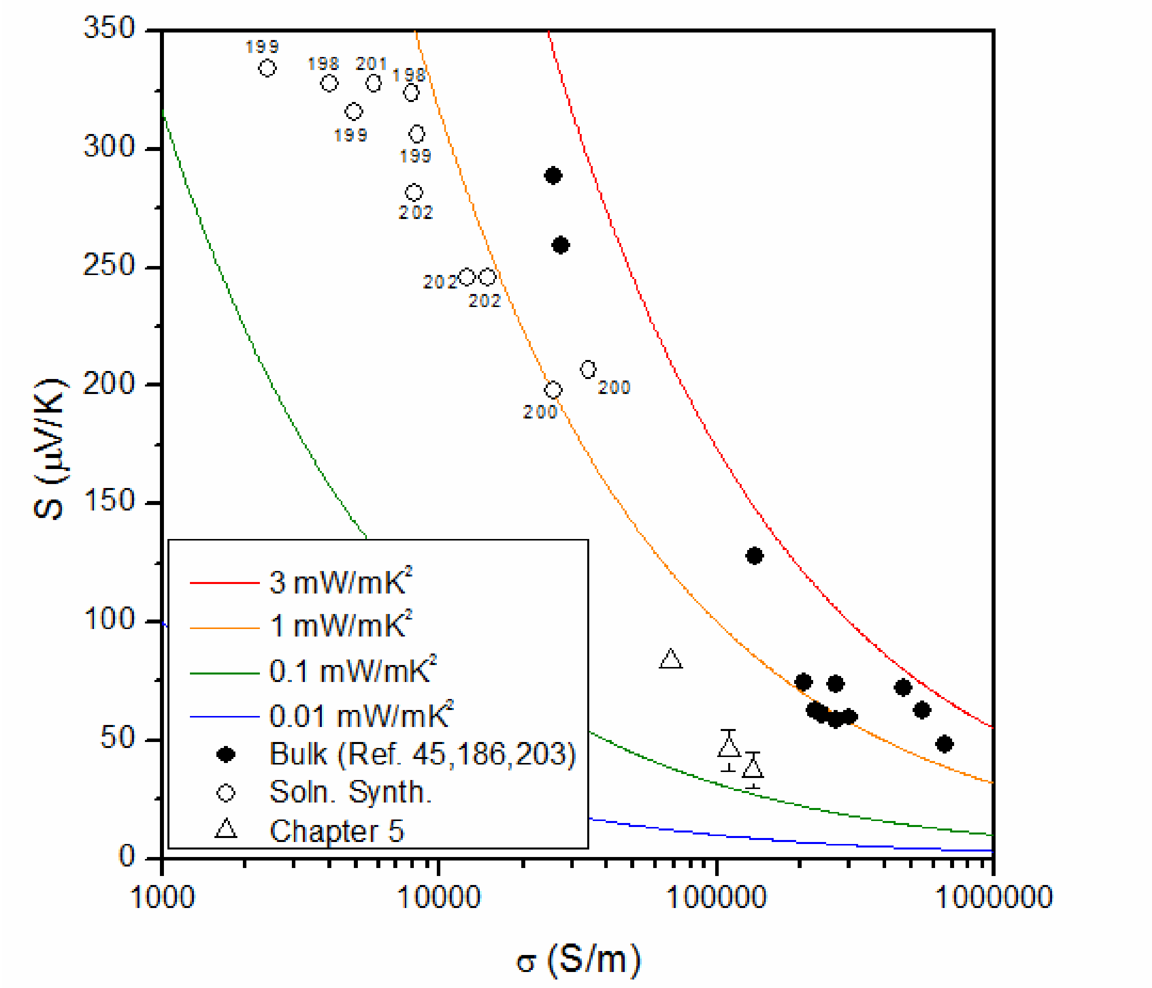

Figure 5.15 Seebeck coefficient versus electrical conductivity near room temperature for p-type PbTe.

Figure 5.15 allows for the comparison of the room temperature properties of the Na-doped PbTe described in chapter 5 with those of other solution synthesized and large-grained p-type PbTe in literature. Clearly, the Seebeck coefficients observed in the present materials are within the range associated with the optimal carrier concentration in p-type PbTe. This is a significant feat that had not been achieved in solution synthesized p-type PbTe previously. While the hole mobilities of the present Na-doped material are lower than those of large-grained PbTe, the porosity and fine microstructure in the nanowire-based material likely results in a decrease in lattice thermal conductivity which could lead to comparable ZT values. Furthermore, the three representative Na-doped samples are formed using processes that are far from optimized. Presumably, superior hot pressing facilities which allow for air-free processing could improve the charge carrier mobility of the solution synthesized material. Thus, additional work on Na-doped discs made from PbTe nanowires should focus on improved processing and ultimately a full characterization of the materials in order to determine the ZT values in the temperature range of 300-750 K.

5.4 Conclusions

Both Bi-doping and Na-doping are effective methods to increase the carrier concentration of PbTe nanowires. In the case of Bi-doped PbTe nanowires, the addition of a Bi precursor during the solution synthesis has a minimal effect on the morphology and phase of the as-synthesized PbTe nanowires, yet has a significant effect on the electrical properties of SPS'd discs made from Bi-doped PbTe nanowire powder. The short sintering times involved in the typical SPS procedure are apparently sufficient to allow Bi to diffuse and act as an n-type dopant. Furthermore, the carrier concentration can be tuned by the amount of Bi precursor added during the solution synthesis.

In the case of Na-doped PbTe nanowire discs, partial hydrazine washing is shown to result in high relative densities, electrical conductivities, and carrier concentrations in hot pressed discs. However, the properties are not stable at high temperature. For Na-doped PbTe discs made from fully washed PbTe nanowires, the hot pressed discs have low electrical conductivities and carrier concentrations. These can be improved significantly with minimal grain growth by annealing at high temperature in an inert environment. Future work should focus on using an appropriate high temperature compression method to form high relative density discs of Na-doped PbTe nanowires, which can then be annealed to form material with improved thermoelectric properties, especially at high temperature.

CHAPTER 6. ENVIRONMENTALLY BENIGN SYNTHESIS OF LEAD TELLURIDE AND CADMIUM TELLURIDE NANOWIRES

6.1 Introduction

The solution synthesis of PbTe nanowires, described in chapter 3 and applied in chapters 4 and 5, has many excellent qualities. Namely, it is rapid, scalable, high yield, and produces nanowires with diameters below 15 nm. However, one issue exists in the synthesis method: it employs significant amounts of anhydrous hydrazine, which is extremely hazardous. A search of the literature reveals that many other metal telluride synthesis methods employ hydrazine as a reducing agent.[103,171,246–249,251] Alternative reducing agents such as hydroxylamine[105] and sodium borohydride[128,201,284] are still moderately hazardous or highly flammable. Meanwhile, ascorbic acid (vitamin C) is a relatively safe reducing agent that has been used in many solution syntheses of inorganic materials[285–290] including Te nanowires.[238,291,292] In a few cases, ascorbic acid has been used to synthesize metal telluride nanowires, yet prior synthesis methods have resulted in nanowires with several nanometer thick carbonaceous sheaths[293,294] or poor control over the nanostructure morphology when synthesizing a broad range of metal tellurides.[295] This chapter describes the synthesis of PbTe and CdTe nanowires using ascorbic acid as a reducing agent. This research is part of a larger project in which Bi_2Te_3, Ag_2Te, and $Cu_{1.75}Te$ nanowires are synthesized using similar methods.[111]

6.2 Synthesis and Characterization Methods

For the synthesis of metal telluride nanowires TeO_2 (≥99%), PVP (Molecular Weight 40,000), KOH (90%), L-Ascorbic acid (≥99%), $Pb(CH_3CO_2)_2$•$3H_2O$ (≥99.99%), and $Cd(CH_3CO_2)_2$•$2H_2O$ (98%) are purchased from Sigma Aldrich. Ethylene glycol (≥99%) is purchased from VWR. In a typical synthesis, 0.160 g TeO_2 (1 mmol), 0.5 g PVP, 1.5 g KOH, and 15 ml ethylene glycol are added to a 50 ml round bottom flask and heated to 85 ° C. Meanwhile, a solution of 1.89 M ascorbic acid in DI water is made in a separate glass container by heating to 80 °C. When the Te solution reaches 85 °C, 3 ml of the ascorbic acid solution are rapidly injected and nitrogen gas is applied to the reaction solution using a Schlenk line. Upon ascorbic acid addition, the reaction solution changes from transparent yellow to opaque black/brown within approximately two minutes. The reaction proceeds at 85 °C for 24 hours to allow the Te precursor to fully convert to Te nanowires.

For conversion to PbTe, 0.455 g (1.2 mmol) $Pb(CH_3CO_2)_2$•$3H_2O$ and 0.1 g PVP are dissolved in 4 ml ethylene glycol by heating to 80 °C in a separate container. This Pb precursor solution is injected into the Te reaction solution followed by the addition of 3 ml of 1.89 M ascorbic acid in water. The conversion to PbTe proceeds for 24 hours after which the reaction solution is cooled to room temperature. The reaction products are washed 3 times with DI water and then dispersed in ethanol or DI water for preparation of samples for XRD and TEM. The conversion of Te nanowires to CdTe follows an identical procedure except that $Pb(CH_3CO_2)_2{\bullet}3H_2O$ is replaced by 0.320 g $Cd(CH_3CO_2)_2{\bullet}2H_2O$ (1.2 mmol).

For ultraviolet-visible (UV-vis) studies of CdTe nanowires, washed nanowires are dispersed in water in a cuvette. The concentration is adjusted in order to obtain an appropriate amount of absorption during the UV-vis studies.

For studies on the reaction over time, aliquots are taken from the reactions by collecting 1-2 ml and quenching in water. The material is washed two times with water, dispersed in ethanol, and drop cast onto TEM grids or amorphous glass for XRD measurements.

6.3 Analysis of Final Reaction Products

6.3.1 XRD Analysis

The XRD pattern of the Te produced in the first step is shown in Figure 6.1. The pattern corresponds well to that of Te except that peaks from planes such as (001) are diminished or absent. This suggests that the (001) planes of the crystals are preferentially aligned perpendicularly to the surface of the substrate used during XRD. This phenomenon is observed in the nanowires described in chapter 3 and in several other nanowire materials.[254,296–298] Furthermore, all peaks present are quite broad, indicating a small crystal size. Both of these observations agree with the TEM analysis, described later, which reveals ultra-thin Te nanowires with c-axes perpendicular to the substrate.

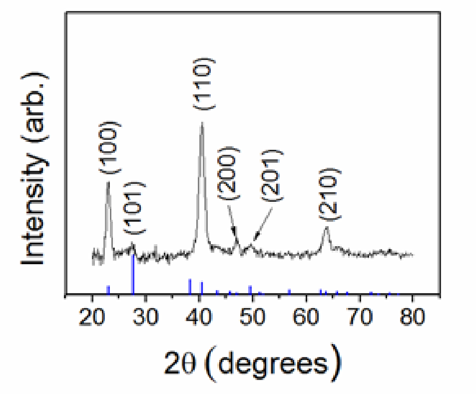

Figure 6.1 XRD pattern of Te nanowires produced in the first step of the ascorbic acid-based synthesis. Blue lines are standard peaks for Te (JCPDS # 35-1452).

The XRD pattern for the PbTe nanowires synthesized in the second step is shown in Figure 6.2. The experimental results match well with the standard diffraction pattern for PbTe and the peaks are broad, signifying small grain sizes.

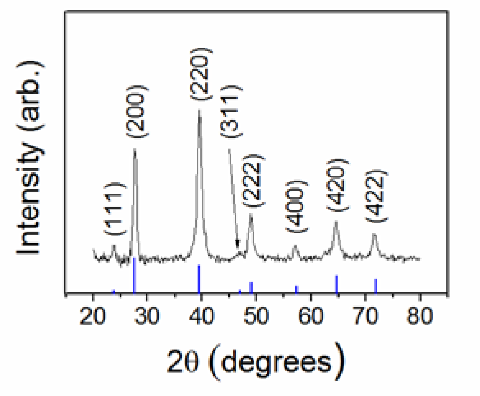

Figure 6.2 XRD pattern of PbTe nanowires synthesized using the ascorbic acid-based method. Blue lines are standard peaks for PbTe (JCPDS # 01-077-0246)

The XRD pattern for the CdTe nanowires is shown in Figure 6.3. Since CdTe commonly takes either the zinc blende or wurtzite crystal structure, Figure 6.3a shows the experimental pattern with the zinc blende reference peaks while Figure 6.3b shows the same experimental pattern with the wurtzite reference peaks. While most of the experimental peaks align well with peaks in the wurtzite reference pattern, certain expected major peaks are absent, particularly the peaks at 32.9° and 42.8°. As shown in Figure 6.3a, the reference peaks for zinc blende CdTe are well expressed in the experimental pattern. Thus, it appears from the XRD results that the material is mostly or fully comprised of zinc blende CdTe.

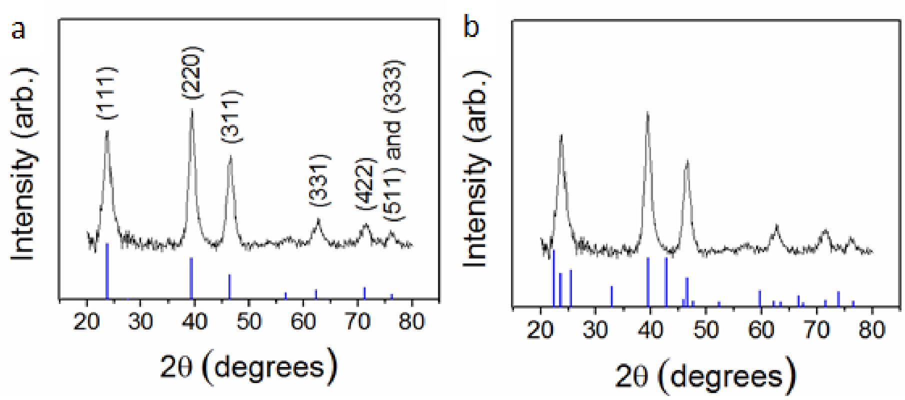

Figure 6.3 XRD pattern of CdTe nanowires synthesized using the ascorbic acid-based method. (a) Reference pattern is zinc blend CdTe (JCPDS # 01-070-8041). (b) Reference pattern is wurtzite CdTe (JCPDS # 01-073-2871).

6.3.2 TEM Analysis

TEM analysis of the Te nanowires synthesized in the first step is given in Figure 6.4. The low magnification image in Figure 6.4a shows that the nanowires are flexible with lengths in the range of several microns. The medium magnification image in Figure 6.4b shows the small diameter, the distribution of which is shown in Figure 6.4d. Figure 6.4c shows a HRTEM image of a small single crystalline section of a Te nanowire with the nanowire axis aligned with the [001] direction. Although HRTEM is not performed along the entire length of any single Te nanowire, there is no evidence of polycrystalline nanowires in any of the HRTEM images taken. Thus, it seems that most or all of the Te nanowires are single crystalline. As with the Te nanowires synthesized using hydrazine, the nanowire morphology here is due to the anisotropic crystal structure of Te[103,239] as well as the presence of PVP as a structure directing agent.[240,241]

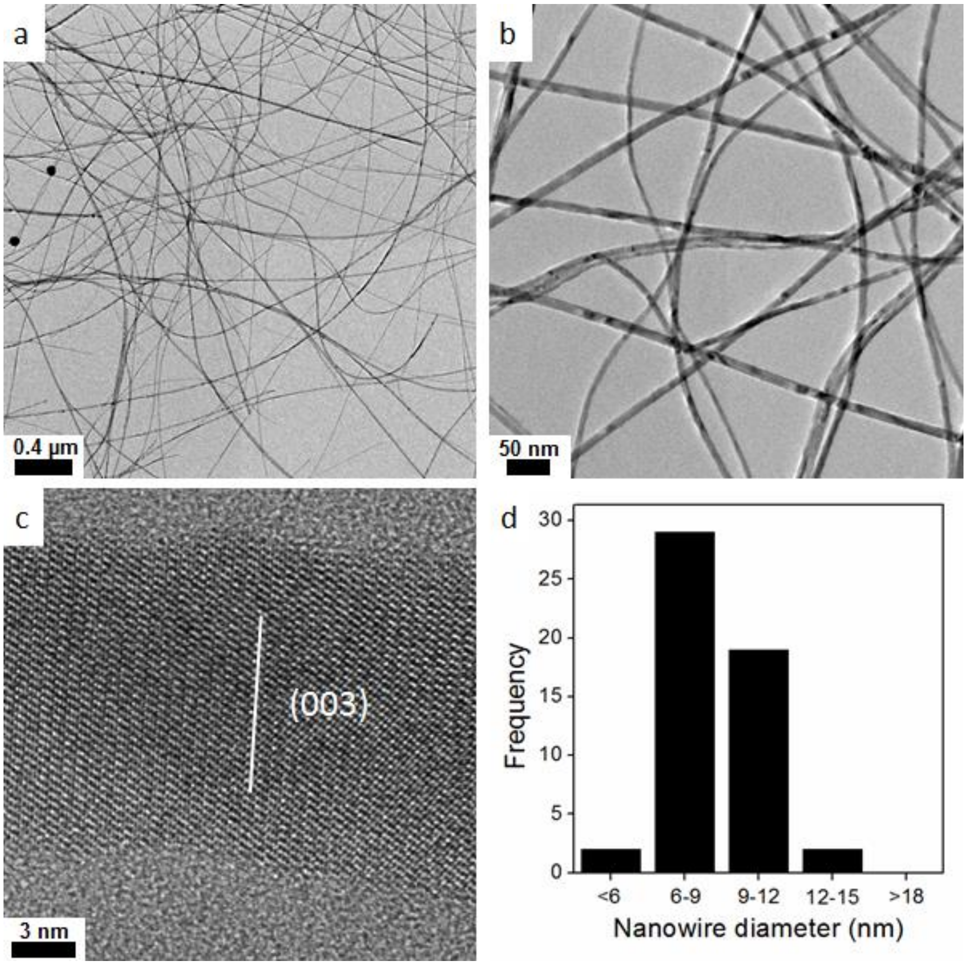

Figure 6.4 TEM and HRTEM analysis of Te nanowires. (a) Low magnification image. (b) Medium magnification image. (c) HRTEM image with the (003) plane highlighted. (d) Diameter distribution.

As shown in Figure 6.5, after the 24 hour conversion to PbTe, the original nanowire morphology is preserved. In the hydrazine-based synthesis, the nanowires become much shorter after conversion to PbTe. In the ascorbic acid-based synthesis, the PbTe nanowires appear to be several microns long (Figure 6.5a), just like the original Te nanowires. The diameters of the PbTe nanowires are slightly larger than those of the Te nanowires as evidenced by a comparison of the histograms in Figure 6.4d and Figure 6.5d.

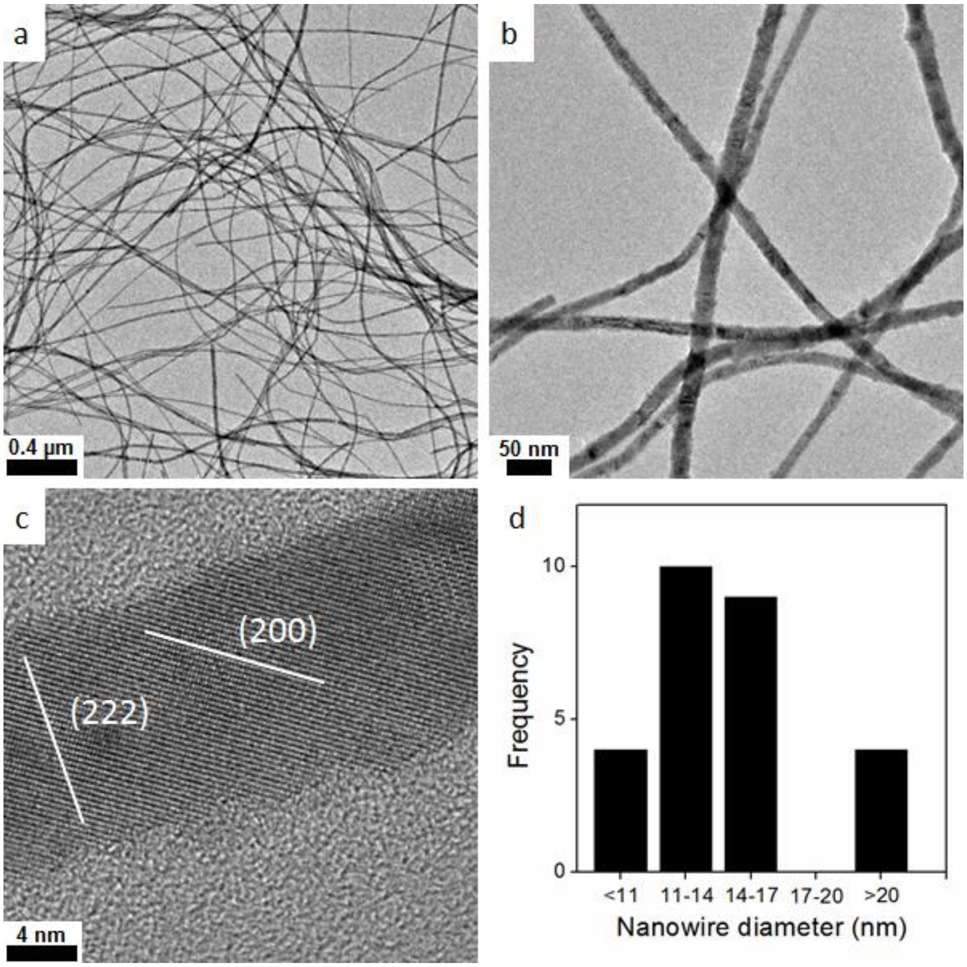

Figure 6.5 TEM and HRTEM analysis of PbTe nanowires. (a) Low magnification image. (b) Medium magnification image. (c) HRTEM image with the (222) and (200) planes highlighted. (d) Diameter distribution.

The HRTEM image of a single PbTe nanowire in Figure 6.5c shows that the axial direction is aligned with the [111] crystal direction. Additionally, a small fraction of PbTe nanowires showed regions with axial directions aligned with the [110] crystal direction

(Figure 6.6). This is similar to the chapter 3 results for PbTe nanowires synthesized using Te nanowire templates, which showed both [111] and [110] axial directions and is different from the [100] axial direction observed in PbTe nanowires grown using two-step hydrothermal methods.[251,293] The mechanism behind the formation of such a junction between the two crystalline domains is unclear.

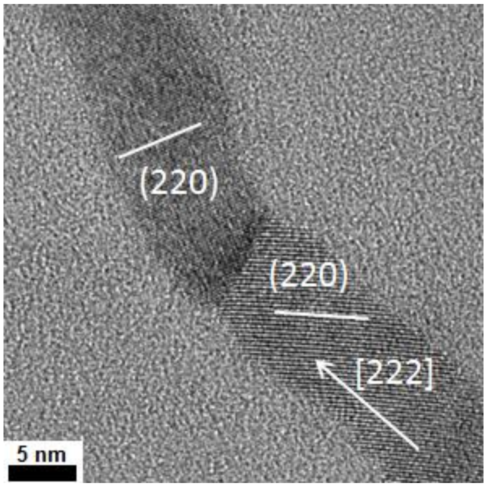

Figure 6.6 HRTEM image of a PbTe nanowire that shows sections in which the nanowire axis is aligned with the [110] and the [111] direction.

TEM analysis of the CdTe products in Figure 6.7 shows that they too possess nanowire morphology with lengths of several microns, similar to the original Te nanowires. As with the PbTe nanowires, the diameters of the CdTe nanowires are slightly larger than the original Te nanowires. Figure 6.7c shows the HRTEM of a typical CdTe nanowire; it is polycrystalline with numerous small grains, yet the FFT (Figure 6.8) indicates diffraction spots that can be indexed as zinc-blende CdTe with a few spots from wurtzite CdTe.

Thus, while XRD indicates that the majority of CdTe is in the zinc-blende phase, a small amount takes the wurtzite phase. Some solution syntheses can yield single crystalline zinc-blende CdTe nanowires,[105,293,299] yet the presence of defects is fairly common for CdTe nanowire synthesized in solution[247,300] and it is common for both wurtzite and zinc blende phases to be observed within single nanowires.[105,297,301]

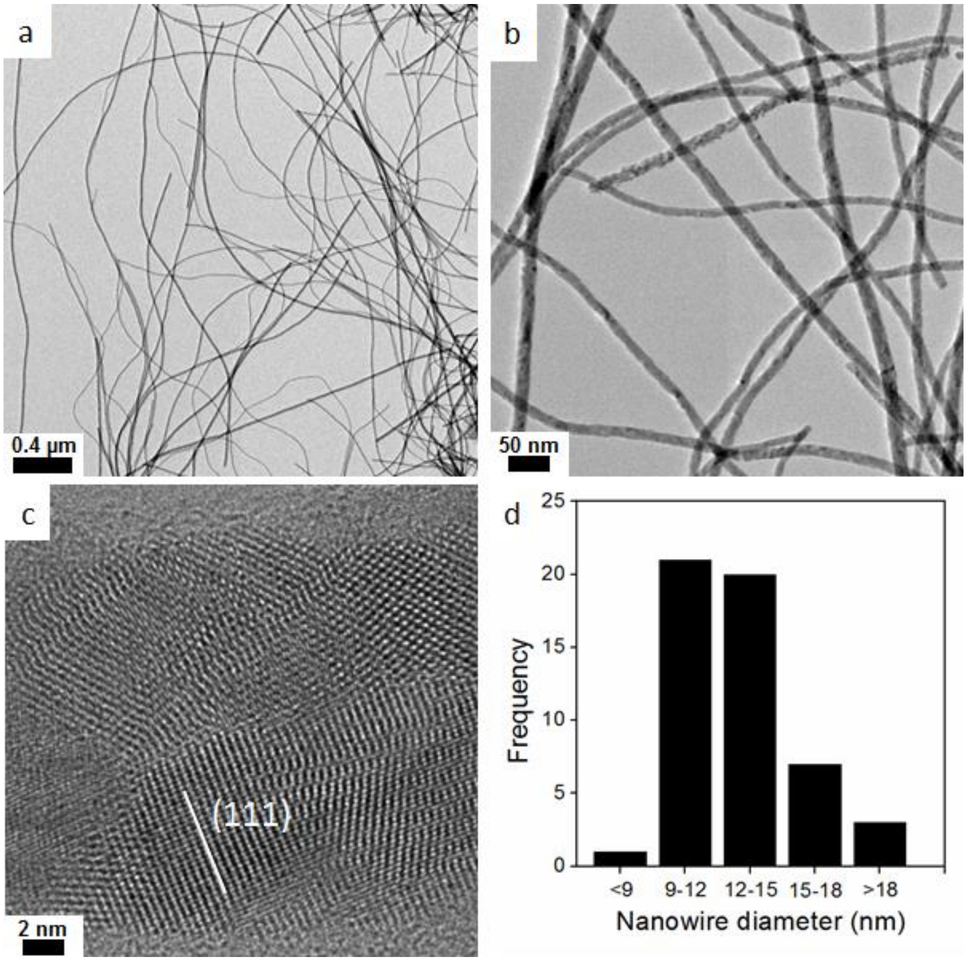

Figure 6.7 TEM and HRTEM analysis of CdTe nanowires. (a) Low magnification image. (b) Medium magnification image. (c) HRTEM image with the (111) plane highlighted. (d) Diameter distribution.

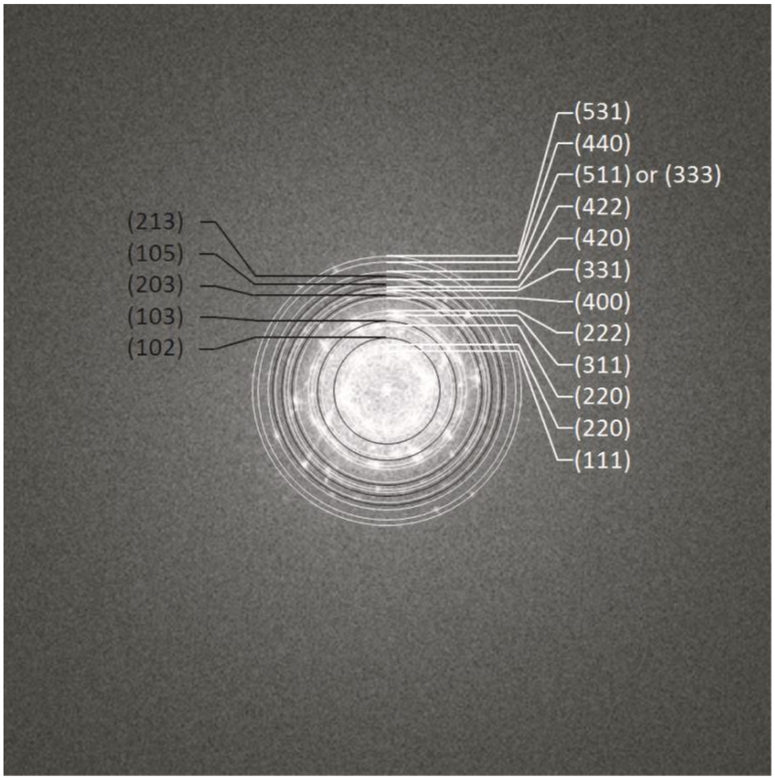

Figure 6.8 FFT of HRTEM image of CdTe nanowire showing diffraction spots which can be indexed as zinc blende (white rings) and wurtzite (black rings).

6.3.3 Yield and Composition

The yield of each metal telluride nanowire synthesis is calculated based on the mass of starting precursors and the mass of the washed and dried reaction products. For PbTe and CdTe the yields are approximately 83.3% and 87.5%, respectively, which points to the feasibility of efficient large-scale synthesis of these materials.

The composition of the PbTe nanowires is found by EDS analysis to be 49.60 ± 0.04 atomic % Pb and 50.40 ± 0.04 atomic % Te. Interestingly, these nanowires possess much less excess Te than similar nanowires synthesized using hydrazine. It is possible that this is partly associated with the long reaction time allowed for the conversion to PbTe in the ascorbic acid-based method. It could also be due to the 20 % excess Pb, which is added to encourage full conversion from Te to PbTe. Given the near stoichiometric composition of the PbTe produced using ascorbic acid, SPS'd discs from this material would likely possess different electrical and thermal properties than material produced using hydrazine. Future work should involve the scaling up of the environmentally benign synthesis of PbTe nanowires to ultimately produce high relative density discs for a full evaluation of ZT as a function of temperature. The doping methods described in chapter 5 could also be applied to enhance the ZT values at high temperature.

The composition of the CdTe nanowires is 54.5 ± 1.7 atomic % Cd and 45.5 ± 1.7 atomic % Te. Thus, the CdTe nanowires are considerably rich in Cd. Considering the small grained polycrystalline nature and the nanowire morphology of the CdTe, such deviations from stoichiometry should pose no issues with regard to the phase purity. The presence of excess Cd could be due to the 20 % excess Cd precursor added during the synthesis.

6.3.4 UV-vis Analysis

As CdTe is a useful absorber of solar radiation for photovoltaics, UV-Vis absorption measurements are performed to estimate the band gap of the CdTe nanowires synthesized in this study.[302,303] The results are shown in Figure 6.9. By extrapolating the linear portion of the curve of $(E\alpha)^2$ versus E, the band gap is estimated to be 1.45 eV. However, the calculated value might have been slightly higher if an appropriate amount of background subtraction could be performed. As it is, there is not sufficient data at low energy to determine a background level. Nevertheless, the experimental absorption results and an estimated band gap of 1.45 eV or slightly higher are quite similar to the results for other similarly sized CdTe nanowires reported in literature and even to bulk CdTe.[295,299] This is not surprising as considerably smaller sizes are required to observe quantum-confinement induced increases in band gap of CdTe.[304]

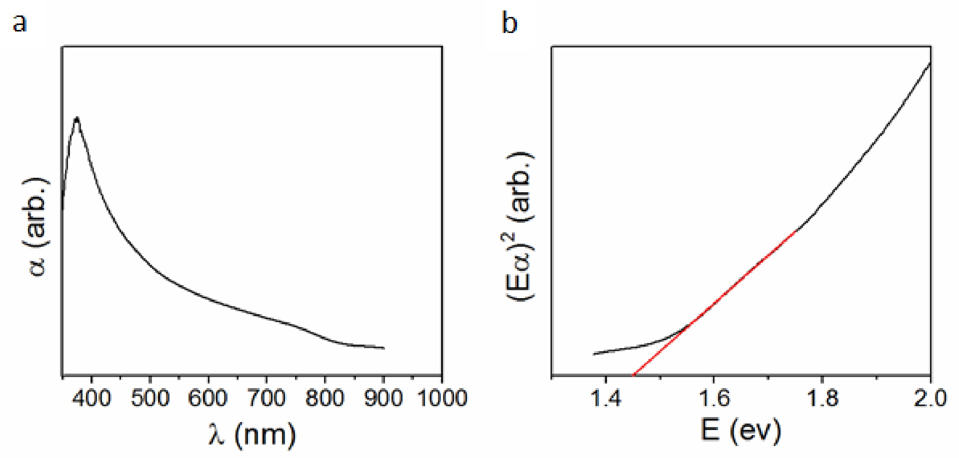

Figure 6.9 UV-vis absorption results for CdTe nanowires. (a) Absorption versus wavelength. (b) Tauc plot used to estimate band gap.

6.4 Nanowire Growth and Transformation Over Time

6.4.1 Te Nanowire Growth

To better understand the Te nanowire formation mechanism as well as the reaction rate achieved using ascorbic acid, experiments are performed to observe the reaction products over time during the Te nanowire growth step. Aliquots are obtained 5 minutes, 20 minutes, 1.5 hours, 3.5 hours, 7.25 hours, and 24 hours after ascorbic acid addition. As the reaction mixture very gradually changes from transparent to opaque within two minutes, it is not surprising that the product in the aliquot taken at five minutes is too dilute to observe any solids after centrifuging.

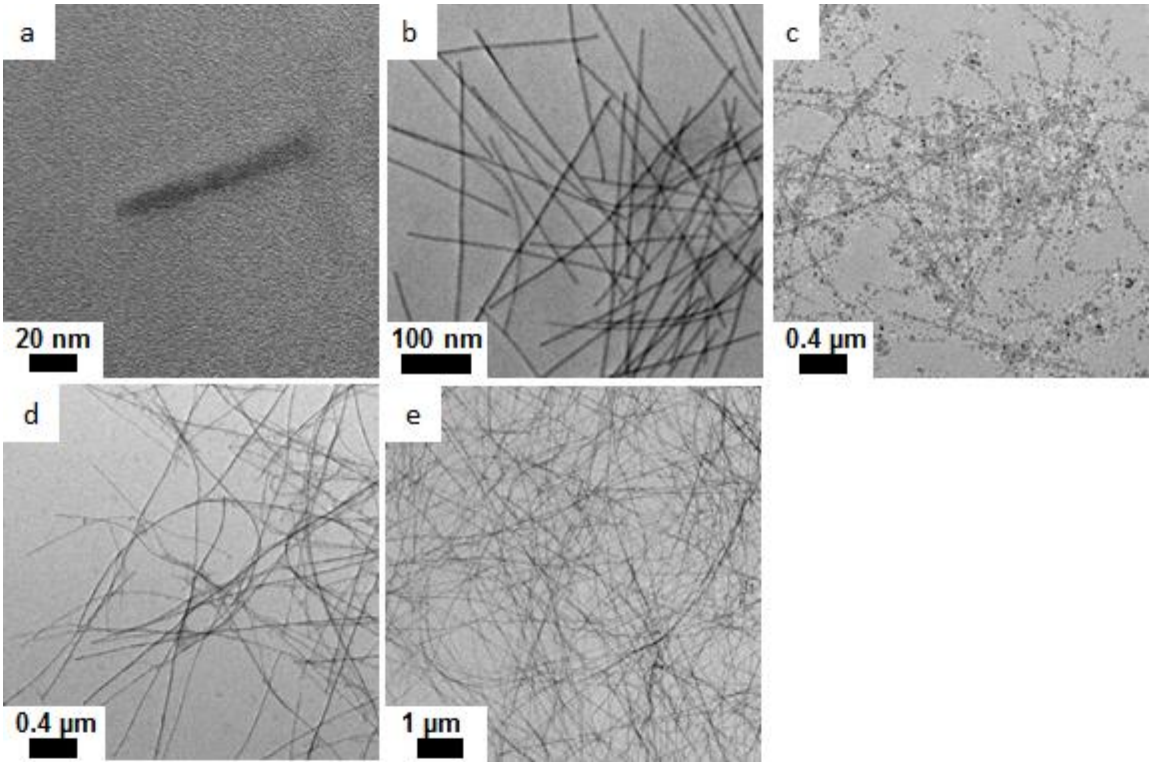

Figure 6.10 TEM images of material in aliquots taken at various times after the initial ascorbic acid solution addition during the Te nanowire growth step. (a) 20 minutes. (b) 1.5 hours. (c) 3.5 hours. (d) 7.25 hours. (e) 24 hours.

Figure 6.10a-e shows TEM images of the products obtained from the remaining 5 aliquots. As seen in Figure 6.10a, the nanowires begin as short nanorods with small diameters. As the reaction continues, the nanowire diameter stays approximately constant, while the length increases almost linearly with time up to greater than 7 µm after 24 hours. These trends are shown graphically in Figure 6.11. The spherical particles observed at 3.5 hours are likely amorphous Te, which is later absorbed into the crystalline nanowires through the ripening process as described in literature and as suggested by their absence from the products obtained after 24 hours.[237,305]

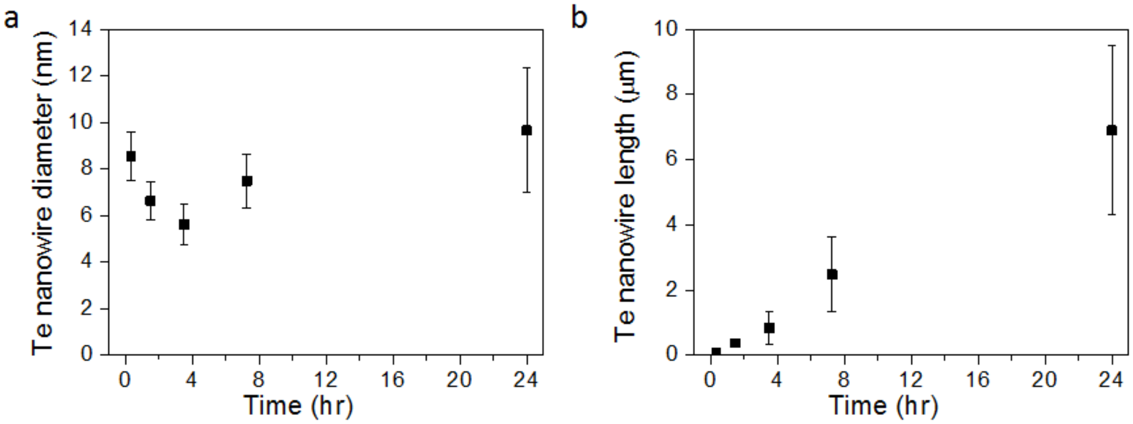

Figure 6.11 Te nanowire dimensions as a function of time elapsed after the ascorbic acid synthesis. (a) Diameter. (b) Length.

Overall, it is clear that the Te nanowires grown using ascorbic acid follow a similar mechanism as those grown using hydrazine. Small nuclei form and readily grow in the [001] direction with minimal grown in other directions. Over time, additional dissolved Te precursor reacts with the nanowire/nanorod ends and the reaction ends when all of the dissolved Te precursor is consumed.

The major difference between the two methods is the rate. The slow growth of Te nanowires induced by ascorbic acid agrees with the long growth times (≥12 hours) employed in several hydrothermal and other solution syntheses of Te nanowires using ascorbic acid[238,291,293] or other weak reducing agents such as starch,[236] PVP,[240] ethylene glycol,[239] or alginic acid.[306] Conversely, solution synthesis of Te nanowires under similar conditions occurs within one hour or less when hydrazine is used as the reducing agent, not only in the method described in chapter 3, but in other methods as well.[160,171,255,256] This highlights the relatively high strength of hydrazine as a reducing agent as compared with ascorbic acid. That similar products can be produced using reducing agents with such different strengths is an interesting phenomenon which requires further investigation to better comprehend.

6.4.2 Conversion to PbTe

Similar aliquot studies during the second reaction step are performed to observe the transformation from Te to metal tellurides. The transformation to PbTe is presented in Figure 6.12. XRD patterns obtained from reactions products immediately prior to Pb precursor addition as well as 5 minutes, 20 minutes, 1.5 hours, 3.5 hours, 7.25 hours, and 24 hours after Pb precursor addition are shown in order from bottom to top. The diffraction peaks for PbTe appear after only 5 minutes, yet a shoulder from the Te peak at 40.5 ° is present even after 1.5 hours and is mostly absent after the conversion reaction proceeds for 3.5 hours. Therefore, like the Te growth step, the conversion to PbTe when using ascorbic acid is much slower than when using hydrazine.[160,256]

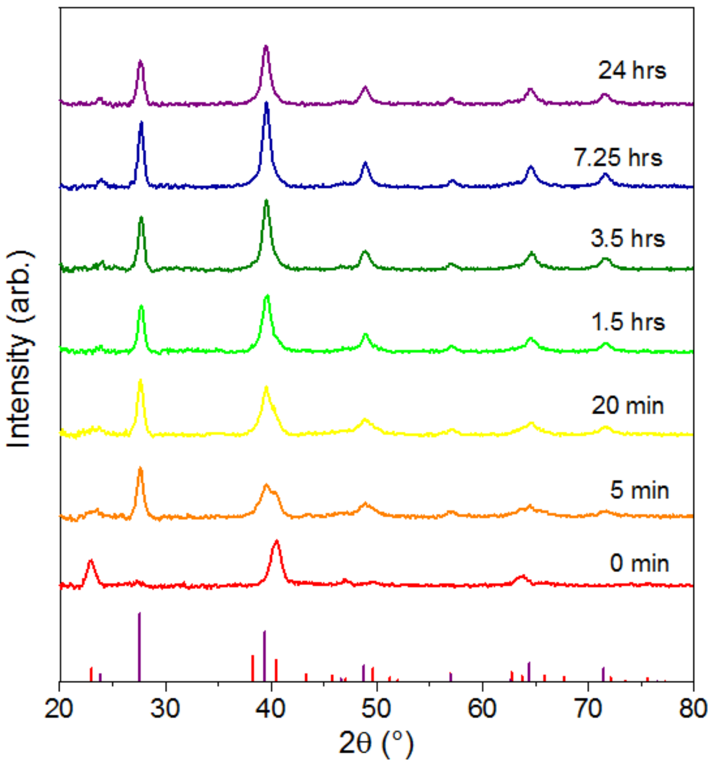

Figure 6.12 XRD patterns of aliquots taken at various times during the conversion from Te nanowires to PbTe nanowires. The red standard peaks are Te (JCPDS # 35-1452). The purple standard peaks are PbTe (JCPDS # 01-077-0246)

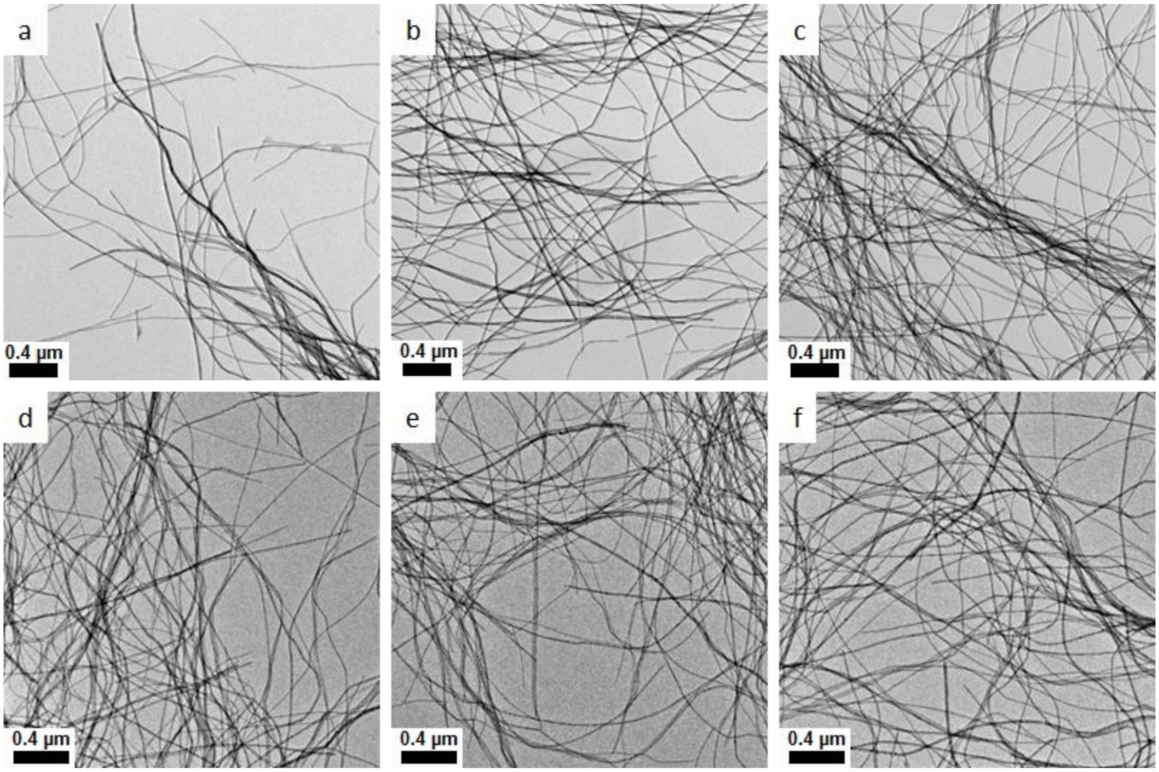

Figure 6.13 Low magnification images of nanowires during the transformation to PbTe at specified times after the Pb precursor addition. (a) 5 minutes. (b) 20 minutes. (c) 1.5 hours. (d) 3.5 hours. (e) 7.25 hours. (f) 24 hours.

Material from the same aliquots from the PbTe transformation is also used for TEM imaging. The low magnification images in Figure 6.13 show no significant change in the morphology with time. Medium magnification images in Figure 6.14 similarly show no distinct difference in the morphology as the reaction progresses. The nanowire diameter evaluated using these medium magnification images is shown in Figure 6.15. The initial increase in diameter within the first five minutes is immediately apparent. The variation in the nanowire diameter afterwards is not well understood and could be associated with statistical variation associated with small sample sizes (10-20 wires) compared with the large overall population.

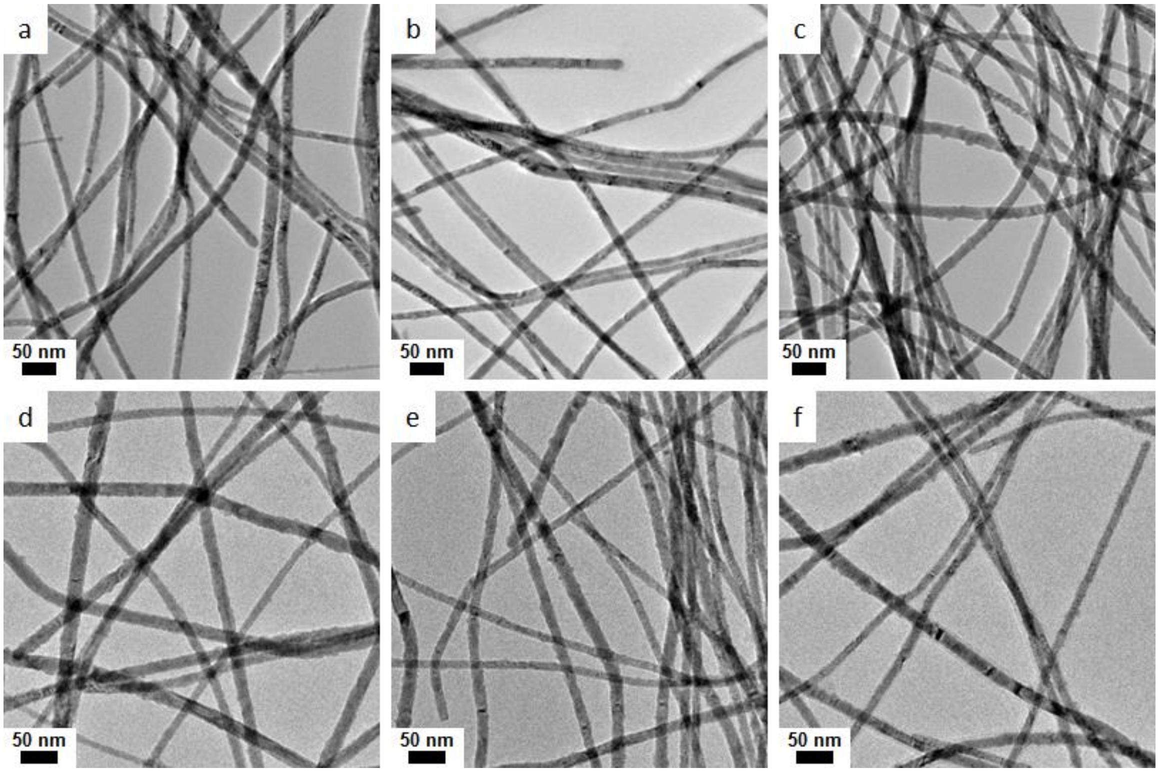

Figure 6.14 Medium magnification images of nanowires during the transformation to PbTe at specified times after the Pb precursor addition. (a) 5 minutes. (b) 20 minutes. (c) 1.5 hours. (d) 3.5 hours. (e) 7.25 hours. (f) 24 hours.

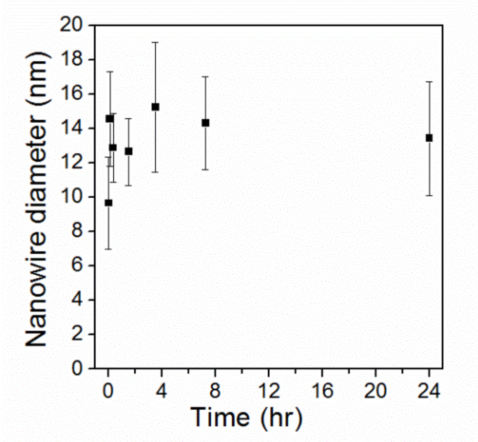

Figure 6.15 Nanowire diameter versus time elapsed during the conversion from Te to PbTe.

In addition to the low and medium magnification imaging, HRTEM imaging is performed on material from the aliquot taken five minutes after Pb addition. The nanowire in Figure 6.16 shows lattice fringes with a spacing of 0.59 nm, consistent with the (001) planes of Te, that are present only in the central portion of the nanowire, while lattice fringes associated with PbTe are mainly present on the nanowire surface. This suggests that Pb atoms are incorporated into the Te nanowire radially from the outside to the inside instead of axially beginning from the nanowire ends. Such a mechanism for the conversion from Te nanowires to metal telluride nanowires is suggested in several previous reports,[247,249,293,295] yet this represents perhaps the first observation of such a mechanism by HRTEM.

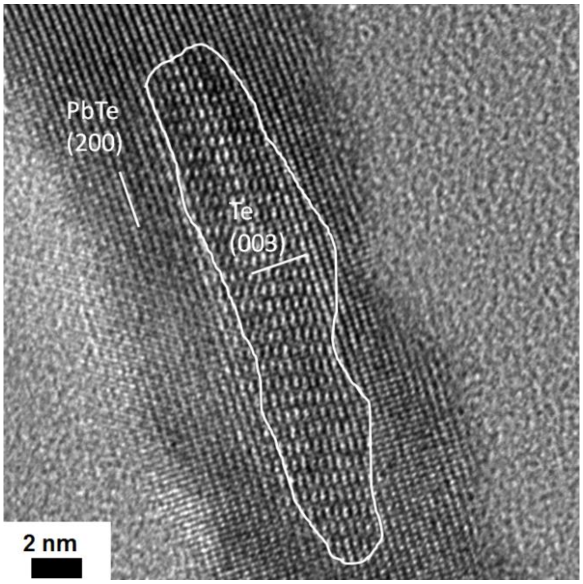

Figure 6.16 HRTEM image of a nanowire from the aliquot taken five minutes after Pb addition, which shows lattice fringes associated with Te in the center.

Also, a minority of HRTEM images of material obtained after 24 hours possess FFT spots associated with the (001) planes of Te; however these are noticeably diminished in intensity as compared with those of the sample taken only five minutes after Pb addition. Therefore, it appears that the conversion from Te to PbTe is not 100 % complete even after 24 hours despite the use of 20 % excess Pb precursor. Still, the XRD patterns in Figure 6.2 and Figure 6.12 show that the conversion is very nearly 100% complete after 24 hours. Potentially, the very small amount of Te that remains could be eliminated if the reaction time or temperature were increased in future experiments.

6.4.3 Conversion to CdTe

XRD patterns of material in aliquots taken during the transformation to CdTe are shown in Figure 6.17. In contrast to the transformation to PbTe, the transformation to CdTe is rapid. The XRD pattern for the material in the aliquot taken only five minutes after Cd injection appears to have no peaks from Te. As the reaction progresses further, no significant change is observed in the XRD pattern. While the peak intensity changes slightly, this change is not monotonic and is likely associated with unintentional variation in the powder distribution and amount on the glass substrates in XRD samples. Thus, based on XRD results, the reaction appears to require much less time than that which is allotted during hydrothermal syntheses of CdTe, even those which employ hydrazine.[247,293,295]

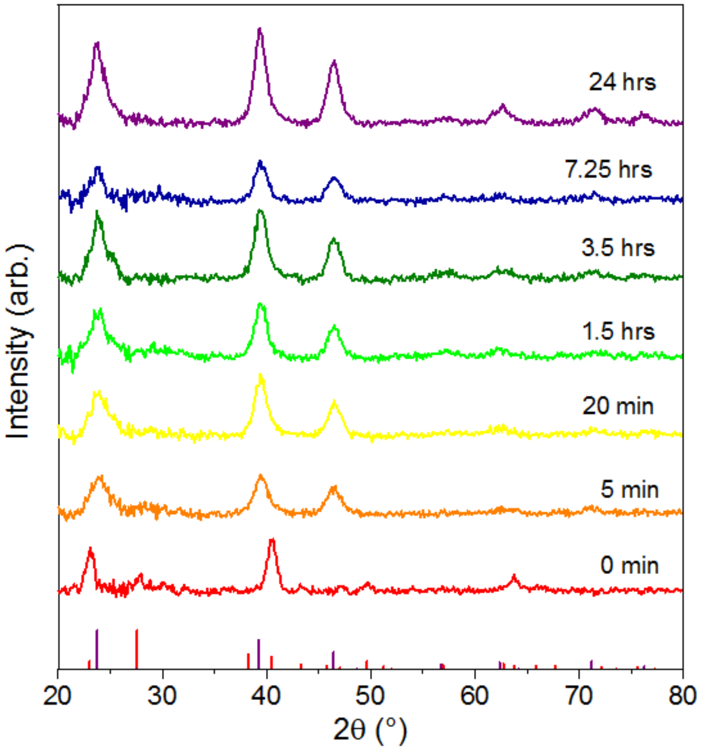

Figure 6.17 XRD patterns of aliquots taken at various times during the conversion from Te nanowires to CdTe nanowires. The red standard peaks are Te (JCPDS # 35-1452). The purple standard peaks are zinc blend CdTe (JCPDS # 01-070-8041).

Low magnification TEM analysis of the material in the various aliquots taken during the transformation from Te to CdTe is shown in Figure 6.18. At such a broad scale, there is no apparent change in the nanowire morphology as the synthesis progresses. In all cases, the nanowires are shown to be curved, to have lengths comparable to the image width, and to have no preferential orientation.

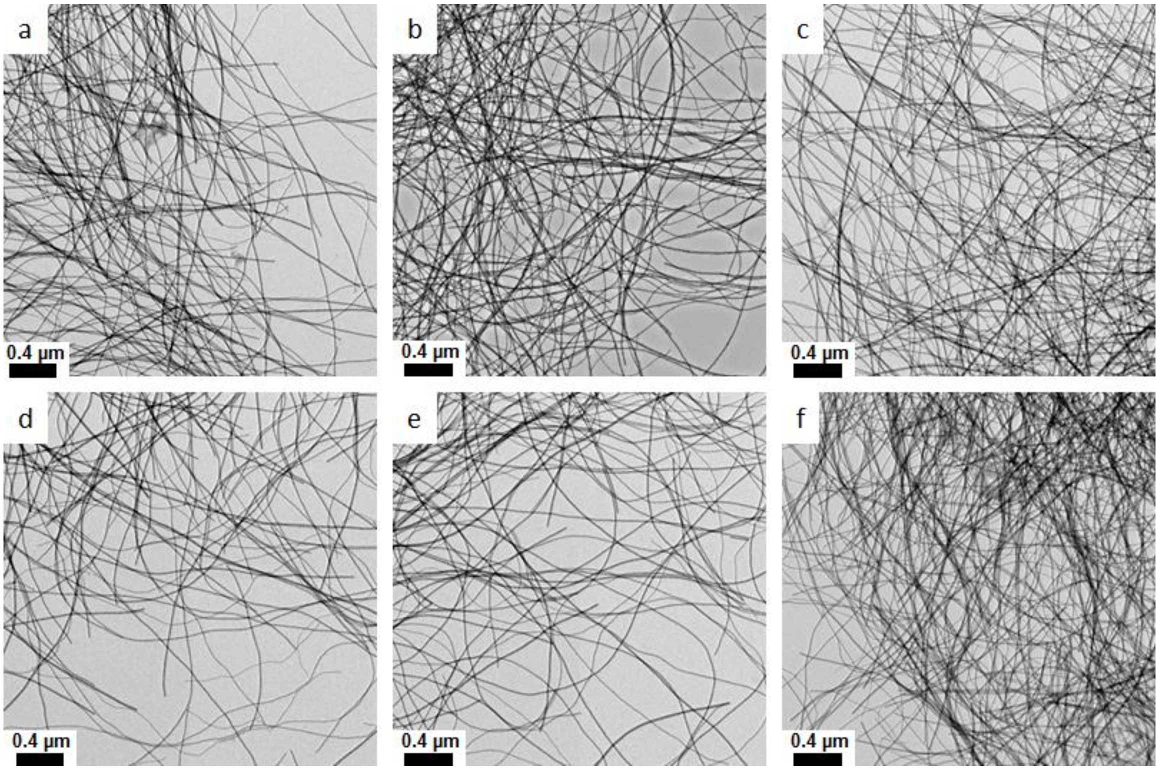

Figure 6.18 Low magnification images of nanowires during the transformation to CdTe at specified times after the Cd precursor addition. (a) 5 minutes. (b) 20 minutes. (c) 1.5 hours. (d) 3.5 hours. (e) 7.25 hours. (f) 24 hours.

Meanwhile, medium magnification TEM images in Figure 6.19 show an interesting trend. The nanowires from the first aliquot have rough surfaces, yet the nanowires obtained after 24 hours are quite smooth by comparison. In fact, there is a general trend of decreasing roughness with reaction time. Therefore, while the XRD and low magnification TEM images reveal no significant change with time, the medium magnification images show that the fine nanostructure of the wires changes significantly. Future studies could perhaps involve a comparison of the electrical properties of rough and smooth CdTe nanowires synthesized using this method.

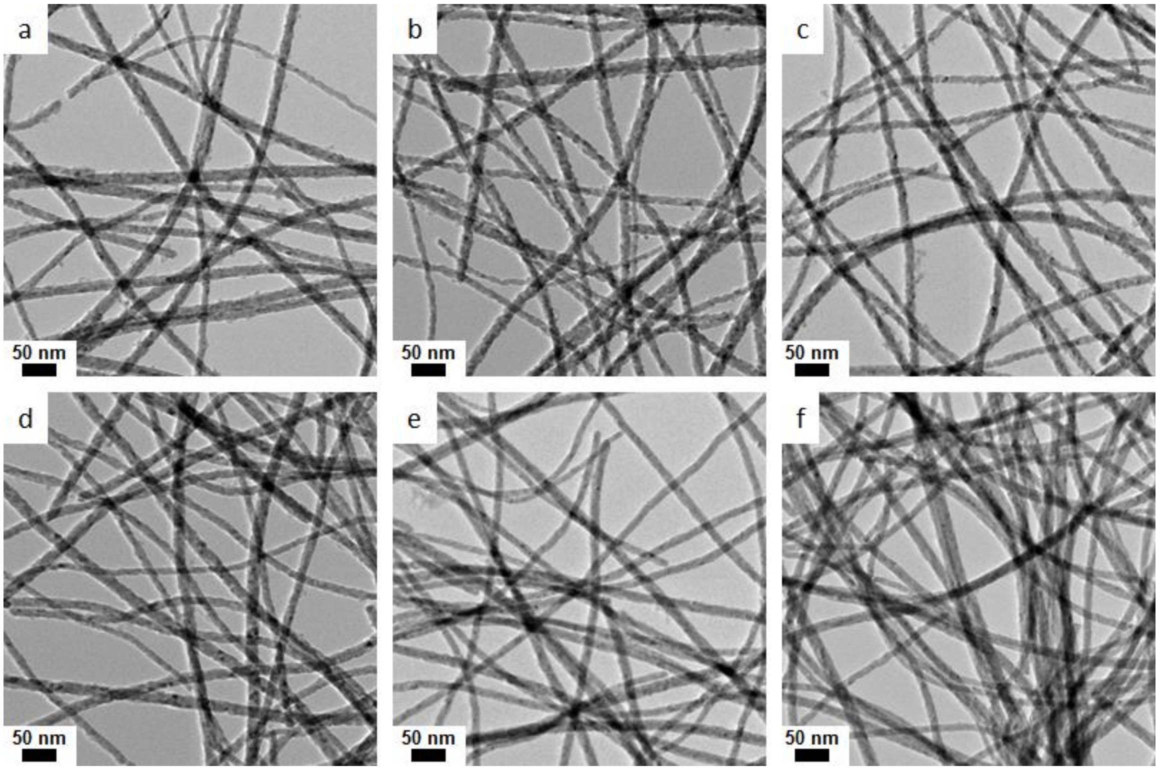

Figure 6.19 Medium magnification images of nanowires during the transformation to CdTe at specified times after the Cd precursor addition. (a) 5 minutes. (b) 20 minutes. (c) 1.5 hours. (d) 3.5 hours. (e) 7.25 hours. (f) 24 hours.

A summary of the nanowire diameter over time is shown in Figure 6.20. The increase in diameter associated with Cd uptake in the first five minutes is clear. By comparison, the nanowire diameter changes little during the following 23 hours and 55 minutes.

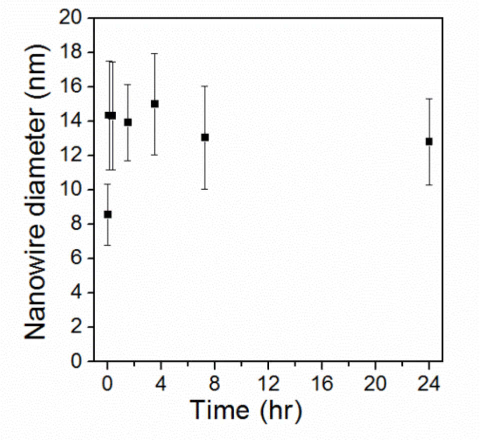

Figure 6.20 Nanowire diameter versus time elapsed during the conversion from Te to CdTe.

6.5 Conclusions

In summary, the two-step Te nanowire self-templated synthesis methods presented here produce pure-phase ultra-thin metal telluride nanowires as shown by XRD and TEM. The reactions proceed through the use of the environmentally benign reducing reagent, ascorbic acid. The Te growth step requires 24 hours, while the conversion to metal tellurides requires 3.5 hours or less. Reaction yields of greater than 75% are achieved during the synthesis of PbTe and CdTe. It is interesting to note that the analysis of the Bi_2Te_3, Ag_2Te, and $Cu_{1.75}Te$ nanowires synthesized by the other researchers working on this project shows pure-phase nanowire morphology with similar lengths and diameters. Thus, the ascorbic acid-based synthesis is quite versatile in its ability to create a variety of metal telluride nanowire materials.

CHAPTER 7. MEASUREMENT OF THERMAL CONDUCTIVITY OF FLEXIBLE LEAD TELLURIDE NANOCRYSTAL COATED GLASS FIBERS USING THE 3-OMEGA METHOD

7.1 Introduction

Traditional thermoelectric materials, such as Bi_2Te_3 and PbTe, are rigid at the millimeter scale. As mentioned in chapter 1, the generation of electricity using body heat would be more likely to be practical if flexible thermoelectric materials were developed. All organic thermoelectric materials are one class of flexible materials which have made great progress recently.[307] Thermoelectric composites that are comprised of at least one flexible material are another class that is of interest. Several conducting polymer/inorganic composites have been synthesized and investigated for thermoelectrics. These include poly(3,4-ethylenedioxythiophene):poly(styrenesulfonate) (PEDOT:PSS) combined with Te nanowires,[292,308,309] poly(3-hexylthiophene) combined with Bi_2Te_3,[310] and others.[311–313] Polymer/carbon nanotube composites have also received significant attention due to the unique combination of high electrical conductivity due to the carbon nanotubes and low thermal conductivity due to the polymer matrix.[314–323] Polymer/graphene composites have also been evaluated recently.[324,325]

Initial attempts at making a high power factor flexible composite in Professor Wu's lab at Purdue focused on physical solution blending of PbTe nanowires and commercial PEDOT:PSS. The composites possessed Seebeck coefficients which monotonically increased with increasing volume fraction of PbTe nanowires. However, the electrical conductivity was significantly reduced as compared with either pure polymer films or SPS'd PbTe nanowires. As a result, the composites possessed lower power factors than either of the pure materials.[326]

A second project was therefore initiated, in which PbTe colloidal nanocrystals were coated onto flexible glass fibers to form a cylindrical core-shell composite material. Initial results were quite promising. The Seebeck coefficient of the composite measured using an MMR Seebeck measurement system was over 1 mV/K from 300 to 400 K. Combined with a measured electrical conductivity of over 1 S/cm, these composited possessed power factors of over 100 μW/mK^2.[327] As both the Seebeck coefficient and electrical conductivity were measured in the axial direction, a more complete understanding of the material requires a method by which to measure the thermal conductivity in the axial direction as well.

Several methods have been developed to measure the thermal properties of wire-like samples in the axial direction. These include the self-heating 3ω method,[328] dc thermal bridge method,[329] thermal flash method,[330] optical heating and electrical thermal sensing,[331] and pulsed laser-assisted thermal relaxation technique[332] Several of these methods are useful for determining thermal diffusivity, but not thermal conductivity. The recently developed technique for measuring single nanowires does determine thermal conductivity, yet it requires complicated microfabrication.[76,77,333,334]

The 3ω method can determine the thermal conductivity of wire-like samples directly. The principal of the measurement is as follows. A sample is placed in a linear four-probe configuration in a vacuum chamber and sinusoidal current is sourced through the outer two electrodes at a frequency of ω. This sinusoidal current heats the sample according to

$$Q = I^2 R \tag{7.1}$$

where I is the time dependent current and R is the resistance of the portion of the sample between the inner electrodes. Thus, the sample is heated at a frequency of 2ω. This periodic heating induces a periodic temperature change at a frequency of 2ω. As a result of the general tendency of materials to have a temperature dependent electrical resistance, the sample experiences a sinusoidal variation in resistance at a frequency of 2ω. The voltage measured across the two inner electrodes therefore has two components, a large 1ω component associated with the average sample resistance and a small 3ω component associated with the change in resistance due to periodic heating. When the sample resistance and temperature coefficient of resistance are known, the 3ω voltage serves as a measure of the rate at which heat is conducted away from sample to the electrodes. With all other factors the same, low thermal conductivity materials are associated with larger 3ω voltages because the Joule heating induced in the wire is not rapidly conducted to the electrodes, so the temperature rise and resistance change are high.

In terms of equations, Lu, Yi, and Zhang derive that the 3ω voltage is given by

$$V_{3\omega,RMS} = \frac{4{I_{RMS}}^3 L_w R R'}{\pi^4 \kappa A_{\perp} \sqrt{1 + \left[2\omega\left(\frac{{L_w}^2}{\pi^2 \alpha}\right)\right]^2}} \tag{7.2}$$

where ω is the frequency of the sinusoidal source current, $V_{3\omega,RMS}$ is the root mean squared (RMS) voltage across the inner electrodes with a frequency of 3ω, I_{RMS} is the RMS current sourced with a frequency of ω, R' is the derivative of resistance with respect to temperature, κ is thermal conductivity as defined previously, $A_{\perp}$ is the cross section area of the sample, L_w is the length of the portion of the wire-like sample between the inner electrodes, and α is the thermal diffusivity of the sample as defined previously.[328] In the low frequency limit, the RMS 3ω voltage is given by

$$V_{3\omega,RMS} = \frac{4{I_{RMS}}^3 L_w R R'}{\pi^4 \kappa A_{\perp}} \tag{7.3}$$

Thus, when the sample dimensions, resistance, and derivative of resistance with respect to temperature are known, low frequency 3ω measurements can be used to directly determine a material's thermal conductivity.

The 3ω method has experienced particularly widespread use on samples with high thermal conductivity, such as carbon nanotube bundles,[328] carbon fibers[335,336] and yarns,[337] platinum wires,[338] and polycrystalline silicon microbridges[339]. However, the 3ω method has not yet been applied to low thermal conductivity wire-like materials such as PbTe-coated glass fibers. Furthermore, while the 3ω method employing a line heater on a substrate has been extended to layered composite planar samples,[309,340,341] the self-heated wire 3ω technique has not yet been employed to determine the thermal properties of composite fibers. This work discusses the first 3ω experiments on composite fibers as well as important radiation effects that future work should consider when measuring the thermal properties of low thermal conductivity high aspect ratio fiber composites such as layered polymer fibers[342,343] and layered oxide fibers.[344–346]

In addition to exploring several important considerations regarding the use of the 3ω method to measure low thermal conductivity composite fibers, this project also involves an initial evaluation of the measurement error and the effect of nanocrystal coating volume fraction on the thermal conductivity of the composite. Such insight is obtained by testing three essentially identical fibers without any nanocrystal coating and three fibers with different nanocrystal coating thicknesses. Table 7-1 summarizes the samples tested in this research project.

Table 7-1 Samples used for 3ω measurements.

Name	Number of coating cycles	Volume % PbTe
Sample 1	0	0
Sample 2	0	0
Sample 3	0	0
Sample 4	4	2.9 ± 1.4
Sample 5	8	5.8 ± 1.6
Sample 6	16	35.8 ± 7.6

7.2 Experimental Methods

7.2.1 PbTe Nanocrystal Synthesis

PbTe nanocrystals are synthesized by the hot injection of trioctylphosphine-Te (TOP-Te) into a Pb-oleate solution similar to other methods.[116,327,347–349] The chemicals including 1-octadecene (ODE, 90%), oleic acid (OA, 90%), lead(II) oxide (PbO, 99.9+%), Te powder (99.8%), hexane (98.5%), and acetone (99.5%) are purchased from Sigma-Aldrich. TOP (97%) is purchased from Strem.

A 0.37 M TOP-Te solution is prepared in a nitrogen glove box by dissolving 0.191 g Te powder in 2 ml TOP by heating at 57 °C and then diluting with 2 ml of ODE, which had been degased by heating at 103 °C under vacuum for 3 hours. The Pb-oleate solution is prepared by dissolving 0.223 g PbO powder in 0.75 ml OA and 12.7 ml ODE in a 50 ml round bottom flask and degassing under vacuum at 103 °C for 1.5 hours. Once degassed, the Pb-oleate solution is switched from vacuum to nitrogen gas positive pressure, the temperature is increased to 160 °C, and 4 ml of 0.37 M TOP-Te is rapidly injected. The TOP-Te injection causes an immediate temperature drop to 152 °C, yet the temperature returns to 160 ± 5 °C within about two minutes. Nine minutes after the TOP-Te injection, the reaction mixture is cooled rapidly to room temperature by immersing the flask in a water bath. The product is precipitated by adding acetone and centrifuging, after which it is re-dissolved in hexane. This washing procedure is repeated three times.

7.2.2 Glass Fiber Coating and Preparation for 3ω Measurements

PbTe nanocrystals are coated onto glass fibers using a three-step dip coating procedure, which is a modification of a method used by Luther and coworkers.[350,351] The required materials including chloroform (99%), hydrazine hydrate solution (80%), and acetonitrile (99.8%) are purchased from Sigma Aldrich. Glass wool is purchased from VWR. Prior to coating, the glass fibers are cleaned using the following method. First, the fibers are treated by ultrasonic in a solution of acetone and isopropanol (50 % acetone by volume). Then, the liquid is discarded and the fibers are rinsed briefly with either acetone or isopropanol. The fibers are then dried in air at 80 °C. Finally, the fibers are treated in an oxygen plasma cleaner for ten minutes.

The fibers are then dipped into a solution of two batches of PbTe nanocrystals dissolved in 10 ml chloroform. During the first coating cycle, the fibers remain immersed for five minutes; in subsequent cycles, the fibers remain immersed for two minutes. Next, the fibers are dried using gentle air flow. They are then exposed to a solution of 0.048 M hydrazine in water for one minute. Without drying, they are then immersed for a few seconds in acetonitrile. They are then dried fully using gentle air flow. This dip coating procedure is completed four to sixteen times depending on the desired nanocrystal coating thickness.

The coated glass fibers are annealed in a tube furnace under vacuum at 300 °C for two hours with 100 sccm of flowing forming gas. For 3ω measurements a single fiber is cut from a coated and annealed bundle and carefully placed on four co-linear Ag epoxy electrodes on a sapphire substrate. The electrodes are then cured at 125 °C for 15 minutes in a nitrogen filled glove box.

Sample 6, which is obtained using 16 coating cycles is conductive enough for stable 3ω measurements. Samples 4 and 5 with thinner coatings are obtained using four and eight coating cycles; the electrical resistances of these samples tend to be larger than is acceptable for 3ω measurements. Therefore, for samples 4 and 5, a thin layer of platinum is applied by sputtering on one side with Pt for 60 seconds using a current of 40 mA. An aluminum foil shadow mask is used to protect the sapphire substrate area between the two middle Ag epoxy electrodes from Pt deposition. Two point probe measurements on the masked portion of the sapphire substrate confirm that the sapphire substrate has negligible electrical conductivity after sputtering. For samples 1-3, which have no PbTe coating, a thin layer of gold is applied by thermal evaporation prior to placement on the Ag epoxy electrodes.

7.2.3 3ω Measurements

The measurements are performed on a variable temperature stage inside a microprobe station as shown schematically in Figure 7.1. At each temperature investigated, sinusoidal current is sourced through the outer electrodes and the RMS 1ω voltage across the inner electrodes is measured using a lock-in amplifier as shown in Figure 7.1.

Five different values of source current are applied in order to determine the electrical resistance at each temperature according to

$$R = \frac{dV_{1\omega,RMS}}{dI_{RMS}} \tag{7.4}$$

where $V_{1\omega,RMS}$ is the first harmonic voltage, which is in phase with the sourced current. Small currents are chosen to ensure negligible Joule heating. Next, a larger sinusoidal current in the range of 0.01 – 400 Hz is sourced and the 3ω voltage is measured by the lock-in amplifier. Prior to all lock-in amplifier measurements, a minimum of 33 periods (inverse of source current frequency) elapse in order to reach time-invariant ac voltages across the inner electrodes. At each temperature and frequency, ten ac voltage measurements are taken and averaged to increase measurement accuracy.

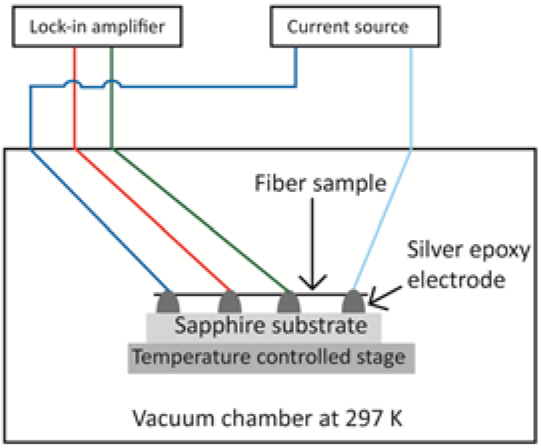

Figure 7.1 Schematic of apparatus used for 3ω measurements.

7.2.4 Emissivity Measurements

As discussed later, sample emissivity is required to properly account for radiation effects in 3ω measurements. To estimate the emissivity of glass fibers with different thicknesses of PbTe, Pt, and Au, four representative samples are prepared on flat glass substrates with dimensions of 12.7 mm x 12.7 mm. For example, to mimic the glass fiber dip coated with four coating cycles of PbTe and sputtered with Pt (sample 4), a flat glass substrate is dip coated with four coating cycles using a nearly identical nanocrystal solution. The sample is annealed and sputtered with Pt for 60 seconds at a current of 40 mA. The samples are then given to Thermophysical Properties Research Lab, Inc where the total radiation emitted from the coated glass samples is compared to that emitted by a black body at the same temperature in order to determine the emissivity of the samples.

7.3 Results

7.3.1 Structural, Compositional, and Geometric Characterization

As shown in Figure 7.2, the PbTe nanocrystals synthesized in this study are nearly cubic with edge lengths of 12.9 ± 1.1 nm, although this is found to vary slightly from batch to batch.

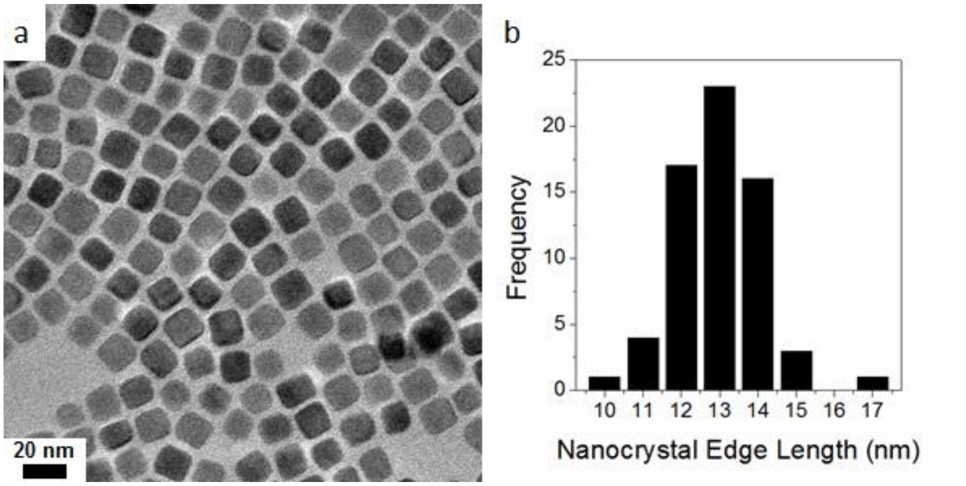

Figure 7.2 (a) Medium magnification TEM image of PbTe nanocrystals. (b) Edge length distribution of PbTe nanocrystals.

HRTEM analysis of a typical PbTe nanocrystal (Figure 7.3) reveals lattice fringes with a spacing of 0.32 nm, which corresponds to the {200} planes of PbTe (JCPDS # 01-077-0246). The HRTEM image also shows more clearly that the nanocrystals are not perfectly cubic, but have rounded corners.

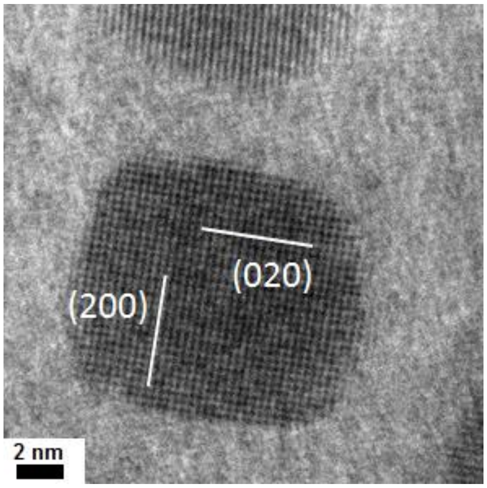

Figure 7.3 HRTEM image of a typical PbTe nanocrystal, showing the [002] zone axis.

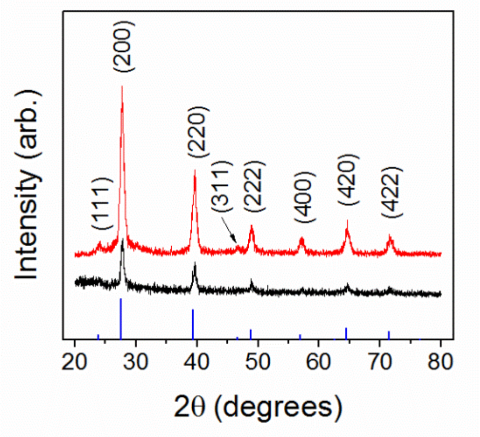

Figure 7.4 XRD pattern of as-synthesized PbTe nanocrystals (upper curve) and annealed PbTe nanocrystal coated fibers (lower curve). The blue reference peaks are PbTe (JCPDS # 01-077-0246)

While the individual nanocrystal in Figure 7.3 is clearly the PbTe phase, the XRD pattern of PbTe nanocrystals shown in Figure 7.4 provides evidence that a large representative ensemble of nanocrystals is PbTe. XRD peak intensities are rather weak for the sample of annealed PbTe nanocrystal coated glass. This is likely due to the difficulty in preparing dense thin samples of coated fibers for XRD experiments. Despite the low signal, the six major peaks associated with PbTe are still visible. The composition of the PbTe nanocrystals is further investigated using EDS. The composition of a drop cast film of PbTe nanocrystals is found to be 49.0 ± 0.5 atomic % Pb and 51.0 ± 0.5 atomic % Te. Thus, the nanocrystals are slightly rich in Te. This is generally associated with p-type behavior in PbTe, which is indeed indicated by the sign of the Seebeck coefficient.[327]

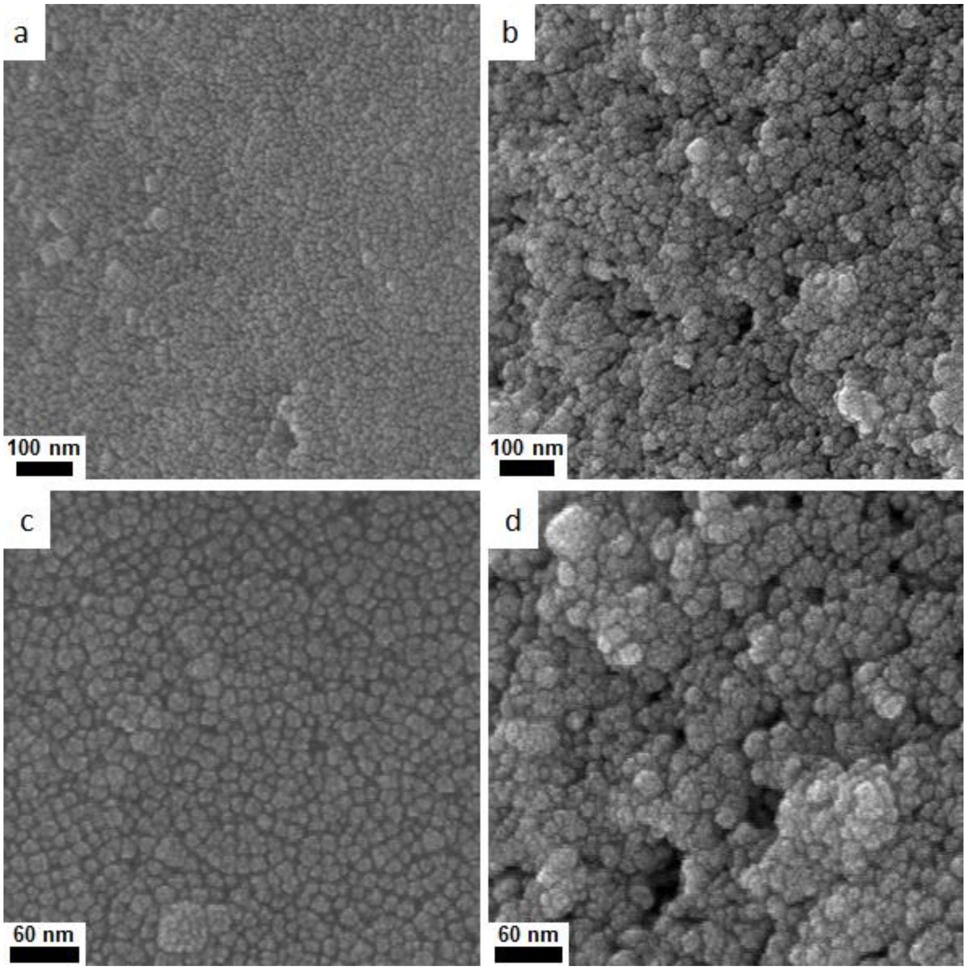

Figure 7.5 (a,b) Medium magnification SEM images of PbTe nanocrystal coated glass fiber. (c,d) High magnification SEM images of PbTe nanocrystal coated glass fiber. (a,c) Before annealing. (b,d) After annealing.

High magnification SEM studies of the coated fiber surface elucidate the effect of annealing the PbTe nanocrystal coated glass fibers. Figure 7.5a,c shows that the as-made nanocrystal coating is smooth with 1-2 nm gaps in between adjacent nanocrystals before annealing. Figure 7.5b,d shows that after annealing, the coating is rough with groups of agglomerated nanocrystals, creating a more effective network for charge carrier transport.

Low magnification SEM images of glass fibers coated with 16 coating cycles are shown in Figure 7.6. The images highlight the effect annealing has on the microstructure of such thick films. Both before and after annealing, the films are rough and even contain protrusions. However, cracks are observed only in annealed fibers.

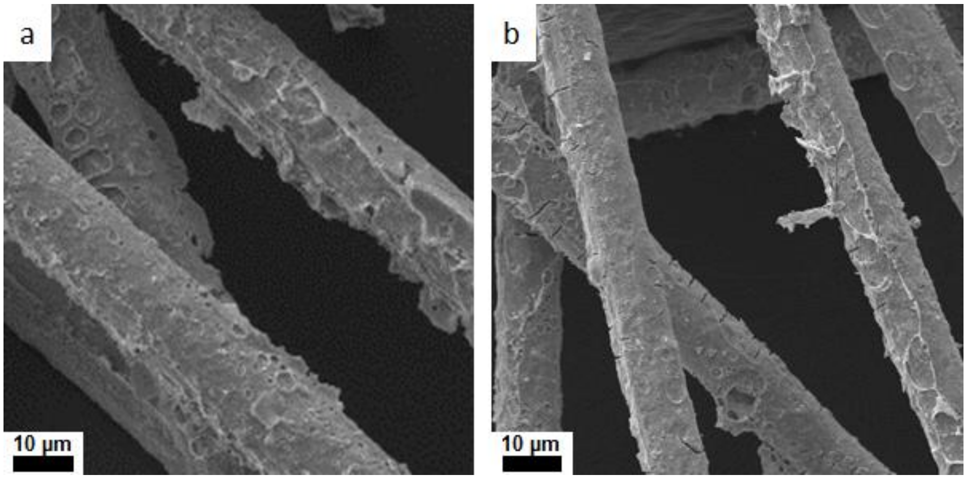

Figure 7.6 Low magnification SEM images of PbTe nanocrystal coated glass fiber. (a) Before annealing. (b) After annealing.

Cracks in thick film coatings have also been observed in Ag coated nylon mesh.[352] One plausible explanation for these cracks is that they are associated with the structural changes observed in Figure 7.5. In principal, the coalescence of nanocrystals that is observed on the nano scale happens on a micro scale in cases when the nanocrystal coating is thick enough. This could be due to the general tendency of nanocrystals to aggregate during the annealing step. The relative importance of the nanocrystal-glass bond in samples with thinner coatings could perhaps overcome the driving force for micro scale aggregation, thus preventing micro scale crack formation as shown in Figure 7.7.

It is also possible that the cracks form as a result of the thermal expansion coefficient mismatch, which is relevant during the annealing step of the composite preparation. Specifically, the thermal expansion coefficients of bulk PbTe and Pyrex glass at around room temperature are 19.8-20.4 x 10^{-6} /°C and 32.5-35 x 10^{-6} /°C, respectively.[353–355] Of course, the thermal expansion coefficient of a PbTe nanocrystal film is likely to be quite different and dependent on its thermal history. Nevertheless, the difference in thermal expansion coefficient could certainly cause cracking to occur, particularly as the composite is reduced in temperature from 300 °C to room temperature at the end of the annealing process. In principle, the aggregated film attempts to reduce in length more than the glass. If there is a strong bond between the nanocrystal coating and the glass, the nanocrystal film cracks apart in order to match the thermal contraction occurring in the glass core.

The microstructural dependence on the number of coating cycles is shown in the low magnification SEM imaging of the fiber sides in Figure 7.7. Sample 1 has minimal overall surface roughness. Due to the nanocrystal coatings, samples 4 and 5 have rough surfaces by comparison. The features which resemble craters could perhaps be associated with the first drying step of the dip coating process in which the chloroform adhered to the fiber surface evaporates. The nanocrystal coating in sample 6 is quite different. In addition to greater qualitative surface roughness than any other sample, cracks with widths of several hundred nanometers exist throughout the film, as discussed above with regard to Figure 7.6.

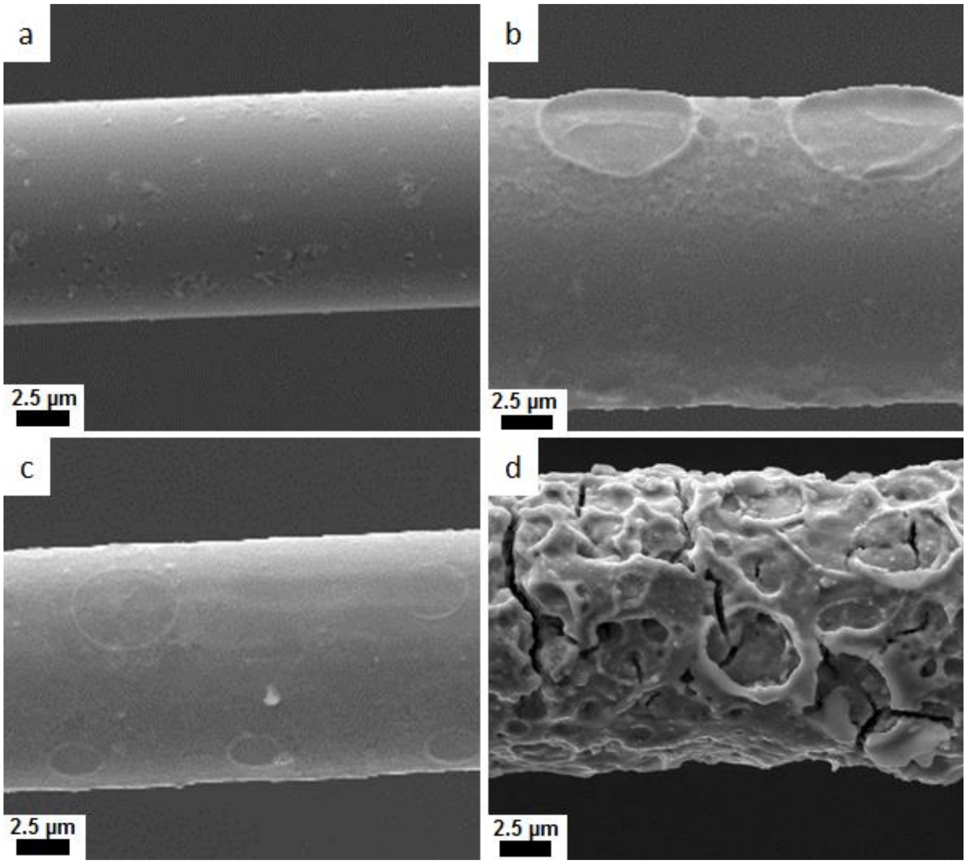

Figure 7.7 SEM images of coated fiber sides. (a) Sample 1. (b) Sample 4. (c) Sample 5. (d) Sample 6.

In addition to the observation of interesting structural features in Figure 7.7, such images are also useful for measuring the average fiber diameter. Similar images were taken along the entire length of the relevant portion of the fibers in order to take many measurements and obtain average diameters for calculations related to the 3ω method.

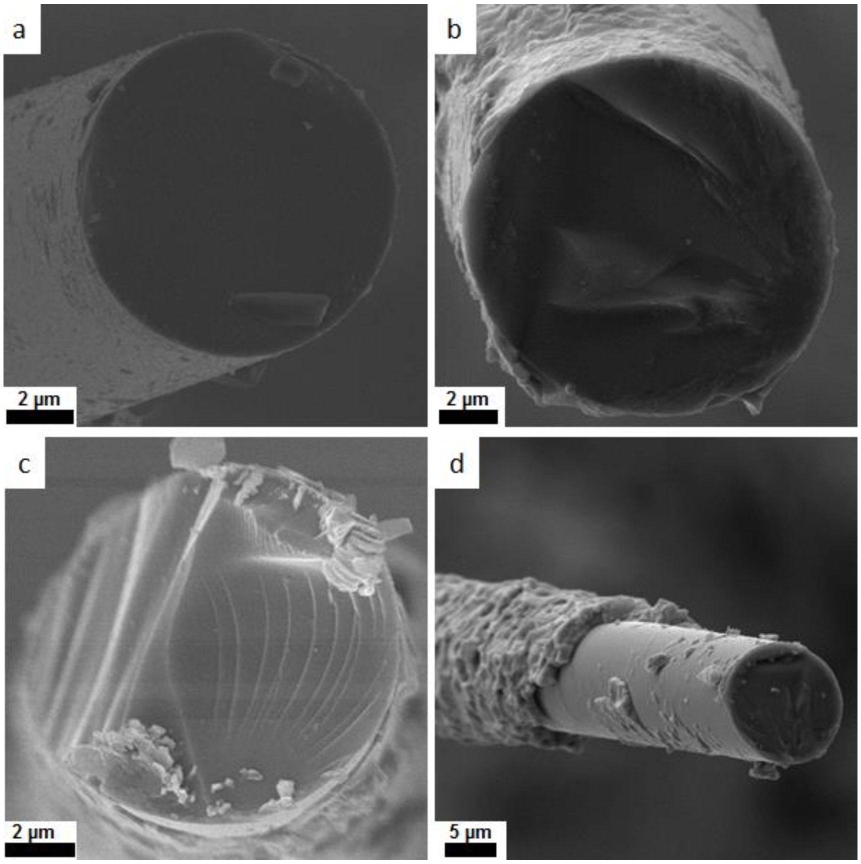

Figure 7.8 SEM images of fiber cross sections. (a) Sample 1. (b) Sample 4. (c) Sample 5. (d) Sample 6.

In order to find the volume fraction of the PbTe coating, cross section SEM images of the fibers are obtained. The atomic mass difference between glass and PbTe as well as some topological aspects result in distinguishable PbTe and glass regions. The images shown in Figure 7.8 provide a broad view of the fiber cross sections. Figure 7.9 then provides close-up views of the edge of the coated fibers. Several measurements of the coating thickness are performed on these images. Of course, sample 1 has no discernable nanocrystal coating thickness. Samples 4, 5, and 6 have nanocrystal coating thickness of 103 ± 51 nm, 164 ± 47 nm, and 1425 ± 324 nm, respectively. Thus, the nanocrystal coating thickness increases monotonically with increasing number of dip coating cycles, as expected. The volume fraction of PbTe calculated using the diameter and coating thickness measurements are shown in Table 7-1.

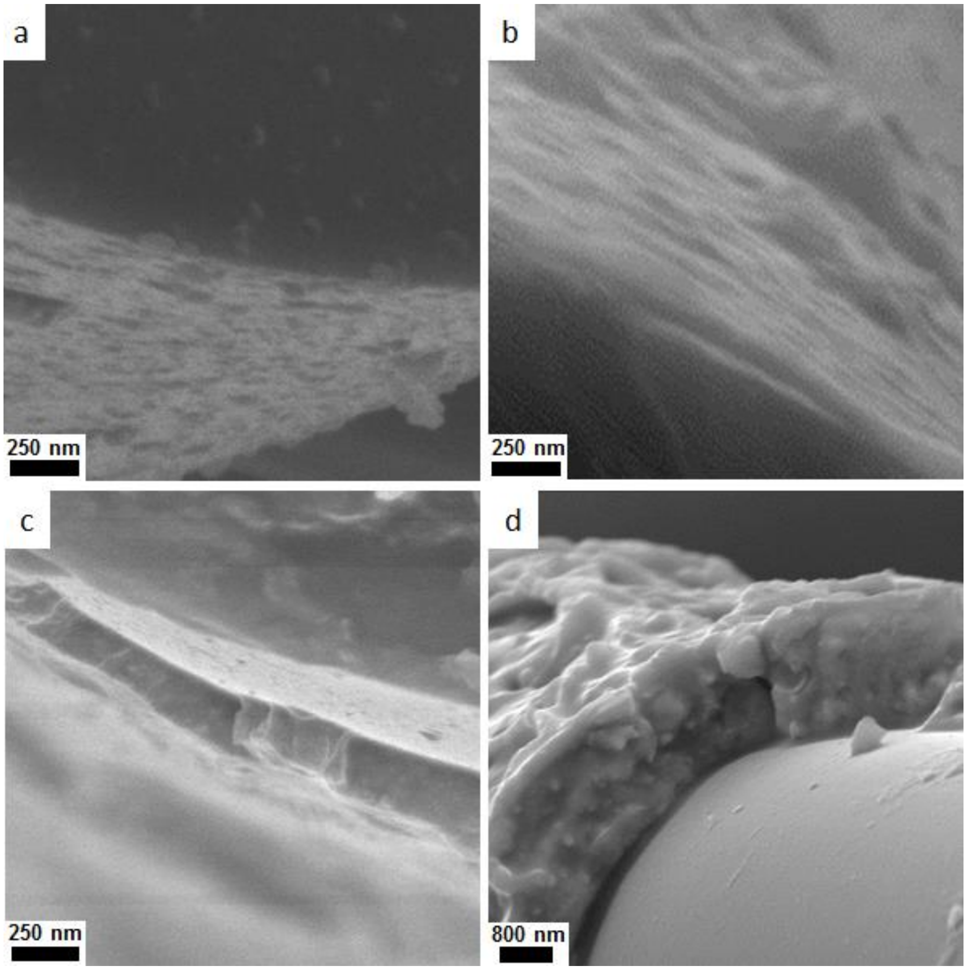

Figure 7.9 SEM images of fiber cross sections, used to measure coating thicknesses. (a) Sample 1. (b) Sample 4. (c) Sample 5. (d) Sample 6.

7.3.2 3ω Measurement Results

Accurate measurement of sample resistance at each temperature investigated is vital in the 3ω method. Figure 7.10 shows typical 1ω voltage vs. current curves for each of the six samples in this study, which are used to determine resistance. A linear relationship is observed for each sample, indicating Ohmic behavior as expected.

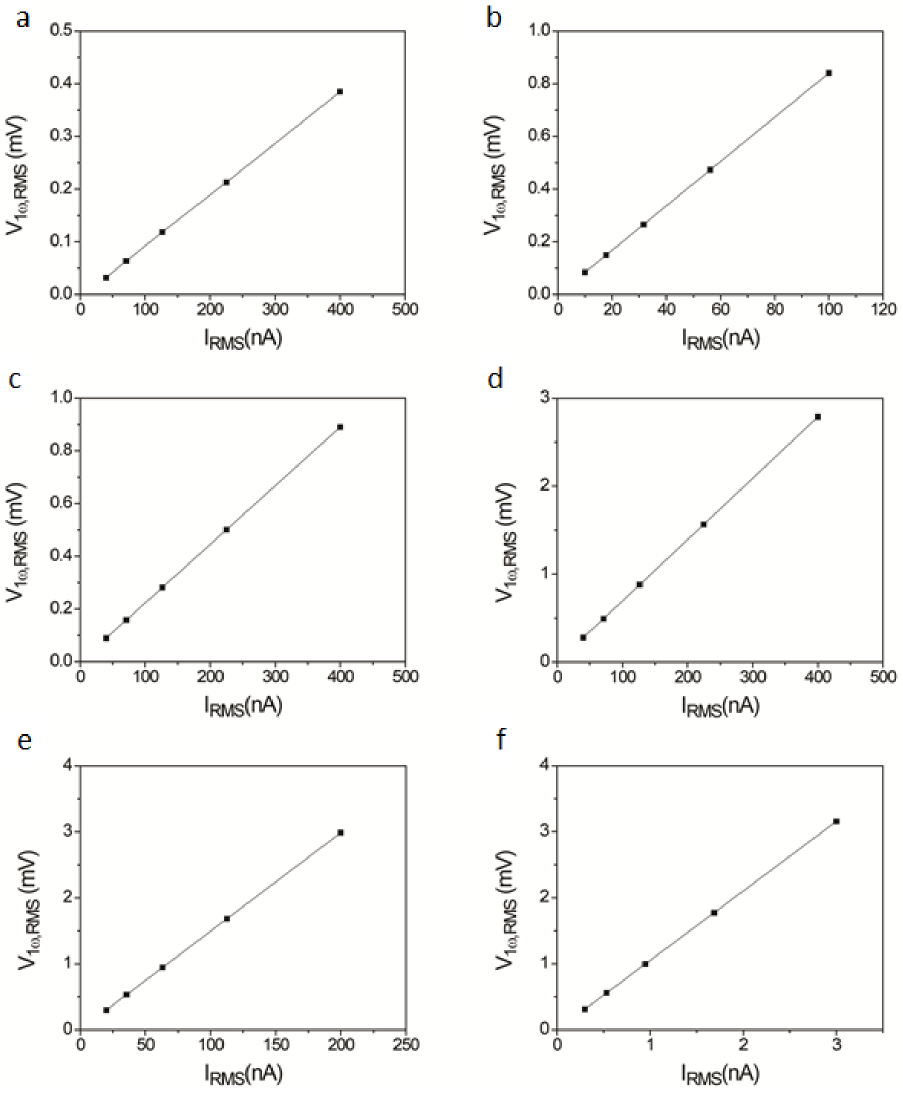

Figure 7.10 Typical voltage vs. current results for coated fibers. (a) Sample 1. (b) Sample 2. (c) Sample 3. (d) Sample 4. (e) Sample 5. (f) Sample 6.

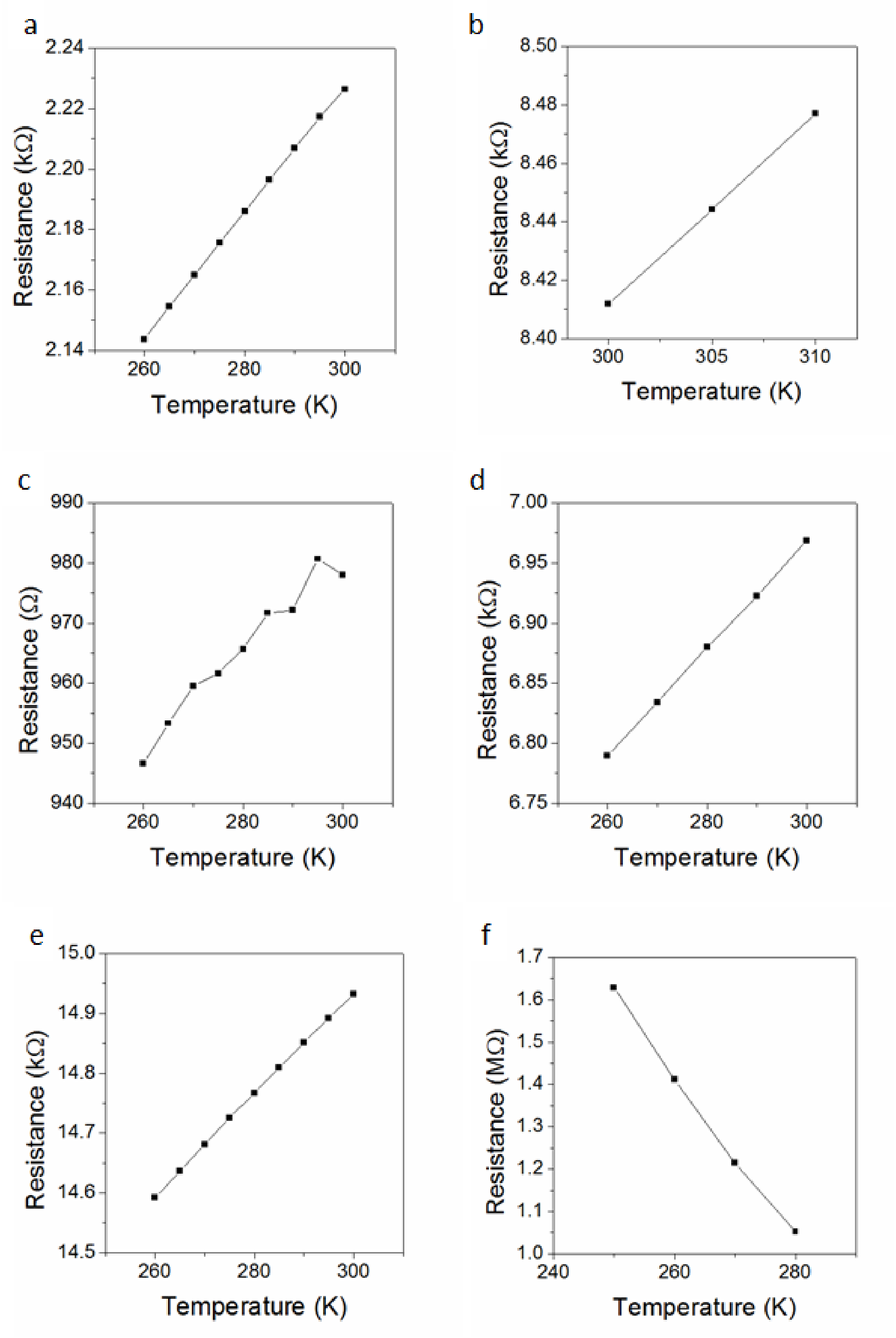

Figure 7.11 Resistance vs. temperature for coated fibers. (a) Sample 1. (b) Sample 2. (c) Sample 3. (d) Sample 4. (e) Sample 5. (f) Sample 6.

The resistance versus temperature curves for the six samples are given in Figure 7.11. It is immediately apparent that the resistance increases with temperature in samples 1-5. Thus, these sample display metallic behavior due to the thin coating of gold or platinum. Conversely, the resistance decreases with temperature in sample 6, which is similar to previous results for PbTe nanocrystal films.[327]

For the purposes of the 3ω method, both the resistance and the slope of resistance with respect to temperature are needed at each temperature of interest. The resistance versus temperature curves for samples 1-5 are all nearly linear, albeit with significant variation in sample 3. Additionally, nearly linear resistance versus temperature curves are expected for metals. Therefore, the slope of resistance with respect to temperature is determined using a linear fit for samples 1-5. For sample 6, a linear curve fitting is a poor approximation to the true trend, so a quadratic fit is used instead and the derivative of the quadratic fit is used to obtain the slope of resistance versus temperature at each temperature of interest.

The results for the third harmonic voltage as a function of frequency are given in Figure 7.12. According to the analytical expression given by Lu, Yi, and Zhang,[328] as frequency decreases, the RMS 3ω voltage should gradually increase and then asymptotically approach a frequency independent value. This is indeed observed for all samples at all temperatures. In order to use the results to calculate the thermal conductivity, the value for $V_{3\omega,RMS}$ that is used to find the thermal conductivity is an average of the values measured at the two or three lowest frequencies. This is particularly appropriate for sample 2, for which the value of $V_{3\omega,RMS}$ at the lowest frequency is actually slightly lower than those at higher frequencies. As this trend does not align with the theoretical prediction, it could possibly be an artifact associated with the difficulty in performing lock in amplifier measurements at such low frequencies.

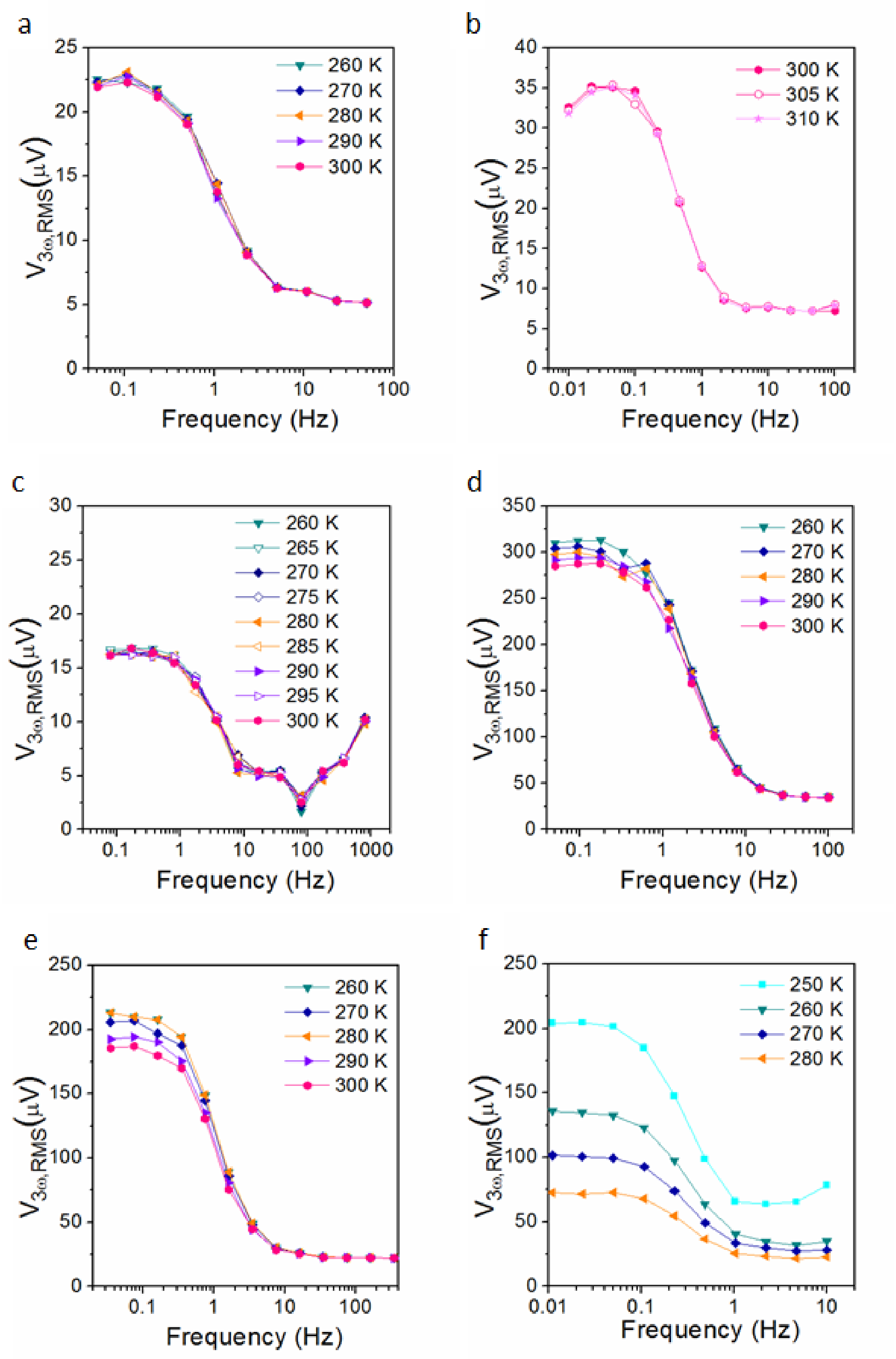

Figure 7.12 Third harmonic voltage vs. frequency at fixed current for coated fibers. (a) Sample 1. (b) Sample 2. (c) Sample 3. (d) Sample 4. (e) Sample 5. (f) Sample 6.

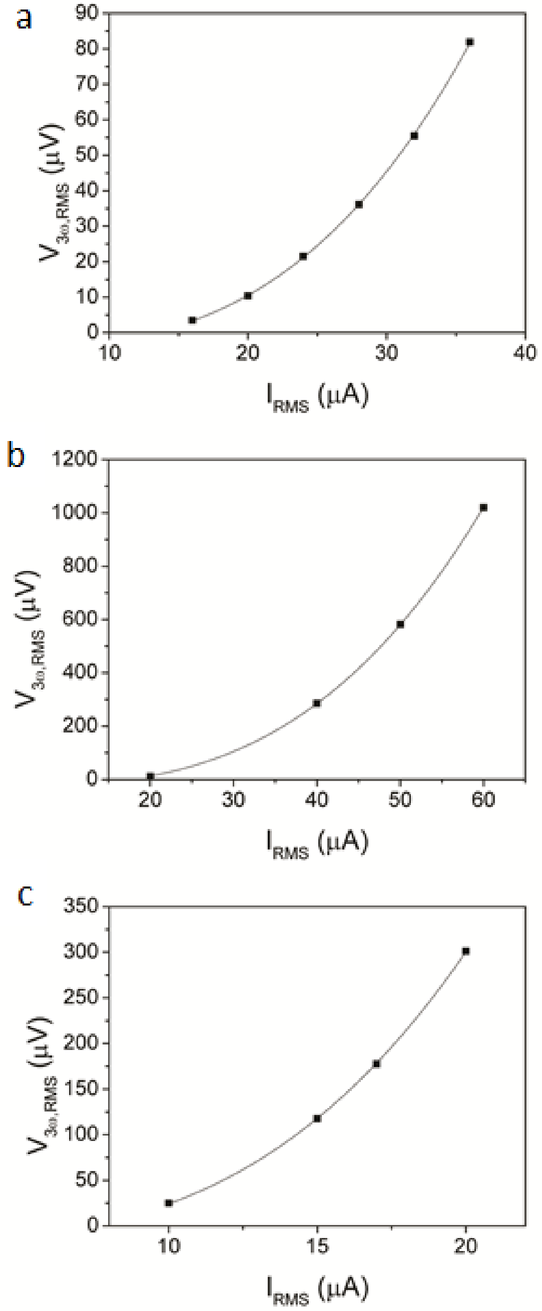

Figure 7.13 Third harmonic voltage versus current at fixed frequency. Points are experimental observations. Curves are best fit cubic relationships with non-zero offsets. (a) Sample 1. (b) Sample 4. (c) Sample 5.

The general agreement between experiments and theory is further verified by observing the relationship between $V_{3\omega,RMS}$ and I_{RMS} at fixed frequency. According to equation 7.2, $V_{3\omega,RMS}$ should be proportional to ${I_{RMS}}^3$. The experimental results of this trend for three samples are shown in Figure 7.13. The curves in the figure are in the form

$$V_{3\omega,RMS} = A + B \cdot {I_{RMS}}^3 \tag{7.5}$$

in which A and B represent fitting parameters. The non-zero values for A are likely associated with a background noise in the measurements. As shown in Figure 7.12, $V_{3\omega,RMS}$ possesses non-zero values at high frequency, which is not explained by the theory and could certainly be associated with background noise in the measurements. Consistent observation of such background noise in 3ω measurements at the Air Force Research Laboratory has led to the general practice of subtracting the background noise level from all values of $V_{3\omega,RMS}$ in order to determine the true thermal conductivity. In this research project, this practice is followed for samples 1-5. For sample 6, the background subtraction is not completed because the 3ω voltage did not asymptotically approach a constant value at high frequency, but rather began to increase. This is particularly easy to observe at 250 K and is not well understood at this point.

7.3.3 Impact of Radiation

In the simplest case, the thermal conductivity can be determined from the 3ω results by a simple rearrangement of equation 7.3.

$$\kappa = \frac{4{I_{RMS}}^{3}RR'L_{w}}{\pi^{4}V_{3\omega,RMS}A_{\perp}} \tag{7.6}$$

This equation assumes that thermal conduction is the only mechanism by which heat is transported out of the fiber. Operating in vacuum eliminates convection, but it does not eliminate radiation. If the fiber is fully surrounded by an environment at the same temperature as the electrodes and underlying substrate, then the amount of heat radiated from the sample to its surroundings is small. Furthermore, to a first order approximation, this radiation is proportional to the temperature difference between the sample and the surroundings, which varies at a frequency of 2ω. Therefore, the radiation in this case is time varying radiation. As derived by Lu, Yi, and Zhang, this can be considered analytically. The thermal conductivity corrected for the effect of time varying radiation is given by

$$\kappa = \frac{4{I_{RMS}}^{3}RR'L_{w}}{\pi^{4}V_{3\omega,RMS}A_{\perp}} - \frac{16\epsilon\sigma_{SB}{T_{0}}^{3}{L_{w}}^{2}}{\pi^{2}D} \tag{7.7}$$

where ϵ is the sample emissivity, σ_{SB} is the Stephan-Boltzmann constant, T_0 is the electrode temperature, and D is the sample diameter.

In the current study, the temperature controlled stage-sapphire-epoxy system is varied from as low as 250 K to as high as 310 K while the probe station chamber environment remains at 297 K. As approximately half of the fiber surface is exposed to radiation from a room temperature environment, radiation heats/cools the fiber resulting in a time invariant temperature rise/fall in the fiber when the stage temperature is below/above

297 K. Figure 7.14 schematically shows a fiber below room temperature being heated by radiation such that the average temperature is slightly higher than that of the electrodes and sapphire stage. The inset graph shows how the net radiation into the sample includes a time varying part as well as a time invariant offset that is not considered in equation 7.7. The energy balance for this complicated heat transfer problem includes a T^4 term due to the time invariant radiation effect. Therefore an analytical derivation is not pursued. Instead, a numerical simulation is performed like that described by Feng, Li, and Zhang.[338]

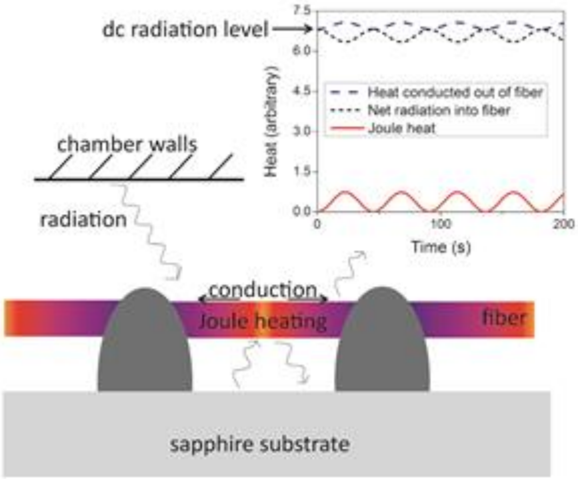

Figure 7.14 Schematic of the heat transfer occurring during the 3ω measurement on the coated fiber. The graph shows how the time invariant radiation level is non-zero due to the temperature difference between the chamber walls and the fiber.

7.3.4 Emissivity Results

The results obtained by Thermophysical Properties Research Laboratory, Inc. for the emissivities of planar samples made using techniques identical to those used to make the fiber samples are shown in Table 7-2. The measured emissivities of all samples, especially those with thin coatings of PbTe, are quite similar to that of glass as given in literature.[356] For subsequent modeling and thermal conductivity calculations, the measured emissivity values are used.

Table 7-2 Emissivity of coated glass and bare glass samples.

Sample description	Normal emissivity at room temperature
Glass substrate, 15 nm Ag deposited by thermal evaporation (mimic samples 1-3)	0.850
Glass substrate, 4 coating cycles of PbTe nanocrystals, annealed, Pt deposited by sputtering 60 seconds (mimic sample 4)	0.890
Glass substrate, 8 coating cycles of PbTe nanocrystals, annealed, Pt deposited by sputter 60 seconds (mimic sample 5)	0.786
Glass substrate, 16 coating cycles of PbTe nanocrystals, annealed (mimic sample 6)	0.736
Glass (polished)[356]	0.87-0.91
Glass (Pyrex)[356]	0.8
Glass (smooth)[356]	0.91

7.3.5 Thermal Conductivity Results

In order to extract the accurate thermal conductivity while considering the radiation heating/cooling, the time dependent temperature profile of the fiber during the 3ω experiment is simulated by collaborators in the Purdue School of Mechanical Engineering. The simulations take into account the periodic Joule heating, the heat conducted to the electrodes, and all radiation into or out of the fiber. The simulation details are described in the publication on this work.[357]

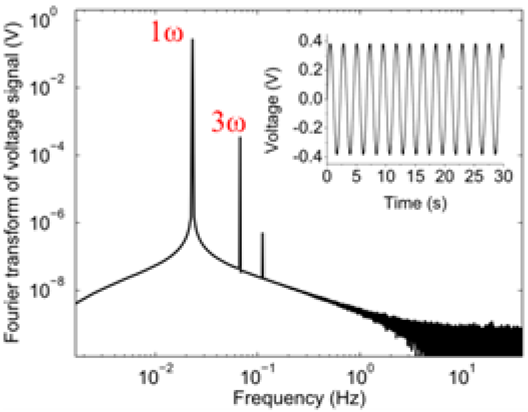

Figure 7.15 Simulated voltage during a typical 3ω measurement in the frequency domain. Inset shows the same results in the time domain.

In the simulation, the thermal and electrical conduction are described by Fourier's law and Ohm's law, respectively. The radiation is described by the Stephan-Boltzmann law. The transient voltage between the two inner electrodes recorded in the simulation is approximately a sine wave with frequency ω, as shown in the inset of Figure 7.15. A Fourier transform of this voltage signal can thus be used to extract the 3ω voltage. As shown in Figure 7.15, the 3ω signal can be identified clearly in the frequency domain. Operation of the simulation requires an accurate relation between the resistance and the temperature. Due to the existence of radiation, the experiment only yields R as a function of the electrode temperature T_0 rather than the wire temperature, T_w. To extract the $R(T_w)$ relation from the $R(T_0)$ relation, requires the derivation of the average temperature of the fiber at each value of T_0, which requires knowledge of the $\kappa(T_w)$ relation. Therefore, the problem needs to be solved in an iterative manner. The iterative process ultimately converges to a final $\kappa(T_w)$ relation.

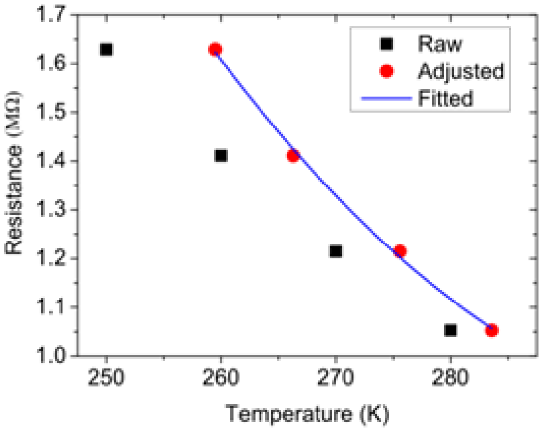

Figure 7.16 Temperature-dependent resistance of Sample 6 before (raw) and after (adjusted) the iteration process, and the quadratically fitted adjusted relation.

The overall effect of the time invariant radiation is significant, particularly for Sample 6 as shown in Figure 7.16. The derivative of resistance with respect to temperature is considerably larger in magnitude after the adjustment, which significantly affects the value of $V_{3\omega,RMS}$ determined by the simulation and measured in the experiment.

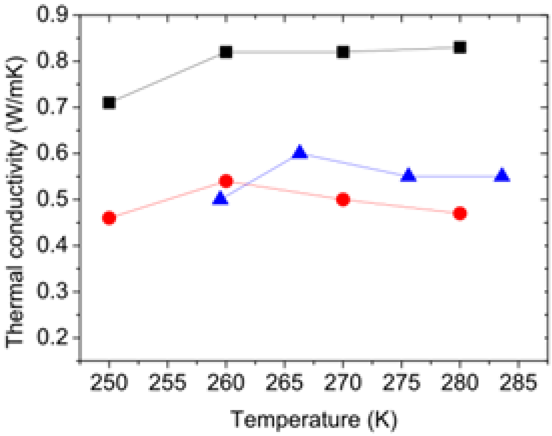

Figure 7.17 Comparison between the thermal conductivity of Sample 6 as a function of temperature calculated assuming no radiation effect (black squares), only the time varying radiation (red circles), and all radiation effects according to the simulation and iterative method (blue triangles).

The importance of considering the time invariant radiation is further exemplified in Figure 7.17, which shows the thermal conductivity of Sample 6 found using the two analytical expressions and using the iterative simulation approach. One important aspect of the results is that the actual temperatures to which the data pertains are quite different from the measured electrode temperatures due to significant amounts of radiation entering the fiber from the room temperature surroundings. Also, the thermal conductivity determined using the simulation is higher than that determined using the analytical expression that considers time varying radiation due mostly to the adjustment in the value of R'.

While the gold and platinum coatings on samples 1-5 are quite thin, they do contribute significantly to the thermal conductivity of the composites. Therefore, the final step in determining thermal conductivity is to subtract the contribution of the gold or platinum. The total thermal conductance of a sample coated with metal is given by

$$\frac{1}{R_{th,total}} = \frac{1}{R_{th,metal}} + \frac{1}{R_{th,core}} \tag{7.8}$$

where $R_{th,total}$, $R_{th,metal}$, and $R_{th,core}$ are the thermal resistances of the total composite, metal coating, and core composite, respectively. In terms of resistances, the Wiedemann-Franz Law is given by

$$R_{th,metal} = \frac{R}{LT_w} \tag{7.9}$$

where L is the Lorenz number as defined previously. This equation assumes a negligible contribution of the PbTe coating to the overall electrical conductance in samples 4 and 5. This assumption is valid as the resistances of samples 4 and 5 are reduced by a factor of more than 100 by coating with platinum. By next incorporating the dimensions of the sample, the total composite thermal conductivity is found to be

$$\kappa_{total} = \frac{L_w}{A_{\perp}}\left(\frac{LT_w}{R} + \frac{\kappa_{core}A_{\perp}}{L_w}\right) \tag{7.10}$$

where κ_{total} is the total composite thermal conductivity and κ_{core} is the thermal conductivity of the core composite, excluding the metal. With all relevant dimensions as well as Lorenz numbers for metallic thin films given in literature,[358,359] the thermal conductivity of the core composite can be found.

In Figure 7.18, the temperature dependent thermal conductivities of all six samples are shown. The thermal conductivity of each sample does not change much in the range of temperatures studied here, but it differs considerably between different samples, due to the difference in PbTe volume fraction as well as inherent measurement uncertainty. The thermal conductivity of bare glass fiber is found to be 0.70 ± 0.10 W/mK, which is lower than results for bulk Pyrex glass in literature.[360–362] With the addition of a thin layer of PbTe nanocrystals, the near room temperature fiber thermal conductivity initially increases to 0.93 ± 0.13 W/mK for the composite with 5.8 % PbTe, but then decreases to 0.55 ± 0.08 W/mK for the composite with 35.8% PbTe. This non-monotonic trend could be explained by the onset of cracking in samples with thick nanocrystal coatings shown in Figure 7.7.

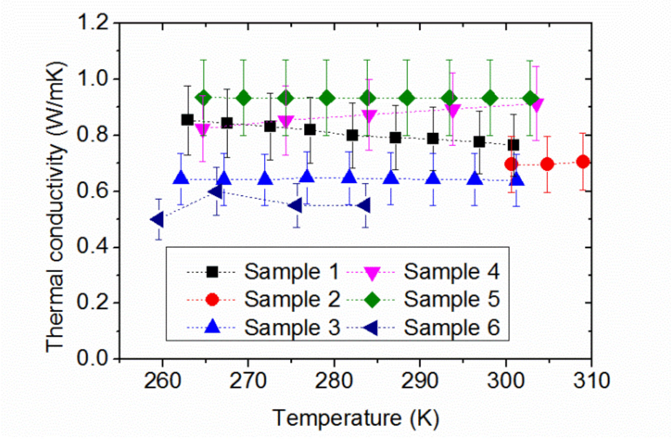

Figure 7.18 Temperature dependent thermal conductivity of all samples.

The range of near room temperature thermal conductivities shown in Figure 7.18 is around a factor of three larger than the value given in the previous publication on PbTe nanocrystal coated glass fibers.[327] Most likely, this discrepancy is due to the nature of the samples used for the different thermal conductivity measurements. For the previous publication, several grams of PbTe nanocrystal coated glass fibers were compressed at high temperature (>400 °C) by SPS to form a thin disc. The thermal diffusivity and specific heat of the disc were measured using the laser flash method and differential scanning calorimetry. The density was also measured and the thermal conductivity was calculated using equation (4.1. The composite nature of the disc helps to explain why the thermal conductivities in the previous publication are significantly below those of the present study.

In the previous study, the Seebeck coefficient of a small fiber bundle was measured in the axial direction using an MMR Seebeck measurement system. The electrical conductivity was measured in the axial direction using a four probe technique. In the present study, the thermal conductivity of PbTe nanocrystal coated fibers is measured in the axial direction. While the same exact sample was not used for each of the three measurements, they process by which the samples were made was intended to be identical and much of the structural characterization suggests that they are quite similar. Therefore, it is possible to at least estimate the ZT of PbTe nanocrystal coated glass fibers in the axial direction at around 300 K as approximately 0.06, which is less than the value of 0.2 reported previously.[327] The recently observed overestimation of the Seebeck coefficient by the MMR system suggests that the true ZT value of the coated fibers in the axial direction may be lower still. These issues of measurement accuracy and the need for similarity of samples used for the three transport measurements are obviously critical and should be given more attention in future work.

7.4 Conclusions

In summary, the thermal conductivities of PbTe nanocrystal coated glass fibers in the axial direction are investigated using the self-heated 3ω technique. The low thermal conductivities of the samples combined with the time invariant radiation from the room temperature microprobe station walls violate assumptions inherent in the analytical expressions derived by Lu, Yi, and Zhang. Therefore, a finite difference method is used to accurately simulate the 3ω measurements with the radiation effect. By iterating thermal conductivity values in the simulations to obtain agreement with experimental 3ω voltages, the thermal conductivities are found to be 0.50-0.93 W/mK in the temperature range 260-310K. The process of including both an experimental approach and numerical modeling could be useful to study the thermal conductivity of other wire-like samples with low thermal conductivities and high aspect ratios. Thus, this study broadens the application of the 3ω measurement technique.

CHAPTER 8. PROTOTYPE FLEXIBLE THERMOELECTRIC DEVICES COMPRISED OF SILVER TELLURIDE NANOCRYSTAL COATED NYLON

8.1 Introduction

The PbTe nanocrystal coated glass fibers described in the previous chapter serve as a proof of concept of flexible nanocrystal coated fiber thermoelectric materials. Another research project in Yue Wu's group established the synthesis of n-type colloidal PbTe nanocrystals.[209] These and traditional p-type PbTe nanocrystals were coated onto glass fibers to make a prototype thermoelectric device.[363] However, the device based on PbTe nanocrystal coated glass fibers has two issues. First, the resistance is quite high at 33 MΩ for a device made using one p-type and one n-type leg. Despite the 1 mV/K Seebeck coefficient of the p-n pair, the high device resistance leads to a power output of only 5.3 pW when a 20 K temperature difference is applied. The second issue is that the PbTe nanocrystal coated glass fibers require an annealing temperature of at least 300 °C in order to have measurable electrical conductances.

Ag_2Te is a good candidate to replace PbTe for several reasons. Bulk Ag_2Te is well established as a good thermoelectric material, with ZT values of around 0.33-0.45 at room temperature.[364,365] The solution synthesis of colloidal Ag_2Te nanocrystals has been described previously as well.[261,366–368] Initial work done in Professor Yue Wu's lab has shown that Ag_2Te nanocrystals can be dip coated onto glass and that the resulting films are electrically conductive even prior to high temperature treatment. Therefore, Ag_2Te satisfies the essential criteria for coating onto flexible substrates, even ones that are not stable above 200 °C such as nylon.[369]

This chapter describes the synthesis and characterization of Ag_2Te nanocrystal coated nylon mesh formed using a three-step dip coating procedure. Studies are performed to better understand the effect of the second and third dip coating steps. The Ag_2Te nanocrystal films are found to be conductive immediately after coating. Yet, the general conclusions from chapter 2 motivate an investigation on the effect of annealing.[399] Additionally, the effect of oxygen plasma treatment is explored as motivated by significant impact such treatment is known to have on the electrical properties of a variety of thin film materials.[370–373] Finally, prototype flexible thermoelectric devices comprised of Ag_2Te nanocrystal coated nylon mesh and PEDOT:PSS coated nylon mesh are made and their power output is measured in response to a temperature gradient.

8.2 Experimental Methods

For this project, Ag_2Te nanocrystals are synthesized in solution using a modified procedure from the literature. The nanocrystals are dispersed in chloroform and dip coated onto nylon mesh. The coated nylon mesh is then treated in order to improve its thermoelectric properties. Various methods are used to characterize the coated nylon before and after nanocrystal dip coating and treatment. Finally, the treated coated nylon is used to make prototype thermoelectric devices whose power outputs and Seebeck coefficients are measured using applied temperature gradients.

8.2.1 Ag_2Te Nanocrystal Synthesis

The Ag_2Te nanocrystals are synthesized using a modified version of the procedure described by Liu et. al.[366] The required materials including 4-tert-butyltoluene (95 %), 1-dodecanethiol (98 %), and Te powder (99.8 %) are purchased from Sigma Aldrich. $AgNO_3$ (99.9 %) is purchased from Alfa Aesar and TOP (97 %) is purchased from Strem.

First, solution A is made by mixing 80 ml 4-tert-butyltoluene with 1.28 ml 1-dodecanethiol in a glass beaker. Solution B is made by mixing 0.364 g (2.1 mmol) with 80 ml DI water and treating with ultrasonic for one to two minutes until the $AgNO_3$ is fully dissolved. Then solution B is added to solution A, which is then stirred for two to three hours to transfer the Ag into the organic phase. Solution C is made in a nitrogen filled glove box by mixing 0.287 g Te powder (2.2 mmol) in 3 ml TOP. The Te is dissolved by stirring and heating to 60 °C for at least 30 minutes.

Solution A is then transferred to a separatory funnel so that the water phase can be removed and the pure organic phase can be added to a glass three-neck flask. Nitrogen gas positive pressure is applied to the flask via a Schlenk line and the Ag precursor mixture is heated to 97 °C. Solution C is rapidly injected into the flask, causing an immediate color change from white or clear to black. The reaction proceeds at 97 °C for

24 hours. It is then quenched to room temperature by immersing the flask in a water bath.

Due to the tendency of the synthesis to form nanocrystals and nanocrystal aggregates with a broad range of sizes, a series of centrifugation steps are used to remove particularly small nanocrystals and large aggregates. First, 8 ml hexane is added to the reaction product solution, which is then centrifuged at 4300 rpm for five minutes. The precipitate from this step is discarded (waste sample #1). The dark supernatant is added to an equal volume of ethanol and centrifuged at 6000 rpm from five minutes. The supernatant is then discarded. The precipitate is combined with 10-20 ml hexane and centrifuged at 4000 rpm for five minutes. The precipitate is discarded (waste sample #2) and the supernatant is saved for dip coating. In order to transfer the nanocrystals to chloroform, the hexane solution is combined with an equal volume of ethanol and centrifuged at 8400 rpm for one minute. The clear supernatant is discarded and the nanocrystals can be either combined with chloroform immediately or stored in a nitrogen filled glove box for later use.

8.2.2 Dip Coating of Ag_2Te Nanocrystals onto Nylon Mesh

Nylon 6/6 mesh is purchased as a Sefar America, Inc. Lab Pak (Mesh opening 35 micron, 12” x 12”, 6 pieces). Nanocrystals are coated onto this flexible substrate using a procedure similar to that described in chapter 7 for obtaining PbTe nanocrystal coated glass fiber. In order to first prepare nylon mesh for dip coating, it is treated as follows.

First, it is placed in a glass beaker and submersed in an approximately 50/50 (v/v) mixture of isopropanol and acetone and treated with ultrasonic for ten minutes. The liquid is then removed and the nylon is rinsed with isopropanol or acetone. The nylon is dried in an oven at less than 100 °C and treated in an oxygen plasma cleaner for 30 minutes. The oxygen plasma cleaner is used to remove any remaining contaminants from the nylon surface as well as to improve the adhesion of material to the surface.[374]

The nylon is then dipped into a solution of one batch of Ag_2Te nanocrystals dissolved in 10 ml chloroform. During the first coating cycle, the fibers remain immersed for five minutes; in subsequent cycles, the fibers remain immersed for two minutes. Next, the fibers are dried using gentle air flow. They are then exposed to a solution of 0.048 M hydrazine in ethanol for one minute. Without drying, they are immersed for a few seconds in ethanol. They are then dried fully using gentle air flow. This dip coating procedure is completed 30 to 50 times.

The above procedure is used in general. However, in one experiment, the second dip coating step (hydrazine/ethanol) is eliminated. Such an experiment is useful for determining the effect of the hydrazine/ethanol soak step. In another experiment, both the second and third steps of the dip coating procedure are eliminated such that the nylon is simply dipped into the Ag_2Te nanocrystal solution, dried, and then this first and only step is repeated.

8.2.3 Coated Nylon Treatment Methods

The nylon coated with Ag_2Te nanocrystals is electrically conductive immediately after coating. However, treatment methods are found to improve its properties. For the first treatment method, Ag_2Te nanocrystal coated nylon mesh is placed in a horizontal tube furnace. The tube is brought to a pressure of approximately one torr and heated to 127 °C in 30 minutes. The temperature is held at 127 °C for 30 minutes and then cooled down to near room temperature over a period of approximately one hour. For the second treatment method, Ag_2Te nanocrystal coated nylon is treated in an oxygen plasma cleaner for ten minutes.

8.2.4 Preparation of PEDOT:PSS Coated Nylon Mesh

A commercial formulation of PEDOT:PSS in water, Clevios PH 1000, is purchased from Heraeus. It is sold as a 1.0-1.3 % solids dispersion in water with a PEDOT:PSS ratio of 1:2.5 by weight.[375] Two high boiling solvents, dimethylsulfoxide (DMSO, ≥99.9 %) and ethylene glycol (≥99 %), are purchased from VWR. PEDOT:PSS is coated onto nylon mesh using a technique similar to that described previously.[376,377] Solutions of Clevios PH 1000 and 5 % (v/v) of an additive of either DMSO or ethylene glycol are made by mixing the liquids in glass vials. Pieces of nylon mesh with dimensions of approximately 2 mm x 20 mm are cleaned using the same procedure as that used to prepare nylon for coating with Ag_2Te nanocrystals. They are placed on a glass petri dish and approximately 100 µl of the Clevios PH 1000 solution with an additive are drop cast onto the nylon mesh. The petri dish is then placed on a hot plate set to 150 °C and left for ten minutes. The hot plate is then turned off so that the PEDOT:PSS/nylon composite can slowly cool to room temperature. After drying, the nylon pieces are peeled off of the glass petri dish.

8.2.5 Sheet Resistance Measurements

For nanocrystal or PEDOT:PSS coated nylon samples, the sheet resistance is measured by first using scissors or a razor blade to cut off a piece of sample with dimensions of approximately 2-3 mm x 5-8 mm. The sample ends are glued to a glass slide using fast drying Ag suspension (Ag paint) sold by Ted Pella. It is important to use highly viscous Ag paint to prevent the paint from leaking towards the center of the sample. The resistance of the sample is measured in a two-probe configuration. The sheet resistance is then calculated using the measured resistance and sample dimensions.

8.2.6 Prototype Thermoelectric Device Assembly

The coated nylon is assembled into prototype thermoelectric devices according to the diagram shown in Figure 8.1. The copper plates and glass pieces are attached using double coated carbon tape sold by Ted Pella. The p-type and n-type flexible coated nylon is attached to the glass using Ag paint. With the intention of applying a temperature gradient in the vertical direction, the design follows the typical thermoelectric device architecture in which the thermoelectric materials are electrically in series and thermally in parallel.

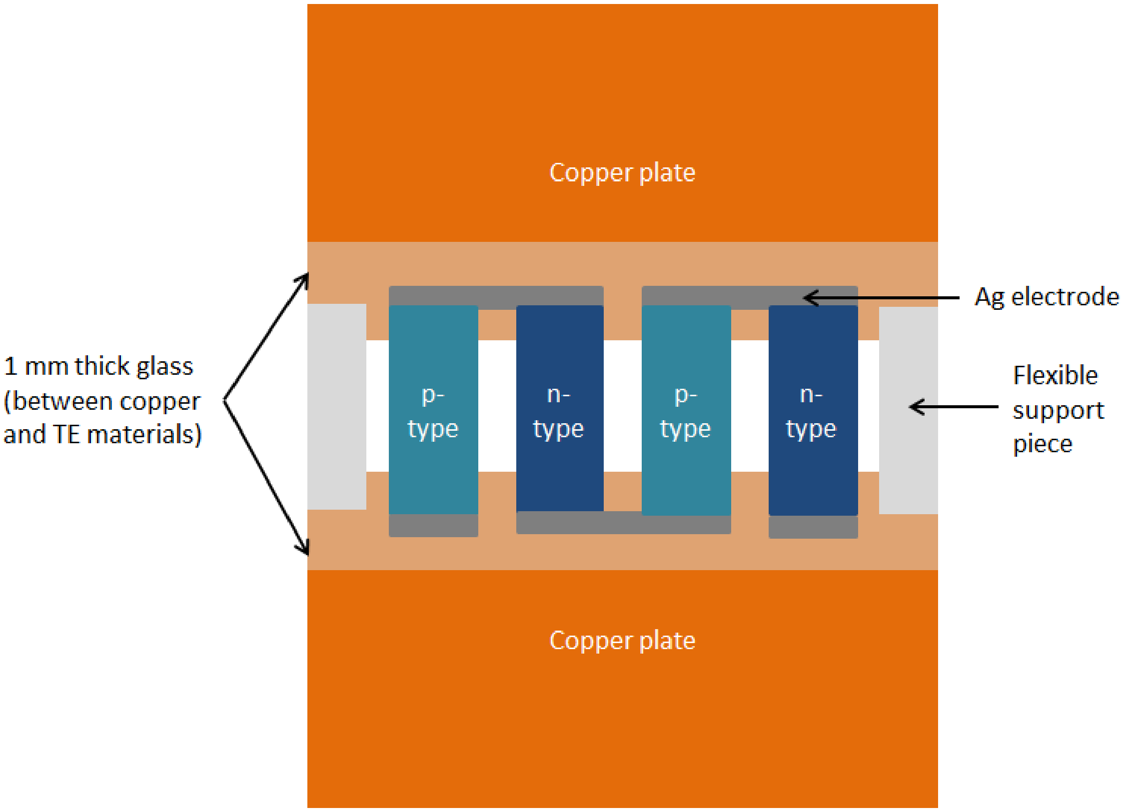

Figure 8.1 Schematic of prototype flexible thermoelectric device.

8.2.7 Prototype Thermoelectric Device Characterization

The thermoelectric performance of prototype devices is evaluated on a home-built setup in a nitrogen filled glove box. The top copper plate is placed on a hot plate while the bottom copper place is placed on a plastic stand. Microprobes are connected to the bottom left Ag electrode and the bottom right Ag electrode so that the device can be connected to various circuits, for which the current and voltages can be measured using an Agilent 4156C semiconductor parameter analyzer. The temperatures of the hot and cold sides are measured using two Craftsman manual ranging multimeters (model

82345). The thermocouples are embedded in Dow Corning 340 heat sink compound on the glass pieces to help ensure accurate temperature measurements.

Figure 8.2 Digital photograph of the measurement of a prototype thermoelectric device, with the hot plate, plastic stand, microprobes, thermocouples, and heat sink compound in view.

Generally, three types of measurements are completed on the devices: Seebeck voltage, power output, and bending tests. The Seebeck voltage is measured by first measuring the open circuit voltage of the device with the hot plate off. Then the hot plate is set to a few °C above room temperature, at least 15 minutes elapse in order to reach steady state, and the open circuit voltage is measured. The hot plate is set two to three °C higher and the process is repeated until the temperature difference measured is 20 °C. The power output is measured at a temperature difference of 20 °C using a set of resistors. A load resistor is placed in series with the thermoelectric device and the current through the resistor and voltage across the resistor are measured sequentially. The experiment is repeated with different load resistances. Finally, the effect of bending is observed by measuring the device resistance and then bending the device slightly. The device resistance is measured again and the device is straightened. This process is completed a total of ten times.

Figure 8.3 A prototype thermoelectric device in the bent position.

8.3 Results

8.3.1 Ag_2Te Nanocrystals

The materials obtained from the solution synthesis method are characterized using TEM and two trends are observed. First, the size-selection procedure is found to remove large aggregates of nanocrystals. Second, significant batch to batch variation is observed by comparing several batches. TEM images of nanocrystals obtained after the complete size selection procedure are shown in Figure 8.4.

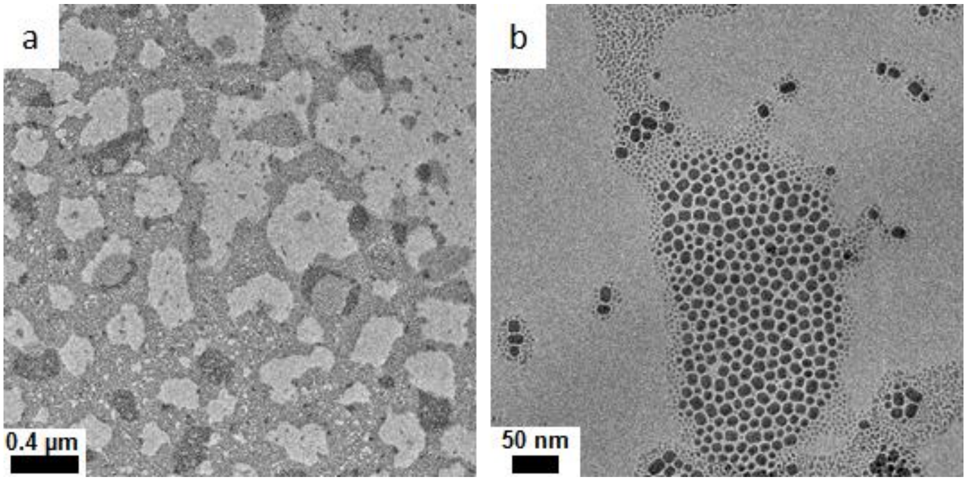

Figure 8.4 TEM images of nanocrystals obtained after the size selection procedure. (a) Low magnification. (b) Medium magnification.

There is essentially a bi-modal distribution of nanocrystals: small nanocrystals with sizes of approximately 1-3 nm and larger nanocrystals with sizes of approximately 9.3 ± 2.1 nm. There are approximately 1-2 nm gaps between adjacent nanocrystals.

Based on the washing procedure, waste sample #1 is comprised of material which precipitates relatively easily from the reaction solution even without the addition of an anti-solvent. Figure 8.5 shows that the material from waste sample #1 is comprised of micro scale aggregates of nanocrystals. The nanocrystals have sizes of approximately

15.6 ± 5.2 nm and no small nanocrystals (1-3 nm) are observed. Adjacent nanocrystals are separated by approximately 1-2 nm, which is surprising since they are clearly aggregated and are not readily re-dispersed in hexane.

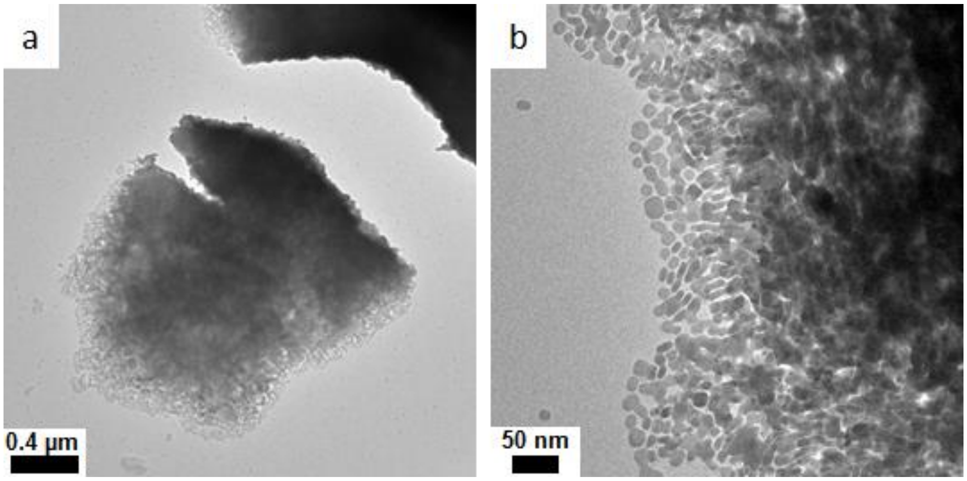

Figure 8.5 TEM images of material in waste sample #1. (a) Low magnification. (b) Medium magnification.

Waste sample #2 is also comprised of material that precipitates relatively easily even in the absence of an anti-solvent. The TEM images in Figure 8.6 show that the material is similar to that in waste sample #1. There are no micron size particles, but rather micron size aggregates of nanocrystals with sizes of approximately 13.6 ± 7.2 nm and inter-particle spacings of approximately 1-2 nm.

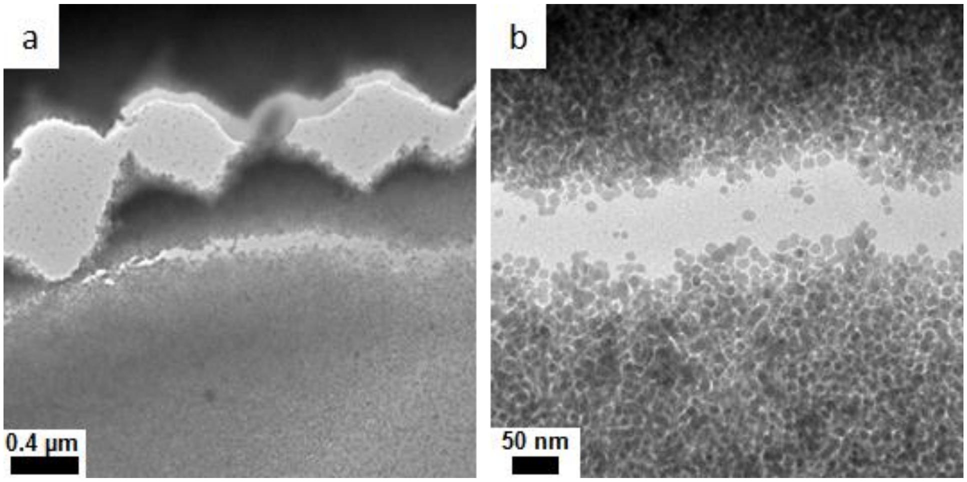

Figure 8.6 TEM images of material in waste sample #2. (a) Low magnification. (b) Medium magnification.

The batch to batch variation is shown in Figure 8.7. The TEM images reveal three general sizes of nanocrystals: small spheres (1-3 nm), medium rounded cubes and rectangular prisms (5-20 nm), and large oddly shaped particles (up to several hundred nanometers from end to end). Interestingly, these three types of nanocrystals are present in very different proportions in different batches. For example, batch 1 almost exclusively contains large nanocrystals, batch 2 has a mix of small, medium, and large nanocrystals, and batch 3 has only small and medium nanocrystals. The source of this batch to batch variation remains unclear and could be the subject of further research.

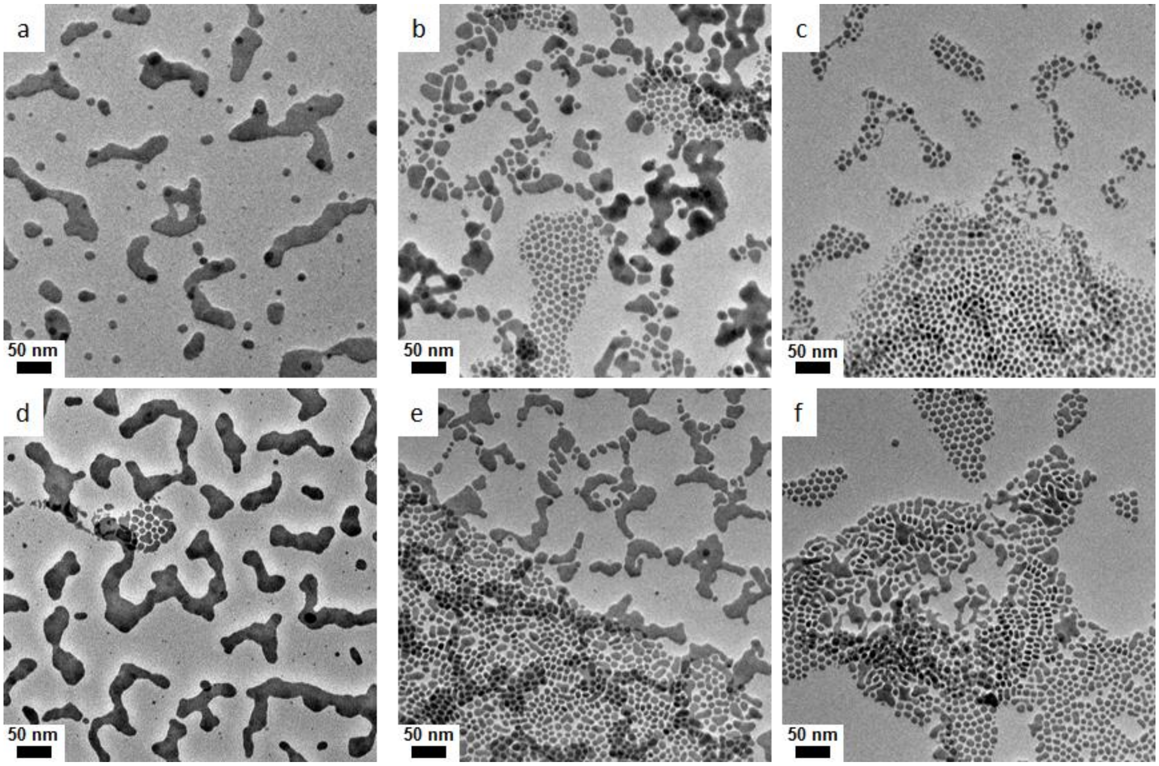

Figure 8.7 TEM images of nanocrystals obtained after the size selection procedure. (a) Batch 1. (b) Batch 2. (c) Batch 3. (d) Batch 4. (e) Batch 5. (f) Batch 6.

8.3.2 Structure and Composition of Coated Nylon

Using SEM, the Sefar nylon mesh is found to be comprised of interwoven nylon fibers, with a clear anisotropy in the weave pattern as shown in Figure 8.8. In the vertical direction, there are pairs of fibers woven together. Therefore, electrical transport properties are specified as being either parallel with these pairs of fibers (2 par) or perpendicular to these pairs of fibers (2 perp).

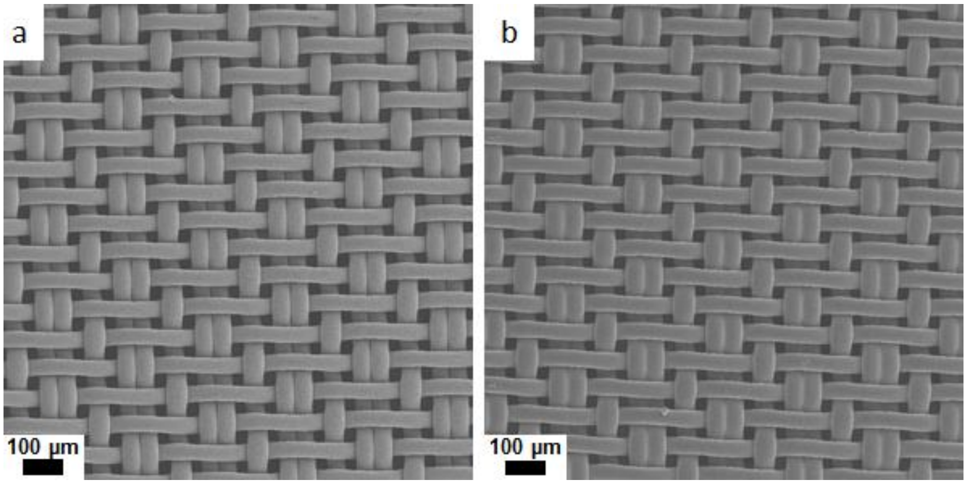

Figure 8.8 SEM images of nylon mesh, showing mesh structure. (a) Before cleaning. (b) After cleaning.

The cleaning procedure apparently has no effect on the overall structure of the mesh. However, higher magnification images of the fiber surface before and after cleaning in Figure 8.9 reveal the cleaning effect. Prior to cleaning, the fibers are quite smooth as suggested by the minimal contrast variation in the secondary electron image. After cleaning, the fibers are rough with omnipresent features with sizes below 100 nm. In previous literature, these features are shown to be the direct result of 30 minutes of oxygen plasma cleaning.[378] This increased surface roughness combined with the removal of a weak cohesive layer and surface functionalization described in literature are expected to result in improved nanoparticle adhesion during the dip coating procedure.[374,379,380]

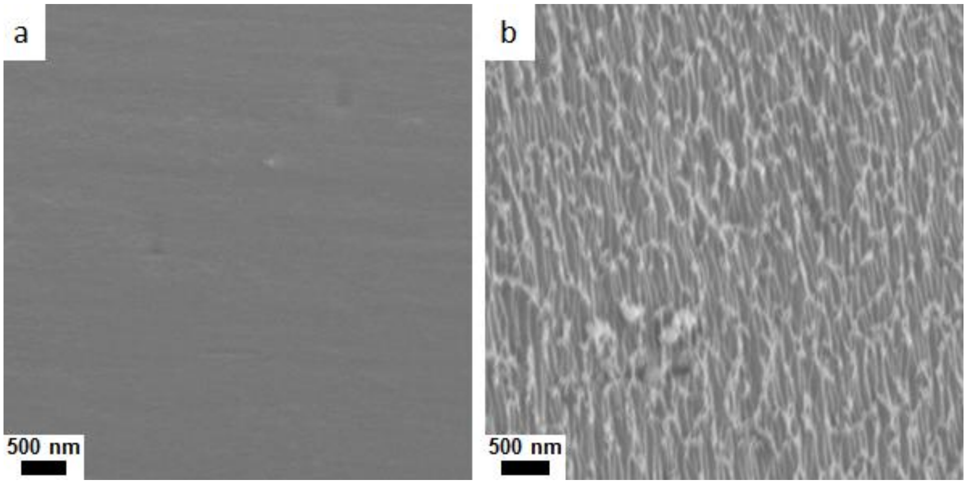

Figure 8.9 SEM of nylon mesh, showing the fiber surface. (a) Before cleaning. (b) After cleaning.

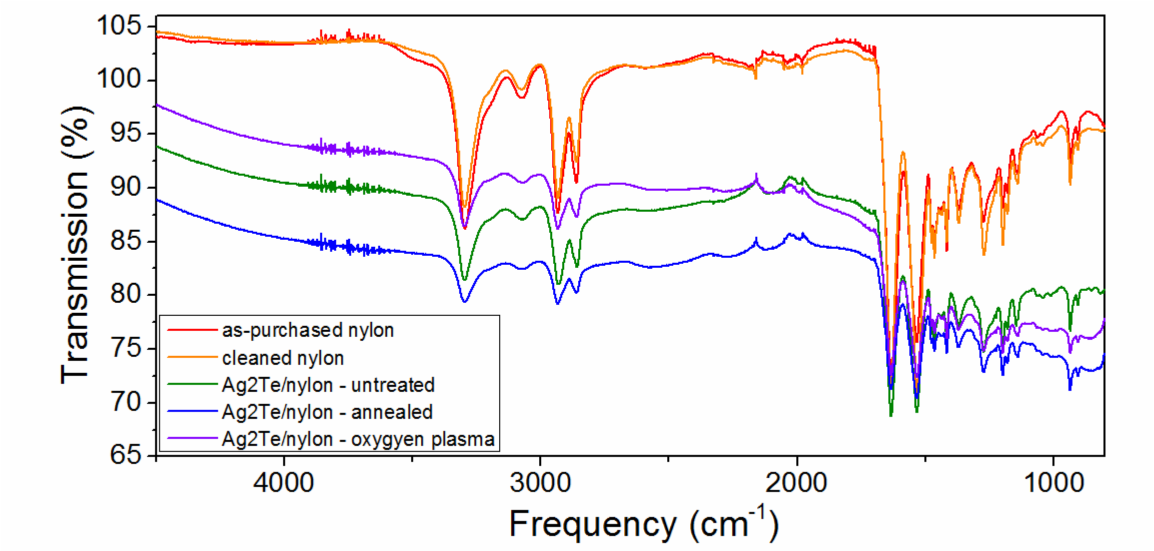

Figure 8.10 FTIR spectra of nylon and coated nylon samples.

Given the significant effect of cleaning on the nylon fiber surface, it is worthwhile to observe the fibers using attenuated total reflectance Fourier transform infrared spectroscopy (FTIR). As shown in Figure 8.10, the FTIR spectrum of the as-purchased nylon and the cleaned nylon are essentially the same; both share nearly all minima observed in previous studies on nylon 6/6.[374,381] Interestingly, the C=O stretch observed at 1731 cm^{-1} is not observed in the present study. Furthermore, the effect of oxygen plasma treatment on the C-O stretch at 1234 cm^{-1} observed previously is also not observed here.[374] This could be due to the loss of surface functionalization during the time between oxygen plasma treatment and FTIR analysis.[379]

After completing 50 cycles of the dip coating procedure, the nylon mesh possesses a coating as shown by the lighter regions in Figure 8.11a. The coating does not fully cover the nylon and possesses many micro scale cracks. The treatment methods exacerbate these issues as shown in Figure 8.11b-c for the nylon mesh after annealing and oxygen plasma treatment, respectively.

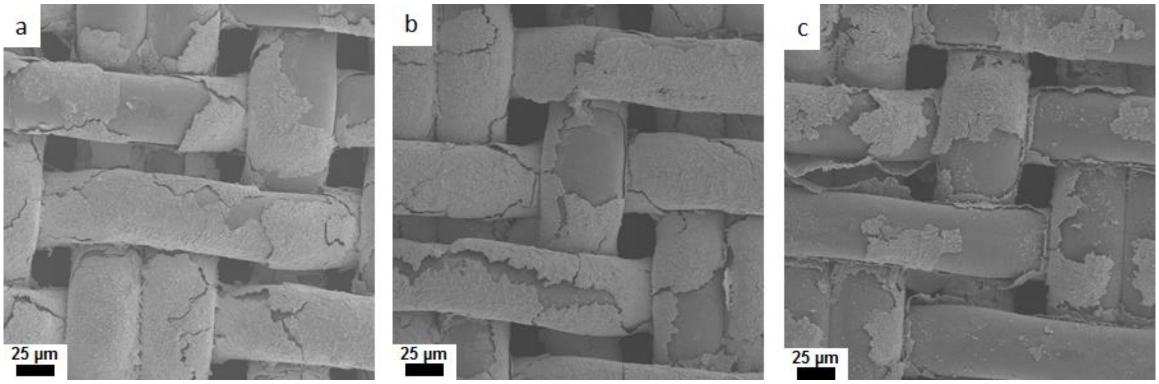

Figure 8.11 Medium magnification SEM images of Ag_2Te nanocrystal coated nylon. (a) Untreated. (b) Annealed. (c) Oxygen plasma treated.

The same three coatings are shown in Figure 8.12 at higher magnification. The coating surface of the untreated sample possesses distinguishable particles that are smaller than 100 nm throughout the entire image. The coating surface of the annealed sample does not possess widespread sub-100 nm features, but has smooth regions with dimensions greater than 0.5 µm. The annealed sample surface also has numerous pores with sizes of approximately 100-400 nm. Thus, it appears that annealing causes the nanocrystals to sinter and form a more continuous solid phase with larger pores, which is a similar phenomenon to that observed in annealed PbTe nanocrystal coatings as described in chapter 7. The coating surface of the oxygen plasma treated sample is unique in that it possesses large smooth regions, 100-400 nm pores, and sub-100 nm particles.

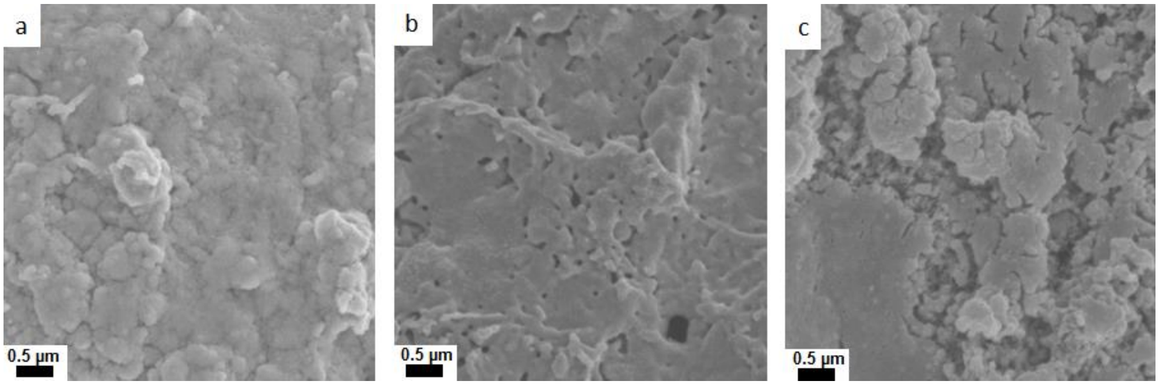

Figure 8.12 High magnification SEM images of Ag_2Te nanocrystal coated nylon, showing the coating surfaces. (a) Untreated. (b) Annealed. (c) Oxygen plasma treated.

Elemental mapping in Figure 8.13, Figure 8.14, and Figure 8.15 shows that for all three types of samples, the lighter contrast regions in the secondary electron images do indeed correspond to regions in which Ag and Te are present in large concentrations. Meanwhile, the darker contrast regions in the secondary electron images correspond to regions in which Ag and Te are absent and carbon exists on the surface instead, which is indicative of nylon. The elemental maps in Figure 8.13 and Figure 8.14 also make it clear that the Ag_2Te coating fills some of the inter-fiber pores in the nylon mesh.

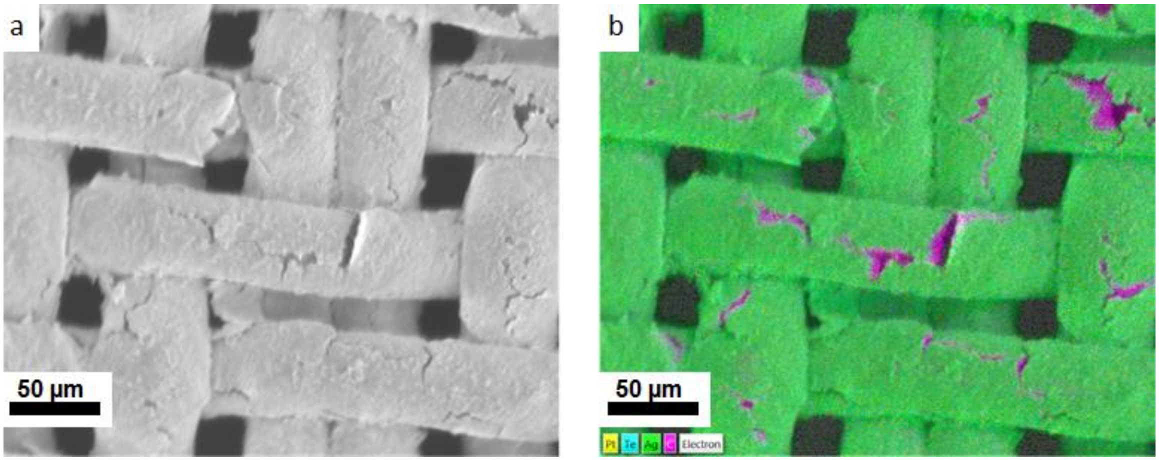

Figure 8.13 Untreated Ag_2Te coated nylon. (a) Secondary electron image. (b) Elemental map.

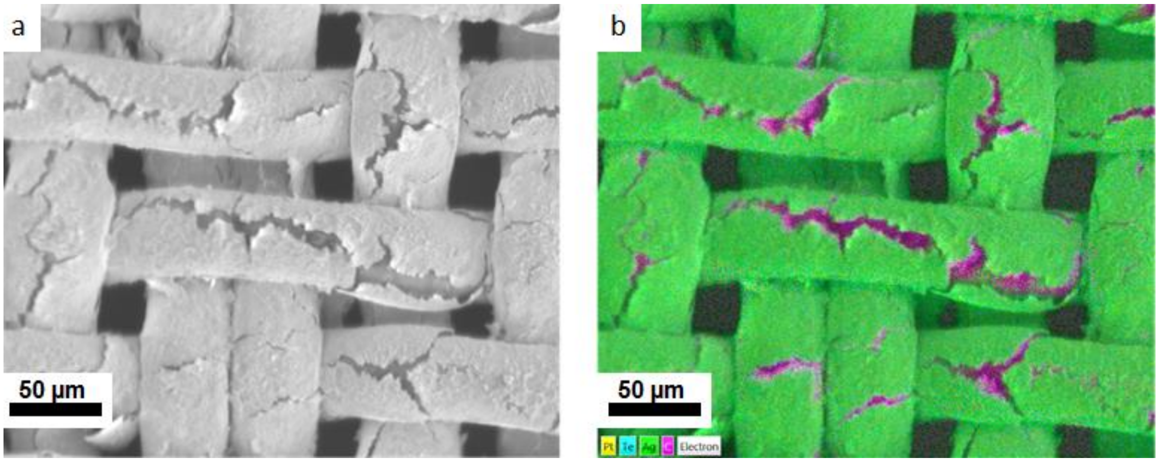

Figure 8.14 Annealed Ag$_2$Te coated nylon. (a) Secondary electron image. (b) Elemental map.

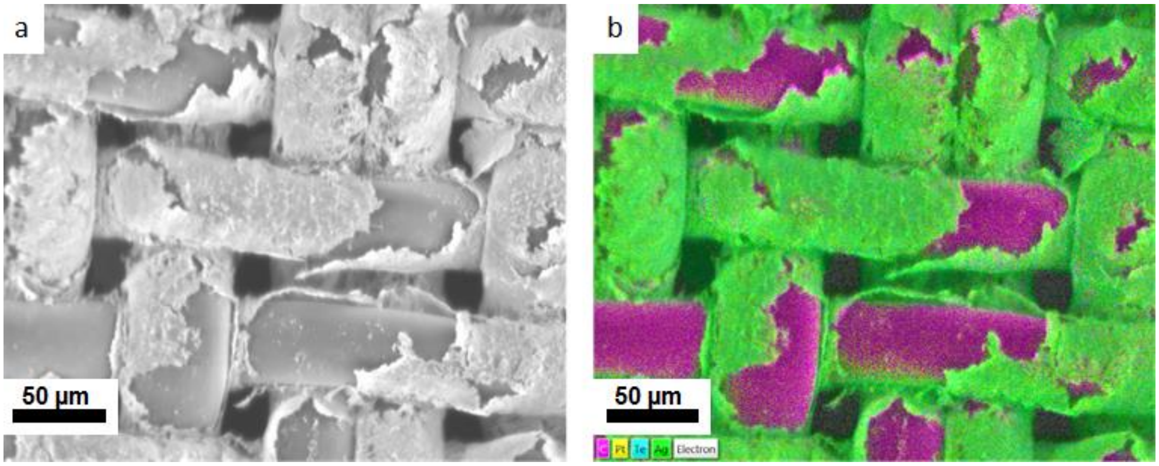

Figure 8.15 Oxygen plasma treated Ag$_2$Te coated nylon. (a) Secondary electron image. (b) Elemental map.

According to quantitative elemental analysis of the coated nylon, the Ag:Te ratio is 2.11 ± 0.03, 2.08 ± 0.01, and 3.86 ± 0.29 for the untreated, annealed, and oxygen plasma treated samples. Thus, the untreated and annealed samples possess compositions very similar to that expected for stoichiometric Ag$_2$Te, while the oxygen plasma treated sample has a considerable amount of excess Ag. According to the Ag-Te phase diagram, there is no stable phase of Ag-Te with a Ag:Te ratio of greater than two.[382] Therefore, while the off-stoichiometry observed for the untreated and annealed samples could perhaps be explained by the large surface to volume ratio of both the nanocrystals and the thin film coatings, the extent of off-stoichiometry for the oxygen plasma treated sample is likely associated with the presence of a pure Ag phase.

XRD analysis provides additional evidence that the untreated and annealed samples are pure phase Ag_2Te and the oxygen plasma treated sample is a combination of Ag_2Te and Ag. While the signal to noise ratios for such thin film samples are low, several of the main diffraction peaks associated with monoclinic Ag_2Te such as those associated with $(21\bar{1})$, (012), $(31\bar{2})$, and many other planes are present in all three samples. Furthermore, the diffraction peaks associated with the (111) and (220) planes of Ag are visible in the oxygen plasma treated sample and absent in the other samples.

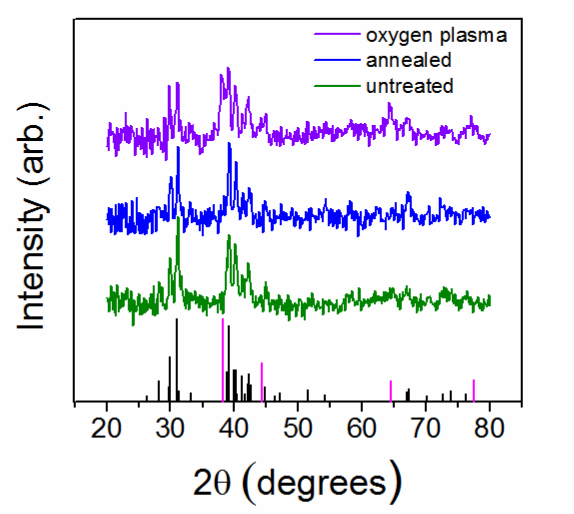

Figure 8.16 XRD patterns of coated nylon samples. Black standard lines are Ag_2Te (JCPDS # 01-081-1820). Magenta standard lines are Ag (JCPDS # 01-089-3722).

The formation of Ag metal during the oxygen plasma treatment is necessarily associated with the loss of Te from Ag_2Te because no Ag source is present in the oxygen plasma chamber during operation. According to previous studies, oxygen plasma treatment is capable of inducing a reaction between oxygen and gaseous Te to form films of TeO_2.[383–385] Meanwhile, even high surface area Ag nanoparticles have been shown to be resistant to oxidation during oxygen plasma treatment.[386,387] Furthermore, Te has a vapor pressure that is many orders of magnitude larger than that of Ag across a broad range of temperatures.[265,388] Considering all of this, it is likely that the low pressure environment and high energy plasma cause Te to preferentially sublime and react with oxygen to form TeO_2, which deposits away from the coated nylon and leaves the coating rich in Ag, which naturally leads to the phase segregation of Ag and Ag_2Te. Thus, the oxygen plasma treatment acts as a selective etch process.[389]

As a final note about the effect of the treatment methods, the FTIR results in Figure 8.10 show that the signatures associated with nylon are still present after the coating and treatment process. Thus, the coating and treatment processes do not appear to affect the underlying nylon chemical structure.

SEM images of the PEDOT:PSS coated nylon mesh made from a solution containing 5 % ethylene glycol are shown in Figure 8.17. In the medium magnification image, the contour of the nylon fibers is faintly visible, yet the space in between the fibers is filled by the PEDOT:PSS. The high magnification image of the PEDOT:PSS film shows no perceptible surface roughness.

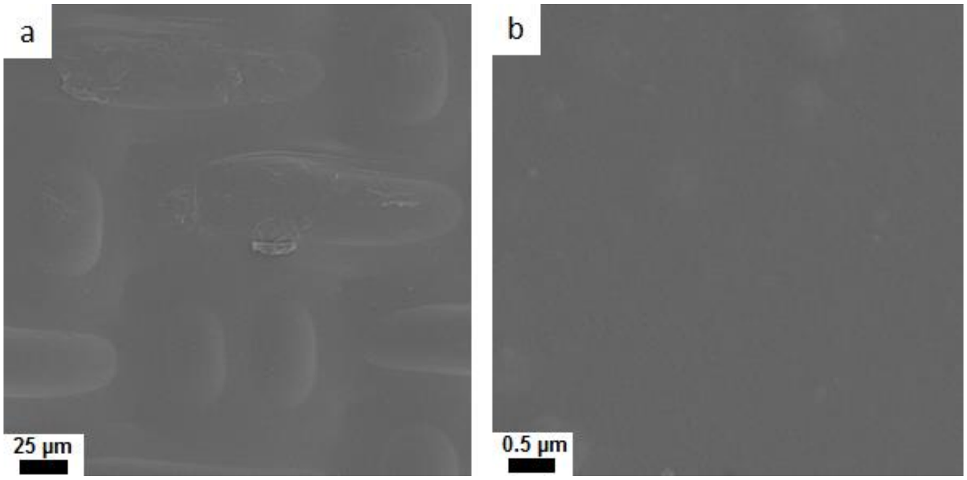

Figure 8.17 SEM images of the PEDOT:PSS coated nylon. (a) Medium magnification. (b) High magnification.

8.3.3 Electrical Properties of Coated Nylon

8.3.3.1 Effect of Nanocrystal Size and Number of Coating Cycles

While it is generally desirable to know the electrical conductivity of thermoelectric materials in order to calculate ZT, the complex geometry and anisotropy of coated nylon mesh makes determination of electrical conductivity prohibitively difficult. Instead, the sheet resistance is used here to compare coated nylon mesh samples. The sheet resistance of untreated Ag_2Te coated nylon is found to be strongly affected by two factors: nanocrystal size distribution and number of coating cycles.

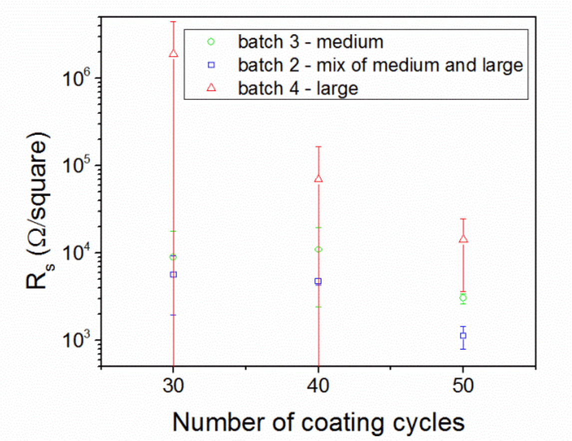

Figure 8.18 Sheet resistance of untreated Ag_2Te nanocrystal coated nylon mesh measured in the 2 par orientation made using the three-step dip coating method. The batch numbers in the legend correspond with those in Figure 8.7.

As shown in Figure 8.18 for samples measured in the 2 par orientation, the sheet resistance is considerably lower for material made using medium-sized nanocrystals or from a mixture of medium and large-sized nanocrystals. Based on the TEM images in

Figure 8.7, one plausible explanation for this trend is that the large nanocrystals are so irregularly shaped that it is not possible for them to pack efficiently enough to have a large amount of inter-nanocrystal contact and high electrical conductivity. It could be that the mixture of medium and large nanocrystals has a low sheet resistance because the medium-size nanocrystals fill the voids between the inefficiently packed large nanocrystals to create an effective network for charge transport.

The results in Figure 8.18 also show that the sample sheet resistance generally degreases with increasing number of coating cycles. However, this is not a monotonic trend for all samples. The plot also shows that the variation in the measurement results is extremely large, especially for the sample made from large nanocrystals. From SEM imaging of large areas (not shown), it appears that the variation in sheet resistance could be associated with coating non-uniformity.

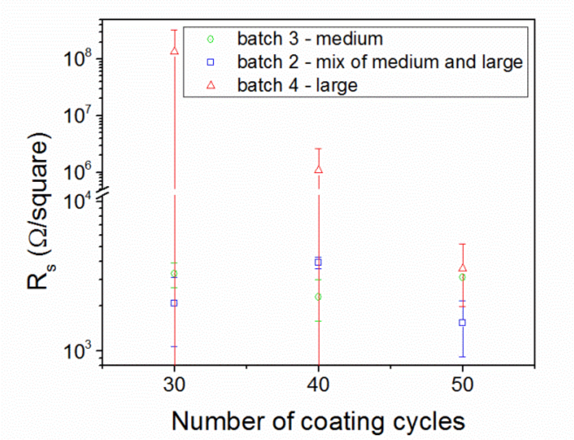

Figure 8.19 Sheet resistance of untreated Ag_2Te nanocrystal coated nylon mesh measured in the 2 perp orientation made using the three-step dip coating method. The batch numbers in the legend correspond with those in Figure 8.7.

In Figure 8.19, sheet resistance results for the same nine coated nylon mesh samples are shown as measured in the 2 perp orientation. Similar trends are observed. Another important observation is that for both the 2 par and 2 perp orientations, the sample made using a mixture of medium and large nanocrystals dip coated 50 times has the lowest sheet resistance. Therefore, further dip coating and treatment studies employed mixtures of large and medium nanocrystals and generally focused on material dip coated 50 times.

8.3.3.2 Effect of Second and Third Dip Coating Step

In order to determine the effect of the second and third dip coating steps, the hydrazine/ethanol soak and the ethanol rinse, experiments are performed in which one or both of these steps is eliminated. Given that mixtures of medium and large nanocrystals result in coated nylon samples with low sheet resistance, only batches with nanocrystal size distributions similar to that of batch 2 are used. First, the results from Figure 8.18 and Figure 8.19 for the samples made from batch 2 using the three-step dip coating procedure are re-plotted in Figure 8.20. The estimated Seebeck coefficients of materials made using the three-step dip coating procedure are generally in the range of -70 to -90 μV/K prior to treatment, which is similar to hydrazine treated Ag_2Te nanocrystal films reported in literature.[367]

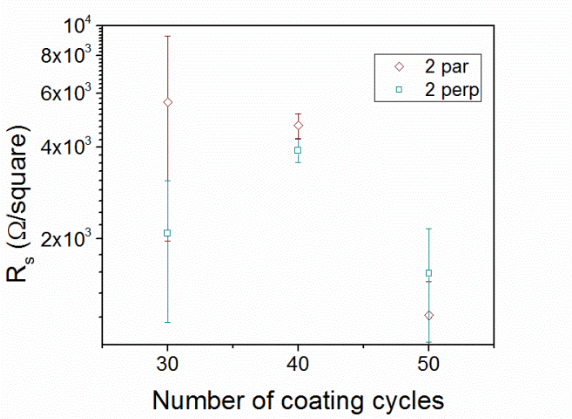

Figure 8.20 Sheet resistance of untreated Ag_2Te nanocrystal coated nylon mesh made using the three-step dip coating method and batch 2.

Next, the results for the samples made using a two-step dip coating procedure, with the hydrazine/ethanol soak eliminated, are presented in Figure 8.21. The lack of error bars indicates that only one sample is measured per plotted point. Interestingly, the sheet resistance generally increases with additional coating cycles, with the samples coated 50 times having the largest sheet resistances. Also, the estimated Seebeck coefficients of these materials are generally in the range of +71 to +78 µV/K. Thus, the hydrazine/ethanol dip coating step has a significant effect on the electrical properties of the coated nylon, resulting in n-type behavior. However, the hydrazine/ethanol step does not result in a significant reduction in sheet resistance, which is quite unlike the phenomenon observed for PbTe and PbSe nanocrystal films. [116,125]

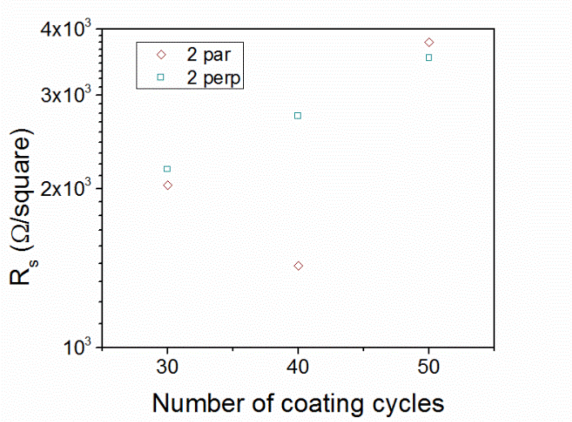

Figure 8.21 Sheet resistance of untreated Ag_2Te nanocrystal coated nylon mesh made using the two-step dip coating method and a batch of similar size distribution to that of batch 2.

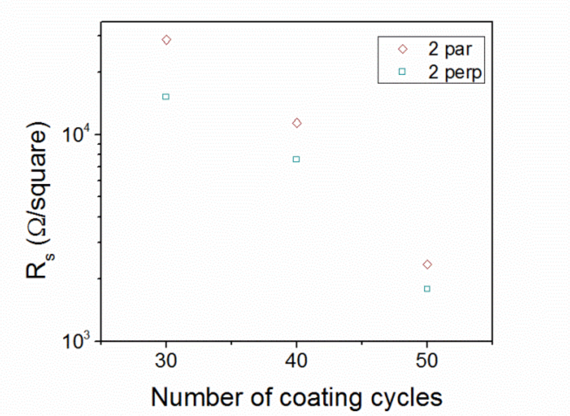

Figure 8.22 Sheet resistance of untreated Ag_2Te nanocrystal coated nylon mesh made using the one-step dip coating method and a batch of similar size distribution to that of batch 2.

Finally, the results for the samples made using a one-step dip coating procedure, with both the hydrazine/ethanol soak and the ethanol rinse eliminated, are presented in Figure 8.22. The sheet resistance monotonically decreases with increasing number of dip coating cycles for both the 2 par and 2 perp orientations. After only 30 cycles, the sheet resistance is around 3-10 times higher than samples made using the two and three-step procedures. However, after 50 cycles, the sheet resistances of the one-step dip coated samples are less than two times higher than samples made using the two and three-step procedures. The estimated Seebeck coefficients of these films are +286 to +290 µV/K, which represent the highest magnitudes observed of all materials in this study on coated nylon. This raises interesting questions regarding conduction mechanisms in these nanocrystals films. These results also suggest that the traditionally used three-step dip coating procedure could be replaced with a much simpler one-step procedure, which could be automated fairly easily for higher throughput experimentation in future research.

8.3.3.3 Effect of Annealing and Oxygen Plasma Treatment

The electrical properties of untreated samples of Ag_2Te nanocrystals coated onto nylon mesh are impressive in some respects. Compared to PbTe nanocrystal coated glass fiber composites which have undetectable electrical conductance prior to annealing, Ag_2Te coated nylon samples are quite conductive prior to annealing or other treatment. Still, treatment methods offer an opportunity to enhance the properties of Ag_2Te nanocrystal coated nylon further.

As specified earlier, untreated Ag_2Te coated nylon samples made using the three-step coating approach with a mixture of medium and large nanocrystals possessed sheet resistances of approximately 1.6 – 1.8 kΩ/square and estimated room temperature Seebeck coefficients in the range of -70 to -90 µV/K. A modified version of the power factor, ${S^2}/{R_s}$, where R_s is the sheet resistance, takes the value of 3.8 ± 1.0 $\mu V^2 \square / K^2 \Omega$ for these samples.

After annealing in vacuum at 127 °C for 30 minutes, the sheet resistance drops by a factor of approximately two and the Seebeck coefficient changes from negative to the range of +65 to +75 µV/K. The reduction in sheet resistance is likely associated in part with the more continuous film observed by SEM as shown in Figure 8.12. The transformation from n-type to p-type is difficult to explain and could be associated with the nanoparticle surfaces and inter-particle bonding. The modified version of the power factor has a value of 5.8 ± 0.9 $\mu V^2\square/K^2\Omega$ for these samples. Therefore, annealing provides two benefits. First, flexible p-type materials are formed, which are necessary for the typical thermoelectric device architecture. Second, the modified power factor is increased.

After treating in an oxygen plasma cleaner for ten minutes, the sheet resistance drops by a factor of approximately 200 and the Seebeck coefficient changes to the range of -20 to -24 μV/K. These effects are likely associated with the presence of metallic Ag observed by XRD and suggested by EDS analysis. The room temperature Seebeck coefficient of pure Ag is in the range of +1.5 to +2.4 μV/K as compared with around -100 μV/K for stoichiometric Ag_2Te.[36,364,365] The electrical conductivity of pure Ag at room temperature is 6.25×10^5 S/cm as compared with the range of 0.3 to 2.5×10^3 S/cm for Ag_2Te.[364,365,390] Therefore the presence of Ag is expected to decrease the absolute value of the Seebeck coefficient and increase the electrical conductivity as observed. The modified version of the power factor has a value of 57 ± 11 $\mu V^2\square/K^2\Omega$ for these samples. Thus, the reduction in Seebeck coefficient is greatly outweighed by the reduction in sheet resistance.

8.3.3.4 PEDOT:PSS Coated Nylon

As-made samples of PEDOT:PSS coated onto nylon mesh showed excellent performance. Samples made using dispersions with DMSO and ethylene glycol both showed sheet resistances of around 2 Ω/□. This value is so low that the two-probe resistance measurement method could potentially induce significant error. MMR Seebeck measurements indicated Seebeck coefficients of +15 and +12.5 μV/K for samples made using dispersions with DMSO and ethylene glycol, respectively. These values are in a similar range to those found in literature for PEDOT:PSS treated with ethylene glycol or DMSO.[72,311,391,392] The material made using ethylene glycol as an additive is considered for further experimentation due to its higher Seebeck coefficient. The PEDOT:PSS coated nylon samples made using ethylene glycol as an additive have modified power factors of approximately 112 $\mu V^2 \square / K^2 \Omega$. Thus they represent an improvement over the annealed Ag_2Te nanocrystal coated nylon. Therefore, the PEDOT:PSS coated nylon samples are ultimately used in the second prototype thermoelectric device.

8.3.4 Prototype Thermoelectric Device Performance

Device #1, the first of two prototype thermoelectric devices is based on the Ag_2Te nanocrystal coated nylon samples with the highest values of the modified power factor. The p-type material is Ag_2Te nanocrystal coated nylon made by dip coating a mixture of large and medium nanocrystals 50 times and then annealing. The n-type material is the oxygen plasma treated version of the same.

The open circuit voltage generated by this four-leg device is shown in Figure 8.23 as a function of temperature difference. A linear relationship is observed, in accordance with the definition of the Seebeck coefficient and assuming it does not change significantly in the temperature range investigated. The slope of the best fit line is 356 μV/K. Theoretically, the slope should be equal to $2(S_p - S_n)$, which is 184 μV/K for device #1. The discrepancy is likely due to the inaccuracy of the MMR Seebeck measurement.

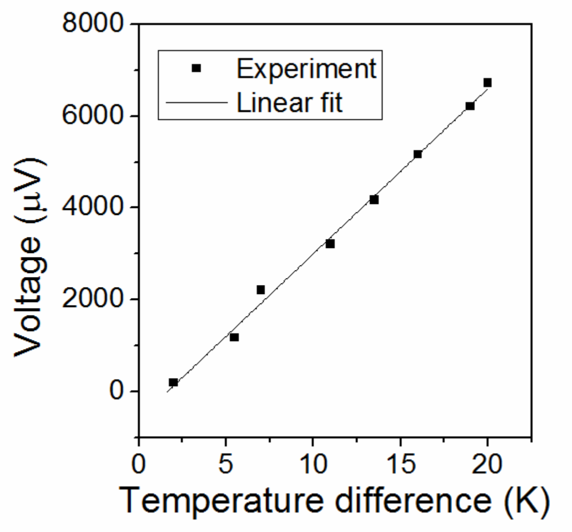

Figure 8.23 Open circuit voltage of device #1.

The voltage and power generated from a 20 °C temperature difference when device #1 is electrically connected to various load resistors is shown in Figure 8.24. As expected, the maximum in power output occurs when the resistance of the load is approximately matched with the initial resistance of the device (shown in Figure 8.25). The maximum output power of device #1 is 0.78 nW.

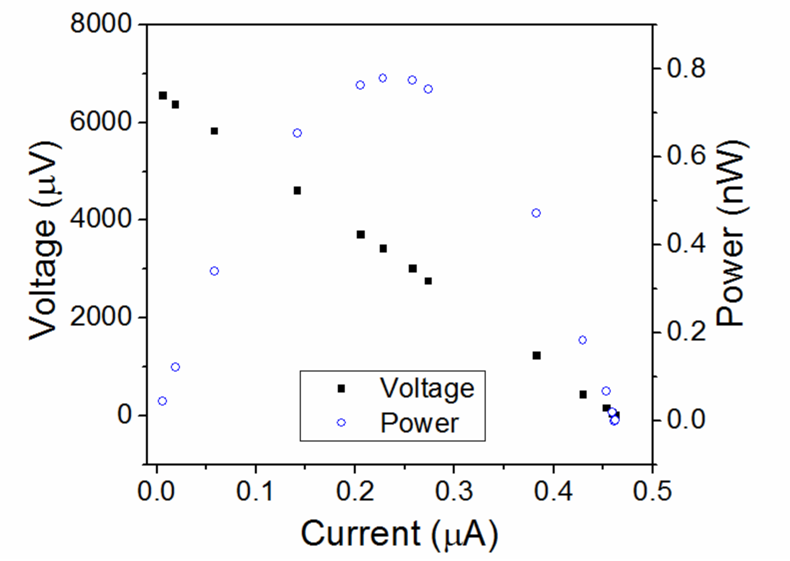

Figure 8.24 Voltage and power output of device #1 when connected to an external load.

As shown in Figure 8.25, the device experiences an increase in resistance due to bending. Considering the straight position, the device resistance increases by a factor of 1.44 due to the bending tests. Such an increase in resistance is not surprising considering the microstructure of the coated nylon as revealed in SEM images in Figure 8.11. Even before bending, the coating is cracked and partially peeled off of the nylon. Bending likely induces additional cracking and peeling. Future research should aim to mitigate this issue.

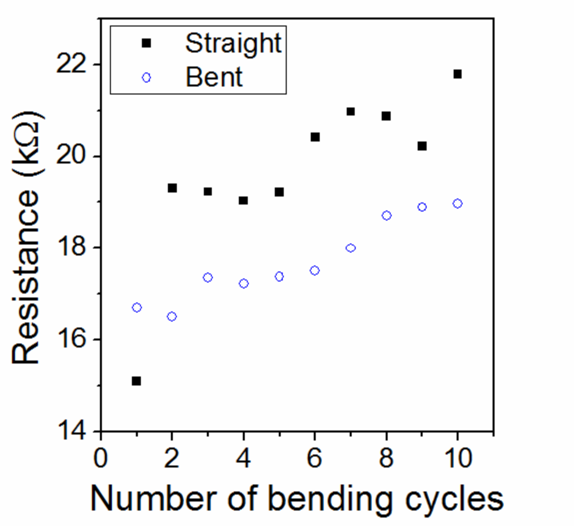

Figure 8.25 Effect of repeated bending on the resistance of device #1.

Device #2 is made using PEDOT:PSS coated nylon as the p-type material. As with device #1, the n-type material is Ag_2Te nanocrystal coated nylon made by dip coating a mixture of large and medium nanocrystals 50 times and then treating in an oxygen plasma cleaner for 30 minutes.

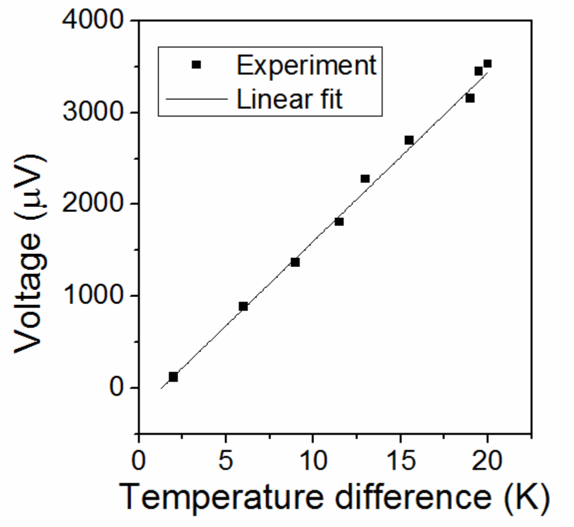

Figure 8.26 Open circuit voltage of device #2.

As illustrated by comparing the open circuit voltage results in Figure 8.23 and Figure 8.26, device #2 has a lower Seebeck voltage than device #1. Specifically, the Seebeck coefficient if device #2 is approximately 187 μV/K. This is similar to the value predicted theoretically using the MMR Seebeck measurements, 170 μV/K.

The voltage and power generated from a 20 °C temperature difference when device #2 is electrically connected to various load resistors is shown in Figure 8.27. As with device #1, the maximum in power output occurs when the resistance of the load is matched with the resistance of the device. The maximum output power of device #1 is 5.63 nW. Increased power output compared to device #1 is due to the approximately 27 times lower device resistance, which more than compensates for the reduced Seebeck voltage.

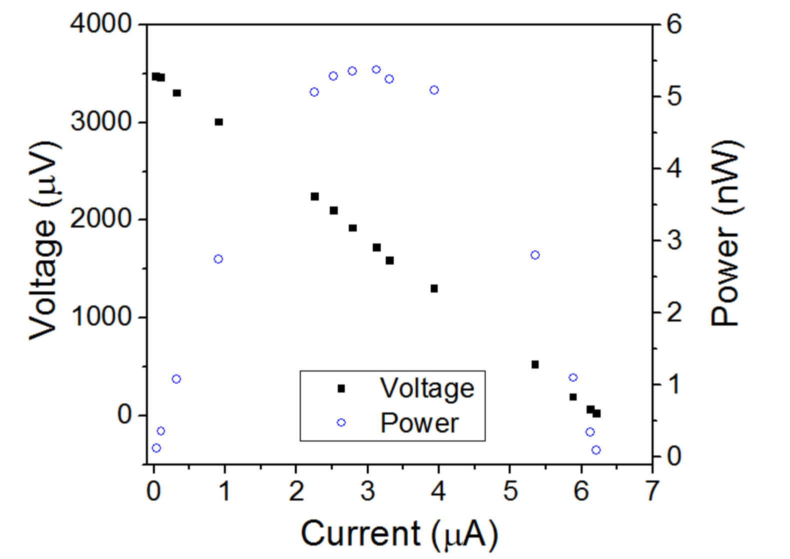

Figure 8.27 Voltage and power output of device #2 when connected to an external load.

The results for the bending test performed on device #2 are shown in Figure 8.28. The first bend causes a significant increase in the resistance, which could be associated with an unintentionally large amount of bending during the first cycle. After this first cycle, the resistance increase by around 1% over the next nine bending cycles, which is a significant improvement compared to device #1.

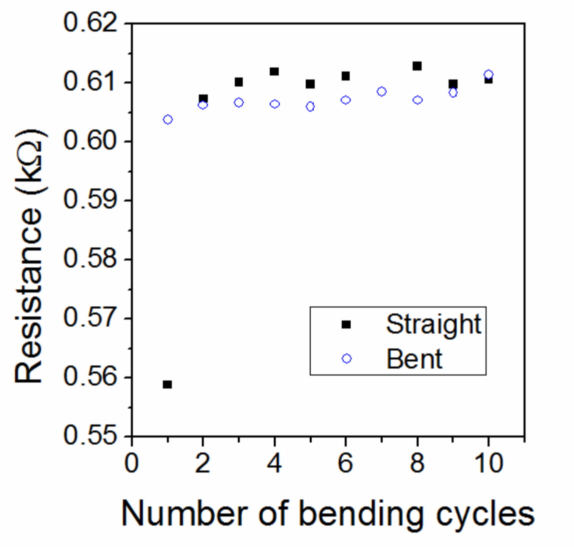

Figure 8.28 Effect of repeated bending on the resistance of device #2.

It is certainly noteworthy that the flexible thermoelectric devices comprised of Ag_2Te and conducting polymer coated nylon are partially locally optimized in this study. However, of even greater concern is how the current results compare with those of other flexible thermoelectric materials reported in literature. Usually, ZT is the appropriate figure of merit by which to compare thermoelectric materials. In the case of flexible thermoelectric composites, the measurement of electrical and/or thermal conductivity can be quite difficult as shown in chapter 7. Therefore, Table 8-1 shows the power output of several flexible thermoelectric devices described here and in literature. The power output is normalized by the cross section area perpendicular to the temperature gradient and is given as either the experimental or estimated value in a temperature difference of 20 K.

Table 8-1 Summary of flexible thermoelectric devices. Data from references 393 and 397 adapted with permission from the American Chemical Society. Copyright 2012 and 2013. See literature cited section for full reference details.

Device	p-type material	n-type material	Substrate	Power output (ΔT = 20 K) (W/m^2)
Ref. 31	Sb_2Te_3	Bi_2Te_3	Glass fiber	5.0
Ref. 393	$Bi_{0.5}Sb_{1.5}Te_3$-8 wt. % Te/epoxy	Metal	Polyimide	<4.7
Device #2	PEDOT:PSS	Oxygen plasma treated Ag_2Te nanocrystals	Nylon mesh	6.3×10^{-3}
Ref. 394	Carbon nanotube /polystyrene	Au	Polyethylene napthalate	4.5×10^{-3}
Ref. 395	Ag	Ni	Silica	3.9×10^{-3}
Ref. 396	Carbon nanotubes	Doped carbon nanotubes	Polytetra fluoroethylene and paper	3.8×10^{-3}
Ref. 397	Carbon nanotubes	Carbon nanotubes	Polylvinylidine fluoride	3.1×10^{-3}
Device #1	Annealed Ag_2Te nanocrystals	Oxygen plasma treated Ag_2Te nanocrystals	Nylon mesh	1.8×10^{-3}
Ref. 363	PbTe nanocrystals	I-doped PbTe nanocrystals	Glass fiber	2.6×10^{-4}
Ref. 398	PEDOT:PSS	Ag	Polyethylene terephthalate	$<3.0 \times 10^{-12}$

The devices with the largest power outputs are those which are comprised of very large percentages of the $(Bi,Sb)_2Te_3$ class of materials. Meanwhile, of the devices comprised of relatively low percentages of telluride materials, device #2 from the present study fairs quite well. Future research in the area would benefit from the use of the composition as an additional metric by which to compare flexible thermoelectric composites.

8.4 Conclusions

Solution synthesized Ag_2Te nanocrystals are dip coated onto nylon and the resulting composites are found to be electrically conductive prior to treatment. The electronic properties of Ag_2Te coated nylon are improved by annealing or treating in an oxygen plasma cleaner, despite the increased amount of cracking and peeling in the film. A device made using p-type Ag_2Te nanocrystal coated nylon and n-type Ag_2Te nanocrystal coated nylon produces 0.78 nW in a 20 °C temperature difference. The high electrical resistance of the p-type Ag_2Te nanocrystal coated nylon allows for the device performance to be improved by using PEDOT:PSS coated nylon as a p-type material instead. The electrical power output of a device made using p-type PEDOT:PSS coated nylon and n-type Ag_2Te nanocrystal coated nylon is 5.63 nW. Normalized by area, the power output of device #2 is the best of the flexible thermoelectric devices that contain a small percentage of telluride materials. The thermoelectric properties of the conducting polymer coated nylon are the best observed in this study. However, low resistance films of n-type Ag_2Te nanocrystals could prove necessary for flexible thermoelectric devices as air stable n-type organic thermoelectric materials are difficult to obtain.[307]

LITERATURE CITED

LITERATURE CITED

1. NETL. Key Issues & Mandates: Secure & Reliable Energy Supplies. (2005).

2. Exxon Mobil. *2009 Summary Annual Report*. (2009). at <http://ir.exxonmobil.com/phoenix.zhtml?c=115024&p=irol-reportsannual>

3. Exxon Mobile. *Summary Annual Report 2013*. (2013). at <http://ir.exxonmobil.com/phoenix.zhtml?c=115024&p=irol-reportsannual>

4. *Factsheet: Paving the Way Towards Cleaner, More Efficient Trucks*. (2011). at <http://www.nhtsa.gov/fuel-economy>

5. Pavley, F. & Nunez, F. *California Global Warming Solutions Act of 2006*. (2006).

6. Baxter, J. *et al.* Nanoscale Design to Enable the Revolution in Renewable Energy. *Energy Environ. Sci.* **2,** 559–588 (2009).

7. Lawrence Livermore National Laboratory. *2013 U.S. Energy Flow Chart*. (2014). at <https://flowcharts.llnl.gov/>

8. Vining, C. B. An Inconvenient Truth About Thermoelectrics. *Nat. Mater.* **8,** 83–85 (2009).

9. Yang, J. & Stabler, F. R. Automotive Applications of Thermoelectric Materials. *J. Electron. Mater.* **38,** 1245–1251 (2009).

10. Williams, J. H. *et al.* The Technology Path to Deep Greenhouse Gas Emissions Cuts by 2050: The Pivotal Role of Electricity. *Science.* **335,** 53–59 (2012).

11. United Nations Environment Programme. *Handbook for the Montreal Protocol on Substances that Deplete the Ozone Layer*. (2012). at <http://ozone.unep.org/new_site/en/resources.php?pt_id=3>

12. United States Environmental Protection Agency. *Section 608 of the Clean Air Act : Stationary Refrigeration and Air Conditioning*. (2010). at <http://www.epa.gov/ozone/title6/608/index.html>

13. Brown, D. R., Stout, T. B., Dirks, J. A. & Fernandez, N. The Prospects of Alternatives to Vapor Compression Technology for Space Cooling and Food Refrigeration Applications. *Energy Eng.* **109,** 7–20 (2012).

14. Snyder, G. J. & Toberer, E. S. Complex Thermoelectric Materials. *Nat. Mater.* **7,** 105–114 (2008).

15. Joffe, A. F. The Revival of Thermoelectricity. *Sci. Am.* **199,** 31–37 (1958).

16. LaLonde, A. D., Pei, Y., Wang, H. & Jeffrey Snyder, G. Lead Telluride Alloy Thermoelectrics. *Mater. Today* **14,** 526–532 (2011).

17. Jayadev, T. S., Henderson, J., Finegold, J. & Benson, D. *Conversion System Overview Assessment*. (1979).

18. Thermoelectric Coolers for Telecom Industry. at <http://rmtltd.ru/products/temodules/ml/>

19. Telecommunications. (2014). at <http://www.marlow.com/industries/telecommunications.html>

20. Riffat, S. B. & Ma, X. Thermoelectrics: A Review of Present and Potential Applications. *Appl. Therm. Eng.* **23,** 913–935 (2003).

21. Bell, L. E. Cooling, Heating, Generating Power, and Recovering Waste Heat with Thermoelectric Systems. *Science.* **321,** 1457–1461 (2008).

22. Climate seats. at <http://www.gentherm.com/en/page/climate-seats>

23. Lofy, J. & Bell, L. Thermoelectrics for Environmental Control in Automobiles. *21st Int. Conf. Thermoelectr.* 471–476 (2002). at <http://ieeexplore.ieee.org/xpls/abs_all.jsp?arnumber=1190362>

24. Snyder, G. J. Small Thermoelectric Generators. *Interface* **17,** 54–56 (2008).

25. Rowe, D. M. Thermoelectrics, an Environmentally-Friendly Source of Electrical Power. *Renew. Energy* **16,** 1251–1256 (1999).

26. Fairbanks, J. W. Thermoelectric Developments for Vehicular Applications. (2006).

27. Fairbanks, J. W. Solid-State Energy Conversion Overview. (2010).

28. Hendricks, T. J., Hogan, T., Case, E. D. & Cauchy, C. J. *Advanced Soldier Thermoelectric Power System for Power Generation from Battlefield Heat Sources*. (2010).

29. Starner, T. Human-Powered Wearable Computing. *IBM Syst. J.* **35,** 618–629 (1996).

30. Leonov, V. & Vullers, R. J. M. Wearable Thermoelectric Generators for Body-Powered Devices. *J. Electron. Mater.* **38,** 1491–1498 (2009).

31. Kim, S. J., We, J. H. & Cho, B. J. A Wearable Thermoelectric Generator Fabricated on a Glass Fabric. *Energy Environ. Sci.* **7,** 1959–1965 (2014).

32. Weber, J. *et al.* Coin-Size Coiled-up Polymer Foil Thermoelectric Power Generator for Wearable Electronics. *Sensors Actuators A Phys.* **132,** 325–330 (2006).

33. Yazawa, K. *et al.* Thermoelectric Topping Cycles for Power Plants to Eliminate Cooling Water Consumption. *Energy Convers. Manag.* **84,** 244–252 (2014).

34. Hendricks, T. & Choate, W. T. *Engineering Scoping Study of Thermoelectric Generator Systems for Industrial Waste Heat Recovery*. (2006).

35. Kraemer, D. *et al.* High-Performance Flat-Panel Solar Thermoelectric Generators with High Thermal Concentration. *Nat. Mater.* **10,** 532–538 (2011).

36. Ioffe, A. F. *Semiconductor Thermoelements and Thermoelectric Cooling*. (Infosearch, 1957).

37. Schaevitz, S. B. A MEMS Thermoelectric Generator. (2000).

38. Yadav, G. Design and Assembly of Nanostructured Complex Metal Oxide Materials for the Construction of Batteries and Thermoelectric Devices. (2013).

39. Cadoff, I. B. & Miller, E. in *Thermoelectr. Mater. Devices* (Cadoff, I. B. & Miller, E.) 18–30 (Reinhold Publishing Corporation, 1960).

40. Snyder, G. J. in *Energy Harvest. Technol.* (Priya, S. & Inman, D. J.) 325–336 (Springer Science+Business Media, LLC, 2009). at <http://link.springer.com/10.1007/978-0-387-76464-1>

41. Yee, S. K., LeBlanc, S., Goodson, K. E. & Dames, C. $ per W Metrics for Thermoelectric Power Generation: Beyond ZT. *Energy Environ. Sci.* **6,** 2561–2571 (2013).

42. Shakouri, A. Recent Developments in Semiconductor Thermoelectrics. *Annu. Rev. Mater. Res.* **41,** 399–431 (2010).

43. Ravich, Y. I., Efimova, B. A. & Smirnov, I. A. *Semiconducting Lead Chalcogenides*. (Plenum Press, 1970).

44. Airapetyants, S. V., Vinogradova, M. N., Dubrovskaya, I. N., Kolomoets, N. V. & Rudnik, I. M. Structure of the Valence Band of Heavily Doped Lead Telluride. *Sov. Phys. - Solid State* **8,** 1069–1074 (1966).

45. Crocker, A. & Rogers, L. Interpretation of the Hall Coefficient, Electrical Resistivity and Seebeck Coefficient of p-type Lead Telluride. *Br. J. Appl. Phys.* **18,** 563–573 (1967).

46. Bahk, J.-H., Bian, Z. & Shakouri, A. Electron Energy Filtering by a Nonplanar Potential to Enhance the Thermoelectric Power Factor in Bulk Materials. *Phys. Rev. B* **87,** 075204 (2013).

47. Kittel, C. *Introduction to Solid State Physics*. (John Wiley & Sons, Inc., 2005).

48. Chantrenne, P. & Barrat, J.-L. Analytical Model for the Thermal Conductivity of Nanostructures. *Superlattices Microstruct.* **35,** 173–186 (2004).

49. Finefrock, S. W. *Lead Telluride Nanostructure-Based Thermoelectric Materials: A Proposal Submitted by Scott Finefrock*. (2012).

50. Gaultois, M. W. *et al.* Data-Driven Review of Thermoelectric Materials: Performance and Resource Considerations. *Chem. Mater.* **25,** 2911–2920 (2013).

51. Goldsmid, H. J. *Introduction to thermoelectricity*. (Springer, 2010). at <http://books.google.com/books?hl=en&lr=&id=LYN3nDy0FccC&oi=fnd&pg=PA1&dq=Introduction+to+Thermoelectricity&ots=qJ5bIjYV4P&sig=zLqP0xwphflmycnUBnXp_jRiph8>

52. Gibbs, Z. M., LaLonde, A. & Snyder, G. J. Optical band gap and the Burstein–Moss Effect in Iodine Doped PbTe Using Diffuse Reflectance Infrared Fourier Transform Spectroscopy. *New J. Phys.* **15,** 075020 (2013).

53. Wood, C. Materials for Thermoelectric Energy Conversion. *Rep. Prog. Phys.* **51,** 459–539 (1988).

54. Lougher, E. H. in *Thermoelectr. Mater. Devices* (Cadoff, I. B. & Miller, E.) 133–142 (Reinhold Publishing Corporation, 1960).

55. Goldsmid, H. J. *Electronic Refrigeration*. (Pion Limited, 1986).

56. Kim, W. *et al.* Thermal Conductivity Reduction and Thermoelectric Figure of Merit Increase by Embedding Nanoparticles in Crystalline Semiconductors. *Phys. Rev. Lett.* **96,** 045901 (2006).

57. Medlin, D. L. & Snyder, G. J. Interfaces in Bulk Thermoelectric Materials. *Curr. Opin. Colloid Interface Sci.* **14,** 226–235 (2009).

58. Slack, G. A. in *CRC Handbook of Thermoelectricity.* (Rowe, D. M.) (CRC Press, 1995).

59. Goldsmid, H. J. *Applications of Thermoelectricity*. (John Wiley & Sons, Inc., 1960).

60. Hicks, L. D. & Dresselhaus, M. S. Thermoelectric Figure of Merit of a One-Dimensional Conductor. *Phys. Rev. B* **47,** 16631–16634 (1993).

61. Hicks, L. D. & Dresselhaus, M. S. Effect of Quantum-Well Structures on the Thermoelectric Figure of Merit. *Phys. Rev. B* **47,** 12727–12731 (1993).

62. Dresselhaus, M. S. *et al.* New Directions for Low-Dimensional Thermoelectric Materials. *Adv. Mater.* **19,** 1043–1053 (2007).

63. Mahan, G. D. & Sofo, J. O. The best thermoelectric. *Proc. Natl. Acad. Sci.* **93,** 7436–7439 (1996).

64. Morelli, D. T. & Meisner, G. P. Low Temperature Properties of the Filled Skutterudite $CeFe_4Sb_{12}$. *J. Appl. Phys.* **77,** 3777–3781 (1995).

65. Caillat, T., Borshchevsky, A. & Fleurial, J.-P. Properties of Single Crystalline Semiconducting $CoSb_3$. *J. Appl. Phys.* **80,** 4442–4449 (1996).

66. Nolas, G. S., Kaeser, M., Littleton, R. T. & Tritt, T. M. High Figure of Merit in Partially Filled Ytterbium Skutterudite Materials. *Appl. Phys. Lett.* **77,** 1855–1857 (2000).

67. Christensen, M., Johnsen, S. & Iversen, B. B. Thermoelectric Clathrates of Type I. *Dalt. Trans.* **39,** 978–992 (2010).

68. Shen, Q. *et al.* Effects of Partial Substitution of Ni by Pd on the Thermoelectric Properties of ZrNiSn-Based Half-Heusler Compounds. *Appl. Phys. Lett.* **79,** 4165–4167 (2001).

69. Sakurada, S. & Shutoh, N. Effect of Ti Substitution on the Thermoelectric Properties of (Zr,Hf)NiSn Half-Heusler Compounds. *Appl. Phys. Lett.* **86,** 082105 (2005).

70. Bubnova, O. *et al.* Optimization of the Thermoelectric Figure of Merit in the Conducting Polymer poly(3,4-ethylenedioxythiophene). *Nat. Mater.* **10,** 429–433 (2011).

71. Bubnova, O. *et al.* Semi-Metallic Polymers. *Nat. Mater.* **13,** 190–194 (2013).

72. Luo, J. *et al.* Enhancement of the Thermoelectric Properties of PEDOT:PSS Thin Films by Post-Treatment. *J. Mater. Chem. A* **1,** 7576–7583 (2013).

73. Kim, G.-H., Shao, L., Zhang, K. & Pipe, K. P. Engineered Doping of Organic Semiconductors for Enhanced Thermoelectric Efficiency. *Nat. Mater.* **12,** 719–723 (2013).

74. Liang, W. *et al.* Thermoelectric Properties of p-type PbSe Nanowires. *Nano Res.* **2,** 394–399 (2010).

75. Kim, J. *et al.* Thermoelectricity in Semiconductor Nanowires. *Phys. status solidi - Rapid Res. Lett.* **7,** 767–780 (2013).

76. Boukai, A. I. *et al.* Silicon Nanowires as Efficient Thermoelectric Materials. *Nature* **451,** 168–171 (2008).

77. Hochbaum, A. *et al.* Enhanced Thermoelectric Performance of Rough Silicon Nanowires. *Nature* **451,** 163–167 (2008).

78. Venkatasubramanian, R., Siivola, E. & Colpitts, T. Thin-Film Thermoelectric Devices with High Room-Temperature Figures of Merit. *Nature* **413,** 597–602 (2001).

79. Tan, M., Deng, Y. & Wang, Y. Ordered Structure and High Thermoelectric Properties of $Bi_2(Te,Se)_3$ Nanowire Array. *Nano Energy* **3,** 144–151 (2014).

80. Qi, Y., Wang, Z., Zhang, M., Yang, F. & Wang, X. Thermoelectric Devices Based on One-Dimensional Nanostructures. *J. Mater. Chem. A* **1,** 6110–6124 (2013).

81. Kim, R., Datta, S. & Lundstrom, M. S. Influence of Dimensionality on Thermoelectric Device Performance. *J. Appl. Phys.* **105,** 034506 (2009).

82. LeBlanc, S., Yee, S. K., Scullin, M. L., Dames, C. & Goodson, K. E. Material and Manufacturing Cost Considerations for Thermoelectrics. *Renew. Sustain. Energy Rev.* **32,** 313–327 (2014).

83. Lan, Y., Minnich, A., Chen, G. & Ren, Z. Enhancement of Thermoelectric Figure-of-Merit by a Bulk Nanostructuring Approach. *Adv. Funct. Mater.* **20,** 357–376 (2010).

84. Poudel, B. *et al.* High-Thermoelectric Performance of Nanostructured Bismuth Antimony Telluride Bulk Alloys. *Science.* **320,** 634–638 (2008).

85. Wang, X. W. *et al.* Enhanced Thermoelectric Figure of Merit in Nanostructured n-type Silicon Germanium Bulk Alloy. *Appl. Phys. Lett.* **93,** 193121 (2008).

86. Joshi, G. *et al.* Enhanced Thermoelectric Figure-of-Merit in Nanostructured p-type Silicon Germanium Bulk Alloys. *Nano Lett.* **8,** 4670–4674 (2008).

87. Yang, J. *et al.* Solubility Study of Yb in n-type Skutterudites $Yb_xCo_4Sb_{12}$ and Their Enhanced Thermoelectric Properties. *Phys. Rev. B* **80,** 115329 (2009).

88. Kanatzidis, M. G. Nanostructured Thermoelectrics: The New Paradigm? *Chem. Mater.* **22,** 648–659 (2010).

89. Hsu, K. F. *et al.* Cubic $AgPb_{(m)}SbTe_{(2+m)}$: Bulk Thermoelectric Materials with High Figure of Merit. *Science.* **303,** 818–821 (2004).

90. Androulakis, J. *et al.* Spinodal Decomposition and Nucleation and Growth as a Means to Bulk Nanostructured Thermoelectrics: Enhanced Performance in $Pb_{1-x}Sn_xTe$-PbS. *J. Am. Chem. Soc.* **129,** 9780–9788 (2007).

91. Sootsman, J. R. *et al.* Large Enhancements in the Thermoelectric Power Factor of Bulk PbTe at High Temperature by Synergistic Nanostructuring. *Angew. Chem. Int. Ed. Engl.* **47,** 8618–8622 (2008).

92. Pei, Y., Lensch-Falk, J., Toberer, E. S., Medlin, D. L. & Snyder, G. J. High Thermoelectric Performance in PbTe Due to Large Nanoscale Ag_2Te Precipitates and La Doping. *Adv. Funct. Mater.* **21,** 241–249 (2011).

93. Pei, Y., Heinz, N. a., LaLonde, A. & Snyder, G. J. Combination of Large Nanostructures and Complex Band Structure for High Performance Thermoelectric Lead Telluride. *Energy Environ. Sci.* **4,** 3640–3645 (2011).

94. Biswas, K. *et al.* Strained Endotaxial Nanostructures with High Thermoelectric Figure of Merit. *Nat. Chem.* **3,** 160–166 (2011).

95. Zhao, L.-D. *et al.* Raising the Thermoelectric Performance of p-Type PbS with Endotaxial Nanostructuring and Valence-Band Offset Engineering Using CdS and ZnS. *J. Am. Chem. Soc.* **134,** 16327−16336 (2012).

96. Biswas, K. *et al.* High-Performance Bulk Thermoelectrics with All-Scale Hierarchical Architectures. *Nature* **489,** 414–418 (2012).

97. Zhao, L. D. *et al.* All-Scale Hierarchical Thermoelectrics: MgTe in PbTe Facilitates Valence Band Convergence and Suppresses Bipolar Thermal Transport for High Performance. *Energy Environ. Sci.* **6,** 3346–3355 (2013).

98. Wu, Y., Finefrock, S. W. & Yang, H. Nanostructured Thermoelectric: Opportunities and Challenges. *Nano Energy* **1,** 651–653 (2012).

99. Gupta, R. P. *et al.* Inorganic Colloidal Solution-Based Approach to Nanocrystal Synthesis of $(Bi,Sb)_2Te_3$. *J. Electron. Mater.* **41,** 1573–1578 (2012).

100. Byrappa, K. & Adschiri, T. Hydrothermal Technology for Nanotechnology. *Prog. Cryst. Growth Charact. Mater.* **53,** 117–166 (2007).

101. Walton, R. I. Subcritical Solvothermal Synthesis of Condensed Inorganic Materials. *Chem. Soc. Rev.* **31,** 230–238 (2002).

102. Jianfeng, Y. & Limin, Q. Solution-Phase Synthesis of One-Dimensional Semiconductor Nanostructures. *J. Mater. Sci. Technol.* **24,** 529–540 (2008).

103. Liang, H., Liu, J., Qian, H. & Yu, S. Multiplex Templating Process in One-Dimensional Nanoscale: Controllable Synthesis, Macroscopic Assemblies, And Applications. *Acc. Chem. Res.* **46,** 1450–1461 (2013).

104. Zhang, G., Yu, Q. & Li, X. Wet Chemical Synthesis and Thermoelectric Properties Of V-VI One- and Two-Dimensional Nanostructures. *Dalt. Trans.* **39,** 993–1004 (2010).

105. Moon, G. D., Ko, S., Xia, Y. & Jeong, U. Chemical Transformations in Ultrathin Chalcogenide Nanowires. *ACS Nano* **4,** 2307–2319 (2010).

106. Wang, Y. Y., Cai, K. F. & Yao, X. Facile Synthesis of PbTe Nanoparticles And Thin Films in Alkaline Aqueous Solution at Room Temperature. *J. Solid State Chem.* **182,** 3383–3386 (2009).

107. Samal, A. K. & Pradeep, T. Room-Temperature Chemical Synthesis of Silver Telluride Nanowires. *J. Phys. Chem. C* **113,** 13539–13544 (2009).

108. Wan, B., Hu, C., Xi, Y., Xu, J. & He, X. Room-Temperature Synthesis and Seebeck Effect of Lead Chalcogenide Nanocubes. *Solid State Sci.* **12,** 123–127 (2010).

109. Cao, Y. Q., Zhu, T. J. & Zhao, X. B. Low Thermal Conductivity and Improved Figure of Merit in Fine-Grained Binary PbTe Thermoelectric Alloys. *J. Phys. D. Appl. Phys.* **42,** 015406 (2009).

110. Soni, A. *et al.* Enhanced Thermoelectric Properties of Solution Grown $Bi_2Te_{3-x}Se_x$ Nanoplatelet Composites. *Nano Lett.* **12,** 1203–1209 (2012).

111. Yang, H., Finefrock, S. W., Albarracin Caballero, J. D. & Wu, Y. Environmentally Benign Synthesis of Ultrathin Metal Telluride Nanowires. *J. Am. Chem. Soc.* **136,** 10242–10245 (2014).

112. Yong, K., Sahoo, Y. & Zeng, H. Formation of ZnTe Nanowires by Oriented Attachment. *Chem. Mater.* **19,** 4108–4110 (2007).

113. Stavila, V. *et al.* Wet-Chemical Synthesis and Consolidation of Stoichiometric Bismuth Telluride Nanoparticles for Improving the Thermoelectric Figure-of-Merit. *ACS Appl. Mater. Interfaces* **5,** 6678–6686 (2013).

114. Zhao, Y., Dyck, J. S., Hernandez, B. M. & Burda, C. Improving Thermoelectric Properties of Chemically Synthesized Bi_2Te_3-Based Nanocrystals by Annealing. *J. Phys. Chem. C* **114,** 11607–11613 (2010).

115. Son, J. S. *et al.* n-Type Nanostructured Thermoelectric Materials Prepared from Chemically Synthesized Ultrathin Bi_2Te_3 Nanoplates. *Nano Lett.* **12,** 640–647 (2012).

116. Urban, J. J., Talapin, D. V, Shevchenko, E. V & Murray, C. B. Self-Assembly of PbTe Quantum Dots into Nanocrystal Superlattices and Glassy Films. *J. Am. Chem. Soc.* **128,** 3248–3255 (2006).

117. Dong, G.-H. & Zhu, Y.-J. One-Step Microwave-Solvothermal Rapid Synthesis of Sb Doped PbTe/Ag_2Te Core/Shell Composite Nanocubes. *Chem. Eng. J.* **193-194,** 227–233 (2012).

118. Dong, G.-H., Zhu, Y.-J. & Chen, L.-D. Microwave-Assisted Rapid Synthesis of Sb_2Te_3 Nanosheets and Thermoelectric Properties of Bulk Samples Prepared by Spark Plasma Sintering. *J. Mater. Chem.* **20,** 1976–1981 (2010).

119. Liu, J.-W. *et al.* Rapid Microwave-Assisted Synthesis of Uniform Ultralong Te Nanowires, Optical Property, and Chemical Stability. *Langmuir* **26,** 11372–11377 (2010).

120. Dong, G.-H., Zhu, Y.-J., Cheng, G.-F. & Ruan, Y.-J. $Cu_{(2-X)}Te$ Nanowires Synthesized by a Microwave-Assisted Solvothermal Method Using a Self-Sacrificial Template and Their Electrical Conductivity. *Mater. Lett.* **76,** 69–72 (2012).

121. Zhou, B., Ji, Y., Yang, Y., Li, X. & Zhu, J. Rapid Microwave-Assisted Synthesis of Single-Crystalline Sb_2Te_3 Hexagonal Nanoplates. *Cryst. Growth Des.* **8,** 4394–4397 (2008).

122. Pei, J. *et al.* Crooked Ag_2Te Nanowires With Rough Surfaces: Facile Microwave-Assisted Solution Synthesis, Growth Mechanism, and Electrical Performances. *New J. Chem.* **38,** 59–62 (2014).

123. Cho, S., Jung, S.-H. & Lee, K.-H. Morphology-Controlled Growth of ZnO Nanostructures Using Microwave Irradiation: from Basic to Complex Structures. *J. Phys. Chem. C* **112,** 12769–12776 (2008).

124. Mehta, R. J. *et al.* A New Class Of Doped Nanobulk High-Figure-of-Merit Thermoelectrics by Scalable Bottom-up Assembly. *Nat. Mater.* **11,** 233–240 (2012).

125. Talapin, D. V & Murray, C. B. PbSe Nanocrystal Solids for n- and p-Channel Thin Film Field-Effect Transistors. *Science.* **310,** 86–89 (2005).

126. Lu, Z. *et al.* Aqueous Solution Synthesis of $(Sb, Bi)_2(Te, Se)_3$ Nanocrystals with Controllable Composition And Morphology. *J. Mater. Chem. C* **1,** 6271–6277 (2013).

127. Li, D. *et al.* Improved Thermoelectric Properties For Solution Grown $Bi_2Te_{3-x}Se_x$ Nanoplatelet Composites. *RSC Adv.* **3,** 2632–2638 (2013).

128. Kim, C., Kim, D., Kim, H. & Chung, J. Significant Enhancement in the Thermoelectric Performance of a Bismuth Telluride Nanocompound through Brief Fabrication Procedures. *ACS Appl. Mater. Interfaces* **4,** 2949–2954 (2012).

129. Kim, C. *et al.* Study of Reaction Mechanisms and Synthetic Manipulations of Bismuth Tellurium Selenide Nanomaterials for Enhanced Thermoelectric Performance. *J. Alloys Compd.* **584,** 108–113 (2014).

130. Yashina, L. V *et al.* A Combined Photoelectron Spectroscopy and ab Initio Study of the Adsorbate System O_2/PbTe (001) and the Oxide Layer Growth Kinetics. *J. Phys. Chem. C* **112,** 19995–20006 (2008).

131. Guillon, O. *et al.* Field-Assisted Sintering Technology/Spark Plasma Sintering: Mechanisms, Materials, and Technology Developments. *Adv. Eng. Mater.* **16,** 830–849 (2014).

132. Munir, Z. a., Anselmi-Tamburini, U. & Ohyanagi, M. The Effect of Electric Field and Pressure on the Synthesis and Consolidation of Materials: A Review of the Spark Plasma Sintering Method. *J. Mater. Sci.* **41,** 763–777 (2006).

133. Garay, J. E. Current-Activated, Pressure-Assisted Densification of Materials. *Annu. Rev. Mater. Res.* **40,** 445–468 (2010).

134. Chowdhury, I. *et al.* On-Chip Cooling by Superlattice-Based Thin-Film Thermoelectrics. *Nat. Nanotechnol.* **4,** 235–238 (2009).

135. Kutasov, V. A., Lukyanova, L. N. & Vedernikov, M. V. in *Thermoelectr. Handb. Macro to Nano* (Rowe, D. M.) **2,** 37–1 – 37–18 (Taylor& Francis, 2006).

136. Heremans, J. P., Dresselhaus, M. S., Bell, L. E. & Morelli, D. T. When Thermoelectrics Reached the Nanoscale. *Nat. Nanotechnol.* **8,** 471–473 (2013).

137. Oh, M. W. *et al.* Antisite Defects in n-type $Bi_2(Te,Se)_3$: Experimental and Theoretical Studies. *J. Appl. Phys.* **115,** 133706 (2014).

138. Scanlon, D. O. *et al.* Controlling Bulk Conductivity in Topological Insulators: Key Role of Anti-Site Defects. *Adv. Mater.* **24,** 2154–2158 (2012).

139. Scherrer, H. & Scherrer, S. in *Thermoelectr. Handb. Macro to Nano* (D. M. Rowe) 27–1 – 27–18 (Taylor& Francis, 2006).

140. Xie, W. *et al.* High Performance Bi_2Te_3 Nanocomposites Prepared by Single-Element-Melt-Spinning Spark-Plasma Sintering. *J. Mater. Sci.* **48,** 2745–2760 (2012).

141. Wang, S., Xie, W., Li, H. & Tang, X. Enhanced Performances of Melt Spun $Bi_2(Te,Se)_3$ for n-type Thermoelectric Legs. *Intermetallics* **19,** 1024–1031 (2011).

142. Ge, J.-P. & Li, Y.-D. Ultrasonic Synthesis of Nanocrystals of Metal Selenides and Tellurides. *J. Mater. Chem.* **13,** 911–915 (2003).

143. Chen, Z. *et al.* Hydrothermal Synthesized Nanostructure Bi–Sb–Te Thermoelectric Materials. *J. Alloys Compd.* **588,** 384–387 (2014).

144. Liu, C.-J., Liu, G.-J., Tsao, C.-W. & Huang, Y.-J. Improvement of Thermoelectric Power Factor of Hydrothermally Prepared $Bi_{0.5}Sb_{1.5}Te_3$ Compared with its Solvothermally Prepared Counterpart. *J. Electron. Mater.* **38,** 1499–1503 (2009).

145. Scheele, M. *et al.* ZT Enhancement in Solution-Grown $Sb_{(2-x)}Bi_xTe_3$ Nanoplatelets. *ACS Nano* **4,** 4283–4291 (2010).

146. Zhao, Y., Dyck, J. S., Hernandez, B. M. & Burda, C. Enhancing Thermoelectric Performance of Ternary Nanocrystals Through Adjusting Carrier Concentration. *J. Am. Chem. Soc.* **132,** 4982–4983 (2010).

147. Ren, W., Cheng, C., Ren, Z. & Zhong, Y. The Effect of The Precursor Nanopowder Size on the Thermoelectric Properties of Nanostructured Bi–Sb–Te Bulk Materials. *Phys. B Condens. Matter* **405,** 4931–4936 (2010).

148. Kovalenko, M. V *et al.* Semiconductor Nanocrystals Functionalized With Antimony Telluride Zintl Ions for Nanostructured Thermoelectrics. *J. Am. Chem. Soc.* **132,** 6686–6695 (2010).

149. Zhang, Y. *et al.* Hydrothermal Synthesis And Thermoelectric Properties Of Nanostructured $Bi_{0.5}Sb_{1.5}Te_3$ Compounds. *Mater. Res. Bull.* **46,** 760–764 (2011).

150. Liu, C.-J., Liu, G.-J., Liu, Y.-L., Chen, L.-R. & Kaiser, A. B. Enhanced Thermoelectric Performance of Compacted $Bi_{0.5}Sb_{1.5}Te_3$ Nanoplatelets with Low Thermal Conductivity. *J. Mater. Res.* **26,** 1755–1761 (2011).

151. Ganguly, S., Zhou, C., Morelli, D., Sakamoto, J. & Brock, S. L. Synthesis and Characterization of Telluride Aerogels: Effect of Gelation on Thermoelectric Performance of Bi_2Te_3 and $Bi_{2-x}Sb_xTe_3$ Nanostructures. *J. Phys. Chem. C* **116,** 17431–17439 (2012).

152. Zhang, Y. *et al.* Silver-Based Intermetallic Heterostructures in Sb_2Te_3 Thick Films with Enhanced Thermoelectric Power Factors. *Nano Lett.* **12,** 1075–1080 (2012).

153. Schulz, S. *et al.* Synthesis of Hexagonal Sb_2Te_3 Nanoplates by Thermal Decomposition of the Single-Source Precursor $(Et_2Sb)_2Te$. *Chem. Mater.* **24,** 2228–2234 (2012).

154. Pelz, U. *et al.* An Aqueous-Chemistry Approach to Nano-Bismuth Telluride and Nano-Antimony Telluride as Thermoelectric Materials. *J. Electron. Mater.* **41,** 1851–1857 (2012).

155. Dyck, J. S., Mao, B., Wang, J., Dorroh, S. & Burda, C. Effect of Sintering on the Thermoelectric Transport Properties of Bulk Nanostructured $Bi_{0.5}Sb_{1.5}Te_3$ Pellets Prepared by Chemical Synthesis. *J. Electron. Mater.* **41,** 1408–1413 (2012).

156. Liu, C.-J., Lai, H.-C., Liu, Y.-L. & Chen, L.-R. High Thermoelectric Figure-of-Merit in p-type Nanostructured $(Bi,Sb)_2Te_3$ Fabricated via Hydrothermal Synthesis and Evacuated-and-Encapsulated Sintering. *J. Mater. Chem.* **22,** 4825–4831 (2012).

157. Sun, S. *et al.* Template-Free Solvothermal Synthesis and Enhanced Thermoelectric Performance of Sb_2Te_3 Nanosheets. *J. Alloys Compd.* **558,** 6–10 (2013).

158. Chai, Z. *et al.* Thermoelectric Metal Tellurides with Nanotubular Structures Synthesized by the Kirkendall Effect and their Reduced Thermal Conductivities. *CrystEngComm* **16,** 3507–3514 (2014).

159. Testardi, L. R., Bierly, J. N. & Donahoe, F. J. Transport Properties of p-type Bi_2Te_3-Sb_2Te_3 Alloys in the Temperature Range 80-370K. *J. Phys. Chem. Solids* **23,** 1209–1217 (1962).

160. Finefrock, S. W., Fang, H., Yang, H., Darsono, H. & Wu, Y. Large-Scale Solution-Phase Production of Bi_2Te_3 And PbTe Nanowires Using Te Nanowire Templates. *Nanoscale* **6,** 7872–7876 (2014).

161. Zhang, Y., Hu, L. & Zhu, T. High Yield Bi_2Te_3 Single Crystal Nanosheets with Uniform Morphology via a Solvothermal Synthesis. *Cryst. Growth Des.* **13,** 645–651 (2013).

162. Ni, H. L., Zhu, T. J. & Zhao, X. B. Hydrothermally Synthesized and Hot-Pressed $Bi_2(Te,Se)_3$ Thermoelectric Alloys. *Phys. B Condens. Matter* **364,** 50–54 (2005).

163. Ni, H. L., Zhu, T. J. & Zhao, X. B. Thermoelectric Properties Of Hydrothermally Synthesized and Hot Pressed n-type Bi_2Te_3 Alloys with Different Contents of Te. *Mater. Sci. Eng. B* **117,** 119–122 (2005).

164. Dirmyer, M. R., Martin, J., Nolas, G. S., Sen, A. & Badding, J. V. Thermal and Electrical Conductivity of Size-Tuned Bismuth Telluride Nanoparticles. *Small* **5,** 933–937 (2009).

165. Scheele, M. *et al.* Synthesis and Thermoelectric Characterization of Bi_2Te_3 Nanoparticles. *Adv. Funct. Mater.* **19,** 3476–3483 (2009).

166. Mi, J.-L. *et al.* Biomolecule-Assisted Hydrothermal Synthesis and Self-Assembly of Bi_2Te_3 Nanostring-Cluster Hierarchical Structure. *ACS Nano* **4,** 2523–2530 (2010).

167. Wang, R. Y. *et al.* Universal and Solution-Processable Precursor to Bismuth Chalcogenide Thermoelectrics. *Chem. Mater.* **22,** 1943–1945 (2010).

168. Sun, Z., Liufu, S. & Chen, L. Synthesis and Characterization of Nanostructured Bismuth Selenide Thin Films. *Dalt. Trans.* **39,** 10883–10887 (2010).

169. Xu, H. *et al.* Electrical Transport Properties of Microwave-Synthesized $Bi_2Se_{3-x}Te_x$ Nanosheet. *CrystEngComm* **15,** 5626–5632 (2013).

170. Kim, C. *et al.* Development of Bismuth Tellurium Selenide Nanoparticles for Thermoelectric Applications via a Chemical Synthetic Process. *Mater. Res. Bull.* **46,** 407–412 (2011).

171. Zhang, G. *et al.* Rational Synthesis of Ultrathin n-Type Bi_2Te_3 Nanowires with Enhanced Thermoelectric Properties. *Nano Lett.* **12,** 56–60 (2011).

172. Kim, C. *et al.* Fabrication of Bismuth Telluride Nanoparticles Using a Chemical Synthetic Process and Their Thermoelectric Evaluations. *Powder Technol.* **214,** 463–468 (2011).

173. Kim, C. *et al.* A Study of the Synthesis of Bismuth Tellurium Selenide Nanocompounds and Procedures for Improving Their Thermoelectric Performance. *J. Alloys Compd.* **509,** 9472–9478 (2011).

174. Fu, J. *et al.* Bi_2Te_3 Nanoplates and Nanoflowers: Synthesized by Hydrothermal Process and Their Enhanced Thermoelectric Properties. *CrystEngComm* **14,** 2159–2165 (2012).

175. Zhang, Y. *et al.* A Mesoporous Anisotropic n-type Bi_2Te_3 Monolith with Low Thermal Conductivity as an Efficient Thermoelectric Material. *Adv. Mater.* **24,** 5065–5070 (2012).

176. Saleemi, M., Toprak, M. S., Li, S., Johnsson, M. & Muhammed, M. Synthesis, Processing, and Thermoelectric Properties of Bulk Nanostructured Bismuth Telluride (Bi_2Te_3). *J. Mater. Chem.* **22,** 725–730 (2012).

177. Li, D. *et al.* Thermoelectric Properties of Hydrothermally Synthesized $Bi_2Te_{3-x}Se_x$ Nanocrystals. *Scr. Mater.* **67,** 161–164 (2012).

178. Bai, T. *et al.* Synthesis of Various Metal Selenide Nanostructures Using The Novel Selenium Precursor 1,5-bis(3-methylimidazole-2-selone)pentane. *CrystEngComm* **15,** 6483–6490 (2013).

179. Min, Y., Roh, J., Yang, H. & Park, M. Surfactant-Free Scalable Synthesis of Bi_2Te_3 and Bi_2Se_3 Nanoflakes and Enhanced Thermoelectric Properties of Their Nanocomposites. *Adv. Mater.* **25,** 1425–1429 (2013).

180. Song, S., Fu, J., Li, X., Gao, W. & Zhang, H. Facile Synthesis and Thermoelectric Properties of Self-Assembled Bi_2Te_3 One-Dimensional Nanorod Bundles. *Chem. A Eur. J.* **19,** 2889–2894 (2013).

181. Xu, H. *et al.* Enhancement of the Seebeck Coefficient in Stacked Bi_2Se_3 Nanoplates by Energy Filtering. *Eur. J. Inorg. Chem.* **2014,** 2625–2630 (2014).

182. Yim, W., Fitzke, E. & Rosi, F. Thermoelectric Properties of Bi_2Te_3-Sb_2Te_3-Sb_2Se_3 Pseudo-Ternary Alloys in the Temperature Range 77 to 300 K. *J. Mater. Sci.* **1,** 52–65 (1966).

183. Ji, X. H., Zhao, X. B., Zhang, Y. H., Lu, B. H. & Ni, H. L. Synthesis and Properties of Rare Earth Containing Bi_2Te_3 Based Thermoelectric Alloys. *J. Alloys Compd.* **387,** 282–286 (2005).

184. Datta, A. *et al.* Facile Chemical Synthesis of Nanocrystalline Thermoelectric Alloys Based on Bi−Sb−Te−Se. *Cryst. Growth Des.* **10,** 3983–3989 (2010).

185. Zhao, L.-D., Dravid, V. P. & Kanatzidis, M. G. The Panoscopic Approach to High Performance Thermoelectrics. *Energy Environ. Sci.* **7,** 251–268 (2014).

186. Pei, Y., LaLonde, A., Iwanaga, S. & Snyder, G. J. High Thermoelectric Figure of Merit in Heavy Hole Dominated PbTe. *Energy Environ. Sci.* **4,** 2085–2089 (2011).

187. LaLonde, A. D., Pei, Y. & Snyder, G. J. Reevaluation of $PbTe_{1-x}I_x$ As High Performance n-type Thermoelectric Material. *Energy Environ. Sci.* **4,** 2090–2096 (2011).

188. Pei, Y. *et al.* Convergence of Electronic Bands for High Performance Bulk Thermoelectrics. *Nature* **473,** 66–69 (2011).

189. Jaworski, C. M. *et al.* Valence-Band Structure of Highly Efficient p-type Thermoelectric PbTe-PbS Alloys. *Phys. Rev. B* **87,** 045203 (2013).

190. Gibbs, Z. *et al.* Temperature Dependent Band Gap in PbX (X= S, Se, Te). *Appl. Phys. Lett.* **103,** 262109 (2013).

191. Mühlberg, M. & Hesse, D. TEM Precipitation Studies in Te-Rich As-Grown PbTe Single Crystals. *Phys. status solidi* **76,** 513–524 (1983).

192. Lin, J. C., Hsleh, K. C., Sharma, R. C. & Chang, Y. A. The Pb-Te (Lead-Tellurium) System. *Bull. Alloy Phase Diagrams* **10,** 340–347 (1989).

193. Zhang, Q. *et al.* Heavy Doping and Band Engineering by Potassium to Improve the Thermoelectric Figure of Merit in p-Type PbTe, PbSe, and $PbTe_{1-y}Se_y$. *J. Am. Chem. Soc.* **134,** 10031–10038 (2012).

194. Heremans, J. P. *et al.* Enhancement of Thermoelectric Efficiency in PbTe by Distortion of the Electronic Density of States. *Science.* **321,** 554–557 (2008).

195. Pei, Y., LaLonde, A. D., Wang, H. & Snyder, G. J. Low Effective Mass Leading to High Thermoelectric Performance. *Energy Environ. Sci.* **5,** 7963–7969 (2012).

196. Fritts, R. W. in *Thermoelectr. Mater. Devices* 143–162 (Reinhold Publishing Corporation, 1960).

197. Zhang, W., Zhang, L., Cheng, Y., Hui, Z. & Zhang, X. Synthesis of Nanocrystalline Lead Chalcogenides PbE (E = S , Se , or Te) from Alkaline Aqueous Solutions. *Mater. Res. Bull.* **35,** 2009–2015 (2000).

198. Martin, J., Nolas, G. S., Zhang, W. & Chen, L. PbTe Nanocomposites Synthesized from PbTe Nanocrystals. *Appl. Phys. Lett.* **90,** 222112 (2007).

199. Paul, B. & Banerji, P. Grain Structure Induced Thermoelectric Properties in PbTe Nanocomposites. *Nanosci. Nanotechnol. Lett.* **1,** 208–212 (2009).

200. Martin, J., Wang, L., Chen, L. & Nolas, G. S. Enhanced Seebeck Coefficient Through Energy-Barrier Scattering In PbTe Nanocomposites. *Phys. Rev. B* **79,** 115311 (2009).

201. Paul, B., V, A. K. & Banerji, P. Embedded Ag-Rich Nanodots in PbTe: Enhancement of Thermoelectric Properties Through Energy Filtering of the Carriers. *J. Appl. Phys.* **108,** 064322 (2010).

202. Finefrock, S. W. *et al.* Structure and Thermoelectric Properties of Spark Plasma Sintered Ultrathin PbTe Nanowires. *Nano Lett.* **14,** 3466–3473 (2014).

203. LaLonde, A. D., Ikeda, T. & Snyder, G. J. Rapid Consolidation of Powdered Materials by Induction Hot Pressing. *Rev. Sci. Instrum.* **82,** 025104 (2011).

204. Noda, Y., Orihashi, M. & Nishida, I. Thermoelectric Properties of p-type Lead Telluride Doped with Silver or Potassium. *Mater. Trans.* **39,** 602–605 (1998).

205. Zhang, Q. *et al.* Effect of Silicon and Sodium on Thermoelectric Properties of Thallium-Doped Lead Telluride-Based Materials. *Nano Lett.* **12,** 2324–2330 (2012).

206. Hillman, P. & Stacy, A. M. Electrodeposition of Group III Doped PbTe Nanowires. in *MRS Proc.* Q09–04 (2010).

207. Yadav, G. G., Susoreny, J. a., Zhang, G., Yang, H. & Wu, Y. Nanostructure-Based Thermoelectric Conversion: an Insight into the Feasibility and Sustainability for Large-Scale Deployment. *Nanoscale* **3,** 3555–3562 (2011).

208. Popescu, A., Datta, A., Nolas, G. S. & Woods, L. M. Thermoelectric Properties of Bi-Doped PbTe Composites. *J. Appl. Phys.* **109,** 103709 (2011).

209. Fang, H., Luo, Z., Yang, H. & Wu, Y. The Effects of the Size and the Doping Concentration on the Power Factor of n-type Lead Telluride Nanocrystals for Thermoelectric Energy Conversion. *Nano Lett.* **14,** 1153–1157 (2014).

210. Pei, Y., Gibbs, Z. M., Balke, B., Zeier, W. G. & Snyder, G. J. Optimum Carrier Concentration in n-Type PbTe Thermoelectrics. *Adv. Energy Mater.* **4,** 1400486 (2014).

211. Liu, M.-L., Chen, I.-W., Huang, F.-Q. & Chen, L.-D. Improved Thermoelectric Properties of Cu-Doped Quaternary Chalcogenides of $Cu_2CdSnSe_4$. *Adv. Mater.* **21,** 3808–3812 (2009).

212. Shi, X., Xi, L., Fan, J., Zhang, W. & Chen, L. Cu−Se Bond Network and Thermoelectric Compounds with Complex Diamondlike Structure. *Chem. Mater.* **22,** 6029–6031 (2010).

213. Zeier, W. G. *et al.* Influence of a Nano Phase Segregation on the Thermoelectric Properties of the P-Type Doped Stannite Compound $Cu_{(2+x)}Zn_{(1-x)}GeSe_4$. *J. Am. Chem. Soc.* **134,** 7147–7154 (2012).

214. Ibáñez, M. *et al.* $Cu_2ZnGeSe_4$ Nanocrystals: Synthesis and Thermoelectric Properties. *J. Am. Chem. Soc.* **134,** 4060–4063 (2012).

215. Xue, D.-J. *et al.* Synthesis of wurtzite $Cu_2ZnGeSe_4$ Nanocrystals and Their Thermoelectric Properties. *Chem. Asian J.* **8,** 2383–2387 (2013).

216. Fan, F.-J. *et al.* Colloidal Synthesis of $Cu_2CdSnSe_4$ Nanocrystals and Hot-Pressing to Enhance the Thermoelectric Figure-of-Merit. *J. Am. Chem. Soc.* **133,** 15910–15913 (2011).

217. Iba, M. *et al.* Composition Control and Thermoelectric Properties of Quaternary Chalcogenide Nanocrystals: The Case of Stannite $Cu_2CdSnSe_4$. *Chem. Mater.* **24,** 562–570 (2012).

218. Song, J.-M. *et al.* Hot-Injection Synthesis and Characterization of Monodispersed Ternary Cu_2SnSe_3 Nanocrystals for Thermoelectric Applications. *J. Alloys Compd.* **581,** 646–652 (2013).

219. Ibáñez, M. *et al.* Colloidal Synthesis and Thermoelectric Properties of Cu_2SnSe_3 Nanocrystals. *J. Mater. Chem. A* **1,** 1421–1426 (2013).

220. Fan, F.-J., Wang, Y.-X., Liu, X.-J., Wu, L. & Yu, S.-H. Large-Scale Colloidal Synthesis of Non-Stoichiometric $Cu_2ZnSnSe_4$ Nanocrystals for Thermoelectric Applications. *Adv. Mater.* **24,** 6158–6163 (2012).

221. Ibáñez, M., Zamani, R. & Li, W. Crystallographic Control at the Nanoscale to Enhance Functionality: Polytypic Cu_2GeSe_3 Nanoparticles as Thermoelectric Materials. *Chem. Mater.* **24,** 4615–4622 (2012).

222. Li, W. *et al.* Colloidal Synthesis and Functional Properties of Quaternary Cu-Based Semiconductors: $Cu_2HgGeSe_4$. *J. Nanoparticle Res.* **16,** 2297 (2014).

223. Li, W. *et al.* $Cu_2HgSnSe_4$ Nanoparticles: Synthesis and Thermoelectric Properties. *CrystEngComm* **15,** 8966–8971 (2013).

224. Shavel, A., Cadavid, D., Ibáñez, M., Carrete, A. & Cabot, A. Continuous Production of Cu_2ZnSnS_4 Nanocrystals in a Flow Reactor. *J. Am. Chem. Soc.* **134,** 1438–1441 (2012).

225. Yang, H., Jauregui, L. A., Zhang, G., Chen, Y. P. & Wu, Y. Nontoxic and Abundant Copper Zinc Tin Sulfide Nanocrystals for Potential High-Temperature Thermoelectric Energy Harvesting. *Nano Lett.* **12,** 540–545 (2012).

226. Liang, D., Ma, R., Jiao, S., Pang, G. & Feng, S. A Facile Synthetic Approach for Copper Iron Sulfide Nanocrystals with Enhanced Thermoelectric Performance. *Nanoscale* **4,** 6265–6268 (2012).

227. Long, Y.-Z., Yu, M., Sun, B., Gu, C.-Z. & Fan, Z. Recent Advances in Large-Scale Assembly of Semiconducting Inorganic Nanowires and Nanofibers for Electronics, Sensors and Photovoltaics. *Chem. Soc. Rev.* **41,** 4560–4580 (2012).

228. Cao, L. *et al.* Engineering Light Absorption in Semiconductor Nanowire Devices. *Nat. Mater.* **8,** 643–647 (2009).

229. Zhu, J. *et al.* Optical Absorption Enhancement in Amorphous Silicon Nanowire and Nanocone Arrays. *Nano Lett.* **9,** 279–282 (2009).

230. Lu, W. & Lieber, C. M. Semiconductor Nanowires. *J. Phys. D. Appl. Phys.* **39,** R387–R406 (2006).

231. Yang, Y. *et al.* Synthesis of PbTe Nanowire Arrays Using Lithographically Patterned Nanowire Electrodeposition. *Nano Lett.* **8,** 2447–2451 (2008).

232. Yang, Y. *et al.* Wafer-Scale Patterning of Lead Telluride Nanowires: Structure, Characterization, and Electrical Properties. *ACS Nano* **3,** 4144–4154 (2009).

233. Fardy, M., Hochbaum, a. I., Goldberger, J., Zhang, M. M. & Yang, P. Synthesis and Thermoelectrical Characterization of Lead Chalcogenide Nanowires. *Adv. Mater.* **19,** 3047–3051 (2007).

234. Jang, S. Y. *et al.* Transport Properties of Single-Crystalline n-type Semiconducting PbTe Nanowires. *Nanotechnology* **20,** 415204 (2009).

235. Zhang, B., Hou, W., Ye, X., Fu, S. & Xie, Y. 1D Tellurium Nanostructures: Photothermally Assisted Morphology-Controlled Synthesis and Applications in Preparing Functional Nanoscale Materials. *Adv. Funct. Mater.* **17,** 486–492 (2007).

236. Lu, Q., Gao, F. & Komarneni, S. A Green Chemical Approach to the Synthesis of Tellurium Nanowires. *Langmuir* **21,** 6002–6005 (2005).

237. Gautam, U. K. & Rao, C. N. R. Controlled Synthesis of Crystalline Tellurium Nanorods, Nanowires, Nanobelts and Related Structures by a Self-Seeding Solution Process. *J. Mater. Chem.* **14,** 2530–2535 (2004).

238. Xi, G. *et al.* Large-Scale Synthesis, Growth Mechanism, and Photoluminescence of Ultrathin Te Nanowires. *Cryst. Growth Des.* **6,** 2567–2570 (2006).

239. Song, J. M. *et al.* Superlong High-Quality Tellurium Nanotubes: Synthesis, Characterization, and Optical Property. *Cryst. Growth Des.* **8,** 1902–1908 (2008).

240. Zhu, Y.-J., Hu, X.-L. & Wang, W.-W. Poly(vinylpyrrolidone): A New Reductant for Preparation of Tellurium Nanorods, Nanowires, and Tubes from TeO_2. *Nanotechnology* **17,** 645–650 (2006).

241. Qiang, H.-S., Yu, S.-H., Gong, J.-Y., Luo, L.-B. & Fei, L. High-Quality Luminescent Tellurium Nanowires of Several Nanometers in Diameter and High Aspect Ratio Synthesized by a poly (vinyl pyrrolidone)-Assisted Hydrothermal Process. *Langmuir* **22,** 3830–3835 (2006).

242. Zhu, Y.-J., Wang, W.-W., Qi, R.-J. & Hu, X.-L. Microwave-Assisted Synthesis of Single-Crystalline Tellurium Nanorods and Nanowires in Ionic Liquids. *Angew. Chemie* **43,** 1410–1414 (2004).

243. Liang, H.-W., Liu, S. & Yu, S.-H. Controlled Synthesis of One-Dimensional Inorganic Nanostructures using Pre-Existing One-Dimensional Nanostructures as Templates. *Adv. Mater.* **22,** 3925–3937 (2010).

244. Yu, H., Gibbons, P. & Buhro, W. Bismuth, Tellurium, and Bismuth Telluride Nanowires. *J. Mater. Chem.* **14,** 595–602 (2004).

245. Liu, J. *et al.* Fabrication of DNA-Templated Te and Bi_2Te_3 Nanowires by Galvanic Displacement. *Langmuir* **29,** 11176–11184 (2013).

246. Wang, K., Liang, H.-W., Yao, W.-T. & Yu, S.-H. Templating Synthesis of Uniform Bi_2Te_3 Nanowires with High Aspect Ratio in Triethylene Glycol (TEG) and Their Thermoelectric Performance. *J. Mater. Chem.* **21,** 15057–15062 (2011).

247. Liang, H.-W., Liu, S., Wu, Q.-S. & Yu, S.-H. An Efficient Templating Approach for Synthesis of Highly Uniform CdTe and PbTe Nanowires. *Inorg. Chem.* **48,** 4927–4933 (2009).

248. Mu, L. *et al.* A Room Temperature Self-sacrificing Template Route to Ag_2Te Fibers. *Chem. Lett.* **34,** 52–53 (2005).

249. Tai, G., Guo, W. & Zhang, Z. Hydrothermal Synthesis and Thermoelectric Transport Properties of Uniform Single-Crystalline Pearl-Necklace-Shaped PbTe Nanowires. *Cryst. Growth Des.* **8,** 2906–2911 (2008).

250. He, J. *et al.* Preparation and Electrochemical Property of PbTe Nanorods. *Mater. Sci. Semicond. Process.* **12,** 217–223 (2009).

251. Tai, G., Zhou, B. & Guo, W. Structural Characterization and Thermoelectric Transport Properties of Uniform Single-Crystalline Lead Telluride Nanowires. *J. Phys. Chem. C* **112,** 11314–11318 (2008).

252. Zhang, H., Hyun, B.-R., Wise, F. & Robinson, R. D. A Generic Method for Rational Scalable Synthesis of Monodisperse Metal Sulfide Nanocrystals. *Nano Lett.* **12,** 5856–5860 (2012).

253. Zhou, W. *et al.* Binary-Phased Nanoparticles for Enhanced Thermoelectric Properties. *Adv. Mater.* **21,** 3196–3200 (2009).

254. Grebinski, J., Hull, K. & Zhang, J. Solution-Based Straight and Branched CdSe Nanowires. *Chem. Mater.* **16,** 5260–5272 (2004).

255. Zhang, G. *et al.* Design Principle of Telluride-Based Nanowire Heterostructures for Potential Thermoelectric Applications. *Nano Lett.* **12,** 3627–3633 (2012).

256. Fang, H., Feng, T., Yang, H., Ruan, X. & Wu, Y. Synthesis and Thermoelectric Properties of Compositional-Modulated Lead Telluride-Bismuth Telluride Nanowire Heterostructures. *Nano Lett.* **13,** 2058–2063 (2013).

257. Jin, R. *et al.* PbTe Hierarchical Nanostructures: Solvothermal Synthesis, Growth Mechanism and Their Electrical Conductivities. *CrystEngComm* **13,** 2106–2113 (2011).

258. Dong, J. *et al.* In-Situ Synthesis and Thermoelectric Properties of PbTe/Graphene Nanocomposites by Utilizing a Facile and Novel Wet Chemical Method. *J. Mater. Chem. A* **1,** 12503–12511 (2013).

259. Wang, Q., Chen, G. & Yin, H. New Insights into the Growth Mechanism of Hierarchical Architectures of PbTe Synthesized Through a Triethanolamine-Assisted Solvothermal Method and their Shape-Dependent Electrical Transport Properties. *J. Mater. Chem. A* **1,** 15355–15369 (2013).

260. Scheele, M. *et al.* Thermoelectric Properties of Lead Chalcogenide Core-Shell Nanostructures. *ACS Nano* **5,** 8541–8551 (2011).

261. Cadavid, D. *et al.* Bottom-up Processing of Thermoelectric Nanocomposites from Colloidal Nanocrystal Building Blocks: The Case of Ag_2Te–PbTe. *J. Nanoparticle Res.* **14,** 1328 (2012).

262. Ibáñez, M., Zamani, R., Gorsse, S. & Fan, J. Core–Shell Nanoparticles As Building Blocks for the Bottom-Up Production of Functional Nanocomposites: PbTe–PbS Thermoelectric Properties. *ACS Nano* **7,** 2573–2586 (2013).

263. Yan, Q. *et al.* A Simple Chemical Approach for PbTe Nanowires with enhanced Thermoelectric Properties. *Chem. Mater.* **20,** 6298–6300 (2008).

264. Kishimoto, K. & Koyanagi, T. Preparation of Sintered Degenerate n-type PbTe with a Small Grain Size and its Thermoelectric Properties. *J. Appl. Phys.* **92,** 2544–2549 (2002).

265. Ubelis, A. P. Temperature Dependence of the Saturated Vapor Pressure of Tellurium. *J. Eng. Phys.* **42,** 309–315 (1982).

266. Langford, J. I. & Wilson, A. J. C. Scherrer after Sixty Years: A Survey and Some New Results in the Determination of Crystallite Size. *J. Appl. Crystallogr.* **11,** 102–113 (1978).

267. Pei, Y., Lalonde, A. D., Heinz, N. A. & Snyder, G. J. High Thermoelectric Figure of Merit in PbTe Alloys Demonstrated in PbTe – CdTe. *Adv. Energy Mater.* **2,** 670–675 (2012).

268. Brebrick, R. F. & Allgaier, R. S. Composition Limits of Stability of PbTe. *J. Chem. Phys.* **32,** 1826–1831 (1960).

269. Allgaier, R. S. Valence Bands in Lead Telluride. *J. Appl. Phys.* **32,** 2185 (1961).

270. Aukerman, L. W. & Willardson, R. K. High-Temperature Hall Coefficient in GaAs. *J. Appl. Phys.* **31,** 939 (1960).

271. Heremans, J. P., Thrush, C. & Morelli, D. Thermopower Enhancement in Lead Telluride Nanostructures. *Phys. Rev. B* **70,** 115334 (2004).

272. Levin, E. M., Heremans, J. P., Kanatzidis, M. G. & Schmidt-Rohr, K. Electronic Inhomogeneity in n- and p-type PbTe Detected by ^{125}Te NMR. *Phys. Rev. B* **88,** 115211 (2013).

273. Lee, Y. *et al.* Contrasting Role of Antimony and Bismuth Dopants on the Thermoelectric Performance of Lead Selenide. *Nat. Commun.* **5,** 3640 (2014).

274. Fritts, R. Design Parameters for Optimizing the Efficiency of Thermoelectric Generators Utilizing p-type and n-type Lead Telluride. *Am. Inst. Electr. Eng. Part I Commun. Electron. Trans.* **78,** 817–820 (1960).

275. Allgaier, R. S. & Scanlon, W. W. Mobility of Electrons and Holes in PbS, PbSe, and PbTe Between Room Temperature and 4.2-Degrees-K. *Phys. Rev.* **388,** 1029 (1958).

276. Strauss, A. J. Effect of Pb- and Te-Saturation on Carrier Concentrations in Impurity-Doped PbTe. *J. Electron. Mater.* **2,** 553–569 (1973).

277. Christakudi, T. A., Christakudis, G. C. & Borissova, L. D. Thermoelectric Power of Solid Solutions (PbTe)1-x(Bi_2Te_3)x with 0<x<0.02. *Phys. Status Solidi* **537,** 537–544 (1995).

278. Yang, J., Chen, R., Fan, X., Bao, S. & Zhu, W. Thermoelectric Properties of Silver-Doped n-type Bi2Te3-Based Material Prepared by Mechanical Alloying and Subsequent Hot Pressing. *J. Alloys Compd.* **407,** 330–333 (2006).

279. Zhu, P. *et al.* Composition-Dependent Thermoelectric Properties of PbTe Doped with Bi_2Te_3. *J. Alloys Compd.* **420,** 233–236 (2006).

280. Crocker, A. The Role of Sodium in Lead Telluride. *J. Phys. Chem. Solids* **28,** 1903–1912 (1967).

281. Crocker, A. & Dorning, B. Diffusion of Sodium in Lead Telluride. *J. Phys. Chem. Solids* **29,** 155–161 (1968).

282. Firsova, L. P. & Simirskaya, G. P. Radiochemical Investigation of the Dissolution and Migration Processes of Bismuth in Lead Telluride and Solid Solutions Based on It. *Sov. Radiochem.* **30,** 143–146 (1988).

283. Ikeda, T., Toussaint, M. B., Bergum, K., Iwanaga, S. & Jeffrey Snyder, G. Solubility and Formation of Ternary Widmanstätten Precipitates in PbTe in the Pseudo-Binary PbTe–Bi_2Te_3 System. *J. Mater. Sci.* **46,** 3846–3854 (2011).

284. Ramasamy, K. *et al.* A New Route to Lead Chalcogenide Nanocrystals. *Eur. J. Inorg. Chem.* **2011,** 5196–5201 (2011).

285. Jana, N., Gearheart, L. & Murphy, C. Wet Chemical Synthesis of High Aspect Ratio Cylindrical Gold Nanorods. *J. Phys. Chem. B* **105,** 4065–4067 (2001).

286. Jana, N. R., Gearheart, L. & Murphy, C. J. Wet Chemical Synthesis Of Silver Nanorods and Nanowires of Controllable Aspect Ratio. *Chem. Commun.* 617–618 (2001).

287. Jana, N., Gearheart, L. & Murphy, C. Seed-Mediated Growth Approach for Shape-Controlled Synthesis of Spheroidal and Rod-Like Gold Nanoparticles Using a Surfactant Template. *Adv. Mater.* **13,** 1389–1393 (2001).

288. Magdassi, S., Grouchko, M., Berezin, O. & Kamyshny, A. Triggering the Sintering of Silver Nanoparticles at Room Temperature. *ACS Nano* **4,** 1943–1948 (2010).

289. Senthil kumaran, C. K. *et al.* Synthesis and Characterization of Selenium Nanowires. *ISRN Nanotechnol.* **2011,** 589073 (2011).

290. Li, Q. & Yam, V. W.-W. High-Yield Synthesis of Selenium Nanowires in Water at Room Temperature. *Chem. Commun.* **1,** 1006–1008 (2006).

291. Yang, L. *et al.* Trifold Tellurium One-Dimensional Nanostructures and Their Formation Mechanism. *Cryst. Growth Des.* **13,** 4796–4802 (2013).

292. See, K. C. *et al.* Water-Processable Polymer-Nanocrystal Hybrids for Thermoelectrics. *Nano Lett.* **10,** 4664–4667 (2010).

293. Xi, G., Wang, C., Wang, X., Qian, Y. & Xiao, H. Te/Carbon and Se/Carbon Nanocables: Size-Controlled in Situ Hydrothermal Synthesis and Applications in Preparing Metal M/Carbon Nanocables (M = Tellurides and Selenides). *J. Phys. Chem. C* **112,** 965–971 (2008).

294. Yong, S., Muralidharan, P., Kim, D. & Kim, D. One-step Hydrothermal Synthesis of Carbon-coated PbTe Nanowires for Thermoelectric Applications. *Rev. Adv. Mater. Sci* **28,** 13–16 (2011).

295. Jiang, L., Zhu, Y.-J. & Cui, J.-B. Nanostructures of Metal Tellurides (PbTe, CdTe, $CoTe_2$, Bi_2Te_3, and Cu_7Te_4) with Various Morphologies: A General Solvothermal Synthesis and Optical Properties. *Eur. J. Inorg. Chem.* **2010,** 3005–3011 (2010).

296. Hull, K., Grebinski, J., Kosel, T. & Kuno, M. Induced Branching in Confined PbSe Nanowires. *Chem. Mater.* **17,** 4416–4425 (2005).

297. Kuno, M., Ahmad, O., Protasenko, V., Bacinello, D. & Kosel, T. H. Solution-Based Straight and Branched CdTe Nanowires. *Chem. Mater.* **18,** 5722–5732 (2006).

298. Jiang, F., Liu, J., Li, Y. & Fan, L. Ultralong CdTe Nanowires: Catalyst-Free Synthesis and High-Yield Transformation into Core–Shell Heterostructures. *Adv. Funct. Mater.* **22,** 2402–2411 (2012).

299. Gong, H. *et al.* Facile Aqueous Synthesis and Growth Mechanism of CdTe Nanorods. *Nanotechnology* **19,** 445603 (2008).

300. Tang, Z., Kotov, N. a & Giersig, M. Spontaneous Organization of Single CdTe Nanoparticles into Luminescent Nanowires. *Science.* **297,** 237–240 (2002).

301. Hou, T.-C. *et al.* Nanogenerator Based on Zinc Blende CdTe Micro/Nanowires. *Nano Energy* **2,** 387–393 (2013).

302. Kamat, P. V. Meeting the Clean Energy Demand : Nanostructure Architectures for Solar Energy. *J. Phys. Chem. C* **111,** 2834–2860 (2007).

303. Hillhouse, H. W. & Beard, M. C. Solar Cells from Colloidal Nanocrystals: Fundamentals, Materials, Devices, and Economics. *Curr. Opin. Colloid Interface Sci.* **14,** 245–259 (2009).

304. Jasieniak, J., Califano, M. & Watkins, S. E. Size-Dependent Valence and Conduction Band-Edge Energies of Semiconductor Nanocrystals. *ACS Nano* **5,** 5888–5902 (2011).

305. Tao, H. *et al.* Solution Grown Se/Te Nanowires: Nucleation, Evolution, and The Role of Triganol Te seeds. *Nanoscale Res. Lett.* **4,** 963–970 (2009).

306. Lu, Q., Gao, F. & Komarneni, S. Biomolecule-Assisted Reduction in the Synthesis of Single-Crystalline Tellurium Nanowires. *Adv. Mater.* **16,** 1629–1632 (2004).

307. Bubnova, O. & Crispin, X. Towards Polymer-Based Organic Thermoelectric Generators. *Energy Environ. Sci.* **5,** 9345–9362 (2012).

308. Yee, S. K., Coates, N. E., Majumdar, A., Urban, J. J. & Segalman, R. a. Thermoelectric Power Factor Optimization in PEDOT:PSS Tellurium Nanowire Hybrid Composites. *Phys. Chem. Chem. Phys.* **15,** 4024–4032 (2013).

309. Coates, N. E. *et al.* Effect of Interfacial Properties on Polymer-Nanocrystal Thermoelectric Transport. *Adv. Mater.* **25,** 1629–2633 (2013).

310. He, M. *et al.* Thermopower Enhancement in Conducting Polymer Nanocomposites via Carrier Energy Scattering at the Organic–Inorganic Semiconductor Interface. *Energy Environ. Sci.* **5,** 8351–8358 (2012).

311. Zhang, B., Sun, J., Katz, H. E., Fang, F. & Opila, R. L. Promising Thermoelectric Properties of Commercial PEDOT:PSS Materials and Their Bi_2Te_3 Powder Composites. *ACS Appl. Mater. Interfaces* **2,** 3170–3178 (2010).

312. Kato, K. *et al.* Flexible Porous Bismuth Telluride Thin Films with Enhanced Figure of Merit using Micro-Phase Separation of Block Copolymer. *Adv. Mater. Interfaces* **1,** 1300015 (2014).

313. Yang, Y., Lin, Z.-H., Hou, T., Zhang, F. & Wang, Z. L. Nanowire-Composite Based Flexible Thermoelectric Nanogenerators and Self-Powered Temperature Sensors. *Nano Res.* **5,** 888–895 (2012).

314. Chen, J. *et al.* Superlow Thermal Conductivity 3D Carbon Nanotube Network for Thermoelectric Applications. *ACS Appl. Mater. Interfaces* **4,** 81–86 (2011).

315. Meng, C., Liu, C. & Fan, S. A Promising Approach to Enhanced Thermoelectric Properties Using Carbon Nanotube Networks. *Adv. Mater.* **22,** 535–539 (2010).

316. Hewitt, C. a. *et al.* Varying the Concentration of Single Walled Carbon Nanotubes in Thin Film Polymer Composites, and its Effect on Thermoelectric Power. *Appl. Phys. Lett.* **98,** 183110 (2011).

317. Liu, J., Sun, J. & Gao, L. Flexible Single-Walled Carbon Nanotubes/Polyaniline Composite Films and Their Enhanced Thermoelectric Properties. *Nanoscale* **3,** 3616–3619 (2011).

318. Yu, C., Kim, Y. S., Kim, D. & Grunlan, J. C. Thermoelectric Behavior of Segregated-Network Polymer Nanocomposites. *Nano Lett.* **8,** 4428–4432 (2008).

319. Yao, Q., Chen, L., Zhang, W., Liufu, S. & Chen, X. Enhanced Thermoelectric Performance of Single-Walled Carbon Nanotubes/Polyaniline Hybrid Nanocomposites. *ACS Nano* **4,** 2445–2451 (2010).

320. Kim, D., Kim, Y., Choi, K., Grunlan, J. & Yu, C. Improved Thermoelectric Behavior of Nanotube-Filled Polymer Composites with Poly (3, 4-ethylenedioxythiophene) Poly (styrenesulfonate). *ACS Nano* **4,** 513–523 (2010).

321. Yu, C., Choi, K., Yin, L. & Grunlan, J. C. Light-Weight Flexible Carbon Nanotube Based Organic Composites with Large Thermoelectric Power Factors. *ACS Nano* **5,** 7885–7892 (2011).

322. Bounioux, C. *et al.* Thermoelectric Composites of Poly(3-hexylthiophene) and Carbon Nanotubes with a Large Power Factor. *Energy Environ. Sci.* **6,** 918–925 (2013).

323. Moriarty, G. P., Briggs, K., Stevens, B., Yu, C. & Grunlan, J. C. Fully Organic Nanocomposites with High Thermoelectric Power Factors by using a Dual-Stabilizer Preparation. *Energy Technol.* **1,** 265–272 (2013).

324. Abad, B. *et al.* Improved Power Factor of Polyaniline Nanocomposites with Exfoliated Graphene Nanoplatelets (GNPs). *J. Mater. Chem. A* **1,** 10450–10457 (2013).

325. Wang, L. *et al.* Large Thermoelectric Power Factor in Polyaniline/Graphene Nanocomposite Films Prepared by Solution-Assistant Dispersing Method. *J. Mater. Chem. A* **2,** 11107–11113 (2014).

326. Wu, Y. & Finefrock, S. W. Flexible Polymer-Based Thermoelectric Materials and Fabrics Incorporating the Same. (2014).

327. Liang, D., Yang, H., Finefrock, S. W. & Wu, Y. Flexible Nanocrystal-Coated Glass Fibers for High-Performance Thermoelectric Energy Harvesting. *Nano Lett.* **12,** 2140–2145 (2012).

328. Lu, L., Yi, W. & Zhang, D. L. 3ω Method for Specific Heat and Thermal Conductivity Measurements. *Rev. Sci. Instrum.* **72,** 2996–3003 (2001).

329. Moon, J. *et al.* Note: Thermal Conductivity Measurement of Individual Poly(ether ketone)/Carbon Nanotube Fibers Using a Steady-State dc Thermal Bridge Method. *Rev. Sci. Instrum.* **83,** 016103 (2012).

330. Demko, M. T. *et al.* Application of the Thermal Flash Technique for Low Thermal Diffusivity Micro/Nanofibers. *Rev. Sci. Instrum.* **80,** 036103 (2009).

331. Hou, J., Wang, X. & Zhang, L. Thermal Characterization of Submicron Polyacrylonitrile Fibers Based on Optical Heating and Electrical Thermal Sensing. *Appl. Phys. Lett.* **89,** 152504 (2006).

332. Guo, J., Wang, X., Geohegan, D. B., Eres, G. & Vincent, C. Development of Pulsed Laser-Assisted Thermal Relaxation Technique for Thermal Characterization of Microscale Wires. *J. Appl. Phys.* **103,** 113505 (2008).

333. Li, D. *et al.* Thermal Conductivity of Individual Silicon Nanowires. *Appl. Phys. Lett.* **83,** 2934–2936 (2003).

334. Shi, L. *et al.* Measuring Thermal and Thermoelectric Properties of One-Dimensional Nanostructures Using a Microfabricated Device. *J. Heat Transfer* **125,** 881–888 (2003).

335. Wang, Z. L., Tang, D. W. & Zhang, W. G. Simultaneous Measurements of the Thermal Conductivity, Thermal Capacity and Thermal Diffusivity of an Individual Carbon Fibre. *J. Phys. D. Appl. Phys.* **40,** 4686–4690 (2007).

336. Behabtu, N. *et al.* Strong, Light, Multifunctional Fibers of Carbon Nanotubes with Ultrahigh Conductivity. *Science.* **339,** 182–186 (2013).

337. Aliev, A. E. *et al.* Thermal transport in MWCNT sheets and yarns. *Carbon N. Y.* **45,** 2880–2888 (2007).

338. Feng, B., Li, Z., Zhang, X. & Peterson, G. P. Numerical Approach for the Theory of Harmonic Self-Heating Technique to Measure Thermophysical Properties of Suspended Thin Samples. *J. Vac. Sci. Technol. B Microelectron. Nanom. Struct.* **27,** 2280–2285 (2009).

339. Hopkins, P. E. & Phinney, L. M. Thermal Conductivity Measurements on Polycrystalline Silicon Microbridges Using the 3ω Technique. *J. Heat Transfer* **131,** 043201 (2009).

340. Cahill, D. G., Katiyar, M. & Abelson, J. Thermal conductivity of a-Si: H Thin Films. *Phys. Rev. B* **50,** 6077–6082 (1994).

341. Liu, W. & Balandin, A. a. Temperature Dependence of Thermal Conductivity of $Al_xGa_{1-x}N$ Thin Films Measured by the Differential 3ω Technique. *Appl. Phys. Lett.* **85,** 5230–5232 (2004).

342. Hakansson, E. *et al.* Characterization of Conducting Polymer Coated Synthetic Fabrics for Heat Generation. *Synth. Met.* **144,** 21–28 (2004).

343. Lin, T., Wang, L., Wang, X. & Kaynak, A. Polymerising Pyrrole on Polyester Textiles and Controlling the Conductivity Through Coating Thickness. *Thin Solid Films* **479,** 77–82 (2005).

344. Boakye, E., Hay, R. S. & Petry, M. D. Continuous Coating of Oxide Fiber Tows Using Liquid Precursors : Monazite Coatings on Nextel 720 ^{TM}. *J. Am. Ceram. Soc.* **82,** 2321–2331 (1999).

345. Boakye, E. E., Hay, R. S., Petry, M. D. & Parthasarathy, T. A. Zirconia – Silica – Carbon Coatings on Ceramic Fibers. *J. Am. Ceram. Soc.* **87,** 1967–1976 (2004).

346. Boakye, E. E., Hay, R. S., Mogilevsky, P. & Cinibulk, M. K. Two Phase Monazite/Xenotime $30LaPO_4$-$70YPO_4$ Coating of Ceramic Fiber Tows. *J. Am. Ceram. Soc.* **91,** 17–25 (2008).

347. Murphy, J. E. *et al.* PbTe Colloidal Nanocrystals: Synthesis, Characterization, and Multiple Exciton Generation. *J. Am. Chem. Soc.* **128,** 3241–3247 (2006).

348. Mokari, T., Zhang, M. & Yang, P. Shape, Size, and Assembly Control of PbTe Nanocrystals. *J. Am. Chem. Soc.* **129,** 9864–9865 (2007).

349. Smith, D. K., Luther, J. M., Semonin, O. E., Nozik, A. J. & Beard, M. C. Tuning the Synthesis of Ternary Lead Chalcogenide Quantum Dots by Balancing Precursor Reactivity. *ACS Nano* **5,** 183–190 (2011).

350. Luther, J. M. *et al.* Structural, Optical, and Electrical Properties of Self-Assembled Films of PbSe Nanocrystals Treated with 1,2-ethanedithiol. *ACS Nano* **2,** 271–280 (2008).

351. Luther, J. M. *et al.* Schottky Solar Cells Based on Colloidal Nanocrystal Films. *Nano Lett.* **8,** 3488–3492 (2008).

352. Wang, R. X., Tao, X. M., Wang, Y. & Wang, G. F. Electrical Properties and Fatigue Resistance of Polyamide 6,6 Fabrics with Nanocrystal Silver Coating. *J. Nanosci. Nanotechnol.* **9,** 3062–3066 (2009).

353. Collaboration: Authors and editors of the volumes III/17E-17F-41C: Lead Telluride (PbTe) Crystal Structure, Lattice Parameters, Thermal Expansion. Madelung, O., Rössler, U., Schulz, M. (ed.). SpringerMaterials - The Landolt-Börnstein Database. doi:10.1007/10681727_711

354. Corning Life Sciences. Thermal Properties of Corning Glasses. at <http://catalog2.corning.com/Lifesciences/en-US/Shopping/ProductDetails.aspx?productid=3950(Lifesciences)&categoryname=Fiberglass(Lifesciences)%7CFiberglass+Roving(Lifesciences)&activeview=techDoc>

355. Corning Life Sciences. Product Description: PYREX Fiber Glass, 8 micron. (2013).

356. American Society of Heating, Refrigerating and Air-Conditioning Engineers, I. *2009 ASHRAE Handbook - Fundamentals (I-P Edition)*. (2009).

357. Finefrock, S. W. *et al.* Measurement of Thermal Conductivity of PbTe Nanocrystal Coated Glass Fibers by the 3ω Method. *Nano Lett.* **13,** 5006–5012 (2013).

358. Lin, H., Xu, S., Li, C., Dong, H. & Wang, X. Thermal and Electrical Conduction in 6.4 nm Thin Gold Films. *Nanoscale* **5,** 4652–4656 (2013).

359. Zhang, X. *et al.* Thermal and Electrical Conductivity of a Suspended Platinum Nanofilm. *Appl. Phys. Lett.* **86,** 171912 (2005).

360. Yang, G., Migone, A. & Johnson, K. Heat Capacity and Thermal Diffusivity of a Glass Sample. *Phys. Rev. B. Condens. Matter* **45,** 157–160 (1992).

361. Log, T. & Metallinou, M. M. Thermal Conductivity Measurements Using a Short Transient Hot-Strip Method. *Rev. Sci. Instrum.* **63,** 3966–3971 (1992).

362. Miller, M. S. & Kotlar, a. J. Technique for Measuring Thermal Diffusivity/Conductivity of Small Thermal-Insulator Specimens. *Rev. Sci. Instrum.* **64,** 2954–2960 (1993).

363. Zhu, X., Finefrock, S. W. & Wu, Y. Thermoelectric (TE) Device made using PbTe Nanocrystal Coated Glass Fibers. Paper 73 (2014).

364. Taylor, P. F. & Wood, C. Thermoelectric Properties of Ag_2Te. *J. Appl. Phys.* **32,** 1–3 (1961).

365. Pei, Y., Heinz, N. a. & Snyder, G. J. Alloying to Increase the Band Gap for Improving Thermoelectric Properties of Ag_2Te. *J. Mater. Chem.* **21,** 18256–18260 (2011).

366. Liu, Y.-W. *et al.* Near-Infrared Absorption of Monodisperse Silver Telluride (Ag_2Te) Nanocrystals and Photoconductive Response of Their Self-Assembled Superlattices. *Chem. Mater.* **23,** 4657–4659 (2011).

367. Ko, D.-K., Urban, J. J. & Murray, C. B. Carrier Distribution and Dynamics of Nanocrystal Solids Doped with Artificial Atoms. *Nano Lett.* **10,** 1842–1847 (2010).

368. Urban, J. J., Talapin, D. V, Shevchenko, E. V, Kagan, C. R. & Murray, C. B. Synergism in Binary Nanocrystal Superlattices Leads to Enhanced p-type Conductivity in Self-Assembled PbTe/Ag_2Te Thin Films. *Nat. Mater.* **6,** 115–121 (2007).

369. *Plastic Material Data Sheets*. *N/A* (N/A). at <https://app.knovel.com/web/toc.v/cid:kpPMDS0001/viewerType:toc/root_slug:plastic-material-data/url_slug:plastic-material-data-sheets?b-q=material_or_substance_name:“nylon 66” AND thermal_expansion_coefficient_mf:[* TO *]&b-subscription=TRUE&b-group-by=true&b-dsQuery=?mn=nylon%2066:and:pn=thermal%20expansion%20coefficient&o=e>

370. Tsunoda, Y., Sameshima, T. & Higashi, S. Improvement of Electrical Properties of Pulsed Laser Crystallized Silicon Films by Oxygen Plasma Treatment. *Jpn. J. Appl. Phys.* **39,** 1656–1659 (2000).

371. Liu, M. & Kim, H. K. Ultraviolet Detection with Ultrathin ZnO Epitaxial Films Treated with Oxygen Plasma. *Appl. Phys. Lett.* **84,** 173–175 (2004).

372. Kim, S. *et al.* Oxygen Plasma Effects on the Electrical Conductance of Single-Walled Carbon Nanotube Bundles. *J. Phys. D. Appl. Phys.* **43,** 305402 (2010).

373. Liau, Y., Scherer, N. & Rhodes, K. Nanoscale Electrical Conductivity and Surface Spectroscopic Studies of Indium-Tin Oxide. *J. Phys. Chem. B* **105,** 3282–3288 (2001).

374. Zhang, W., Johnson, L., Silva, S. R. P. & Lei, M. K. The Effect of Plasma Modification on the Sheet Resistance of Nylon Fabrics Coated with Carbon Nanotubes. *Appl. Surf. Sci.* **258,** 8209–8213 (2012).

375. Heraeus Clevios GmbH. CLEVIOS ™ PH 1000. (2010). at <http://www.heraeus-clevios.com/media/webmedia_local/media/datenblaetter/81076210_Clevios_PH_1000_20101222.pdf>

376. Vosgueritchian, M., Lipomi, D. J. & Bao, Z. Highly Conductive and Transparent PEDOT:PSS Films with a Fluorosurfactant for Stretchable and Flexible Transparent Electrodes. *Adv. Funct. Mater.* **22,** 421–428 (2012).

377. Lipomi, D. J. *et al.* Electronic Properties of Transparent Conductive Films of PEDOT:PSS on Stretchable Substrates. *Chem. Mater.* **24,** 373–382 (2012).

378. Yip, J., Chan, K., Sin, K. M. & Lau, K. S. Low Temperature Plasma-Treated Nylon Fabrics. *J. Mater. Process. Technol.* **123,** 5–12 (2002).

379. Canal, C., Molina, R., Bertran, E. & Erra, P. Wettability, Ageing and Recovery Process of Plasma-Treated Polyamide 6. *J. Adhes. Sci. Technol.* **18,** 1077–1089 (2004).

380. Oh, K. W., Kim, S. H. & Kim, E. A. Improved Surface Characteristics and the Conductivity of Polyaniline-Nylon 6 Fabrics by Plasma Treatment. *J. Appl. Polym. Sci.* **81,** 684–694 (2001).

381. Mehrabanian, M. & Nasr-Esfahani, M. HA/Nylon 6,6 Porous Scaffolds Fabricated by Salt-Leaching/Solvent Casting Technique: Effect of Nano-Sized Filler Content on Scaffold Properties. *Int. J. Nanomedicine* **6,** 1651–1659 (2011).

382. Karakaya, I. & Thompson, W. T. The Ag-Te (Silver-Tellurium) System. *J. Phase Equilibria* **12,** 56–63 (1991).

383. Lakshminarayan, N., Radhakrishnan, M. & Balasubramanian, C. Formation, Structural and Optical Properties of Tellurium Oxide Films Deposited by a Plasma Process (PARBAD). *J. Mater. Sci.* **19,** 2368–2372 (1984).

384. Saito, K., Kobayashi, H., Nakagawa, J. & Murayama, Y. Optical Recording Medium Formed of Chalcogenide Oxide and Method for Producing the Same. (1988).

385. Cho, S. C., Hong, Y. C. & Uhm, H. S. TeO_2 Nanoparticles Synthesized by Evaporation of Tellurium in Atmospheric Microwave-Plasma Torch-Flame. *Chem. Phys. Lett.* **429,** 214–218 (2006).

386. Klecha, E., Ingert, D., Walls, M. & Pileni, M. Immunity of Coated Self-Ordered Silver Nanocrystals: A New Intrinsic Property Due to the Nanocrystal Ordering. *Langmuir* **25,** 2824–2830 (2009).

387. Klecha, E., Arfaoui, I., Richardi, J., Ingert, D. & Pileni, M.-P. 2D Silver Nanocrystal Ordering Modulated by Various Substrates and Revealed Using Oxygen Plasma Treatment. *Phys. Chem. Chem. Phys.* **13,** 2953–2962 (2011).

388. Panish, M. B. Vapor Pressur of Silver. *J. Chem. Eng. Data* **6,** 592–594 (1961).

389. Cvelbar, U., Mozetic, M. & Klanjsek-Gunde, M. Selective Oxygen Plasma Etching of Coatings. *IEEE Trans. Plasma Sci.* **33,** 236–237 (2005).

390. Diefenderfer, A. & Holton, B. *Principles of electronic instrumentation*. (Brooks/Cole, 1994). at <http://ganjeman.allalla.com/w/principles-of-electronic-instrumentation-by-a-james-diefenderfer.pdf>

391. Jiang, Xu, Lu, Xie, Huang, L. Thermoelectric Performance of PEDOTPSS. *Chinese Phys. Lett.* **25,** 2202–2205 (2008).

392. Yue, R. & Xu, J. Poly(3,4-ethylenedioxythiophene) as Promising Organic Thermoelectric Materials: A mini-review. *Synth. Met.* **162,** 912–917 (2012).

393. Madan, D., Wang, Z. & Chen, A. High Performance Dispenser Printed MA p-type $Bi_{0.5}Sb_{1.5}Te_3$ Flexible Thermoelectric Generators for Powering Wireless Sensor Networks. *ACS Appl. Mater. Interfaces* **5,** 11872–11876 (2013).

394. Suemori, K., Hoshino, S. & Kamata, T. Flexible and Lightweight Thermoelectric Generators Composed of Carbon Nanotube–Polystyrene Composites Printed on Film Substrate. *Appl. Phys. Lett.* **103,** 153902 (2013).

395. Yadav, A., Pipe, K. P. & Shtein, M. Fiber-Based Flexible Thermoelectric Power Generator. *J. Power Sources* **175,** 909–913 (2008).

396. Yu, C., Murali, A., Choi, K. & Ryu, Y. Air-Stable Fabric Thermoelectric Modules Made of n- and p-type Carbon Nanotubes. *Energy Environ. Sci.* **5,** 9481–9486 (2012).

397. Hewitt, C. a *et al.* Multilayered Carbon Nanotube/Polymer Composite Based Thermoelectric Fabrics. *Nano Lett.* **12,** 1307–1310 (2012).

398. Søndergaard, R. R., Hösel, M., Espinosa, N., Jørgensen, M. & Krebs, F. C. Practical Evaluation of Organic Polymer Thermoelectrics by Large-Area R2R Processing on Flexible Substrates. *Energy Sci. Eng.* **1,** 81–88 (2013).

399. Finefrock, S. W., Yang, H., Fang, H., Wu, Y. Thermoelectric Properties of Solution Synthesized Nanostructured Materials. Ann. Rev. Chem. Biomol. Eng. (submitted)

VITA

VITA

Scott Finefrock completed a B.S. degree at Case Western Reserve University from 2005 to 2010. During that time, he gained practical research and engineering experience at the Bridgestone Americas Center for Research and Technology, Syracuse University, Invensys Process Systems, and at his home university. Due to his excellent academic performance, he received four awards including the American Institute of Chemical Engineers' Certificate of Achievement and the A.W. Smith Prize. In 2010, he joined Yue Wu's research group at Purdue University where he studied nanostructured thermoelectric materials. Through his research, Scott gained proficiency in a number of skills including solution synthesis, thin film coating, high temperature processing, electron microscopy, X-ray diffraction, and others. During his Ph.D., he completed two summers of research in close collaboration with the Air Force Research Laboratory through the American Society of Engineering Education's Summer Faculty Fellowship Program. After four years at Purdue, Scott moved with Yue Wu to Iowa State University for the remainder of his degree.